Quantifications of global chemical weathering fluxes applying new lithological maps and new parameterizations

Dissertation

zur Erlangung des Doktorgrades der Naturwissenschaften

an der Fakultät für Mathematik, Informatik und Naturwissenschaften

Fachbereich Geowissenschaften

der Universität Hamburg

vorgelegt von

Janine Börker

aus

Osterode am Harz

Hamburg, 2019

Accepted as Dissertation at the Department of Earth Sciences

Day of oral defense:	21.05.2019
Reviewers:	Prof. Dr. Jens Hartmann
	Prof. Dr. Victor Brovkin
Chair of the Subject Doctoral Committee:	Prof. Dr. Dirk Gajewski
Dean of Faculty of MIN:	Prof. Dr. Heinrich Graener

Table of Contents

Abstract

The quantification of chemical weathering fluxes plays an important role for many processes in the Earth system. Chemical weathering regulates, for example, the pCO_2 in the atmosphere over long geological time scales, influences the ocean carbon cycle or releases nutrients that are then available for ecosystems. Chemical weathering is dependent on several parameters, like water fluxes, temperature or the type of lithology. Most weathering models distinguish between carbonate and silicate weathering. In order to quantify the proportion and distribution of carbonates and silicate rocks on the global land surface, global lithological maps are the basis for the research. A continuous improvement of these maps is needed to further enhance weathering models.

For this purpose a new global map database was developed, that reports on the distribution and types of unconsolidated sediments, which covers in this map approximately half of the global land surface. The Global Unconsolidated Sediments Map database (GUM) comprises 911,551 polygons and provides information about sediment types and subtypes, grain sizes, mineralogy, age and thickness of the sediments.

The GUM allowed for analyzing the weathering behavior of loess sediments, which are highly dynamic eolian sediments. It could be shown that loess sediments show a similar weathering pattern than carbonate sedimentary rocks and a new parameterization for loess-derived alkalinity fluxes was developed. By applying this new function, the global alkalinity flux rates increase by about 16% as if compared to neglecting loess sediments. Subsequently, the alkalinity fluxes of loess deposits were quantified for the Last Glacial Maximum and the Mid-Holocene as well. It could be shown that increased alkalinity fluxes from loess deposits during the LGM are compensating for the general decreased alkalinity fluxes derived by silicate weathering and are hence keeping the global alkalinity fluxes stable between glacial-interglacial time scales.

In the third part of this thesis, the quantification of alkalinity fluxes from basaltic regions was improved by considering not only temperature, but also the age of the surface basaltic rocks. A study of alkalinity fluxes from 33 basaltic volcanic areas shows that active Holocene basaltic areas provide ~10 times higher alkalinity flux rates than inactive volcanic fields. This observation led to the development of a new scaling law that increases global CO_2 consumption rates by the consideration of young volcanic systems by about 60%.

This thesis shows that global weathering models still can be improved. Enhanced global lithological maps, providing different kinds of information about sediments and rocks are needed to better understand regional and local processes and to be able to upscale them properly to the global scale. By applying enhanced maps, it could be shown that loess sediments and young basaltic volcanic fields increase global alkalinity fluxes, which could be especially interesting for past times in the Earth's history, since both, loess sediments and volcanoes, are highly dynamic in their evolution.

Zusammenfassung

Die Quantifizierung von chemischen Verwitterungsflüssen spielt eine wichtige Rolle in vielen verschieden Prozessen des Erdsystems. Die chemische Verwitterung reguliert zum Beispiel über lange geologische Zeitskalen den CO_2-Partialdruck in der Atmosphäre, beeinflusst den Kohlenstoff-Kreislauf des Ozeans oder setzt Nährstoffe frei, welche dann für Ökosysteme zur Verfügung stehen. Die chemische Verwitterung hängt von verschiedenen Parametern ab, wie dem Wasserfluss, der Temperatur oder der Art der Lithologie. Die meisten Verwitterungsmodelle unterscheiden zwischen Karbonat- und Silikatverwitterung. Um Anteile und Verbreitungen von karbonatischen und silikatischen Gesteinen auf der globalen Landoberfläche zu bestimmen, bilden globale lithologische Karten die Basis für die Forschung. Eine andauernde Ergänzung dieser Karten ist nötig, um die Verwitterungsmodelle weiter zu verbessern.

Für diesen Zweck wurde ein neuer globaler Karten-Datensatz erstellt, der Informationen über die Verbreitung und Arten von unverfestigten Sedimenten liefert, und ungefähr die Hälfte der globalen Landoberfläche abdeckt. Der globale Datensatz „Global Unconsolidated Sediments Map database (GUM)“ verfügt über 911,551 Polygone und hält Informationen über die Arten und Unterarten, die Korngröße, die Mineralogie, das Alter und die Mächtigkeit der Sedimente bereit.

Die GUM-Datenbank konnte benutzt werden, um das Verwitterungsverhalten von Lösssedimenten, welche hoch dynamische äolische Sedimente sind, zu analysieren. Es konnte gezeigt werden, dass Lösssedimente ein ähnliches Verwitterungsverhalten wie Karbonatgesteine aufweisen und es wurde eine neue Parametrisierung für Löss-Alkalinitätsflüsse entwickelt. Durch die Anwendung dieser Funktion steigt die globale Alkalinitätsflussrate um 16%, verglichen zu einem Szenario ohne Lösssedimente. Die Verwitterungsflüsse von Lössablagerungen wurden anschließend auch für das Letzteiszeitliche Maximum (LGM) und für das Mittlere Holozän bestimmt. Es konnte aufgezeigt werden, dass erhöhte Alkalinitätsflüsse durch die Verwitterung von Lösssedimenten während des LGM die generell niedrigeren Alkalinitätsflüsse von der Silikatverwitterung kompensieren können und somit die globalen glazial-interglazialen Alkalinintätsflüsse stabil hält.

Im dritten Teil dieser Arbeit wurde die Quantifizierung von Alkalinitätsflüssen von basaltischen Gebieten durch die Berücksichtigung von nicht nur Temperatur, sondern auch des Alters der oberflächlichen basaltischen Gesteine, erweitert. Eine Studie von Alkalinititätsflüssen von 33 basaltischen Vulkangebieten zeigt, dass aktive holozäne basaltische Gebiete ungefähr 10-mal höhere Alkalinitätsflüsse aufweisen als inaktive Vulkangebiete. Eine neue Funktion zur Bestimmung von Alkalinitätsflussraten von basaltischen Gebieten wurde entwickelt, die die globalen CO_2-Konsumierungsrate durch die Berücksichtigung der jungen Vulkangebiete um ungefähr 60% erhöht.

Diese Arbeit zeigt, dass globale Verwitterungsmodelle stetig verbessert werden können. Detailliertere globale lithologische Karten, welche verschiedene Informationen zu Sedimenten und Gesteinen liefern, werden benötigt, um regionale und lokale Prozesse besser zu verstehen und um diese verständlicher auf die globale Skala zu projizieren. Durch die Anwendung detaillierterer Karten konnte gezeigt werden, dass Lösssedimente und junge basaltische Vulkangebiete die

globalen Alkalinitätsflüsse erhöhen, welches besonders für vergangene Zeiten in der Erdgeschichte interessant sein könnte, da beide, Lösssedimente und Vulkane, hochdynamisch in ihrer Entwicklung sind.

List of publications

The present thesis contains three chapters, that are either published as articles in peer-reviewed journals or that are prepared for submission. The PhD.-candidate contributed to the following articles. Detailed information about the different contributions are listed in Appendix D:

Börker, J., Hartmann, J., Amann, T., and Romero-Mujalli, G.: Terrestrial Sediments of the Earth: Development of a Global Unconsolidated Sediments Map Database (GUM), Geochemistry, Geophysics, Geosystems, 19, 997-1024, 10.1002/2017gc007273, 2018.

(Chapter 2 of this thesis)

Börker, J., Hartmann, J., Amann, T., Romero-Mujalli, G., 2018. Global Unconsolidated Sediments Map Database v1.0 (shapefile and gridded to 0.5° spatial resolution), https://doi.org/10.1594/PANGAEA.884822, Supplement to: Börker, J., Hartmann, J., Amann, T., and Romero-Mujalli, G.: Terrestrial Sediments of the Earth: Development of a Global Unconsolidated Sediments Map Database (GUM), Geochemistry, Geophysics, Geosystems, 19, 997-1024, 10.1002/2017gc007273, 2018.

Börker, J., Hartmann, J., Romero-Mujalli, G., and Li, G.: Aging of basalt volcanic systems and decreasing CO2 consumption by weathering, Earth Surf. Dynam., 7, 191-197, 10.5194/esurf-7-191-2019, 2019.

(Chapter 4 of this thesis)

Huscroft, J., Gleeson, T., Hartmann, J., and **Börker, J.**: Compiling and mapping global permeability of the unconsolidated and consolidated Earth: GLobal HYdrogeology MaPS 2.0 (GLHYMPS 2.0), Geophysical Research Letters, 45, 1897-1904, 10.1002/2017GL075860, 2018.

Romero-Mujalli, G., Hartmann, J., **Börker, J.**, Gaillardet, J., and Calmels, D.: Ecosystem controlled soil-rock pCO2 and carbonate weathering – Constraints by temperature and soil water content, Chemical Geology, https://doi.org/10.1016/j.chemgeo.2018.01.030, 2018.

Romero-Mujalli, G., Hartmann, J., and **Börker, J.**: Temperature and CO2 dependency of global carbonate weathering fluxes – Implications for future carbonate weathering research, Chemical Geology, https://doi.org/10.1016/j.chemgeo.2018.08.010, 2018.

In preparation:

Börker, J., Hartmann, J., Amann, T., Romero-Mujalli, G., Moosdorf, N. and Jenkins, C.: Chemical weathering of loess during the Last Glacial Maximum, Mid-Holocene and today.

(Chapter 3 of this thesis)

1 Introduction

In Earth System Sciences many natural environments, like the solid Earth, the atmosphere, the ocean or the biosphere, are linked to each other. Therefore, it is important to investigate processes that bridge the gap between different disciplines to understand the Earth System. One important part is the study of rock weathering, which interacts with all of the above named environments. Quantifying chemical weathering fluxes from the land to the ocean is an essential component in studies of the Earth's climate or global elemental cycles (Berner et al., 1983; Hartmann et al., 2014b; Walker et al., 1981). Via chemical rock weathering, carbon from the atmosphere is fixed and transported as bicarbonate ions to the oceans (Bluth and Kump, 1994; Gaillardet et al., 1999) where the carbon precipitates again as carbonate mineral and is hence stored over long time scales (Berner et al., 1983; Bluth and Kump, 1994).

The ocean carbon cycle is directly affected by chemical rock weathering, e.g. ocean acidification can be buffered. Besides, chemical rock weathering releases nutrients that are then available for ecosystems (Hartmann et al., 2013). These effects of chemical weathering fluxes on other Earth Systems have yet to be better understood and should be considered in interdisciplinary studies. Therefore, improving global weathering models, which predict chemical weathering fluxes, is an imperative step in Earth System Sciences.

1.1 Global chemical weathering models

Global chemical weathering models are mostly based on observed river water chemical data and typically dependent on the type of lithology and runoff (Amiotte-Suchet and Probst, 1995; Bluth and Kump, 1994; Hartmann, 2009; Hartmann and Moosdorf, 2011; Meybeck, 1987). Other factors that regulate rock weathering, and are often co-dependent, are: land temperature, the type of soil that is overlaying the bedrock (Goll et al., 2014; Hartmann et al., 2014b), the tectonic setting (Hartmann, 2009; Stallard, 1995) and the land cover (Moosdorf et al., 2011).

Weathering models generally distinguish between silicate and carbonate weathering. While silicate rock weathering (eq.1) consumes CO_2 from the atmosphere over longer timescales, like millions of years, carbonate rock weathering releases the consumed CO_2 again, when it precipitates as carbonate mineral in the ocean (eq.2), and is hence binding the CO_2 only for hundreds to thousands of years (Berner et al., 1983).

$$MgSiO_3 + 2CO_2 + H_2O \leftrightarrow Mg^{2+} + 2HCO_3^- + SiO_2 \leftrightarrow MgCO_3 + SiO_2 + CO_2 + H_2O \quad \text{(eq.1)}$$

$$CaCO_3 + CO_2 + H_20 \leftrightarrow Ca^{2+} + 2HCO_3^- \leftrightarrow CaCO_3 + CO_2 + H_2O \quad \text{(eq.2)}$$

Although weathering models can provide information about elemental cycles as well, like the silica cycle (Beusen et al., 2009) or the phosphorus cycle (Hartmann et al., 2014b), in this thesis only

alkalinity fluxes are quantified, which can be used to determine global CO_2 consumption rates. The latter is especially important for Earth System models investigating global climate changes. For simplicity, alkalinity fluxes are considered as equal to CO_2 consumption rates for silicate weathering. On the contrary, for carbonate weathering CO_2 consumption rates are equal to only half of the alkalinity fluxes (eq. 2) (Amiotte-Suchet and Probst, 1995). For a reasonable quantification of global alkalinity fluxes and hence CO_2 consumption rates on a global scale, it is necessary to know about the proportions of weathering fluxes from silicate and carbonate weathering. Therefore, global lithological maps are needed, which report on types and characteristics of different lithologies.

1.2 Global lithological maps

Global maps, which hold information on the geospatial distribution to analyze and quantify weathering fluxes from specific lithological rocks and sediments, build the basis for the research. Global maps are not only important for the modelling of weathering fluxes but they also serve for developing hydrological maps, like permeability maps (Gleeson et al., 2014), or for substrate analyses for ecosystems (Porder et al., 2007). Regional small-scale lithological maps help to study processes within smaller catchments and to study the weathering of monolithic lithologies.

Previous maps of global lithology that were used for the calculation of global weathering fluxes are, for instance, the ones from Bluth and Kump (1991), Amiotte Suchet et al. (2003), Dürr et al. (2005) and Hartmann and Moosdorf (2012), which mostly represent the bedrock properties of the Earth's surface. Global detailed maps reporting on the distribution of sediments are missing. Although there exist, for instance, a map reporting on loess sediments in Europe (Haase et al., 2007), global compilations of loess deposits are coarse and do not represent properly the geospatial extent of loess sediments.

Nevertheless, compiling global lithological maps and homogenizing different input datasets into one database is a challenging task. Geological definitions can vary from region to region and compiling a global map database is a semantic challenge as well. Besides, many maps still do not exist in a digital format and have to be digitized in order to be able to use their data in a global database. Still, global compilations of maps can be improved, either by refining the map scales or by adding more information to lithological classes, like physical parameters or geochemical properties of the rocks and sediments. Distinguishing between more classes and subclasses allows for more detailed investigations into global weathering fluxes.

1.3 Research Gaps

Global quantifications of weathering fluxes can be improved by the consideration of sediment weathering. Most of the above named models that quantify global weathering fluxes do not consider unconsolidated sediments properly. In contrast to consolidated rocks, the sedimentary

patterns that overlay the bedrock are highly dynamic and could therefore influence weathering fluxes on short periods, like glacial-interglacial timescales. Loess sediments, which might contribute significantly to global weathering fluxes, are especially of great interest (Goddéris et al., 2013; Kump and Alley, 1994). Because previous loess maps are either not covering the entire globe (Haase et al., 2007) or are at a very coarse scale (Muhs et al., 2014), it is important to obtain a more refined image on the loess distribution. Moreover, it is important to classify loess deposits homogeneously since definitions of loess can vary. Therefore, in order to analyze loess weathering fluxes, a detailed global map representing the geospatial distribution of loess deposits had to be compiled.

Contributions to weathering fluxes from loess deposits have not yet been quantified sufficiently on a global scale. Therefore, the loess weathering behavior has to be tested, especially regarding possible carbonate weathering occurring in loess sediments. The latter is of interest because carbonate minerals weather comparably fast and are easily dissolvable (Gaillardet et al., 2018). They can contribute up to 34-50% to global CO_2 consumption rates at short time scales (Gaillardet et al., 1999; Hartmann et al., 2009). It has to be verified whether weathering fluxes from loess deposits show a similar signature to weathering fluxes from carbonate sedimentary rocks, and their contribution to global alkalinity fluxes has to be determined. Therefore, it is necessary to find a function for loess-derived alkalinity fluxes to predict global alkalinity fluxes. Moreover, it has to be tested if global alkalinity fluxes and CO_2 consumption rates have changed during glacial-interglacial timescales and how much loess weathering contributes to the global weathering flux budget. During the Last Glacial Maximum (LGM), sea level was lower and hence new continental land area was exposed for terrestrial weathering. The lithological patterns, especially the carbonate outcrops on the exposed continental shelf areas, have to be quantified to predict global weathering fluxes.

Besides carbonatic lithologies, basaltic areas strongly contribute to global alkalinity fluxes and hence CO_2 consumption rates. The weathering fluxes from basaltic regions contribute over significantly to global CO_2 consumption rates: about 25-35% of the total CO_2 consumption by silicate weathering (Dessert et al., 2003; Gaillardet et al., 1999; Hartmann et al., 2009) and can be seen as a hotspot system of silicate weathering. Young active volcanic regions provide even higher alkalinity fluxes (Li et al., 2016). It remains to be clarified how this increase in global alkalinity fluxes by young active volcanic basalt regions can be parameterized by a new scaling law considering the surface age distribution of the basaltic rocks and their contribution to alkalinity fluxes, and CO_2 consumption rates have to be quantified on a global scale. Especially for longer timescales than glacial-interglacial, the global alkalinity fluxes and CO_2 consumption rates might have been changed significantly during periods of strong volcanic activity in the past (Schaller et al., 2012).

1.3 Thesis overview

The objectives of this thesis are to investigate how hotspot areas of weathering, like loess weathering and basaltic weathering from young volcanic systems, can be represented in global weathering models for the first time. It shall be tested how dynamic sediments, like loess deposits, contribute to global weathering fluxes and if this contribution changes for different time slices in the past. Besides, it is examined how alkalinity fluxes derived from the weathering of basaltic regions differ regarding the age of their volcanic system.

1. In the first part of this thesis, the development of the new unconsolidated sediments map database is described, which builds the basis for the following chapters.
2. The second part of the thesis analyses the chemical weathering of loess sediments and the contribution to global alkalinity fluxes. Results obtained by applying a new loess weathering parameterization, which quantifies alkalinity fluxes from loess sediments, are compared for three different scenarios: the Last Glacial Maximum, the Mid-Holocene and for the present-day.
3. The last part of this thesis investigates alkalinity fluxes from young basaltic areas based on regional lithological maps of volcanic regions. With a new scaling law for alkalinity fluxes from basaltic regions and a modified new global basalt map, the contribution to global alkalinity fluxes is quantified globally and is compared with previous basalt weathering models.

2 Development of the Global Unconsolidated Sediment Map database (GUM)

This chapter has been published as: Börker, J., Hartmann, J., Amann, T., and Romero-Mujalli, G.: Terrestrial Sediments of the Earth: Development of a Global Unconsolidated Sediments Map Database (GUM), Geochemistry, Geophysics, Geosystems, 19, 997-1024, 10.1002/2017gc007273, 2018.

2.1 Abstract

Mapped unconsolidated sediments cover half of the global land surface. They are of considerable importance for many Earth surface processes like weathering, hydrological fluxes or biogeochemical cycles. Ignoring their characteristics or spatial extent may lead to misinterpretations in Earth System studies. Therefore, a new Global Unconsolidated Sediment Map database (GUM) was compiled, using regional maps specifically representing unconsolidated and quaternary sediments. The new GUM database provides insights into the regional distribution of unconsolidated sediments and their properties. The GUM comprises 911,551 polygons and describes not only sediment types and subtypes, but also parameters like grain size, mineralogy, age and thickness where available. Previous global lithological maps or databases lacked detail for reported unconsolidated sediment areas or missed large areas, and reported a global coverage of 25 to 30%, considering the ice-free land area. Here, alluvial sediments cover about 23% of the mapped total ice-free area, followed by aeolian sediments (~21%), glacial sediments (~20%), and colluvial sediments (~16%). A specific focus during the creation of the database was on the distribution of loess deposits, since loess is highly reactive and relevant to understand geochemical cycles related to dust deposition and weathering processes. An additional layer compiling pyroclastic sediment is added, which merges consolidated and unconsolidated sediments. The compilation shows latitudinal abundances of sediment types related to climate of the past. The GUM database is available at the PANGAEA database (https://doi.org/10.1594/PANGAEA.884822).

2.2 Introduction

Numerous global maps focus on bedrock lithology or soil property distributions. Although unconsolidated sediments cover a substantial proportion of the land surface, a global scale high-resolution map or database, describing the multitude of unconsolidated sediments and their properties, is missing. They control weathering (Goddéris et al., 2013; Hartmann, 2009; Hartmann and Moosdorf, 2011; Moosdorf et al., 2011; Selvaraj and Chen, 2006) and hydrological fluxes (Gleeson et al., 2014; Gleeson et al., 2011), while at the same time they are the substrate for ecosystems, which influence biogeochemical cycles and feedback processes in the Earth system (e.g., Porder et al., 2007). Distribution patterns, thicknesses of sediments and grain size distribution provide insights into dynamical sedimentation processes, as well as erosion patterns and climatic conditions in the past (Muhs and Bettis, 2003; Muhs and Bettis, 2000).

In addition, a precise understanding of the layer between bedrock and soil is needed to assess the global water cycle and specifically water resources for anthropogenic needs (Brantley et al., 2007; de Graaf et al., 2017; Huscroft et al., 2018). For example, global permeability maps were derived from global lithological databases (Gleeson et al., 2014; Gleeson et al., 2011; Huscroft et al., 2018), to improve global water cycle models (de Graaf et al., 2017). These can be advanced by adding refined information on unconsolidated sediments above the bedrock. A more detailed picture is of particular interest since previous global lithological databases reported unconsolidated sediments for large areas, 24.6% of global land (Hartmann and Moosdorf, 2012) or 29.7% of the ice-free land surface (Dürr et al., 2005). However, some areas of the previously published map databases do not include unconsolidated sediments, but provide information on lithological units located below these sediments. To close this gap, an extensive search for regional maps specifically representing unconsolidated sediments was conducted. Based on the new database presented, a second version of the global hydrological maps (GLHYMPS2.0) was created, including grain size distribution (accompanying publication: Huscroft et al. (2018)).

The presented **G**lobal **U**nconsolidated sediment **M**ap database (GUM) focuses on the distribution of loess, and various other sediment types like highly reactive pyroclastic material, glacial sediments (e.g., till or glacially derived peat deposits), alluvial sediments or dune sands. As almost any global map, this work relies on information from heterogenic regional sources. To ensure a unified map, data were re-structured and categorized into a harmonized global scheme. Since availability and quality of data varies with region, additional global map sources were used to fill gaps.

2.3 Methods

The new global map database comprises all kinds of unconsolidated sediments, which are exposed on today's land surface. Furthermore, it contains information about evaporitic, biogenic deposits (e.g., reefs) and water and ice bodies, but no laterites or other residual deposits.

The GUM was derived by different types of input data sets. Preferred data sources were maps of quaternary sediments. If not available, general geological maps that provided both kinds of information, bedrock and sediments, were chosen. In addition, literature data on loess deposits and soil databases with information on the lithological characteristics of sediments were used. Fig. 1 shows the simplified workflow of the GUM development.

Most of the data (126 map sources) were provided by national geological services in a machine readable format (71% of map sources). Further data were derived from analogue and digital imagery (29% of map sources) and vectorized using GIS (ESRI ArcMap 10.4). When no geological maps were available, information on unconsolidated sediments were taken from the Global Lithological Map database GLiM by Hartmann and Moosdorf (2012), given as class *su*. Most of the maps cover national areas, while some maps represent larger regions (e.g., the Balkans or Northern Africa). Where national maps were tiled, they were compiled (e.g., Mexico, Germany, Japan or Brazil).

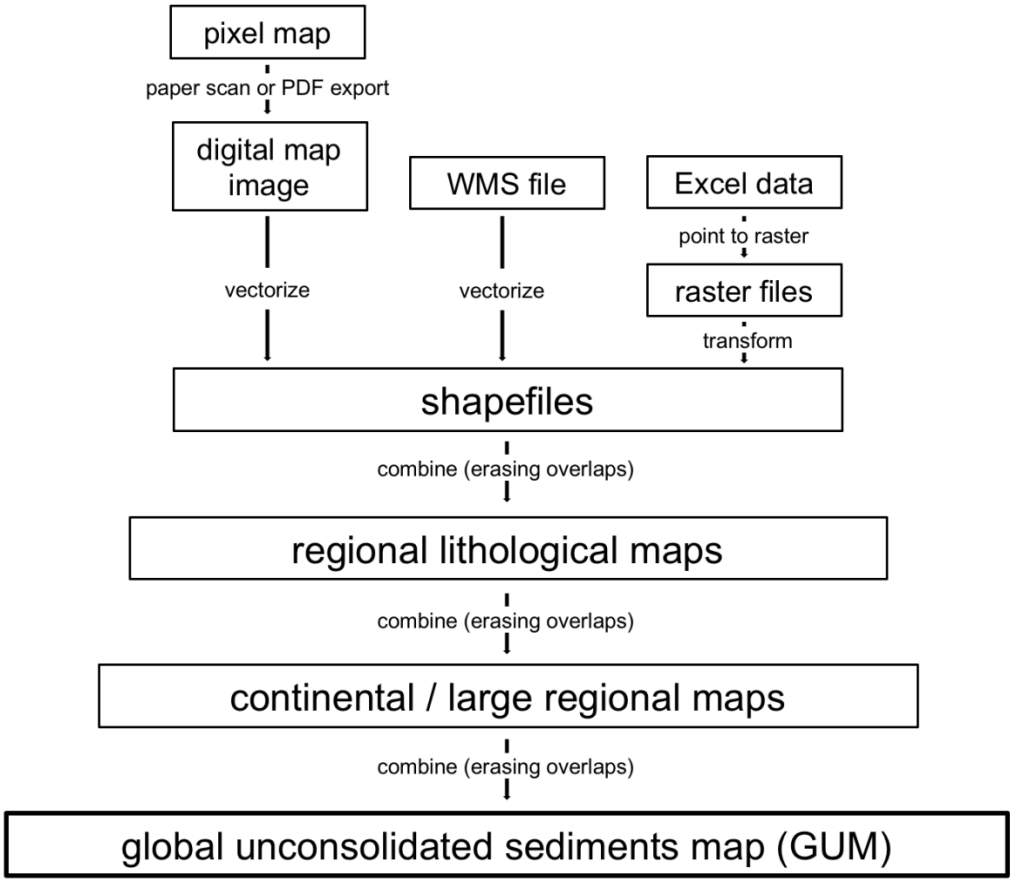

Figure 1: Simplified workflow of the GUM development.

Due to the heterogeneity of input data, a classification was developed (major classes shown in Tab. 1a and 1b; a full classification description is provided in Appendix A.2). To reduce and homogenize the information given in map sources, five different levels of information are represented in the global unconsolidated sediment database. The first level identifies the sediment type (*XX*), which is defined in Appendix section A.2.1. The second to fifth level subclasses indicate properties of the sediments (*YY* – grainsize information, *ZZ* – mineralogical information, *AA* – age information, *DD* – thickness).

All references of the incorporated individual data sets are listed in the Appendix A.

2.4 Results and Discussion

Mapped unconsolidated sediments cover around 50% of the global land area (referring to the total land area of the GLiM (Hartmann and Moosdorf, 2012), excluding ice and water bodies), or 68 x 10^6 km². In total, 911,551 polygons are distributed in the GUM, derived by 126 individual input data sets. The relative coverage and frequency of the sediment types (information level *XX*) can be seen in Tables 1a and 1b. The average map scale of the compiled map is 1:3,000,000 (area weighted).

Alluvial sediments cover ~23% of the mapped global ice-free area. Further larger groups of units are aeolian sediments (20.7%), glacial sediments (20.4%) and colluvial sediments (15.5%). Less areal extent can be observed for coastal sediments (~1.7%), lacustrine and organic deposits (1.2% and 1.1%), evaporitic deposits (0.9%), marine deposits (0.8%) and anthropogenic deposits (0.01%). Pyroclastic deposits are regarded separately since their definition is more complex. In the GUM, unconsolidated pyroclastics represent 0.1% of the total area, but the full extent of pyroclastic material (either consolidated or not further described) represents a larger area, with 0.7% of the total land area (related to the GLiM area; Hartmann and Moosdorf (2012)) respectively.

The remaining 11.7% of sediment cover are grouped as undifferentiated sediments (Us), which is in general a mixture of different sediment types or sediments of an undescribed origin. The comparably large fraction of undifferentiated sediments already points towards a potential to further improve the map database in future studies. The global distribution of the mapped sediment types can be seen in Fig. 2.

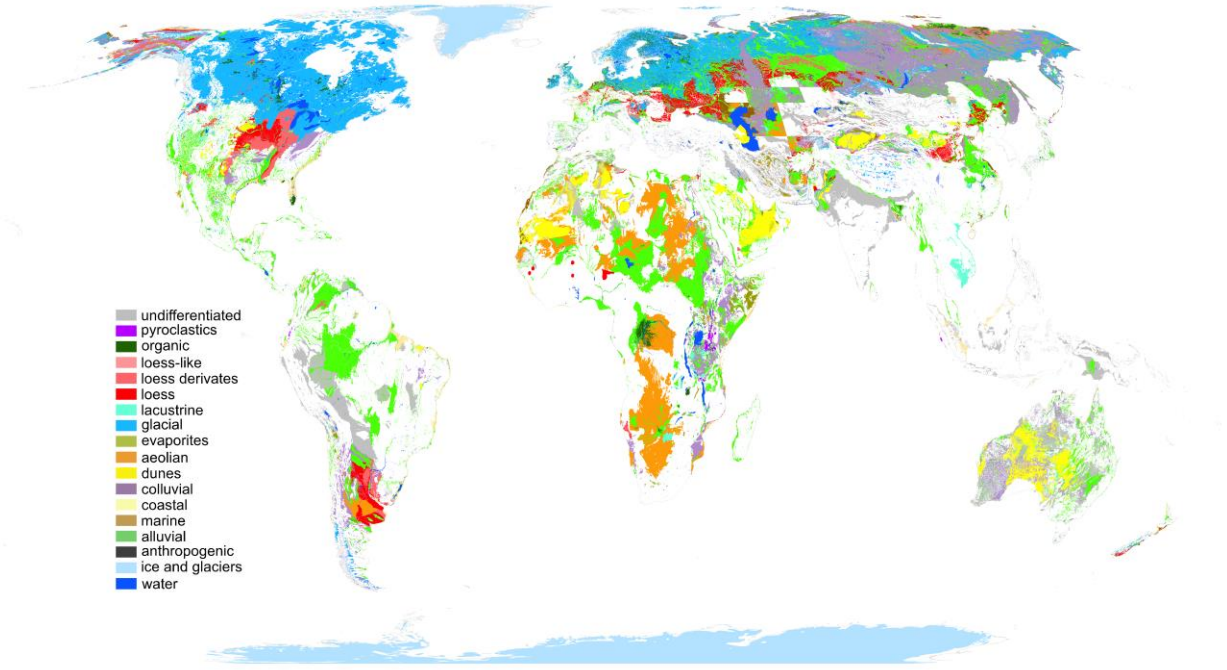

Figure 2: Map of the GUM database showing the different generalized sediment types (information level *XX*). Source: https://doi.org/10.1594/PANGAEA.884822.

Significant regional differences can be observed. The area fraction of the GUM sediments relative to the land surface area shows e.g., that the northern hemisphere >50°N is almost entirely covered by mapped unconsolidated sediments, mostly because of glacial sediments (Fig. 3 and 4). The high fraction of undifferentiated sediments may reflect the potential of a better classification of the sediments in future. Some can be attributed to arid areas, causing two peaks of undifferentiated aeolian deposits and dune deposits at latitudes of about 10° - 30°, N and S, respectively. Note that loess deposits are abundant in the latitudes between glacial sediments and dune deposits. The large

fraction of mapped colluvial units for >50°N may be caused by solifluction, talus or deserptium deposits (stone streams and stone glaciers), which were classified as “colluvial” and are widely abundant in Russia.

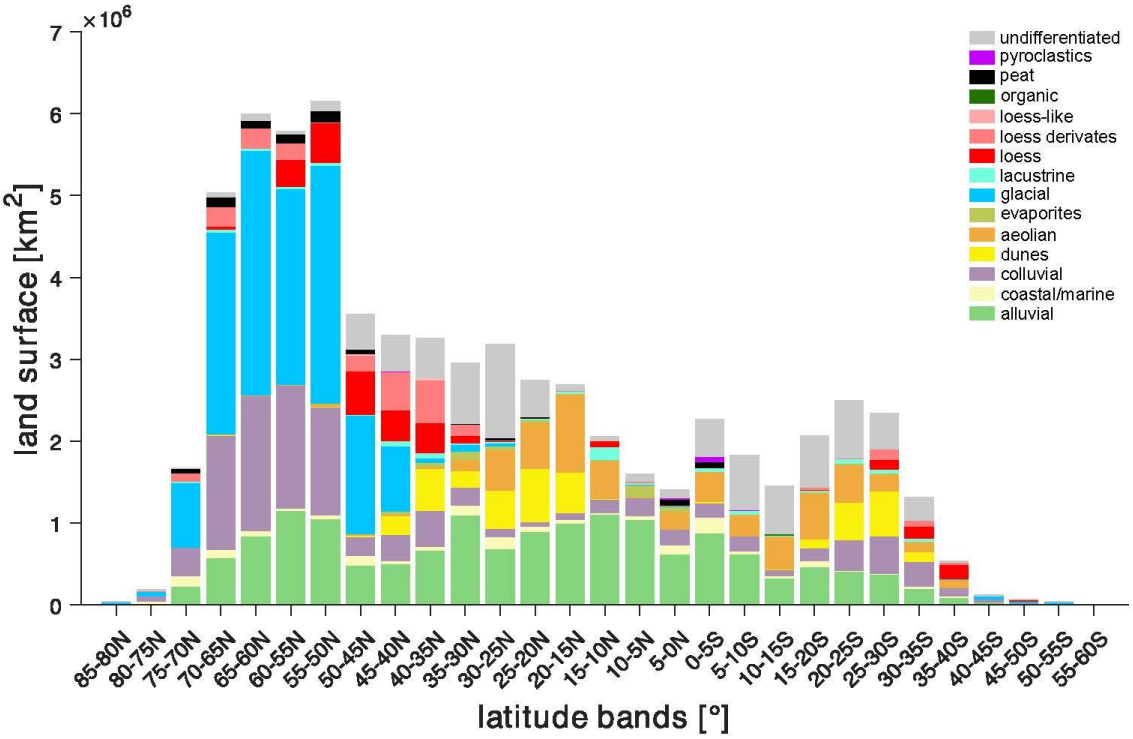

Figure 3: Latitudinal distribution of main sediment types. Source: https://doi.org/10.1594/PANGAEA.884822.

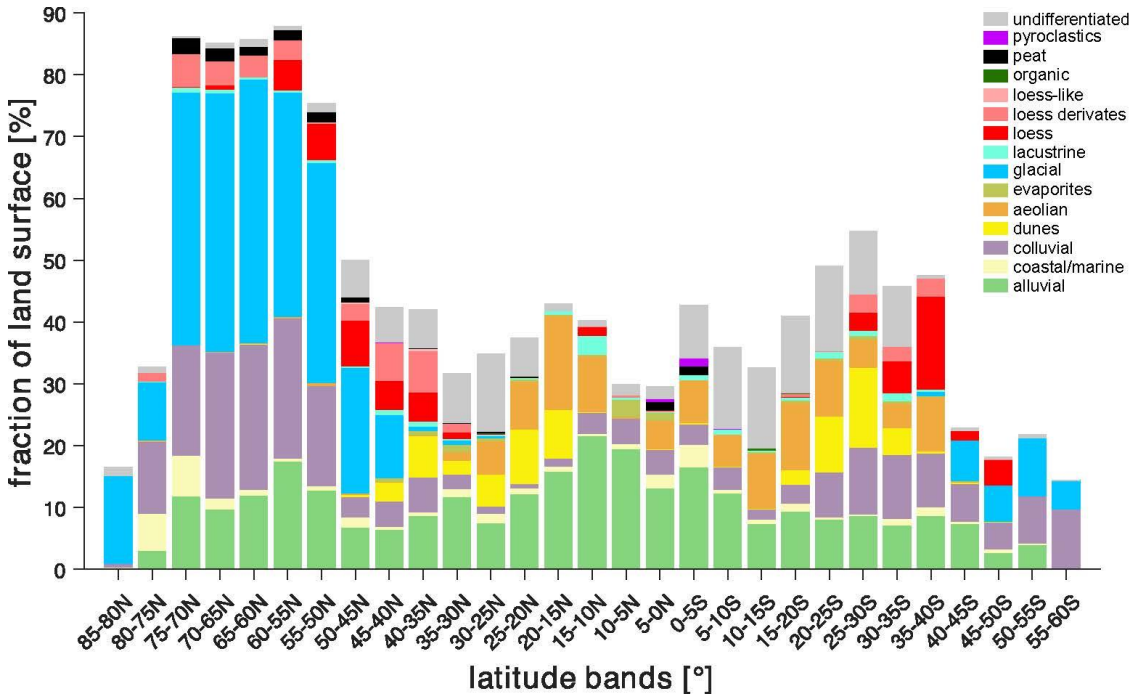

Figure 4: Fraction of land surface area covered by GUM sediments (land surface area, excluding water and ice bodies, derived from Hartmann and Moosdorf (2012)). Source: https://doi.org/10.1594/PANGAEA.884822.

In addition to sediment types, the GUM database provides data on sediment properties that are not often reported, but can give subordinate information on the sediments (Figure 5).

Grainsize information (information level *YY*) is available for about 39% of the polygons (covering 41.7% of the GUM area), excluding ice and water (0.4% clay and finer (cu), 2.7% silt and clay (lc), 3.8% silt (lu), 8.1% mixed (mx), 1.5% sand and clay (sc), 4.5% sand and silt (sl), 18.3% sand and coarser (su)).

Only ~8% of the polygons contain information on the mineralogy (information level *ZZ*) (0.2% acidic (ac), 3.2% carbonatic (ca), 0.2% mafic (ma), 0.8% mixed (mx), 3.4% siliciclastic (ss); excluding ice and water).

Age information (information level *AA*) is available for ~73% of the polygons, excluding ice and water (11% Holocene (hu), 0.7% Early Pleistocene (pe), 7.6% Late Pleistocene (pl), 3.3% Middle Pleistocene (pm), 0.2% Plio-/Pleistocene (pp), 15.4% Pleistocene (pu), 5% Quaternary and/or Tertiary (qt), 28,3% Quaternary (qu), 1.8% Tertiary (tu), 0.03% others).

Information about sediment thicknesses (information level *DD*) is sparsely available for ~2% of the polygons (excluding ice and water).

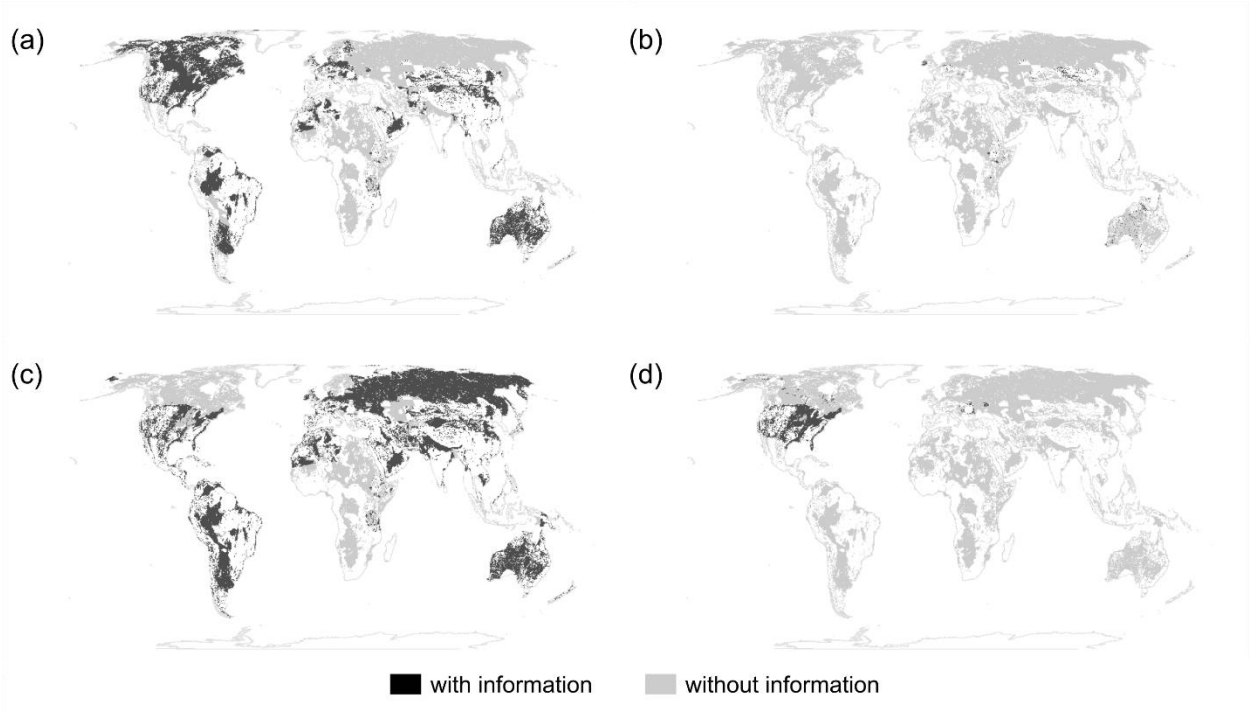

Figure 5: Maps showing the available information on a) grainsize, b) mineralogy, c) age and d) thickness.

Table 1a: Areal coverage of the different sediment types, globally as well as for distinguished areas (related to GUM area). Note that bold values represent main sediment types.

XX	Description	Area [km²]	Africa [%]	North America [%]	South America [%]	Europe [%]	Asia [%]	Australasia [%]	Relative global coverage [%]
A-	**Alluvial - all classes**	**15933162**	**31.80**	**10.11**	**39.17**	**17.56**	**22.35**	**15.98**	**19.21**
Au	Alluvial – Undifferentiated	12321831	30.23	9.62	19.69	13.94	17.84	2.32	14.85
Al	Alluvial – Lacustrine deposits	2196479	1.15		13.85	1.01	4.11		2.65
Ap	Alluvial – Plain deposits	766514		0.25	0.04	0.17		13.61	0.92
At	Alluvial – Terrace deposits	301025	0.41	0.15	1.82	1.59	0.18	0.05	0.36
Ae	Alluvial – Aeolian deposits	255395			3.76	0.18	0.02		0.31
Af	Alluvial – Fan deposits	91647	0.01	0.09		0.65	0.20		0.11
E-	**Aeolian - all classes**	**14411829**	**44.57**	**11.55**	**14.66**	**17.41**	**13.83**	**24.10**	**17.37**
Eu	Aeolian – Undifferentiated	5627447	36.67	0.20	3.42	1.39	1.35		6.78
Ed	Aeolian – Dunes	3871250	7.09	1.40	0.57	0.17	5.20	23.58	4.67
El	Aeolian – Loess deposits	2829142	0.61	3.11	6.71	14.01	4.95	0.50	3.41
Er	Aeolian – Loess derivates	1969164	0.20	6.82	3.96	1.77	1.91	0.02	2.37
Ea	Aeolian – Loess-like silt deposits	114827		0.02		0.07	0.41		0.14
G-	**Glacial - all classes**	**14197795**	**0**	**52.19**	**1.05**	**44.14**	**15.53**	**0.36**	**17.12**
Gt	Glacial – Till	9361460		40.48		25.88	7.17	0.06	11.28
Gl	Glacial – Glaciolacustrine deposits	1367292		4.83		1.54	1.98		1.65
Gu	Glacial – Undifferentiated	1301828			1.05	6.10	3.80	0.30	1.57
Gf	Glacial – Fluvioglacial deposits	1300673		1.79		10.60	2.48		1.57
Gm	Glacial – Glaciomarine deposits	561002		3.21		0.03	0.10		0.68
Gp	Glacial – Proglacial deposits	305540		1.88					0.37
Du	**Ice**	**13288447**	**0**	**12.30**	**0.31**	**0.06**	**0.33**	**0**	**16.02**
C-	**Colluvial - all classes**	**10819028**	**9.18**	**4.45**	**8.83**	**3.75**	**27.29**	**15.44**	**13.04**
Ca	Colluvial – Alluvial deposits	6718296		1.92	7.88	1.78	21.71		8.10
Cu	Colluvial – Undifferentiated	4100732	9.18	2.53	0.94	1.98	5.58	15.44	4.94
Us	**Sediments – Undifferentiated**	**8135182**	**5.20**	**0.49**	**28.09**	**6.00**	**12.21**	**38.98**	**9.81**
W-	**Water - all classes**	**2091321**	**2.36**	**4.85**	**2.15**	**2.65**	**2.75**	**0.30**	**2.52**
Wu	Water bodies – Undifferentiated	2068404	2.34	4.72	2.15	2.65	2.75	0.30	2.49
Wl	Water – Lakes	20113	0.02	0.11					0.02
Wr	Water – Rivers	2803		0.01					0.003
Y-	**Coastal - all classes**	**1152804**	**0.92**	**2.06**	**4.82**	**1.02**	**0.69**	**2.71**	**1.39**
Yu	Coastal – Undifferentiated	994965	0.92	1.84	4.43	0.94	0.57	1.51	1.20
Ys	Coastal – Swamp deposits	69674					0.02	1.21	0.08
Yd	Coastal – Delta sediments	42597		0.04	0.17	0.01	0.09		0.05
Yl	Coastal – Lagoonal sediments	41049		0.16	0.22	0.01			0.05
Yb	Coastal – Beach deposits	3565		0.01		0.06			0.004
Ym	Coastal – Marsh sediments	954				0.01			0.001
Lu	**Lacustrine deposits**	**867833**	**1.20**	**0.65**	**0.02**	**0.29**	**1.80**	**1.94**	**1.05**
O-	**Organic - all classes**	**800934**	**1.27**	**1.14**	**0**	**5.82**	**0.92**	**0.02**	**0.97**
Op	Organic – Peat deposits	762047	1.04	1.10		5.82	0.92	0.02	0.92
Ou	Organic – Undifferentiated	38758	0.23	0.04					0.05
Or	Organic – Reef deposits	130							0.0002
P-	**Evaporites - all classes**	**611160**	**2.44**	**0.21**	**0.72**	**0**	**0.74**	**0**	**0.74**
Ps	Evaporites – Salt deposits	332556	1.25		0.20		0.56		0.40
Pg	Evaporites – Gypsum deposits	133996	0.97	0.01					0.16
Pu	Evaporites – Undifferentiated	92634	0.21		0.52		0.11		0.11
Pp	Evaporites – Playa deposits	51975		0.20			0.07		0.06
Mu	**Marine deposits**	**534283**	**0.43**	**0.01**	**0.05**	**1.04**	**1.53**	**0.11**	**0.64**
Iy	**Pyroclastics**	**101282**	**0.64**	**0**	**0.12**	**0**	**0.01**	**0.08**	**0.12**
Zu	**Anthropogenic deposits**	**10088**	**0**	**0**	**0**	**0.26**	**0.01**	**0**	**0.01**

Table 1b: Sediment type abundance in the map database. Note that bold values represent main sediment types.

XX	Description	Abundance [number of polygons]	Africa [%]	North America [%]	South America [%]	Europe [%]	Asia [%]	Australasia [%]	Extent of global coverage [%]
A-	**Alluvial - all classes**	**212236**	**12.51**	**12.47**	**43.30**	**18.29**	**40.30**	**16.21**	**23.28**
Au	Alluvial – Undifferentiated	129200	11.36	11.88	35.84	15.91	15.33	3.24	14.17
Al	Alluvial – Lacustrine deposits	41406	0.29		4.43	1.59	14.68		4.54
At	Alluvial – Terrace deposits	24947	0.78	0.27	2.82	0.52	9.15	0.11	2.74
Ap	Alluvial – Plain deposits	12942		0.22	0.02	0.03		12.87	1.42
Af	Alluvial – Fan deposits	3656	0.08	0.10		0.24	1.12		0.40
Ae	Alluvial – Aeolian deposits	85			0.18		0.01		0.01
G-	**Glacial - all classes**	**160392**	**0**	**15.24**	**3.12**	**31.79**	**12.53**	**0.55**	**17.60**
Gt	Glacial – Till	82105		8.17		17.33	4.60	0.17	9.01
Gf	Glacial – Fluvioglacial deposits	48706		2.59		10.59	3.22		5.34
Gu	Glacial – Undifferentiated	18403			3.12	3.20	2.33	0.39	2.02
Gl	Glacial – Glaciolacustrine deposits	8207		1.18		0.58	2.29		0.90
Gp	Glacial – Proglacial deposits	1681		2.40					0.18
Gm	Glacial – Glaciomarine deposits	1290		0.89		0.10	0.10		0.14
O-	**Organic - all classes**	**116414**	**49.90**	**0.74**	**0.01**	**14.98**	**3.01**	**0.02**	**12.77**
Op	Organic – Peat deposits	115485	49.36	0.68		14.97	3.01	0.02	12.67
Ou	Organic – Undifferentiated	911	0.54	0.05		0.01			0.10
Or	Organic – Reef deposits	18		0.01	0.01				0
W-	**Water - all classes**	**104121**	**24.52**	**50.19**	**7.75**	**5.22**	**8.56**	**1.50**	**11.42**
Wu	Water bodies – Undifferentiated	95368	24.51	37.80	7.75	5.22	8.55	1.47	10.46
Wl	Water – Lakes	8746	0.02	12.38			0.01	0.03	0.96
Wr	Water – Rivers	7		0.01					0
Us	**Sediments – Undifferentiated**	**99583**	**2.88**	**0.24**	**12.21**	**8.33**	**11.40**	**35.28**	**10.92**
C-	**Colluvial - all classes**	**78173**	**4.79**	**3.16**	**12.99**	**3.13**	**13.60**	**24.27**	**8.58**
Cu	Colluvial – Undifferentiated	50934	4.79	2.13	3.28	2.82	3.76	24.22	5.59
Ca	Colluvial – Alluvial deposits	27239		1.03	9.71	0.31	9.84	0.06	2.99
E-	**Aeolian - all classes**	**67973**	**2.50**	**7.61**	**5.24**	**9.70**	**5.33**	**10.01**	**7.46**
El	Aeolian – Loess deposits	31339	0.02	4.52	2.41	5.20	1.48	4.92	3.44
Eu	Aeolian – Undifferentiated	14688	1.36	0.76	0.22	3.03	0.54		1.61
Ed	Aeolian – Dunes	13969	1.11	0.96	2.00	1.21	0.92	4.80	1.53
Er	Aeolian – Loess derivates	7258	0.01	1.22	0.62	0.24	2.18	0.30	0.80
Ea	Aeolian – Loess-like silt deposits	719		0.15		0.03	0.22		0.08
Y-	**Coastal - all classes**	**22077**	**1.52**	**4.50**	**13.74**	**1.78**	**0.95**	**3.39**	**2.42**
Yu	Coastal – Undifferentiated	16835	1.52	2.06	12.76	1.19	0.65	3.28	1.85
Yb	Coastal – Beach deposits	2025		0.09		0.46		0.01	0.22
Yl	Coastal – Lagoonal sediments	1602		1.94	0.85				0.18
Yd	Coastal – Delta sediments	752		0.40	0.14	0.10	0.02		0.08
Ys	Coastal – Swamp deposits	742					0.27	0.10	0.08
Ym	Coastal – Marsh sediments	121				0.03	0.01		0.01
Lu	**Lacustrine deposits**	**21702**	**0.20**	**0.95**	**0.07**	**2.39**	**1.53**	**8.48**	**2.38**
Zu	**Anthropogenic deposits**	**11717**	**0**	**0**	**0.09**	**3.11**	**0.02**	**0.03**	**1.29**
Mu	**Marine deposits**	**9096**	**0.15**	**0.05**	**0.40**	**1.10**	**1.79**	**0.22**	**1.00**
Du	**Ice**	**4477**	**0**	**4.53**	**0.02**	**0.17**	**0.24**	**0**	**0.49**
P-	**Evaporites - all classes**	**3056**	**0.84**	**0.32**	**0.68**	**0**	**0.66**	**0**	**0.34**
Ps	Evaporites – Salt deposits	1964	0.70		0.07		0.41		0.22
Pu	Evaporites – Undifferentiated	619			0.62		0.19		0.07
Pp	Evaporites – Playa deposits	321		0.30			0.05		0.04
Pg	Evaporites – Gypsum deposits	152	0.13	0.02					0.02
Iy	**Pyroclastics**	**534**	**0.18**	**0**	**0.39**	**0.01**	**0.08**	**0.03**	**0.06**

Although the GUM database provides very detailed information about the distribution of unconsolidated sediments in some regions, e.g., Northern Europe or North America, there still remain some regions where identified data are comparably sparse, e.g., NE part of South America, SE Europe and central/SE Asia. Since unconsolidated sediments do not cover the entire globe, it remains unclear if "white areas" contain unmapped sediments or no sediments at all (Fig. 6).

Different mapping techniques or data handling by different institutions naturally lead to heterogeneity of available classifications and rock/sediment characterization. Some institutions distinguish very strictly between bedrock and sediment, while others neglect sediments or classify them as soils. Future refinements should clarify the classification systems into rock, sediment and soil. Residual deposits (e.g., laterites or latosols) are not considered in this map database because we defined them as soils here. Another future target would be to obtain a multi-layered global map database of soils, sediments and bedrock to derive a most-comprehensive representation of the critical zone.

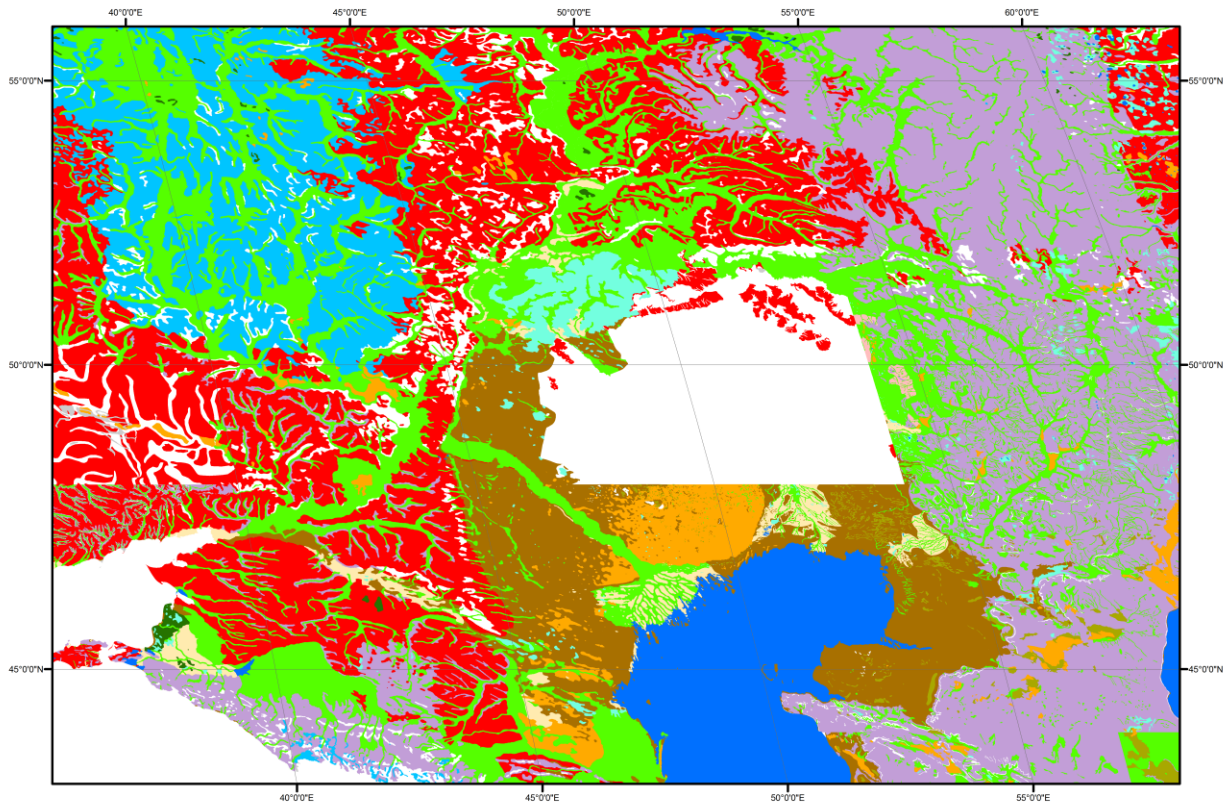

Figure 6: GUM sediment distribution in Central Asia. Since in the southern part of Russia remaining "white areas" are representing bedrock outcrops, some regions were not filled with data in this version of the GUM (e.g., NW Kazakhstan).

2.4.1 Global loess deposits

Loess deposits are reactive sediments with significant impact on the aquatic chemistry (Goddéris et al., 2013). Fertile soils can develop on top of loess sediments (Muhs et al., 2014) and due to their age, distinguishable, e.g., by luminescence analyses, loess deposits can be used to understand dynamic sedimentation processes in the past (Muhs and Bettis, 2003). They are important archives for studying long-term dust deposition and atmospheric circulation and, together with intercalated paleosols, they can represent detailed terrestrial records of glacial-interglacial cycles (Muhs et al., 2014). Thus, they are particularly interesting for climate studies. Loess sediments are distributed around the entire globe (Fig. 7) but they vary significantly in thickness (from few cm to >400m, e.g., at Jingyuan in China (Derbyshire et al., 1998)).

Due to the intensive research on loess sediments, a global distribution pattern is of high demand. There exist various regional studies, but compiling a large-scale map database is challenging because of varying loess definitions, since there are several ways to generate, transport and accumulate silt particles (Muhs et al., 2014; Wright, 2001). Whether individual loess deposits are of glacial or non-glacial origin is not reported in the GUM. The loess sediments of the GUM are subdivided, following a classification after Pye (1984), into:

1. Loess deposits (El): aeolian silt deposits
2. Loess derivates (Er): reworked loess deposits
3. Loess-like sediments (Ea): silt deposits, but not of aeolian kind

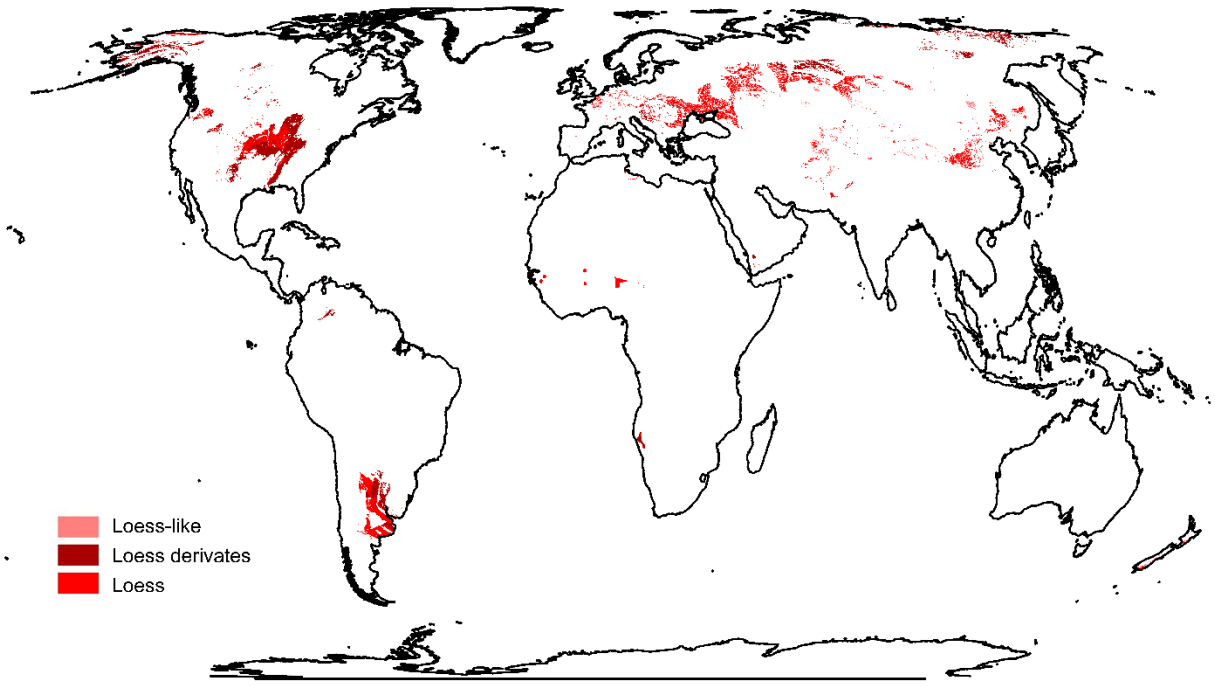

Figure 7: Global loess distribution derived from the GUM. Source: https://doi.org/10.1594/PANGAEA.884822.

Comparing a previous European loess map by Haase et al. (2007) with the GUM loess, the map of Haase et al. (2007) shows a quite homogeneous loess distribution with relatively large polygons. The new GUM loess map, with a higher resolution of mapped loess from used sources, provides for Western Europe a significantly smaller mapped loess area (about 40%, c.f. Fig. 8).

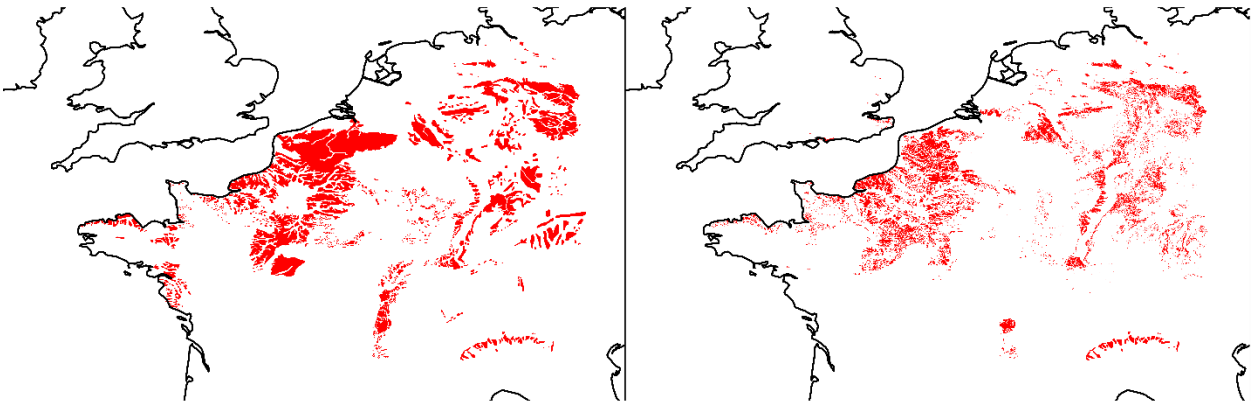

Figure 8: Loess distribution in Western Europe. Left: loess distribution of Haase et al. (2007), right: GUM loess (both loess and their related deposits), showing the different map resolutions. Whereas the loess coverage of Haase et al. (2007) is about 106,758 km², the GUM reveals a loess area extent of 64,056 km².

The largest differences in spatial extent between the two maps in the European loess distribution can be seen in Belarus, the Ukraine and Russia (Fig. 9). Fewer loess sediments are reported for those regions in the GUM because of differences in the loess definitions if compared to Haase et al. (2007). The original data used for the GUM show two types of information in these areas: Information on the sediment type and a lithological description of the sediment cover. For example, in Belarus exists a sediment cover that consists of boulders and sandy loam, but the underlying lithology is defined as of glacial origin (till), which leaves it unclear if the loam was derived by aeolian transport. Hence, this loam is not fitting into the classification system defined above and therefore not considered in the GUM as loess. These cover sediments may be patchy and their thickness might be very low. If loess deposits would have been classified less strictly, the global coverage of loess would increase.

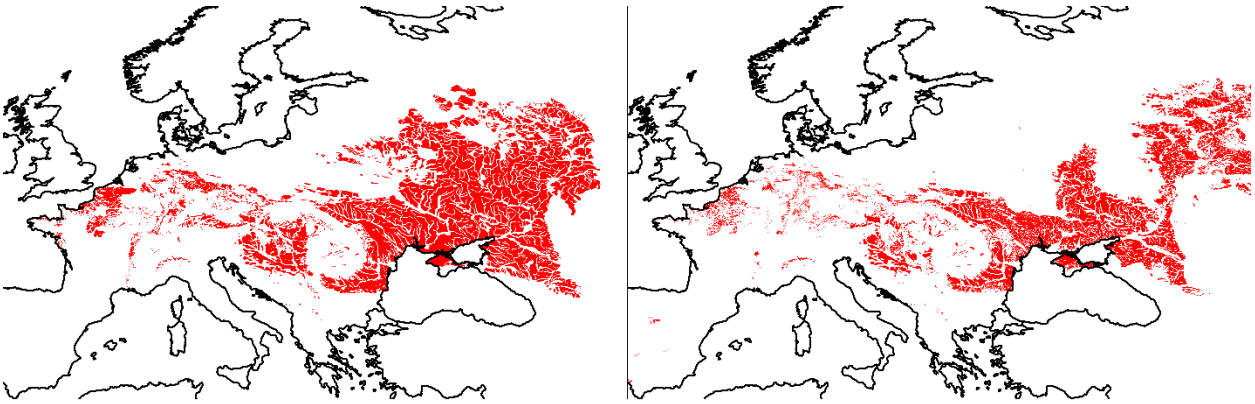

Figure 9: Loess distribution (El, Ea and Er) in Europe (left) after Haase et al. (2007) and (right) GUM loess distribution.

2.5 Summary

The GUM database with its information on global terrestrial unconsolidated sediment distribution and their properties can be applied for a range of investigations on Earth system processes. With its resolution, improved compared to previous global maps (average map scale of 1:3,000,000), it provides information for studies on global surface processes. The special focus on loess, glacial sediments and pyroclastic material yields a large database describing their global distribution. The map database is created in a way that individual areas or regions of interest can be regarded separately and further information can be added to the database.

In addition to the database, a gridded version (0.5°) of the sediment types was created and is available, together with the GUM database, at the PANGAEA database (https://doi.org/10.1594/PANGAEA.884822).

3 Chemical weathering of loess during the Last Glacial Maximum, the Mid-Holocene and today

This chapter is being prepared for submission into an international journal as: Börker, J., Hartmann, J., Amann, T., Romero-Mujalli, G., Moosdorf, N. and Jenkins, C.: Chemical weathering of loess during the Last Glacial Maximum, Mid-Holocene and today.

3.1 Abstract

Loess sediments are windblown silt deposits with, in general, a carbonate grain content of up to 30%. While regionally, loess deposits increase weathering fluxes substantially, their influence on global weathering fluxes is not yet properly quantified. Especially on glacial-interglacial timescales, loess weathering fluxes might have contributed to land-ocean alkalinity flux variability since the loess areal extent during glacial epochs is reported to be larger. To quantify the weathering fluxes of loess deposits, global maps representing the loess distribution were compiled. For the Last Glacial Maximum (LGM) this includes loess on exposed continental shelf areas. Water chemistry of rivers draining today's loess deposits suggest that loess contributes over-proportionally to alkalinity fluxes if compared to the mean of alkalinity fluxes of global rivers (~4110 meq/m²a for rivers draining loess deposits and ~1850 meq/m²a for the total of global rivers), showing comparable alkalinity concentrations patterns in rivers as found for carbonate sedimentary rock lithological classes. Loess deposits increase calculated global alkalinity fluxes to the coastal zone by 16%, while covering ~4% of the ice- and water-free land area. Comparing global alkalinity fluxes of today and the LGM suggests small differences of ~4 % increase during the LGM considering loess. If loess weathering is neglected the changes are more significant (~11% decrease during the LGM). Alkalinity fluxes from silicate dominated lithological classes are ~28-30% lower during the LGM than today (with loess and without loess, respectively) and elevated alkalinity fluxes from loess deposits, compensated for this. Enhanced loess weathering dampens due to a legacy effect therefore the temperature induced changes in silicate dominated lithologies along the glacial-interglacial time period.

3.2 Introduction

Loess sediments are distinctive windblown silt deposits which cover extensive areas on the Earth's surface (Muhs et al., 2014). They can provide insights into dynamical sedimentation processes of the past and serve as terrestrial archives for studying dust deposition and atmospheric circulation (Muhs and Bettis, 2000; Muhs et al., 2014). While loess sediments are widespread around the globe, they are mainly abundant in higher latitudes. Today, they cover about 4.9×10^6 km² (Börker et al., 2018), which represents about 4% of the total ice-free land area (i.e., relative to the GLiM area without ice and water bodies; Hartmann and Moosdorf (2012)).

Loess sediments typically contain quartz, feldspar, mica, and clay minerals, but also carbonate minerals (Muhs et al., 2014). Besides their significance to climate-related studies, loess sediments

are important regarding chemical weathering fluxes. Kump and Alley (1994) mention the possible significance of loess deposits in glacial chemical weathering studies. Goddéris et al. (2013) applied numerical models to quantify the weathering of the Mississippi Valley loess, to simulate climate, the continental biosphere and the weathering processes within the pedon. Because surfaces of loess sediments are often only slightly weathered, and because of their carbonate content and high surface area due to fine grainsize, loess might have a high influence on global weathering fluxes. Zhang et al. (2013) concluded that even in slightly loess–covered areas (18% loess coverage in a lake catchment on the northeastern Chinese Loess Plateau), the weathering processes of loess dominate the weathering fluxes. This might be related to a high erodibility of loess and the amount of carbonate minerals that weather generally faster than silicate minerals (Zhang et al., 2013).

Since loess sediments can have a generally high content of carbonate minerals (up to 30% carbonate grains after Pye (1984) or up to 10 wt% for loess in the Chinese Loess Plateau after Zhang et al. (2013) and references therein), it has to be tested whether they show a similar weathering behavior as carbonate rocks. Previous global carbonate weathering models have been mostly runoff-based (Amiotte-Suchet and Probst, 1995; Bluth and Kump, 1994). New studies have analyzed calcite dissolution in global river catchments and found a Gaussian function, which can describe alkalinity concentrations dependent on land surface temperature (Gaillardet et al., 2018; Romero-Mujalli et al., 2018a). By analyzing river chemistry data of catchments dominated by loess deposits, alkalinity fluxes from loess were analyzed and compared with alkalinity fluxes derived by applying the previous above named carbonate weathering models.

To quantify global changes of alkalinity flux and CO_2 consumption rates, comparing the time of the Last Glacial Maximum (LGM), the Mid-Holocene and today's setting, a spatial reconstruction of loess deposits is needed. A map of loess distribution during the LGM was created by extrapolating geographically today's loess distribution (Börker et al., 2018). For the LGM map, present-day inundated continental shelf areas were also considered, since the sea level was about 134m lower during the LGM (Lambeck et al., 2014), leading to the exposition of large shelf areas to terrestrial weathering. Reports on loess sediments on previously exposed continental shelves are included in the LGM loess map in this study.

In the presented study, global alkalinity fluxes and CO_2 consumption rates were calculated and compared for the LGM, the Mid-Holocene and the present-day. This helps to identify if loess weathering fluxes have a relevant influence on global weathering fluxes now and on glacial-interglacial time scales.

3.3 Methods

3.3.1 Current loess distribution

The current loess distribution was obtained from the Global Unconsolidated Sediments Map database (GUM) (Börker et al., 2018). The map distinguishes between subclasses of primary loess deposits, loess derivates and loess-like silt deposits. In the further analysis, we do not distinguish between the different subtypes of loess. Most of the loess deposits can be found in the high latitudes, 35-70°N and 25-40°S, respectively (Börker et al., 2018). For the Mid-Holocene scenario, we assume that the loess distribution is similar to today.

3.3.2 Loess distribution at the LGM

For the LGM the land area that is equal to today's continents had to be increased by the exposed continental shelves due to a lower sea level.

3.3.2.1 Loess distribution of the LGM on continents

Due to a lack of map data, the global loess distribution for the LGM cannot be reconstructed. Mahowald et al. (1999) state that eolian deposition rates were up to 2-20 times higher during glacial periods and Rousseau et al. (2014) conclude that the dust deposition fluxes during the LGM might have been 2-3 times higher. Since river valleys were reported to have once been covered with loess deposits in some regions, before they were eroded (United States. Army. Corps of Engineers, 1974), the loess extent of today (Börker et al., 2018) was extrapolated to the LGM. This was done using *Esri* ArcMap (v10.6) by transforming the loess shapefile, showing today's distribution, to point data and extrapolating these data by the Euclidean Distance Tool with a maximum distance of 10km. By doing this, river valleys within loess deposits, for example, were filled with loess.

3.3.2.2 Loess distribution on exposed continental shelves

To analyze weathering on exposed continental shelves during the LGM, the subaerial shelf extent was determined using the global relief model ETOPO1 (Amante and Eakins, 2009). By setting the bathymetric line to -130m, (a rounded value derived from Lambeck et al. (2014)), an exposed continental shelf area of about 23 x 10^6 km² was calculated. After subtracting the area that was covered by ice sheets (Ehlers et al., 2011) the total area of exposed shelves that were affected by weathering is therefore 19 x 10^6 km^2.

For several regions of the continental shelves, it was possible to reconstruct loess deposits from literature studies and digitize these areas with *GIS*. In the English Channel, evidence for loess deposits was described by Lefort et al. (2013). Extensive loess deposits on the Arctic shelf were made available by Biryukov et al. (1988). For most of the Black Sea, data of shelf loess deposits were made available in Ryan et al. (1997) and for the Argentinian continental shelf by Violante et al. (2014). Besides, data about loess deposits in the China Sea, on the shelves off West Africa, and

in the Indian Ocean and Western Pacific (Fig. 12) were made available by Li et al. (2013) and references therein. Details on the compilation of loess data of the continental shelves can be found in Appendix B.1.

3.3.3 Carbonate content of the shelves' sediments

To quantify alkalinity fluxes from the total continental shelves, which were exposed during the LGM, additional sediment types besides loess were considered. Reconstruction of the sedimentary pattern that was exposed during the LGM is challenging due to strong erosion of the subsequent transgressional phases. As a first assumption, the modern sediments might represent the sediments that were accumulated in the previous sea-level high-stand interglacial period. A global database of chemical, physical and mineralogical data about the ocean sediments from surface samplings and shallow stratigraphy-penetrating cores was used (*dbSEABED* (Bostock et al., 2018; Goff et al., 2008; Jenkins, 1997; Jenkins, 2018)). The database includes the world distribution of coral reefs, which are mostly growing on old karstic low-sea level landscapes (Purdy, 1974), also composed of carbonate. The point data of the carbonate content of all the sediments was interpolated to all shelf areas at a resolution of 0.25° x 0.25° (Fig. 10).

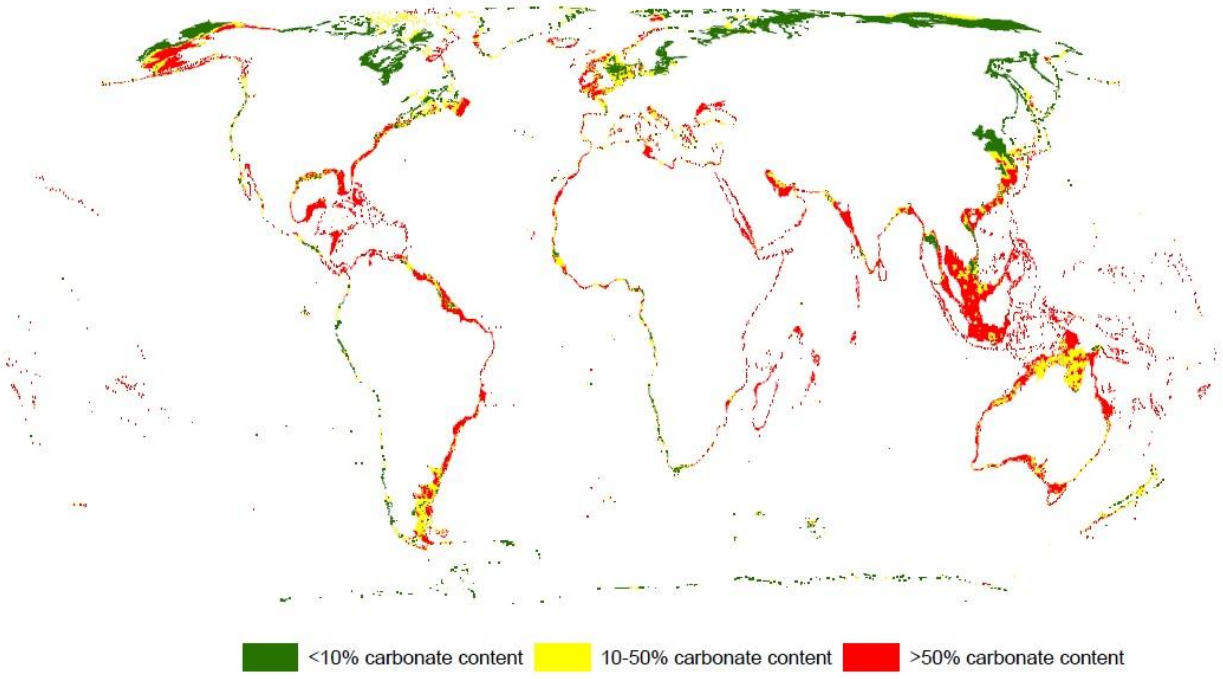

Figure 10: Interpolated carbonate content (resolution: 0.25° x 0.25°) of the modern marine sediments for continental shelves, which were exposed during the LGM, derived by the *dbSEABED* database (Bostock et al., 2018; Goff et al., 2008; Jenkins, 1997; Jenkins, 2018).

For global calculations of alkalinity fluxes, the shelf sediments had to be reclassified by their carbonate content, based on the carbonate proportions of lithological classes defined in Dürr et al. (2005):

(i) non-carbonatic sediments (ss) with in general < 10% carbonate content

(ii) mixed sediments (sm) with 10 to 50% carbonate content and

(iii) carbonatic sediments (sc) with > 50% carbonate content

3.3.4 Hydrochemical database

To analyze alkalinity fluxes from loess deposits, the Global River Chemistry Database (GLORICH) was used (Hartmann et al., 2014a). This database comprises 1.27 million samples from over 17,000 sampling locations (Hartmann et al., 2014a). The watersheds of the GLORICH database sampling locations were geometrically intersected with the loess areal extent of today and the hydrochemical data extracted and analyzed. For each sampling location the mean and median values were calculated. In the following, all analyzes are based on the mean values since the median values are not significantly different (see Appendix B.2). Additional data on some rivers draining the Chinese loess plateau was added by extracting chemical data from literature (Ran et al., 2017a; Ran et al., 2017b; Ran et al., 2015; Xiao et al., 2016; Zhang et al., 2013) and creating watersheds for the sampling points in *ArcMap*. The fractions of loess as well as all other lithologies from the Global Lithological Map Database (GLiM) (Hartmann and Moosdorf, 2012) within the watersheds were calculated. Mean annual runoff and temperature values were extracted for the sampling locations from Fekete et al. (2002) and Hijmans et al. (2005), respectively.

3.3.5 Global calculations of alkalinity flux rates and CO_2 consumption

The calculations of alkalinity fluxes and CO_2 consumption were done twice for each time step (LGM, Mid-Holocene and Today), one scenario considering loess deposits and one scenario neglecting loess deposits, using only the lithology from the Global Lithological Map Database (GLiM (Hartmann and Moosdorf, 2012), only considering the first level information “xx” for all polygons and therefore substituting possible loess deposits reported in the GLiM by other or generalized lithologies). The lithological maps were compiled in ArcGIS, and merged following a specific order (Fig. 11). If loess data was available from the GUM database (attributes: xx = El/Er/Ea), these polygons were merged with the GLiM shapefile, which serves as a background lithological map.

For all lithologies, apart from carbonate sedimentary rocks and loess deposits, an alkalinity flux model was applied, which is based on a spatially-explicit runoff-dependent model of chemical weathering, calibrated for 381 catchments in Japan (Hartmann, 2009) and which was later enhanced by considering temperature and a soil-shielding effect (Hartmann et al., 2014b). The different weathering model equations for each lithological class applied to calculate alkalinity fluxes are described in Appendix B.3 and were first used to quantify global alkalinity fluxes by Goll et al. (2014). These equations distinguish between alkalinity fluxes from carbonate and silicate weathering.

For the carbonate sedimentary rocks, the following carbonate weathering functions were applied and the results compared:

(i) Romero-Mujalli et al. (2018a)

$$log_{10}alk = (e^{b1+b2*T+b3*T^2}) \quad \text{(eq.3)}$$

with alk = alkalinity in meq L^{-1},

T = mean annual land temperature in °C,

b1 = -1.73,

b2 = 0.28

b3 = -0.0157

and

a standard deviation of the function of 0.2 (logarithm of meq L^{-1}).

The range of uncertainty in the global calculations was calculated using the standard deviation of the function as follows:

$$Uncertainty\ of\ the\ global\ flux = \sum(Flux\ per\ grid * 0.2 * \log(10)) \quad \text{(eq.4)}$$

(ii) Amiotte-Suchet and Probst (1995)

$$alk = 3.1692 * q \quad \text{(eq.5)}$$

with alk = alkalinity rate in meq alkalinity m^{-2} a^{-1} and

q = runoff in mm^3 mm^{-2} a^{-1}.

(iii) Bluth and Kump (1994)

$$alk = \frac{10^{4.521}(0.1*q)^{0.934}}{1000} \quad \text{(eq.6)}$$

with alk = alkalinity rate in meq alkalinity m^{-2} a^{-1} and

q = runoff in mm/a.

The residual standard deviations for the models in this study were calculated after:

$$residual\ standard\ deviation = \sqrt{\frac{\sum(residuals)^2}{n-1}} \quad \text{(eq. 7)}$$

with residuals = observed flux – predicted flux.

The ice sheet extent for the LGM was taken from Ehlers et al. (2011) and the LGM land mask was given by the shelves extent calculated from ETOPO1 (see section 3.3.2.2). Temperature and runoff data for each time period were taken from Earth System Model outputs of the Max-Planck-Institute (surface runoff and near-surface air temperature for the LGM, Mid-Holocene and pre-industrial (Jungclaus et al., 2012a; Jungclaus et al., 2012b; Jungclaus et al., 2012c). These data had to be pre-processed by calculating the annual mean values of monthly data. The runoff data for the LGM had to be extrapolated from the continents to the exposed continental shelf areas in ArcMap, because the shelf areas were not fully covered by runoff data due to the raster resolution of the input dataset.

The lithological coverage, as well as ice extent, LGM land mask, carbonate content of the ocean sediments, soil-shielding, temperature and runoff data were converted to a 20x20 km grid to run the global calculations.

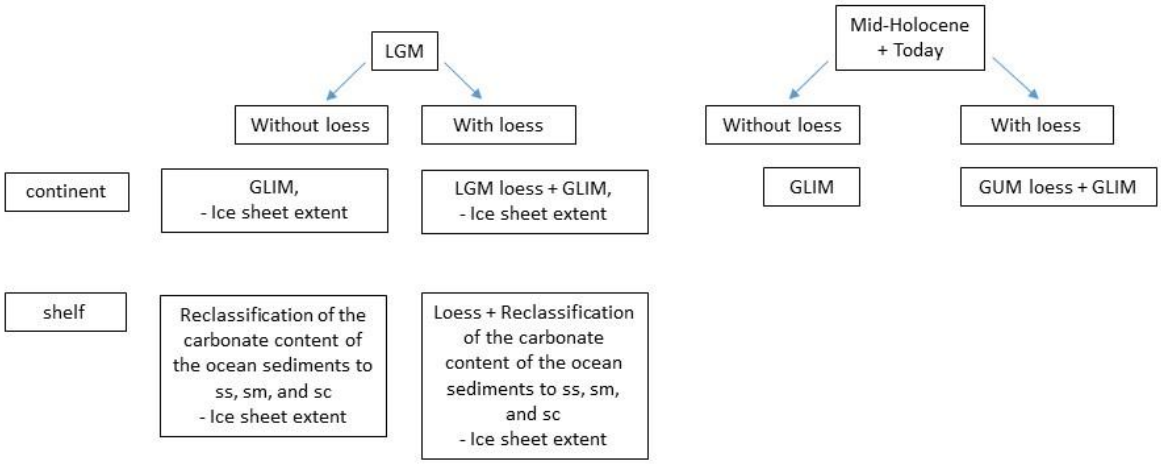

Figure 11: Flowchart of the development of the lithological input datasets for the global calculations. For the Mid-Holocene and today's time period the same lithological map was used. Loess was, where considered, always preferred over other lithological classes.

3.4 Results and Discussion

3.4.1 Changes in loess area

While the loess coverage today is about 5 x 10^6 km², the areal extent during the LGM was ~11 x 10^6 km² in our extrapolation (Fig. 12, Tab. 3).

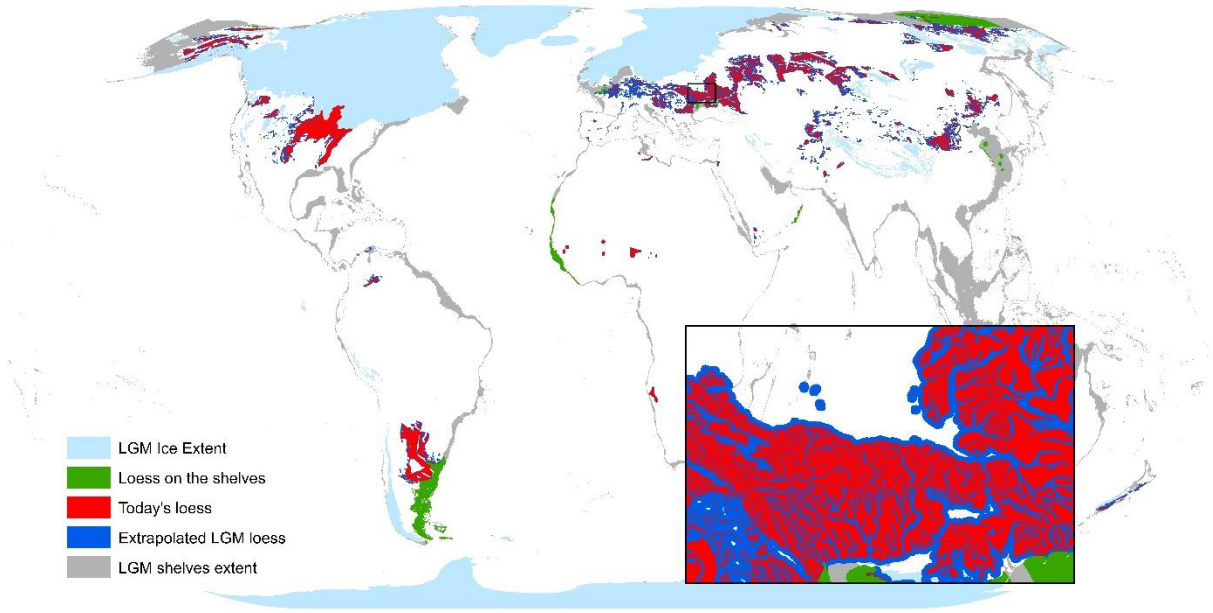

Figure 12: Differences in global loess distribution between the LGM and today. The loess distribution of today is shown in red and the extrapolated areas for the LGM in blue. The green color represents the redrawn loess on the continental shelves and grey the general shelves extent that was exposed during LGM. The LGM ice cover is shown in light blue.

Extrapolating the loess area from today to the LGM is partly speculative, because a constant increase in the areal extent around today's loess deposits is assumed. But it is reasonable as a first approximation because literature studies report 2 – 3 times higher dust deposition fluxes during LGM (Rousseau et al., 2014). Still, estimates on changes of global mass accumulation rates of loess deposits are limited, due to a lack of loess dating. Nevertheless, the DIRTMAP database (Kohfeld and Harrison, 2001) reports on an expansion of loess deposits downwind of deserts and ice sheets and a general increase of loess mass accumulation rates of 1 – 5 times during the LGM (Kohfeld and Harrison, 2001). The LGM was generally drier and less vegetated than today, so that dust release was enhanced.

Since there exists no paleogeographic sedimentary pattern for all the continental shelves, which are submerged today, or the continental land area during the LGM, it might also be possible that the LGM loess extent is under- or overestimated. Besides, loess, which might be present in alluvial

sediments for example and which would have an influence on alkalinity fluxes as well, is not considered separately as loess in our calculations for today's scenario.

Table 3: Differences in loess areal extent, comparing LGM and Mid-Holocene/Today.

	LGM	Mid-Holocene / Today
Loess on continents [x 10^6 km²]	9.28	4.91
Loess on exposed continental shelves [x 10^6 km²]	1.85	0
Total loess [x 10^6 km²]	11.13	4.91

The classification of carbonate content in marine sediments reveals the following proportions of lithologies on the exposed continental shelves:

(i) without loess: 24% siliciclastic sediments, 21% mixed sediments and 55% carbonate sediments
(ii) with loess: 20% siliciclastic sediments, 18% mixed sediments, 51% carbonate sediments and 11% loess sediments

The lithological map of Gibbs and Kump (1994), used in various studies (Ludwig et al., 1999; Munhoven, 2002) to quantify weathering fluxes from the exposed continental shelf areas, provides similar results (55 % of siliciclastic sediments and 45% of carbonate sediments as described in Ludwig et al. (1999)).

3.4.2 Chemical weathering of loess

Zhang et al. (2013) observe a dominance of loess weathering on the weathering fluxes even at 18% watershed loess coverage. Therefore, here a rounded value of 20% loess coverage as boundary condition to identify catchments with significant loess weathering contribution is used.

Of the geospatial data of loess distribution of today and the watersheds of the GLORICH sampling points, and the additional data for the Chinese Loess Plateau, 1,032 sampling locations have watersheds that are covered by more than 20% loess. 683 sampling locations feature alkalinity and/or major ion data (Ca^{2+}). The majority of data points are from the USA and China (Fig. 13).

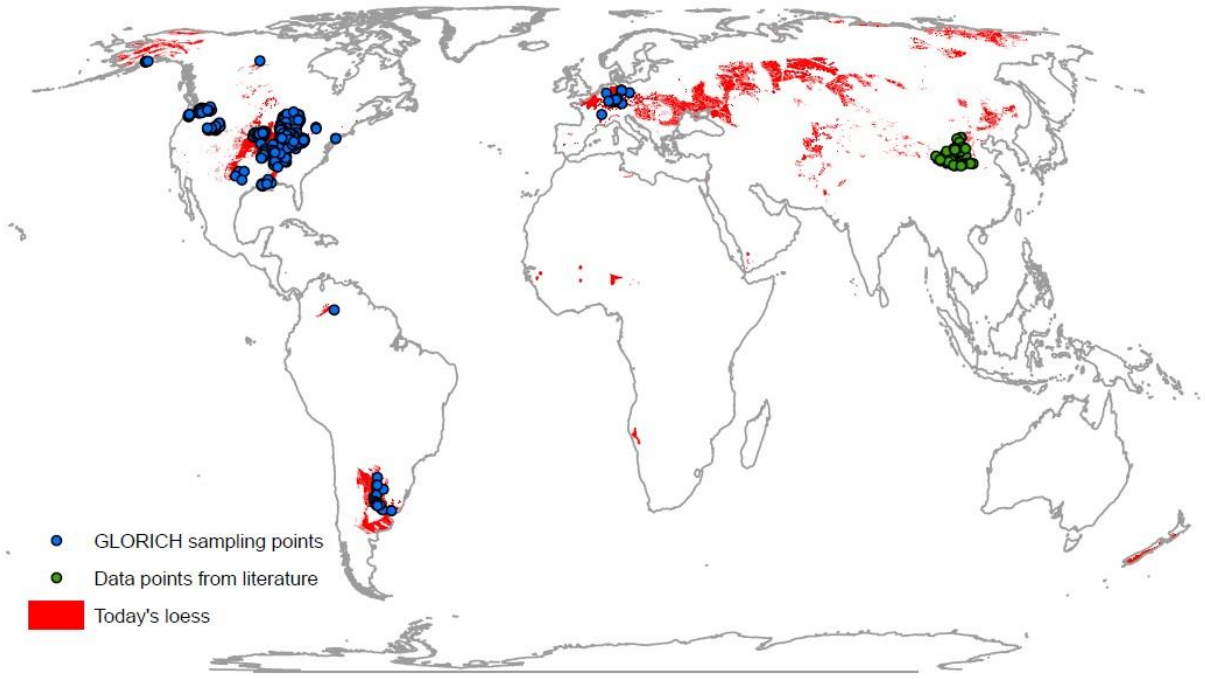

Figure 13: Locations of the water sampling stations, whose watersheds have more than 20% loess coverage and relevant water chemistry data. The GLORICH sampling points are shown in blue and the additional data points taken from literature are shown in green. The red areal extent represents the loess deposits of today (Börker et al., 2018).

Mean alkalinity flux rates in samples with a significant loess coverage of >20% is ~4110 µeq/m² a, whereas the global average river alkalinity flux rate is ~1850 µeq/m² a, suggesting that loess weathering contributes disproportionally to alkalinity in river water and therefore to elevated fluxes compared to the lithological base below the loess deposits.

3.4.2.1 Regional observed differences in loess weathering

The different lithologies below the loess (loess fraction >0.2) do not show a significant pattern in their influence on the alkalinity concentration in global river waters (Fig. 14a). Therefore, it is assumed that the base lithology below the loess does not affect the study of loess weathering and is neglected, which is also supported by the study of Zhang et al. (2013). However, in case of carbonate sedimentary rocks below the loess deposits this may not be the case and their possible effect on loess weathering fluxes is additionally considered in Fig. 16 and 17.

Furthermore, it was tested, whether loess sediments show globally homogeneous weathering patterns. Alkalinity in rivers draining catchments with loess (areal loess fraction >0.2) shows a distinct temperature dependency, comparable to carbonate weathering patterns (Romero-Mujalli et al., 2018a), with some deviations from the patterns for Argentina (Fig. 14a, b). The analysis of major ions reveals some regional differences in the composition of the water (Fig. 14, c-f), which will be explained below.

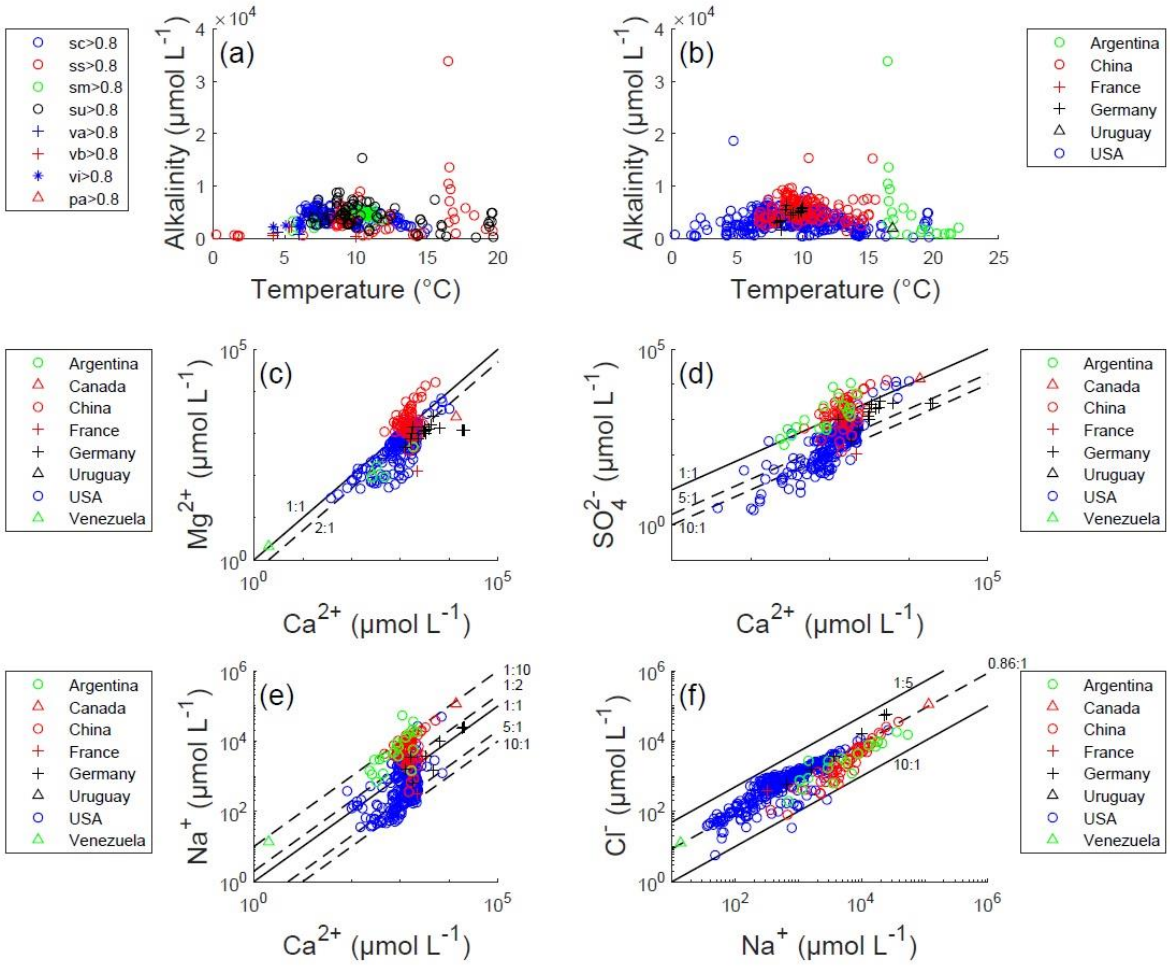

Figure 14: a) Alkalinity concentration versus temperature for loess deposits with a catchment fraction >0.2, grouped by the underlying bedrock (sc = carbonate sedimentary rocks, ss = siliciclastic sedimentary rocks, sm = mixed sedimentary rocks, su = unconsolidated sediments, va = acid volcanic rocks, vb = basic volcanic rocks, vi = intermediate volcanic rocks, pa = acid plutonic rocks). b) The dependency of alkalinity concentrations in rivers draining loess (fraction >0.2), grouped after regions, shows that the Argentinian and Chinese loess have in general higher alkalinity concentrations. Major ion concentrations in rivers draining loess deposits (fraction >0.2) with Ca^{2+}/Mg^{2+} (c), Ca^{2+}/SO_4^{2-} (d), Ca^{2+}/Na^{+} (e) and Na^{+}/Cl^{-} (f).

The Ca^{2+}/Mg^{2+} concentrations in the river water (Fig. 14c), with the dashed line representing the ratio of Ca^{2+}/Mg^{2+} = 2, indicates that other carbonate minerals than calcite (e.g., dolomite) or silicate minerals may be Ca^{2+} sources (Romero-Mujalli et al., 2018a). While the loess regions of France, Germany, Venezuela, Canada and Argentina are not affected by this, China shows the largest positive deviation from this ratio. For the USA, Goddéris et al. (2013) report that dolomite weathering occurs in the loess pedons, which might be reflected here. Dolomite occurrences are also reported for the Chinese Loess Plateau (e.g., Meng et al., 2015). Abundance of Mg^{2+} causes the alkalinity pattern to show elevated values in comparison to calcite dominated catchments for temperatures >11°C (Romero-Mujalli et al., 2018a) as shown in Fig. 14b for some Chinese data points and in Fig. 16 and 17. The Ca^{2+}/SO_4^{2-} ratio (Fig. 14d) shows that most of the water sampling

points are dominated by SO_4^{2-}. This may indicate an influence of sulphate mineral dissolution (Romero-Mujalli et al., 2018a) or anthropogenic inputs as pyrite oxidation might be excluded, assuming that particles transported via air are oxidized quickly. Especially Argentinian and Chinese loess deposits show elevated SO_4^{2-} concentrations (ratio of $Ca^{2+}/SO_4^{2-} \sim 1$), which could be related to evaporation. Sampling points with a $Ca^{2+}/Na^{+} <10$ (Fig. 14e) might be influenced by evaporite dissolution or silicate weathering (Gaillardet et al., 1999), which is the case for almost all samples. Many data points have a ratio different from $Na^{+}/Cl^{-} \sim 0.86$ (Fig. 14f), which indicates that the Na^{+} and Cl^{-} concentrations are affected by other sources than sea salt (ratio molar $Na^{+}/Cl^{-} \sim 0.86$; Möller (1990)).

The general cation distribution pattern suggests that Ca^{2+} is the primary cation released (Fig. 15), supporting that calcite might be the dominant contributor, whereas Na^{+} contributes ~20% to the total cations equivalent flux. Ternary diagrams of the distribution of major cations in the water samples draining loess deposits (fraction >0.2) can be additionally seen in Appendix B.2, showing that carbonate sedimentary rocks provide in general lower concentrations of Na^{+} and K^{+} compared to loess deposits.

Since loess mineralogy is dependent on the provenance and the primary lithologies that it is derived from, it is challenging to find the one typical weathering signature for all regions of loess. The Argentinian loess might be influenced by an input of volcanic ash (Zárate, 2003) or evaporitic processes within the river catchments and therefore shows elevated concentrations of Na^{+} or SO_4^{2-}. Evaporation can be expected in some regions of the Chinese Loess Plateau since it is the largest arid and semi-arid zone in China (Huang et al., 2008), which might explain increased concentrations of SO_4^{2-} or Na^{+}. Moreover, dolomite contribution to alkalinity fluxes, which is represented by increased/elevated Mg^{2+} concentrations, might be expected for regions of the Chinese loess deposits and some regions of the loess deposits of the USA (Goddéris et al., 2013; Meng et al., 2015).

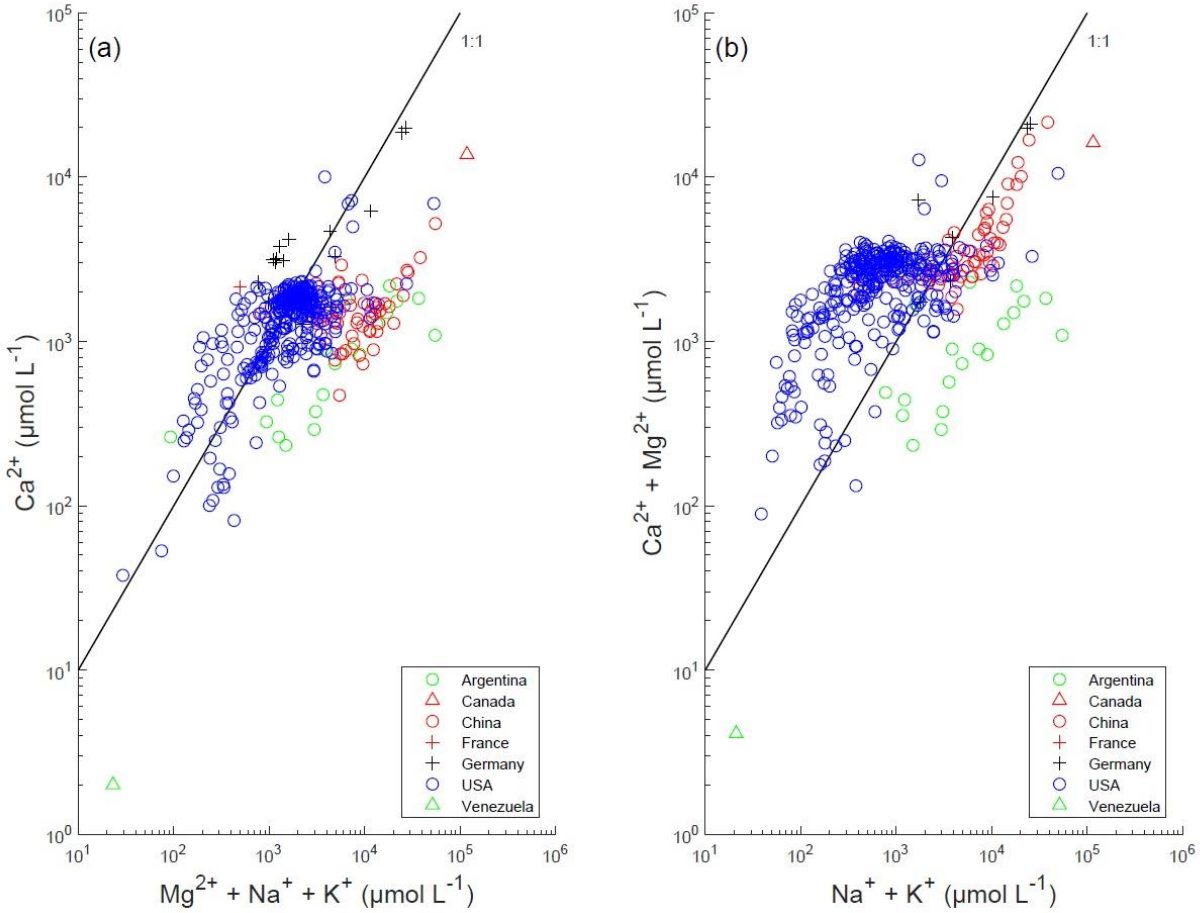

Figure 15: The ratio of Ca^{2+} vs. $Mg^{2+}+Na^{+}+K^{+}$ (a) and ratio of $Ca^{2+}+Mg^{2+}$ vs. $Na^{+}+K^{+}$ (b) in the water samples draining watersheds of >20% of loess coverage. The solid line represents the 1:1-line. Note that for cations where no data was available the value was set to 0 for comparison.

3.4.3 Comparison with previous carbonate weathering functions

To test the hypothesis that loess weathering derived alkalinity fluxes are comparable to carbonate rock alkalinity fluxes at the broader scale, previous global carbonate weathering models were compared with the new dataset compiled here. Used global carbonate weathering functions are runoff-dependent (Amiotte-Suchet and Probst, 1995; Bluth and Kump, 1994) and include in case of the function for calcite weathering (Romero-Mujalli et al., 2018a) a temperature adjustment, comparable in shape as shown for loess alkalinity in Fig. 14a and b. The general increase in alkalinity with increasing temperature up to ~11°C in the model of Romero-Mujalli et al. (2018a) can be explained by increasing biological activity and hence elevated soil-rock pCO_2 driving the weathering reactions. However, for higher temperatures (>11°C) alkalinity concentrations in rivers seem to decrease, which is related to the temperature effect on the carbonate system (Romero-Mujalli et al., 2018a). Gaillardet et al. (2018) analyzed the climate control on carbonate weathering using $Ca^{2+}+Mg^{2+}$ concentrations to display the intensity of carbonate weathering and found that the maximum of carbonate weathering intensity can be observed with mean annual air

temperatures between 5 and 15°C following a bell-shaped curve, which is consistent with the results of Romero-Mujalli et al. (2018a).

These identified bell-shape-patterns for calcite weathering conditions are also observed using all water samples whose catchments have a loess fraction >0.2 and showing alkalinity and Ca^{2+}+Mg^{2+} concentrations dependent on temperature (Fig. 16 and 17). Both figures show the identified function of Romero-Mujalli et al. (2018a) with its range of the calculated uncertainty for comparison.

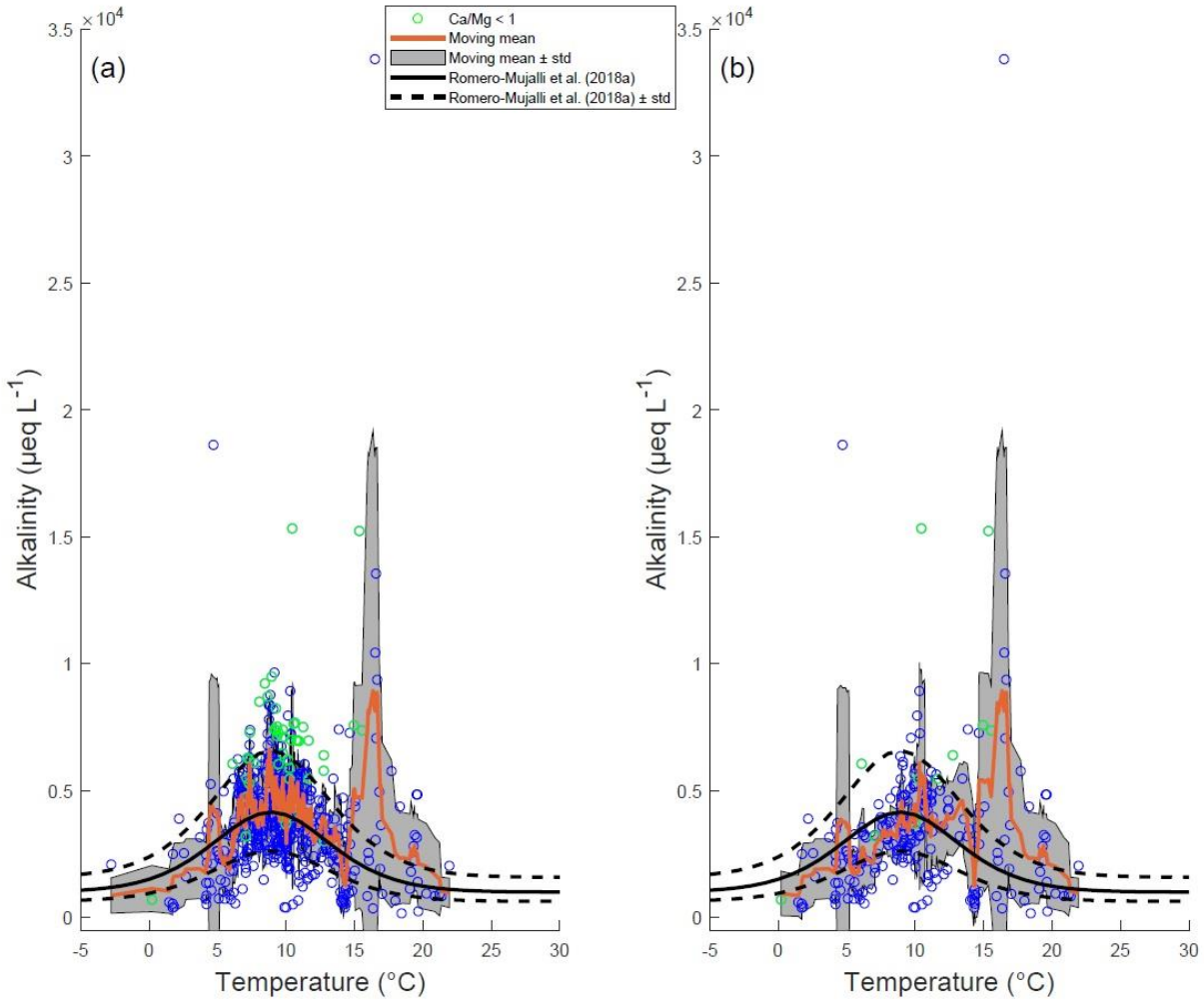

Figure 16: Alkalinity concentration of river catchments with a loess fraction >0.2, dependent on temperature (a). Carbonate sedimentary rocks as underlying lithology were excluded (sc >0.2) to test their influence on the alkalinity concentrations (b). The solid black line in both plots represents the function for carbonate weathering identified by Romero-Mujalli et al. (2018a) with the range of uncertainty as dashed lines for typical calcite weathering. The green points indicate water samples with Ca^{2+}/Mg^{2+}<1 and shows that outliers are partly because of elevated Mg^{2+} concentrations. Additionally the moving mean value of alkalinity concentration is shown (in orange) with the range of the standard deviation (in grey).

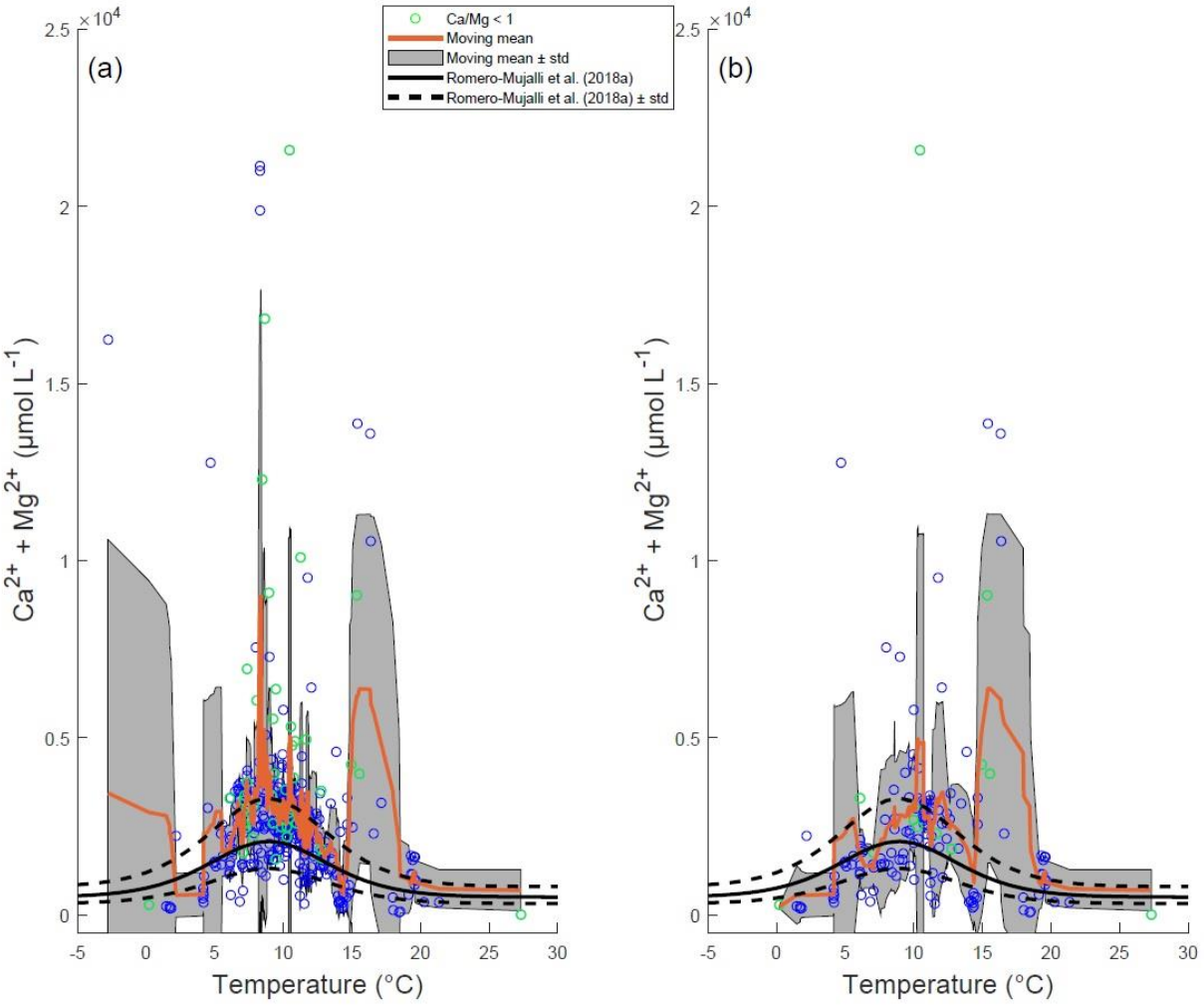

Figure 17: Ca^{2+}+Mg^{2+} concentration of river catchments with a loess fraction >0.2, dependent on temperature (a). Carbonate sedimentary rocks as underlying lithology were excluded (sc >0.2) to test their influence on the water chemical species (b). The solid black line represents in both plots the function for carbonate weathering identified by Romero-Mujalli et al. (2018a) with the range of uncertainty as dashed lines for typical calcite weathering. The red points indicate water samples with Ca^{2+}/Mg^{2+}<1. Additionally the moving mean value of the Ca^{2+}+Mg^{2+} concentration is shown (in orange) with the range of the standard deviation (in grey).

Despite the above identified bell-shape pattern it has to be stressed out that the function of Romero-Mujalli et al. (2018a) was drained for catchments with predominant calcite weathering, while catchments with significant Mg^{2+} contribution showed a tendency to elevated alkalinity values. Therefore, this approach is reasonable for weathering from lithologies with dominant calcite weathering, but might underestimate alkalinity fluxes for other sources that add for example Mg^{2+}. The scattering and elevated concentrations might be due to the dissolution of other carbonate minerals (e.g., dolomite, indicated by elevated Mg^{2+} concentrations), silicate minerals or internal processes like evaporation. It cannot be concluded that the elevated concentrations are due to a

lower runoff in those sampling points in general (Fig. 18). However, very low runoff areas with a runoff <1mm/a have a clear tendency to elevated concentrations. The model of Romero-Mujalli et al. (2018a) shows a bias for temperatures between 15-20°C, but the data points that scatter in this temperature range represent mostly the data points of Argentina, which might be dominated by silicate weathering due to an input of volcanic ash and predominantly volcanic rocks as source rock (Zárate, 2003). Nevertheless, the bias in the global calculations could be small considering that regions with mean annual temperatures between 15-20°C cover today only ~13% and for the LGM ~20% of the ice- and water-free land area (temperature dataset used for the pre-industrial and LGM in this study, resolution 20 x 20km, landmask derived by the consideration of all lithologies used for calculations in this study).

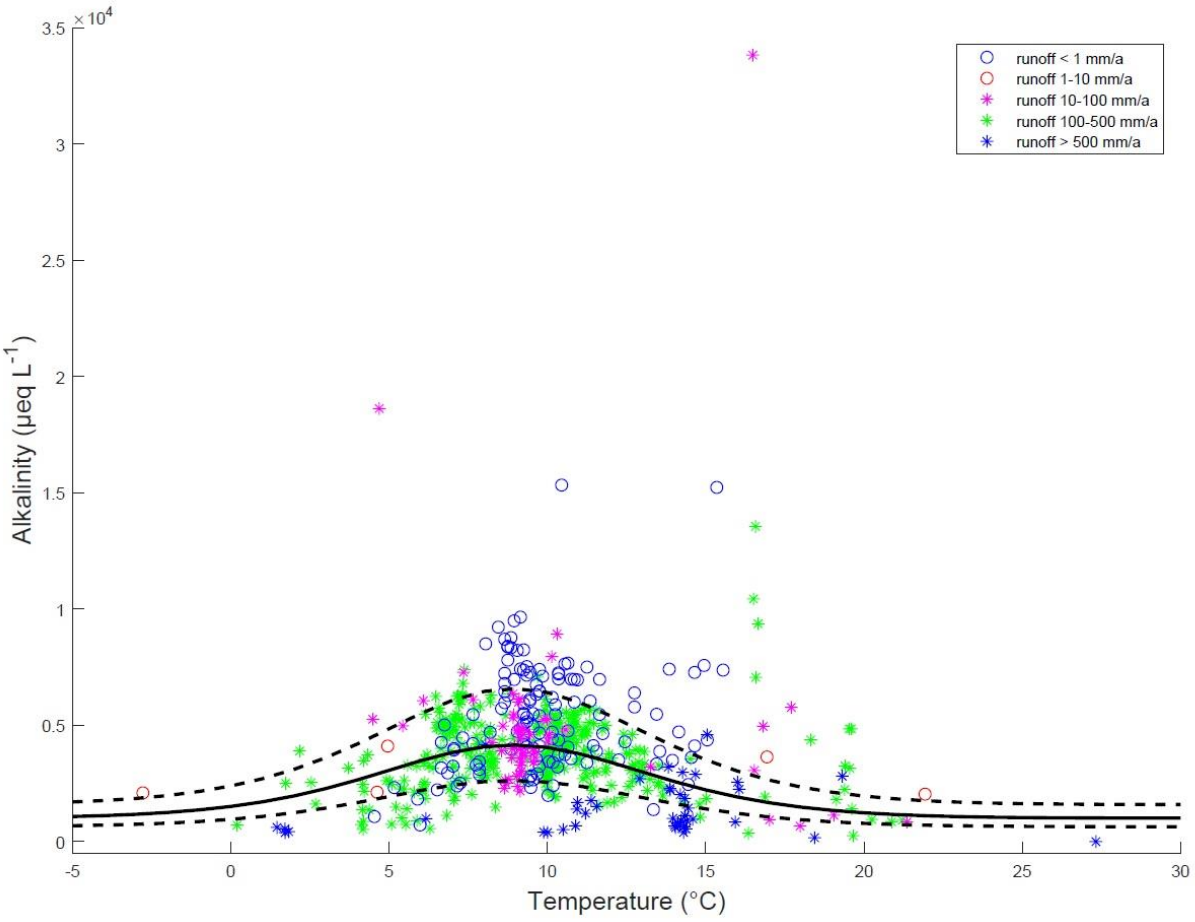

Figure 18: Alkalinity concentration of river catchments with a loess fraction >0.2, dependent on temperature and grouped after runoff. The solid black line represents the function for carbonate weathering identified by Romero-Mujalli et al. (2018a) with the range of the uncertainty as dashed lines for typical calcite weathering.

While the alkalinity concentration patterns seem to show the bell-shape pattern, dependent on temperature, runoff is in general the dominant control on the flux, which is intended to be modelled in the following. Alkalinity concentrations of river waters draining loess sediments (fraction >0.2)

generally decrease with increasing runoff (Fig. 19a). The dilution effect seems to be strong after a threshold of about 200 mm/a (Fig. 19a and b) and ~26% of all global loess deposits today have runoff values >200 mm/a, so that the dilution effect should be considered in global calculations of loess weathering.

Therefore, a new function was developed, based on a non-linear regression method for the observed runoff and alkalinity flux rates (Fig. 19b) applying a four-parameter logistic function, which fits best the observed data points and allows for assuming a constant alkalinity flux rate for high runoff values. One parameter was set manually to 9 to represent the maximum values of alkalinity flux rate of the data points. The function was built after:

$$log_{10} alkalinity\ flux\ rate = \frac{9}{1+exp^{-a(log_{10} runoff+b)}} + c\ , \quad \text{MSE} = 0.08 \qquad \text{(eq. 8)}$$

with $\log_{10}$alkalinity flux rate in µeq/km² a

$\log_{10}$runoff in mm³/mm² a

a = 0.63

b = 0.76

and c = -2.00.

The range of uncertainty in the global calculations of eq. 8 was calculated as follows:

$$Uncertainty\ of\ the\ global\ flux = \sum(Flux\ per\ grid * 0.08 * \log(10)) \qquad \text{(eq. 9)}$$

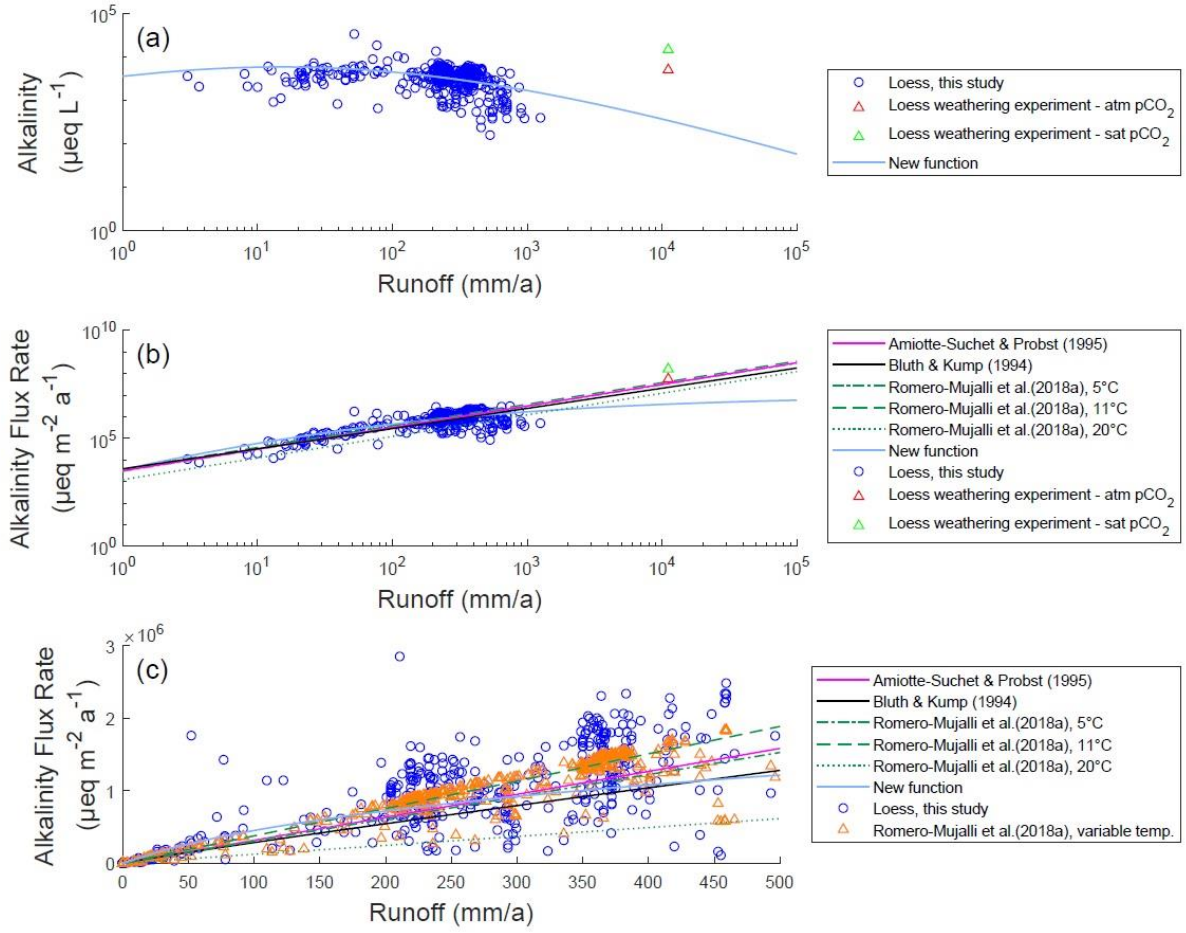

Figure 19: Relationship between runoff and alkalinity concentration (a) and relationship between runoff and alkalinity flux rate (b) with the previous models of Amiotte-Suchet and Probst (1995), Bluth and Kump (1994) and Romero-Mujalli et al. (2018a) and the new function for comparison. The red triangle represents the sample of a loess column experiment under atmospheric pCO_2 conditions and the green triangle the loess column experiment under saturated pCO_2 conditions, preventing the dilution effect by forcing percolation of water. The relationship between alkalinity flux rate and runoff, comparing the models, with a zoom into runoff values of 0–500 mm/a is shown in (c). The orange triangles show here the dispersion of alkalinity flux rate values considering the temperature of the sampling points applying the model of Romero-Mujalli et al. (2018a).

Calculating the uncertainties of the alkalinity flux rates of the four models (observed-predicted, eq.7), shows that the smallest residual standard deviation can be found for the model of Romero-Mujalli et al. (2018a) (0.5×10^6 µeq/m^2/a), whereas for Amiotte-Suchet and Probst (1995), Bluth and Kump (1994) and the new function the values are 1×10^6, 4.2×10^6 and 2.7×10^6 µeq/m^2/a, respectively.

The residuals distribution of the modelled alkalinity flux rates of the four carbonate weathering models compared to different variables can be seen in Fig. 20. The relative residual distribution is additionally shown in Appendix B.

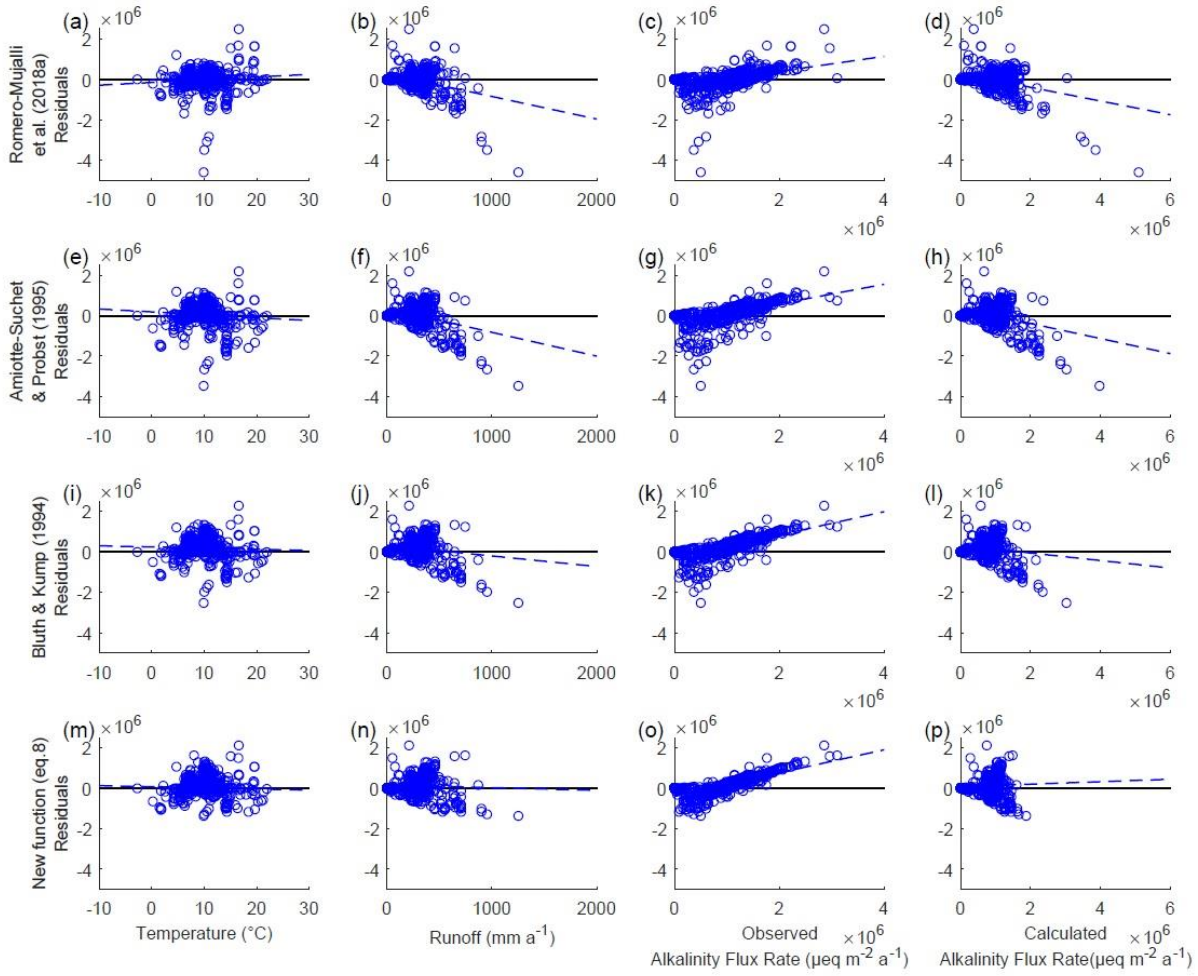

Figure 20: Residual analyses (observed flux-predicted flux) compared to different variables of the four models for Romero-Mujalli et al. (2018a) (a-d), Amiotte-Suchet and Probst (1995) (e-h), Bluth and Kump (1994) (i-l), and the new function (eq.8) (m-p). Trendlines are shown in dashed blue.

The new function (eq. 8) can best predict the observed alkalinity flux rates with an r^2=0.46 (r^2=0.42 for Romero-Mujalli et al. (2018a), r^2=0.33 for Amiotte-Suchet and Probst (1995) and r^2=0.34 for Bluth and Kump (1994)). The model of Romero-Mujalli et al. (2018a), however, shows a reduced dispersion for temperature (excluding extreme values), while for the runoff-dependent models the residuals show a higher dispersion and seem to display the "bellshape pattern" (Fig. 20 e,I,m). They might underestimate alkalinity flux rates for temperatures about 10°C, but for lower and higher temperatures, the runoff-dependent models might overestimate alkalinity fluxes. Moreover, it can be seen that all previous models overestimate fluxes for high runoff values (Fig. 20 c,f,j), whereas the new function (eq. 8) considers the dilution effect.

Although the model of Romero-Mujalli et al. (2018a) considers as well the climate variable temperature, it might underestimate global alkalinity fluxes from loess deposits because the inputs

of, for instance, Mg-minerals like dolomite, are neglected. The carbonate weathering functions of Amiotte-Suchet and Probst (1995) and Bluth and Kump (1994) represent total carbonate weathering fluxes, including other carbonate minerals than calcite. Nevertheless, they assume almost constant alkalinity values, which is not consistent with the observed alkalinity concentrations in rivers draining loess deposits (Fig. 21). For the global alkalinity flux calculations the new function for loess weathering (eq. 8) was applied since it can best predict alkalinity fluxes from loess deposits and considers the dilution effect for regions with high runoff values.

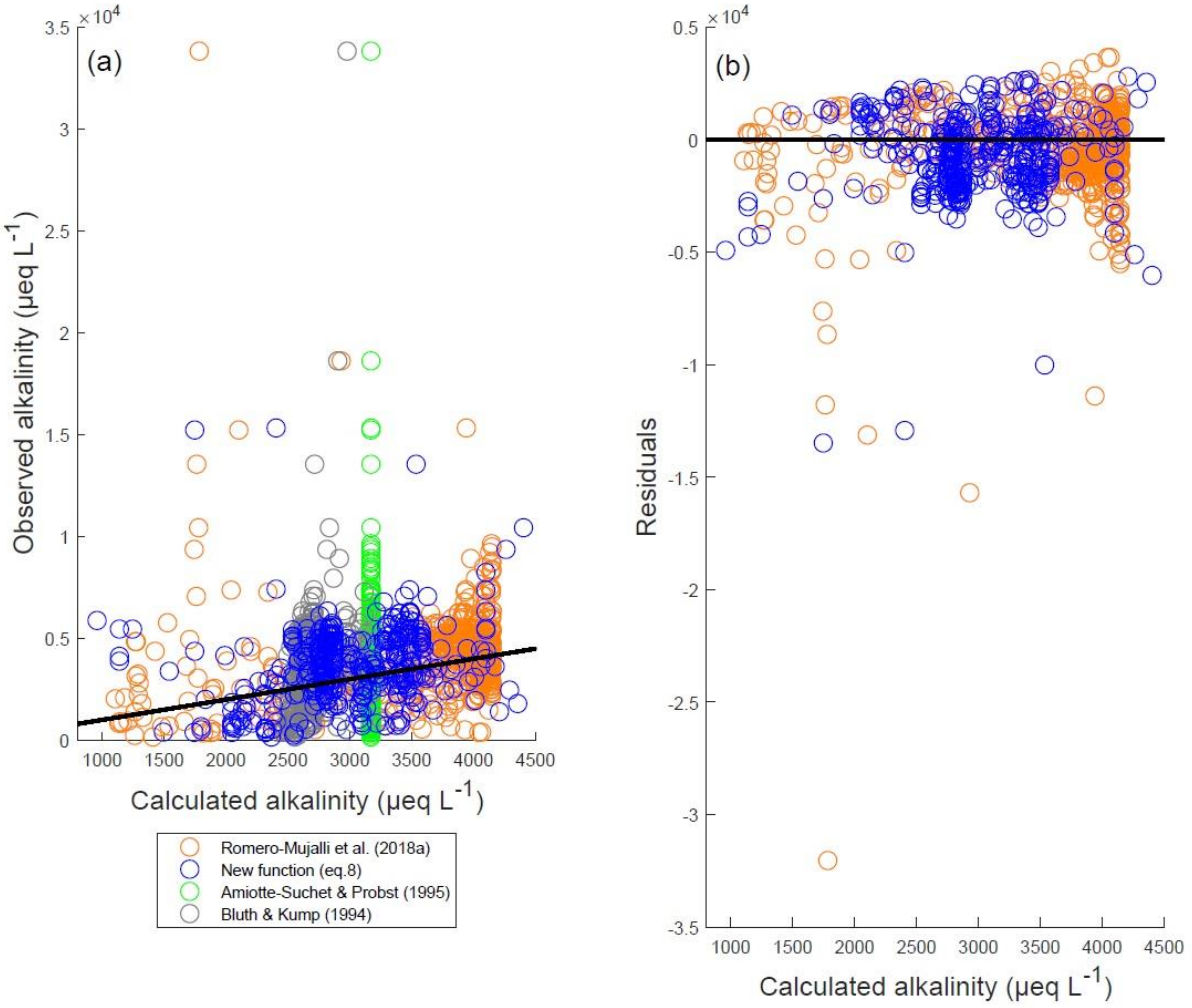

Figure 21: Observed alkalinity concentration in rivers draining loess deposits (loess fraction > 0.2) versus calculated alkalinity concentration applying different models. The solid line represents the 1:1 line (a). Residuals distribution applying the model of Romero-Mujalli et al. (2018a) and the new function (eq.8) (b).

3.4.4 Global alkalinity fluxes including loess deposits

For the global calculations of alkalinity flux and CO_2 consumption rates from loess deposits the new function (eq. 8), whereas for carbonate sedimentary rocks the models of Romero-Mujalli et al. (2018a), Amiotte-Suchet and Probst (1995) and Bluth and Kump (1994) were used and their results are listed in Tab. 4 and 5 and Fig. 22. For simplicity, in the following, the global alkalinity flux and CO_2 consumption values are compared for the different time slices applying the model of Romero-Mujalli et al. (2018a) for carbonate sedimentary rocks. For all other lithologies the model of Goll et al. (2014) was applied. Note that the CO_2 consumption rates of loess deposits might be regarded as the lower boundary, because additional silicate weathering happening in the loess sediments can increase the CO_2 consumption rates.

It can be shown that loess weathering increases the global alkalinity fluxes compared to the base lithology below (~36% for the LGM, ~15% for the Mid-Holocene and ~16% for today).

Table 4: Contribution of loess weathering to global CO_2 consumption rates for different time slices. Note that for Romero-Mujalli et al. (2018a) and the new function the range of uncertainty of the global calculations is given in the brackets. The combination of both uncertainty estimations was derived as: total uncertainty = $\sqrt{(uncertainty\ Romero-Mujalli\ et\ al.\ (2018a)^2 + uncertainty\ new\ function^2)}$. "*"-values are calculated for the exposed continental shelves.

		LGM [Mt C/a]		Mid-Holocene [Mt C/a]		Today [Mt C/a]	
	Model	With loess	Without loess	With loess	Without loess	With loess	Without loess
Silicate-dominated lithologies (su,vb,pb,py,va, vi, partly: mt, ss, pi,sm, pa) [+]	Goll et al. (2014)	28+3*	28+3*	44	45	43	44
Carbonate-influenced lithologies (partly: mt, ss, pi, sm, pa)[+]	Goll et al. (2014)	12+2*	13+2*	20	20	20	20
Carbonate sedimentary rocks (sc)	Romero-Mujalli et al. (2018a)	12 [6;17] + 8 [4;12]*	13 [7;18] + 9 [5;13]*	15 [8;22]	16 [8;23]	15 [8;21]	16 [9;23]
Carbonate sedimentary rocks (sc)	Amiotte-Suchet and Probst (1995)	17+18*	18+19*	23	23	22	24
Carbonate sedimentary rocks (sc)	Bluth and Kump (1994)	14+16*	16+16*	19	20	19	20
Loess	(eq. 8)	18 [15;22] + 2 [2;3]*	-	11 [9;13]	-	12 [10;14]	-
Total, with sc from Romero-Mujalli et al. (2018a)		85 ± 8	68 ± 7	90 ± 8	81 ± 8	90 ± 7	80 ± 7
Total, with sc from Amiotte-Suchet and Probst (1995)		100	83	98	88	97	88
Total, with sc from Bluth and Kump (1994)		95	78	94	85	94	84

[+] su = unconsolidated sediments, sm = mixed sedimentary rocks, ss = siliciclastic sedimentary rocks, va = acid volcanic rocks, vb = basic volcanic rocks, vi = intermediate volcanic rocks, pa = acid plutonic rocks, pb = basic plutonic rocks, pi = intermediate plutonic rocks, py = pyroclastics, mt = metamorphics

Table 5: Contribution of loess weathering to global alkalinity flux rates for different time slices. Note that for Romero-Mujalli et al. (2018a) and the new function the range of uncertainty of the global calculations is given in the brackets. The combination of both uncertainty estimations was derived as: total uncertainty = $\sqrt{(uncertainty\ Romero-Mujalli\ et\ al.\ (2018a)^2 + uncertainty\ new\ function^2)}$. "*"-values are calculated for the exposed continental shelves.

		LGM [Mt C/a]		Mid-Holocene [Mt C/a]		Today [Mt C/a]	
	Model	With loess	Without loess	With loess	Without loess	With loess	Without loess
Silicate-dominated lithologies (su,vb,pb,py,va, vi, partly: mt, ss, pi,sm, pa) [+]	Goll et al. (2014)	28+3*	28+3*	44	45	43	44
Carbonate-influenced lithologies (partly: mt, ss, pi, sm, pa)[+]	Goll et al. (2014)	25+4*	26+4*	40	41	39	40
Carbonate sedimentary rocks (sc)	Romero-Mujalli et al. (2018a)	23 [13;34] +16 [9;24]*	25 [14;37] +17 [9;25]*	30 [16;43]	31 [17;46]	29 [16;43]	32 [17;46]
Carbonate sedimentary rocks (sc)	Amiotte-Suchet and Probst (1995)	33+37*	37+38*	45	47	45	47
Carbonate sedimentary rocks (sc)	Bluth and Kump (1994)	28+31*	31+33*	38	39	38	40
Loess	(eq. 8)	37 [30;44] +4 [4;5]*	-	21 [17;25]	-	23 [19;28]	-
Total, with sc from Romero-Mujalli et al. (2018a)		140 ± 15	103 ± 14	135 ± 14	117 ± 15	134 ± 14	116 ± 15
Total, with sc from Amiotte-Suchet and Probst (1995)		171	136	150	133	150	131
Total, with sc from Bluth and Kump (1994)		160	125	143	125	143	124

[+] su = unconsolidated sediments, sm = mixed sedimentary rocks, ss = siliciclastic sedimentary rocks, va = acid volcanic rocks, vb = basic volcanic rocks, vi = intermediate volcanic rocks, pa = acid plutonic rocks, pb = basic plutonic rocks, pi = intermediate plutonic rocks, py = pyroclastics, mt = metamorphics

Increased alkalinity fluxes due to loess deposits are especially interesting because mapped loess deposits today cover only about 4% of the global ice-free land area (relative to the GLiM area without ice and water bodies; Hartmann and Moosdorf (2012)). Loess areal extent reported in the GUM (Börker et al., 2018) might underestimate the land area where loess weathering occurs because thin loess covers might not be mapped in geological maps. This implicates that the influence on global alkalinity fluxes and CO_2 consumption rates could become even larger. Some literature studies report a global loess cover today of about 10% (Muhs and Bettis, 2003; Pécsi, 1990). Taking the LGM loess-cover and applying it for today's climate setting results in a mean increase of about 34% for alkalinity flux rates and about 25% for CO_2 consumption rates if compared to today's alkalinity flux and CO_2 consumption rates without loess. Because the extrapolated LGM loess cover partly includes river valleys and therefore alluvial sediments, which might contain relevant amounts of loess today, the approach of comparing global alkalinity fluxes derived by loess deposits might be seen as conservative, since the distributed LGM loess might still influence the today's weathering fluxes.

The calculated global weathering fluxes are generally lower than estimates from previous studies, which can be explained by in general lower runoff values in the datasets used for the global calculations in this study (Jungclaus et al., 2012a; Jungclaus et al., 2012b; Jungclaus et al., 2012c) to allow a comparison with runoff as a forcing parameter based on the same model outputs. Applying a runoff dataset, which was used to calibrate the new loess function (eq. 8) and which includes observed river discharge information (Fekete et al., 2002), yields 106 to 124% higher values (Tab. 6). Therefore, only the relative changes between time slices are interpreted here.

Table 6: Global alkalinity flux rates and CO_2 consumption rates for today applying the runoff dataset of Fekete et al. (2002) and applying the LGM loess cover.

	Today – MPI runoff [Mt C/a]	Today – Fekete et al. (2002) runoff [Mt C/a]	change to MPI runoff today [%]	Today –applying LGM loess cover + MPI runoff [Mt C/a]	change to MPI runoff today [%]
Alkalinity flux rates	134 ± 14	276 ± 27	+106	156 ± 15	+16
CO_2 consumption rates	90 ± 7	202 ± 14	+124	100 ± 8	+11

The differences in alkalinity flux rates between the Mid-Holocene and the present-day are generally low (Fig. 22), only for loess deposits the alkalinity flux rates during the Mid-Holocene decrease by ~9 %. Alkalinity flux rates derived by silicate weathering are decreasing during the LGM (~30% without loess and ~28% with loess if compared to today). Moreover, the alkalinity fluxes derived by the carbonate weathering proportion of the model of Goll et al. (2014), which was applied for other lithologies than carbonate sedimentary rocks (sc) and loess, are decreasing during the LGM as well (~25% without loess and ~26% with loess).

The alkalinity flux rates from carbonate sedimentary rocks (sc) for the different applied models are regarded separately in the following. Generally, the alkalinity fluxes from carbonate sedimentary rocks increase for all three models during the LGM (Fig. 22). The values derived by applying the carbonate weathering functions of Amiotte-Suchet and Probst (1995) and Bluth and Kump (1994) show the highest positive deviations (mean of both models: ~55% increase for the scenario with loess and ~60% increase for the scenario without loess). Applying the model of Romero-Mujalli et al. (2018a) for the carbonate sedimentary rocks during the LGM shows a smaller deviation (~34% increase with loess and ~31% increase without loess).

These differences might be explained by the alkalinity flux rates derived from carbonate sedimentary rocks (sc) on the exposed continental shelf areas. Previous studies on changes of weathering fluxes at glacial-interglacial timescales report a slight increase of global fluxes of about 20% for the LGM time, mostly because of the abundance of carbonate outcrops on the continental shelves (Gibbs and Kump, 1994; Ludwig et al., 1999). Here, the carbonates of the continental shelf areas contribute to global alkalinity fluxes by about 21% with loess and by about 27% without loess (mean of the two runoff-dependent models). These contribution of carbonate outcrops on the continental shelves to global alkalinity flux rates is less if applying the model of Romero-Mujalli et al. (2018a) (~11% with loess and ~17% without loess). These differences might be related to an overestimation of the fluxes of the only runoff-dependent models for the carbonate outcrops, mostly located in high temperature regions, on the exposed continental shelf areas because the models do not consider temperature. Runoff as possible reason can be excluded because all three models show a comparable bias for runoff. Loess deposits on the continental shelves do not contribute significantly to global alkalinity flux rates (~2% applying the mean of the three models).

The elevated alkalinity fluxes during the LGM from loess sediments (~+78% compared to today) might be slightly too high because the loess regions during the LGM show colder temperatures (with a mean of about -3 °C), which might lead to an overestimation of fluxes for the runoff-dependent new function (eq. 8). Applying the temperature- and runoff-dependent model of Romero-Mujalli et al. (2018a) for the loess deposits shows an increase of about 20% of loess-derived alkalinity fluxes compared to today. Nevertheless, there exists a lack of data points for low temperature regions, but because the residuals of the new function (eq. 8) show a smaller range than the other models, it might be reasonable to apply the new function for loess weathering (eq. 8) as first order approximation.

With the new loess weathering function and applying the model of Romero-Mujalli et al. (2018a) for carbonate sedimentary rocks (sc) to avoid an overestimation of alkalinity fluxes from the exposed continental shelves during the LGM, the differences in the total global alkalinity fluxes between the LGM and today become small (~4% increase for the LGM). Without the consideration of loess weathering the differences in alkalinity fluxes between the LGM and today become larger (~11% decrease during the LGM).

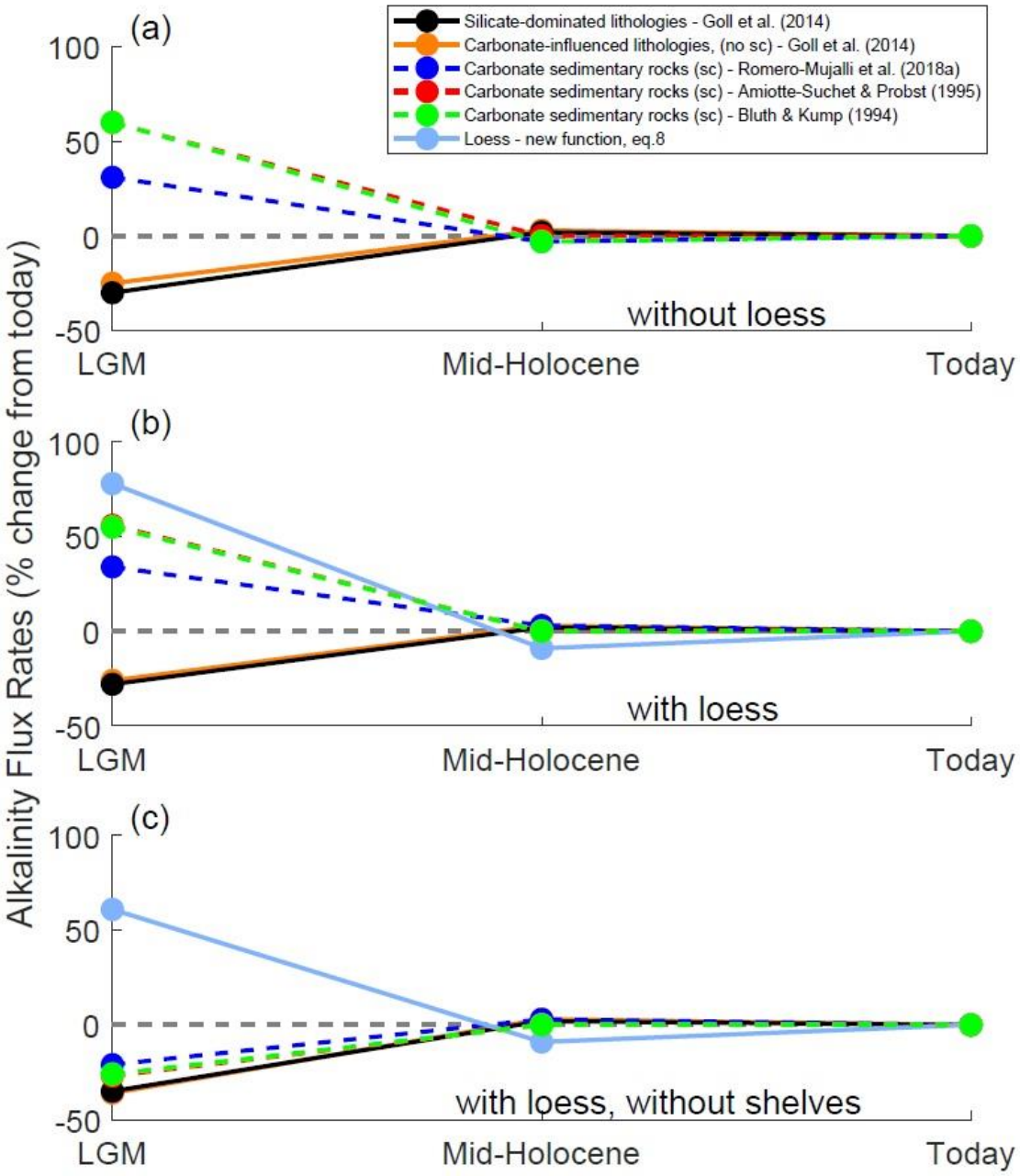

Figure 22: Comparison of the alkalinity flux rates of the different time slices, without the consideration of loess deposits (a) and with loess deposits (b). (c) shows the changes of alkalinity flux rates, without the continental shelves. Note that the equations used to calculate alkalinity fluxes for all other lithologies apart from carbonate sedimentary rocks (sc) and loess from Goll et al. (2014) distinguish between alkalinity fluxes derived by carbonate weathering and by silicate weathering (explanation in Appendix B).

3.5 Conclusion

Loess sediments are widespread around the globe today. They can be very heterogeneous regarding their mineralogy, depending on their provenance or internal processes like evaporation. Nevertheless, it was shown that the application of carbonate weathering functions to quantify alkalinity fluxes and CO_2 consumption rates from loess deposits is reasonable as a first order approximation, and a new function for loess weathering was developed, which considers a dilution effect. To improve weathering flux predictions from loess sediments, global models might consider additional minerals important for weathering processes, like dolomite or sulphate minerals. Furthermore, more data on cold temperature regions, especially interesting for the LGM, is needed to better quantify loess weathering fluxes. Besides, it has to be tested if the global alkalinity fluxes from loess deposits are possibly underestimated, because small loess covers might not be mapped as loess, but still influence the water chemistry.

The three different previous carbonate weathering models show differences in global alkalinity flux rates during the LGM because they react differently to temperature changes. The solely runoff-dependent models probably overestimate fluxes from the carbonate sedimentary rocks on the exposed tropical continental shelves. The temperature- and runoff-dependent model, on the other hand, might underestimate fluxes if other minerals than calcite are abundant. These differences and sensitivities to climate change should be considered in global weathering models.

Applying the new loess weathering function suggests that loess contributes significantly to global alkalinity flux rates. Loess weathering contributes about 16% to global alkalinity flux. Gaillardet et al. (1999) report on a larger proportion of carbonate weathering on global CO_2 consumption fluxes than calculated by Hartmann (2009). This gap could be partly explained by loess weathering. Comparing the LGM and today shows that there exist almost no difference in global alkalinity flux rates (~4% higher alkalinity flux rates during the LGM). Without the consideration of loess weathering the global alkalinity flux rates decrease during the LGM by about 11%, mostly because of lower silicate weathering rates. The enhanced fluxes from loess sediments are hence counteracting the decrease in silicate weathering rates during the LGM. Loess sediments might hence be involved in stabilizing the alkalinity fluxes in the glacial-interglacial climate system, which points to the importance of further consideration of sediments in global weathering models.

4 Aging of basalt volcanic systems and decreasing CO_2 consumption by weathering

This chapter has been published as: Börker, J., Hartmann, J., Romero-Mujalli, G., and Li, G.: Aging of basalt volcanic systems and decreasing CO2 consumption by weathering, Earth Surf. Dynam., 7, 191-197, 10.5194/esurf-7-191-2019, 2019.

4.1 Abstract

Basalt weathering is one of many relevant processes balancing the global carbon cycle via land-ocean alkalinity fluxes. The CO_2 consumption by weathering can be calculated using alkalinity and is often scaled with runoff and/or temperature. Here it is tested if the surface age distribution of a volcanic system derived by geological maps is a useful proxy for changes in alkalinity production with time.

A linear relationship between temperature normalized alkalinity fluxes and the Holocene area fraction of a volcanic field was identified, using information from 33 basalt volcanic fields, with an r^2=0.93. This relationship is interpreted as an aging function and suggests that fluxes from Holocene areas are ~10 times higher than those from old inactive volcanic fields. However, the cause for the decrease with time is probably a combination of effects, including a decrease in alkalinity production from material in the shallow critical zone as well as a decline in hydrothermal activity and magmatic CO_2 contribution. The addition of fresh reactive material on top of the critical zone has an effect in young active volcanic settings which should be accounted for, too.

A comparison with global models suggests that global alkalinity fluxes considering Holocene basalt areas are ~60% higher than the average from these models imply. The contribution of Holocene areas to the global basalt alkalinity fluxes is today however only ~5%, because identified, mapped Holocene basalt areas cover only ~1% of the existing basalt areas. The large trap basalt proportion on the global basalt areas today reduces the relevance of the aging effect. However, the aging effect might be a relevant process during periods of globally, intensive volcanic activity, which remains to be tested.

4.2 Introduction

Basalt areas, despite their limited areal coverage, contribute significantly to CO_2 sequestration by silicate rock weathering (Dessert et al., 2003; Gaillardet et al., 1999; Hartmann et al., 2009). The sensitivity of basalt weathering to climate change (Coogan and Dosso, 2015; Dessert et al., 2001; Dessert et al., 2003; Li et al., 2016) supports a negative weathering feedback in the carbon cycle that maintains the habitability of the Earth's surface over geological time scales (Berner et al., 1983; Li and Elderfield, 2013; Walker et al., 1981). Changes in volcanic weathering fluxes due to emplacement of large volcanic provinces or shifts in the geographic distribution of volcanic fields

associated with continental drift may have contributed to climate change in the past (Goddéris et al., 2003; Kent and Muttoni, 2013; Schaller et al., 2012).

The role of basalt weathering in the carbon cycle and its feedback strength in the climate system depends, besides the release of geogenic nutrients, on the amount of associated CO_2 consumption and related alkalinity fluxes. The factors that modulate these fluxes are a subject to uncertainty. Previous studies suggest that basalt weathering contributes 25–35% to the global silicate CO_2 consumption by weathering (Dessert et al., 2003; Gaillardet et al., 1999; Hartmann et al., 2009). However, their estimations do not consider the potential aging of a weathering system (e.g., Taylor and Blum, 1995). Young volcanic areas can show much higher weathering rates compared to older ones, as was shown for the Lesser Antilles, where a rapid decay of weathering rates within the first 0.5 Ma was observed (Rad et al., 2013). Such an aging effect of volcanic areas is difficult to parameterize for global basalt weathering fluxes, due to a lack of global compilations.

A practical approach to resolve this issue is to distinguish older and inactive volcanic fields (IVFs) and active volcanic fields (AVFs) (Li et al., 2016) and compare weathering fluxes with factors driving the weathering process, like land surface temperature or hydrological parameters. By compiling data from 37 basaltic fields globally, Li et al. (2016) showed that spatially explicit alkalinity fluxes (or CO_2 consumption rates) associated with basalt weathering correlate strongly with land surface temperature for IVFs but not for AVFs. They suggested that previously observed correlations between weathering rates and runoff in global data sets originate partly from the coincidence of high weathering rates and high runoff of AVFs rather than a direct primary runoff control on the weathering rate. Many studied AVFs are located near the oceans and have an elevated topography, a combination which can cause elevated runoff due to an orographic effect (Gaillardet et al., 2011). However, the effect of aging on weathering rates from a volcanic system discussed here has not been evaluated.

The age distribution of the surface area of a whole volcanic system might be used as a first-order proxy to study the variability of weathering fluxes of AVFs. However, the exact surface age of volcanic areas is rarely mapped in detail, but Holocene areas are often reported in geological maps. Here, basalt alkalinity fluxes are related to the calculated Holocene areal proportion of volcanic fields at the catchment scale. For this, the concept of weathering reactivity is introduced, which is the relative alkalinity flux of AVFs to the alkalinity flux estimated for IVFs. This reactivity R is compared with the relative age distribution of surface areas, using the proportion of total area occupied by Holocene lavas. From this comparison, a function for the decay of alkalinity fluxes with increasing proportion of older land surface area is derived and discussed.

4.3 Methods

The volcanic fields used to establish the relationship between weathering reactivity and Holocene coverage are predominantly described as basalt areas (Li et al., 2016). Based on the availability of detailed geological maps, 33 volcanic provinces were selected, with 19 IVFs and 14 AVFs. A detailed description is given in Appendix C. The 14 AVFs are geographically widespread and diverse (Fig. 23a). If the absolute age distribution of the volcanic rocks is available, the Holocene

areas were mapped using the age range from 11.7 ka to the present, according to the International Commission on Stratigraphy version 2017/02 (Cohen et al., 2013). If possible, coordinates of water sample locations were used to constrain catchment boundary to calculate the Holocene fraction for monitored areas. In all cases, already existing alkalinity flux calculations were taken from Li et al. (2016). Detailed information on additional mapping and calculations for each system can be found in Appendix C.

The weathering reactivity *R* of each volcanic field is calculated by normalizing the observed alkalinity flux of the AVF ($F_{calculated}$, in 10^6 mol km^{-2} a^{-1}) to that of the expected flux if the AVF would be an IVF ($F_{expected}$):

$$R = \frac{F_{calculated}}{F_{expected}} \quad \text{(eq. 10)}$$

where the expected alkalinity flux $F_{expected}$ for IVFs is given by the function (Fig. 23b):

$$F_{expected}\,[10^6\ mol\ km^{-2}a^{-1}] = 0.23 * e^{(0.06*T\,(^{\circ}C))}, \quad \text{RMSE} = 0.3 \quad \text{(eq. 11)}$$

The root mean square error of the function is represented by RMSE. The parameters of the equation were derived by using a Monte Carlo method, simulating 10,000 runs (for more information see Appendix C).

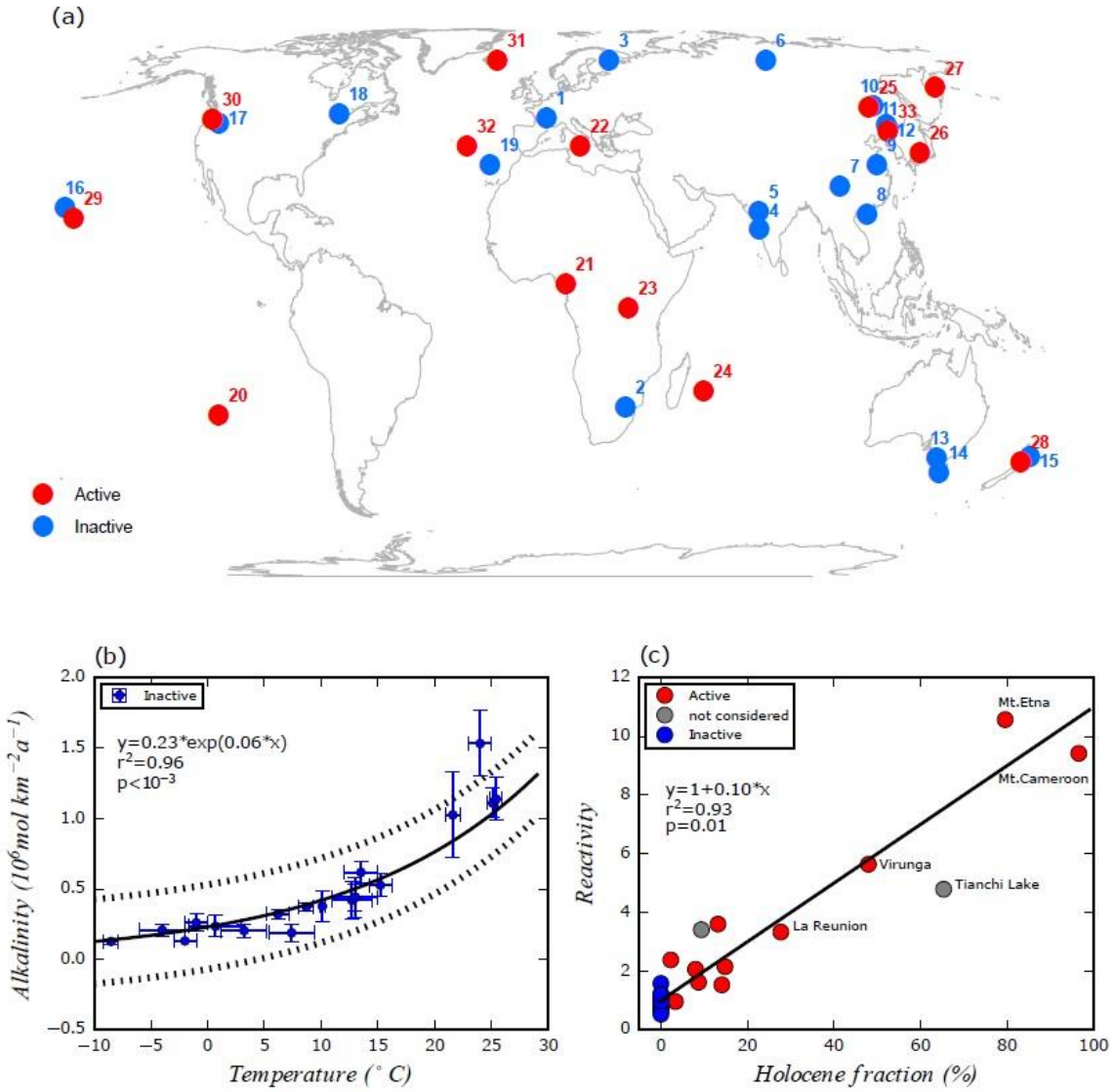

Figure 23: 2(a) The global map shows the locations of the active volcanic fields (in red) and the inactive volcanic fields (in blue) used in this study (1.Massif Central, 2.South Africa, 3.Karelia, 4.coastal Deccan, 5.interior Deccan, 6.Siberian Traps, 7.Mt. Emei, 8.Leiqiong, 9.Nanjing, 10.Xiaoxinganling, 11.Tumen River, 12.Mudan River, 13.southeast Australia, 14.Tasmania, 15.North Island, NZ, 16.Kauai, Hawaii, 17.Columbia Plateau, 18.northeast North America, 19.Madeira Island, 20.Easter Island, 21.Mt.Cameroon, 22.Mt.Etna, 23.Virunga, 24.La Réunion, 25.Wudalianchi Lake, 26.Japan, 27.Kamchatka, 28.Taranaki, 29.Big Island, Hawaii, 30.High Cascades, 31.Iceland, 32.São Miguel Island, 33.Tianchi Lake). (b) The exponential relationship between area specific alkalinity flux rates and the land surface temperature for IVFs. The dashed lines represent the range of the mean residual standard deviation of the function (see Appendix). Note that r^2 and the p value were derived by a linear regression of calculated alkalinity flux rates vs. estimated alkalinity flux rates using the new scaling law. (c) The relationship between the Holocene area fraction of the used watersheds from the volcanic fields and the weathering reactivity R. Note that Tianchi Lake and São Miguel are excluded from the calculation of the regression line because the applied catchments where not dominated by basalt but by trachytic volcanic rock types. Both data points still seem

to follow the identified regression trend line for AVFs. r^2 and the p value were calculated by a linear regression of the Holocene fraction vs. reactivity for all AVFs.

IVFs group around a reactivity R=1 in Fig. 23c, while having a Holocene fraction of zero. The reactivity R (eq. 10) of an AVF can be estimated by the Holocene area fraction as implied by the significant linear correlation identified in Fig. 23c. The theoretical reactivity of a 100% Holocene area H might be estimated by the equation given by Fig. 23c substituting y and x and setting H to 100:

$$R_{100\%\,Holocene} = 1 + 0.10 * H = 11 \quad \text{(eq. 12)}$$

With this, the flux from a young system of only Holocene age is

$$F_{Holocene} = R_{100\%\,Holocene} * F_{expected} \quad \text{(eq. 13)}$$

Global alkalinity fluxes from basalt areas were calculated by using eq. 11 for areas older than Holocene age and eq. 13 for mapped Holocene areas. These equations (eq.11 and the following, using information based on eq.2) were calibrated for areas with a runoff > 74 mm a^{-1} (lowest runoff value in the data compilation of Li et al. (2016) and therefore limit of the model setup) to avoid too-high alkalinity fluxes from drier areas with high temperature (e.g., the Sahara), assuming that neglecting fluxes from areas with lower runoff is not biasing the comparison (Tab. C1 in the Appendix). In this case, an overestimation is avoided. For the global calculation of CO_2 consumption by the new scaling law, a Monte Carlo method simulating 10,000 runs was applied (see Appendix).

Results are compared with four previous global empirical alkalinity flux models (Amiotte-Suchet and Probst, 1995; Bluth and Kump, 1994; Dessert et al., 2003; Goll et al., 2014). Alkalinity fluxes were translated into CO_2 consumption to allow for comparison with previous literature. For all models, the same data input was used: a newly compiled global basalt map (mostly derived by the basalt lithological layer from the GLiM, but enhanced by mapped Holocene areas (see Appendix C; Hartmann and Moosdorf, 2012), additional regional geological maps describing basalt areas and the maps of the volcanic fields used in this study; for detailed information see Appendix C), temperature (Hijmans et al., 2005) and runoff (Fekete et al., 2002).

4.4 Results and Discussion

Studied IVFs are characterized by a Holocene volcanic surface area of 0% with weathering reactivity R ranging between 0.5 and 1.6 (Fig. 23c). In contrast, AVFs show a large range of Holocene coverage, from 0.2% (High Cascades) to 96.6% (Mount Cameroon), and weathering reactivity between 0.9 (High Cascades) and 10.6 (Mount Etna). The weathering reactivity correlates strongly with the percentage of Holocene area (r^2 = 0.93; Fig. 23c), suggesting Holocene

surface area distribution is a good predictor for the enhanced alkalinity fluxes from a volcanic system:

$$F_{alkalinity} = (1 + 0.10 * H) * 0.23 * e^{(0.06*T)} [10^6 \ mol\ km^{-2} a^{-1}], \quad \text{RMSE} = 0.3 \qquad \text{(eq. 14)}$$

where *H* is the Holocene fraction of a volcanic system in percent and *T* is land surface temperature in °C.

The Holocene fraction is not interpreted as the physical cause for elevated alkalinity fluxes. Instead, magmatic CO_2 contribution, geothermal-hydrothermal activity and the input of new volcanic material on top of the surface (properties and "freshness" of the surface area for reaction) are contributing to enhanced alkalinity fluxes. Volcanic ashes and ejecta might contribute to elevated weathering fluxes because of a relatively high content of glass. Glass dissolution rates are relatively high compared to mineral dissolution rates in general, but base cation content release varies dependent on the Si:O ratio (Wolff-Boenisch et al., 2006).

The magmatic CO_2 contributions to alkalinity fluxes in young volcanic systems may be large in general, but data are scarce to evaluate the global relevance for AVFs. For the Lesser Antilles a magmatic contribution of 23 to 40% to the CO_2 consumed by weathering was identified (Rivé et al., 2013). High ^{13}C-dissolved inorganic carbon (DIC) values suggest that magmatic CO_2 contributes significantly to the alkalinity fluxes from the Virunga system (Balagizi et al., 2015). The magmatic CO_2 contribution derived from volcanic calcite dissolution on Iceland was estimated to be about 10% of the alkalinity fluxes for the studied area (Jacobson et al., 2015). In case of the Etna, 7% of the CO_2 emitted due to volcanic activity may be captured by weathering (Aiuppa et al., 2000). These examples suggest that significant amounts of magmatic carbon may be transferred to the ocean directly via intravolcanic weathering from AVFs.

These examples show that in case of active volcanic fields the traditional view on kinetic vs. supply limitation in the "shallow" critical zone in context of tectonic settings does not hold (e.g., Ferrier et al., 2016). In contrast, the supply of fresh material on top of the classical critical zone and the weathering from below the classical critical zone suggest that these hot spots of silicate weathering in active volcanic areas, which contribute over proportionally to the global CO_2 consumption by silicate weathering, demand likely a different way of looking at it. The blue data points (IVFs) in Fig. 24d suggest a kinetic limited regime and follow a temperature dependency. The red points (AVFs) however are located above the data points of IVFs in general. Taking into account that the four AVFs (Mt. Etna, Mt. Cameroon, Virunga and La Réunion) have the highest Holocene fractions (96.6%-27.7%) and that the further AVFs, which have less than 15% Holocene coverage, are located in general above the regression line for IVFs, supports the argument that a combination of elevated geothermal fluxes, magmatic CO_2 and fresh material supplied on top of the classical critical zone contributes to the observed elevated alkalinity fluxes for AVFs in general.

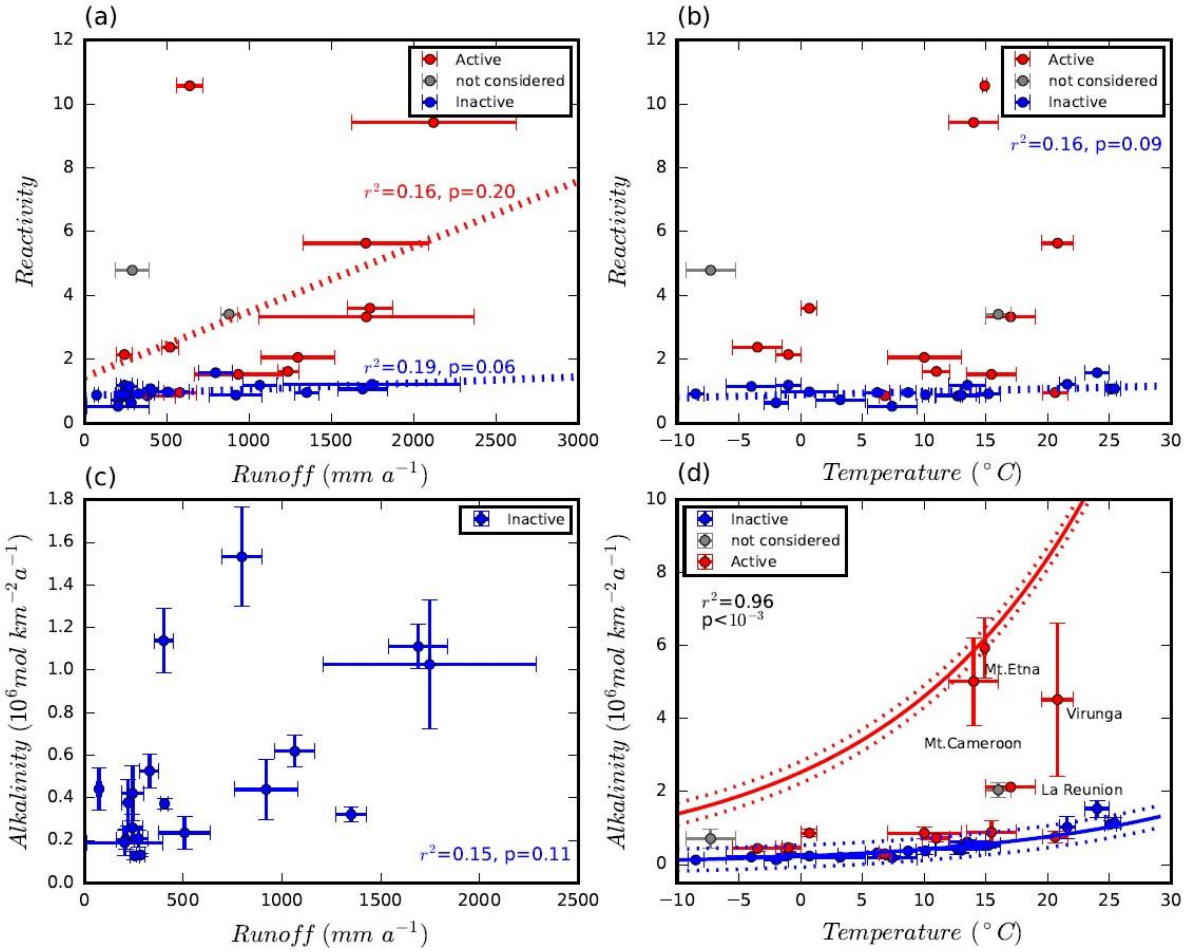

Figure 24: Panel 3(a) shows the runoff-reactivity relationship of all studied volcanic fields. The blue regression line (IVFs) suggests almost no correlation of reactivity with runoff; also, for the AFVs no significant correlation is identified (r^2=0.16, p=0.20). (b) Reactivity vs. temperature suggests no bias of reactivity due to a temperature effect for AVFs, as reactivity is based on a temperature normalized parameterization. For the IVFs (r^2=0.16, p=0.09), no bias with temperature can be identified due to the good correlation of alkalinity fluxes with land surface temperature (blue line) (c) Runoff vs. alkalinity flux rates for inactive volcanic fields shows no significant correlation (r^2=0.15, p=0.11) (d) Temperature vs. alkalinity flux rates for all volcanic fields of the study. The blue line represents the new scaling law for IVFs and the red line the new scaling law for AVFs with 100% Holocene area coverage (calculated deviation is represented by dashed lines). r^2 and p value are derived by a linear regression of calculated alkalinity flux rates vs. observed alkalinity flux rates for all volcanic fields.

The calculated global basalt weathering alkalinity fluxes based on previous global models (Amiotte-Suchet and Probst, 1995; Bluth and Kump, 1994; Dessert et al., 2003; Goll et al., 2014) give alkalinity fluxes ranging between 0.8 and 1.7 $\times 10^{12}$ mol a^{-1}. These values are different from previously published results based on the same models because a different geological map and climate data are used in this study. The new scaling law calculation based on the temperature dependence of weathering rate and the age dependence of weathering reactivity (eq. 13) results in higher global alkalinity fluxes of 1.9×10^{12} mol a^{-1} and 3.3×10^{12} mol a^{-1} for regions with > 74mm

a^{-1} runoff, and for all areas, respectively. The latter higher estimate is mainly due to the modeled contribution from dry and hot regions and shows that it is relevant to apply the runoff cutoff.

Using the introduced new approach, considering the aging of a volcanic system, reveals that alkalinity fluxes from Holocene areas contribute today only 5% to the global basalt weathering alkalinity flux. This is because so far identified mapped Holocene volcanic areas cover only ~1% of all basalt areas. This study did not include areas of less mafic volcanic areas, like andesites, or Central American volcanics.

The Holocene area is probably underestimated due to information gaps in the reported age information of the global map. The strong dependence of weathering reactivity on relative age of the surface of a considered volcanic system suggests that it is relevant to know the global spatial age distribution of volcanic areas in more detail. Therefore, a new global review of the age distribution of basalt areas would be needed, which is beyond the scope of this study. The lithologies, predominantly described as basaltic in the global map, might introduce an additional bias to the global calculations because heterogeneities in the lithology cannot be excluded. Two active volcanic fields (São Miguel and Tianchi Lake) were excluded from the calculation of the scaling law function because available catchments with alkalinity data hold large areas with lithologies of trachytic composition. Nevertheless, their data points (Fig. 23c) seem to show the same weathering behavior.

Table 7: Summary of global basalt CO_2 consumption rates for different models and the new parameterization. For simplicity, it was assumed that alkalinity fluxes equal CO_2 consumption. The percentiles of the values of the global calculation by the new scaling law (Monte Carlo method) can be found in Appendix C. The standard deviation is given below as described in Appendix C.

Models for comparison	Parameters	Global CO_2 consumption rate (10^9 mol a^{-1}) for limited area in comparison (only areas with > 74mm a^{-1} runoff)	Global CO_2 consumption rate (10^9 mol a^{-1})
Dessert et al. (2003)	Runoff, temperature	1669	1684
Amiotte-Suchet and Probst (1995)	Runoff	863	870
Bluth and Kump (1994)	Runoff	746	761
Goll et al. (2014)	Runoff, temperature	1566	1580
New scaling law	Temperature	1930 ± 90	3300 ± 200

The applied time period of the Holocene boundary suggests that the aging of the "weathering motor" of a basaltic volcanic area, including internal weathering, with declining volcanic activity is rather rapid. This implies that peaks in global volcanic activity have probably a short but intensive effect on the CO_2 consumption. A pronounced effect on the global carbon cycle by shifting the global reactivity of volcanic areas may only be relevant for geological periods with significantly elevated production of new volcanic areas, accompanied by geothermal-hydrothermal activity and capture of magmatic CO_2 before its escape to the atmosphere.

Results may have relevance for the carbon cycle and climate studies exploring the emplacement of large igneous provinces like the CAMP (Schaller et al., 2012) or the Deccan traps (Caldeira and Rampino, 1990) with production of large basaltic areas within a short time. However, the biological contribution to CO_2 drawdown, via elevated fertilization effects, e.g., P or Si release due to weathering and elevated CO_2 in the atmosphere, should be taken into account, too.

Looking deeper into Earth's history: variations in the solid Earth CO_2 degassing rate or changes in environmental conditions affecting the weathering intensity (Hartmann et al., 2017; Teitler et al., 2014) may have caused different reactivity patterns in dependence of surface age as shown here.

In conclusion, a simple approach to detect an aging effect, using surface age as a proxy for several combined processes, was chosen due to availability of data. It can be shown that there exists a linear relationship between temperature-normalized alkalinity fluxes and the Holocene area fraction of a volcanic system. Nevertheless, the combined effect on elevated weathering reactivity due to magmatic CO_2 contribution, hydrothermal activity, production of fresh surface area for reaction and hydrological factors of young volcanic systems remains to be disentangled, for single volcanic systems, as well as for the emplacement of larger, trap-style basalt areas.

4.5 Acknowledgements

Funding for this work has been provided by German Research Foundation (DFG) through the Cluster of Excellence CLISAP2 (DFG Exec177, Universität Hamburg) and BMBF-project PALMOD (Ref 01LP1506C) through the German Federal Ministry of Education and Research (BMBF) as part of the Research for Sustainability initiative (FONA) Gaojun Li is supported by National Natural Science Foundation of China (grants 41761144058 and 41730101). The authors thank the editor, Robert Emberson, and one anonymous reviewer for constructive comments on the manuscript.

5 Synthesis

In this thesis, global quantifications of land to ocean alkalinity fluxes and CO_2 consumption rates derived from the chemical weathering of rocks and sediments were investigated. As there were some limitations in previous approaches, like loess abundance and the alkalinity fluxes from loess deposits at the larger scale, or aging effects of volcanic systems, some improvements were the target, to answer the questions if aging of volcanic system is relevant or if loess represents a significant buffer for alkalinity fluxes. The focus on improving these global quantifications lay on two different lithologies, unconsolidated loess sediments and young basaltic regions, both of them underrepresented in global studies of weathering fluxes. For each of them, new parameterizations were developed to represent global alkalinity fluxes. To analyze the contribution to global alkalinity fluxes and CO_2 consumption rates, global maps reporting on the distribution of these different lithologies were needed and built the basis for the studies.

With the new map database on the distribution and properties of global unconsolidated sediments (GUM), weathering fluxes from sediments could be better analyzed and quantified. The newly developed unconsolidated sediments map also helped to improve other Earth System Science studies, for instance hydrological studies. Here, the new map was used as an input dataset to conduct an improved global permeability map including bedrock and sediments (Huscroft et al., 2018). Nevertheless, map databases can be continuously improved and further developed. For instance, adding new information to lithological descriptions like geophysical, geochemical or mineralogical information about the rocks and sediments can help to improve research on the weathering of specific lithologies. Some regions on the Earth are still poorly mapped and merit better mapping and implementation in global lithological maps. The here introduced GUM database shows that there exists the capacity for this improvement and that this can help to improve studies in other research areas as well. Implementing a proper soil layer or the continental shelf areas of the ocean into a homogenized database would help to obtain a broader and more detailed picture of the Earth's surface. Because global maps report only on temporal distribution of rocks or sediments, time slices should be considered, especially interesting for the investigation of weathering fluxes of the past.

Besides maps, other databases can be used to conduct research on chemical weathering fluxes. A river chemistry database (Hartmann et al., 2014a) was used in this thesis to investigate weathering fluxes from loess deposits (chapter 3 of this thesis). Romero-Mujalli et al. (2018b) and Romero-Mujalli et al. (2018a) used spring water and river chemistry databases to analyze weathering fluxes from carbonate lithologies. They describe the weathering of carbonate rocks dominated by calcite weathering as being dependent on the soil-rock pCO_2, which can be parameterized by surface temperature and soil water content. The observation of temperature dependency of carbonate rocks (Gaillardet et al., 2018; Romero-Mujalli et al., 2018b) led to a new global approach to quantify weathering fluxes from carbonate rocks dominated by calcite weathering (Romero-Mujalli et al.,

2018a), which is the first approach of considering, besides runoff, the variable temperature for global carbonate weathering modelling and hence provides more insights into the variability of calcite weathering.

In chapter 3 of this thesis, the new carbonate temperature dependency model from Romero-Mujalli et al. (2018a) is compared with a new loess weathering parameterization and previous runoff-dependent carbonate weathering models. The results of the loess analysis show that loess weathering shows a signature of carbonate weathering in general. Nevertheless, a new parameterization for loess-derived alkalinity fluxes was developed because the previous carbonate weathering models could not represent the natural weathering of loess sediments. Moreover, they did not represent the dilution effect for high runoff areas, which is now included in the new function. Loess weathering-derived alkalinity fluxes contribute significantly to global alkalinity fluxes. They increase global alkalinity fluxes today by about 16%, as if compared to neglecting loess sediments. Comparing the time slices of the LGM and the present-day shows that increased alkalinity fluxes from loess deposits during the LGM can counterbalance the general lower silicate weathering fluxes during that time and are buffering the glacial-interglacial system. Hence, loess sediments have a relevant impact in glacial-interglacial budgets of alkalinity fluxes from the land to the ocean and should gain more importance in the future.

Additional to the study about glacial-interglacial changes of alkalinity fluxes due to loess sediments, this thesis also reveals the importance of age-dependent weathering of volcanic systems for the first time at the global scale. The consideration of young Holocene basaltic areas increases global CO_2 consumption rates from basaltic regions by about 60%. Periods of strong volcanic activity might have led to an increase of global CO_2 consumption rates, which would change the global atmospheric pCO_2. Nevertheless, the surface distribution of young basaltic areas cannot be simulated for past times for now. In the future, it might be possible to estimate weathering fluxes from young basaltic areas by reconstructing the activity history for today's volcanoes by dating tephra deposits or the volcanic rocks themselves. On longer time scales, it might be possible to find a correlation between volcanic activity and plate tectonic movements and boundaries to simulate active volcanic regions globally.

The studies presented here on loess and basalt weathering highlight the possibility of further implementing more parameters in weathering models. The investigations on single lithologies might be improved by investigating the influences of further physical or chemical processes, like characteristic hydrological and soil properties or the precipitation of secondary minerals that influence the weathering fluxes. The modelling of basalt weathering fluxes might be enhanced by the consideration of below-surface processes linked to the magmatic chamber, like the quantification of magmatic contribution to the weathering of minerals (Hosono et al., 2018) or the weathering of fine volcanic ashes due to their physical properties. Romero-Mujalli et al. (2018b) showed that the soil-pCO_2 has to be considered for the quantification of weathering fluxes from calcite-dominated limestone areas globally. But, besides the improvement of weathering models for specific minerals or monolithological rocks or sediments, like it was for example done by

Goddéris et al. (2013), it should be kept in mind that on the global scale, the application of these detailed models is complicated because of computational power and too coarse global input datasets of climate parameters.

Both, the representation of the quantification of alkalinity fluxes from loess sediments and basaltic areas could be enhanced in this thesis. It can be shown that it is important to refine global lithological maps and to consider changes of geospatial distributions of sediments or rocks in time, because relatively small proportions of the land surface can already have a high impact on global alkalinity fluxes and CO_2 consumption rates. Both, loess sediments and young basaltic areas increase global alkalinity fluxes significantly and should be considered in global climate studies, because increased alkalinity fluxes from the land to the ocean are affecting other natural environments in global climate models, like the ocean or the atmosphere, and have hence an impact on the global climate.

Bibliography

Aiuppa, A., Allard, P., D'Alessandro, W., Michel, A., Parello, F., Treuil, M., Valenza, M., 2000. Mobility and fluxes of major, minor and trace metals during basalt weathering and groundwater transport at Mt. Etna volcano (Sicily). Geochimica et Cosmochimica Acta, 64(11): 1827-1841.

Alimen, H., Choubert, G., International association for quaternary research, Unesco, 1973. Carte Internationale du Quaternaire de l'Afrique 1:2,500,000 - Afrique du nord / Prepared by the Subcommission of INQUA for the Quaternary map of Africa under the aegis of the National Centre of Scientific Research. United Nations Educational, Scientific and Cultural Organization, Sub-Commission of INQUA for the *Quaternary Map of Africa*, Paris.

Alimen, H., Choubert, G., International association for quaternary research, Unesco, 1978a. Carte Internationale du Quaternaire de l'Afrique 1:2,500,000 - Sahara Central / Prepared by the Subcommission of INQUA for the Quaternary map of Africa with the support of the National Centre of Scientific Research; carte dressée sous la direction de H. Alimen. United Nations Educational, Scientific and Cultural Organization, Sub-Commission of INQUA for the *Quaternary Map of Africa*, Paris.

Alimen, H., Choubert, G., International association for quaternary research, Unesco, 1978b. Carte Internationale du Quaternaire de l'Afrique 1:2,500,000 - Sahara Occidental / Prepared by the Subcommission of INQUA for the Quaternary map of Africa with the support of the National Centre of Scientific Research. United Nations Educational, Scientific and Cultural Organization, Sub-Commission of INQUA for the *Quaternary Map of Africa*, Paris.

Amante, C., Eakins, B., 2009. ETOPO1 1 arc-minute global relief model: procedures, data sources and analysis. National Geophysical Data Center, NOAA, Boulder Colorado.

Amiotte-Suchet, P., Probst, J.L., 1995. A global model for present-day atmospheric/soil CO2 consumption by chemical erosion of continental rocks (GEM-CO2). Tellus B, 47(1-2): 273-280.

Amiotte Suchet, P., Probst, J.L., Ludwig, W., 2003. Worldwide distribution of continental rock lithology: Implications for the atmospheric/soil CO2 uptake by continental weathering and alkalinity river transport to the oceans. Global Biogeochemical Cycles, 17(2).

Antun, P., Gerards, J., Petricec, V., 1971. Carte Géologique du Rwanda, Feuille Ruhengeri Nord (S2/29 NW et NE), Champs Volcanique des Birunga. Institut Géographique Militaire de Belgique.

Ateba, B., Dorbath, C., Dorbath, L., Ntepe, N., Frogneux, M., Aka, F.T., Hell, J.V., Delmond, J.C., Manguelle, D., 2009. Eruptive and earthquake activities related to the 2000 eruption of Mount Cameroon volcano (West Africa). Journal of Volcanology and Geothermal Research, 179(3-4): 206-216.

Balagizi, C.M., Darchambeau, F., Bouillon, S., Yalire, M.M., Lambert, T., Borges, A.V., 2015. River geochemistry, chemical weathering, and atmospheric CO2 consumption rates in the Virunga Volcanic Province (East Africa). Geochemistry, Geophysics, Geosystems, 16(8): 2637-2660.

Benedetti, M.F., Dia, A., Riotte, J., Chabaux, F., Gérard, M., Boulegue, J., Fritz, B., Chauvel, C., Bulourde, M., Déruelle, B., 2003. Chemical weathering of basaltic lava flows undergoing extreme climatic conditions: the water geochemistry record. Chemical Geology, 201(1-2): 1-17.

Berner, R.A., Lasaga, A.C., Garrels, R.M., 1983. The carbonate-silicate geochemical cycle and its effect on atmospheric carbon dioxide over the past 100 million years. Am J Sci, 283: 641-683.

Bettis, E.A., Muhs, D.R., Roberts, H.M., Wintle, A.G., 2003. Last glacial loess in the conterminous USA. Quaternary Science Reviews, 22(18): 1907-1946.

Beusen, A.H.W., Bouwman, A.F., Dürr, H.H., Dekkers, A.L.M., Hartmann, J., 2009. Global patterns of dissolved silica export to the coastal zone: Results from a spatially explicit global model. Global Biogeochemical Cycles, 23(4): n/a-n/a.

Biryukov, V.Y., Faustova, M., Kaplin, P., Pavlidis, Y.A., Romanova, E., Velichko, A., 1988. The paleogeography of Arctic shelf and coastal zone of Eurasia at the time of the last glaciation (18,000 yr BP). Palaeogeography, Palaeoclimatology, Palaeoecology, 68(2-4): 117-125.

Bluth, G.J., Kump, L.R., 1994. Lithologic and climatologic controls of river chemistry. Geochimica et Cosmochimica Acta, 58(10): 2341-2359.

Bluth, G.J.S., Kump, L.R., 1991. Phanerozoic paleogeology. American Journal of Science, 291(3): 284-308.

Börker, J., Hartmann, J., Amann, T., Romero-Mujalli, G., 2018. Terrestrial Sediments of the Earth: Development of a Global Unconsolidated Sediments Map Database (GUM). Geochemistry, Geophysics, Geosystems, 19(4): 997-1024.

Borns, J.H.W., Gadd, N.R., LaSalle, P., Martineau, G., Chauvin, L., Fullerton, D.S., Fulton, R.J., Chapman, W.F., Wagner, W.P., Grant, D.R., 2005. Quaternary Geologic Map of the Quebec 4° X 6° Quadrangle, United States and Canada, Miscellaneous Investigations series, Map I-1420 (NL-19). U.S. Geological Survey, Denver, Colorado.

Bostock, H., Jenkins, C., Mackay, K., Carter, L., Nodder, S., Orpin, A., Pallentin, A., Wysoczanski, R., 2018. Distribution of surficial sediments in the ocean around New Zealand/Aotearoa. Part B: continental shelf. New Zealand Journal of Geology and Geophysics: 1-22.

Branca, S., Coltelli, M., Groppelli, G., Lentini, F., 2011a. Carta Geologica del vulcano Etna (Scala 1:50.000). Istituto Nazionale di Geofisica e Vulcanologia Osservatorio Etneo sezione di Catania, Istituto per la Protezione e la Ricerca Ambientale (ISPRA), Servizio Geologico d'Italia, CNR-Consiglio Nazionale delle Ricerche, Univerità di Catania Dipartimento di Scienze Geologiche.

Branca, S., Coltelli, M., Groppelli, G., Lentini, F., 2011b. Geological map of Etna volcano, 1: 50,000 scale. Italian Journal of Geosciences, 130(3): 265-291.

Brantley, S.L., Goldhaber, M.B., Ragnarsdottir, K.V., 2007. Crossing disciplines and scales to understand the critical zone. Elements, 3(5): 307-314.

British Geological Survey, 2008. Digital Geological Map Data of Great Britain - 625k (DiGMapGB-625).

Bundesamt für Landestopografie, 2005. Geologische Karte der Schweiz, 1:500,000, Wabern, Switzerland.

Bundesanstalt für Geowissenschaften und Rohstoffe, 2007. Geologische Übersichtskarte der Bundesrepublik Deutschland (scale 1:200,000 (GÜK200)). Bundesanstalt für Geowissenschaften und Rohstoffe, Hannover, Germany.

Caldeira, K., Rampino, M.R., 1990. Carbon dioxide emissions from Deccan volcanism and a K/T boundary greenhouse effect. Geophysical Research Letters, 17(9): 1299-1302.

Cheshitev, G., Kancev, I., Valkov, V., Marinova, R., Shilyafova, J., Russeva, M., Iliev, K., 1989. Geological Map of P.R. Bulgaria. Committee of Geology - Department of Geophysical Prospecting and Geological Mapping, Sofia.

China Geological Survey, 2002. Geological Atlas of China - Chinese geological map (scale 1:2,500,000). Geological Press, Beijing.

Cohen, K., Finney, S., Gibbard, P., Fan, J.-X., 2013. The ICS international chronostratigraphic chart. Episodes, 36(3): 199-204.

Colley, H., 1976. Mineral deposits of Fiji (metallic deposits), accompanied by 2 maps: Metallogenic map of Vanua Levu and metallogenic map of Vitu Levu, scale 1:250,000, 123pp. Miner. Resour. Div., Suva, Fiji.

Conrad, O., Bechtel, B., Bock, M., Dietrich, H., Fischer, E., Gerlitz, L., Wehberg, J., Wichmann, V., Böhner, J., 2015. System for Automated Geoscientific Analyses (SAGA) v. 2.1.4. Geosci. Model Dev., 8(7): 1991-2007.

Coogan, L.A., Dosso, S.E., 2015. Alteration of ocean crust provides a strong temperature dependent feedback on the geological carbon cycle and is a primary driver of the Sr-isotopic composition of seawater. Earth and Planetary Science Letters, 415: 38-46.

Coordinating Committee for Geoscience Programmes in East and Southeast Asia, 2004. Digital geologic map of East and Southeast Asia, version 2, *Dig. Geosci. Map, G-2*, scale 1:2,000,000, Geol. Surv. of Jpn., Natl. Inst. of Adv. Ind. Sci. and Technol., Tsukuba.

Crouvi, O., Amit, R., Enzel, Y., Gillespie, A.R., 2010. Active sand seas and the formation of desert loess. Quaternary Science Reviews, 29(17): 2087-2098.

Dargie, G., Lewis, S., Lawson, I., Mitchard, E., Page, S., Bocko, Y., Ifo, S., 2017. Age, extent and carbon storage of the central Congo Basin peatland complex. Nature.

Dasgupta, A.K., Chakravorty, K.K., 1998. Geological map of India, 4 sheets, 7th ed., Geol. Surv. of India, Calcutta, India.

de Graaf, I.E., van Beek, R.L., Gleeson, T., Moosdorf, N., Schmitz, O., Sutanudjaja, E.H., Bierkens, M.F., 2017. A global-scale two-layer transient groundwater model: Development and application to groundwater depletion. Advances in Water Resources, 102: 53-67.

De Mulder, M., Hertogen, J., Deutsch, S., André, L., 1986. The role of crustal contamination in the potassic suite of the Karisimbi volcano (Virunga, African Rift Valley). Chemical geology, 57(1): 117-136.

Denne, J.E., Luza, K.V., Richmond, G.M., Jensen, K.M., Fishman, W.D., Wermund, J.E.G., 2011. Quaternary Geologic Map of the Wichita 4° X 6° Quadrangle, United States, Miscellaneous Investigations series, Map I-1420 (NJ-14). U.S. Geological Survey, Denver, Colorado.

Derbyshire, E., Meng, X., Kemp, R.A., 1998. Provenance, transport and characteristics of modern aeolian dust in western Gansu Province, China, and interpretation of the Quaternary loess record. Journal of arid environments, 39(3): 497-516.

Dessert, C., Dupré, B., François, L.M., Schott, J., Gaillardet, J., Chakrapani, G., Bajpai, S., 2001. Erosion of Deccan Traps determined by river geochemistry: impact on the global climate and the 87Sr/86Sr ratio of seawater. Earth and Planetary Science Letters, 188(3–4): 459-474.

Dessert, C., Dupré, B., Gaillardet, J., François, L.M., Allègre, C.J., 2003. Basalt weathering laws and the impact of basalt weathering on the global carbon cycle. Chemical Geology, 202(3–4): 257-273.

Dessert, C., Gaillardet, J., Dupre, B., Schott, J., Pokrovsky, O.S., 2009. Fluxes of high- versus low-temperature water–rock interactions in aerial volcanic areas: Example from the Kamchatka Peninsula, Russia. Geochimica et Cosmochimica Acta, 73(1): 148-169.

Dijkshoorn, J., Leenaars, J., Huting, J., Kempen, B., 2016. Soil and terrain database of the Republic of Malawi. Report 2016/01, Wageningen, Netherlands.

Dijkshoorn, J.A., 2007. Soil and terrain database for Kenya (ver. 2.0) (KENSOTER). ISRIC - World Soil Information.

Dijkshoorn, J.A., Huting, J.R.M., 2014. Soil and Terrain Database for Senegal and the Gambia (version 1.0) - scale 1:1 million (SOTER_Senegal_Gambia). ISRIC - World Soil Information.

Dijkshoorn, K., Huting, J., 2009. Soil and Terrain database for Tunisia (ver. 1.0). ISRIC - World Soil Information, Wageningen.

Dijkshoorn, K., van Engelen, V., 2003. Soil and Terrain Database for Southern Africa (ver. 1.0). ISRIC - World Soil Information, Wageningen.

Dirección Nacional de Minería y Geología, 1985. Carta geológica, scale 1:500,000, Minist. de Ind., Energia y Miner., Montevideo.

Direction de l'Industrie des Mines et de l'Energie (DIMENC), 1981. Carte de la géologie de la Nouvelle-Calédonie, scale 1:200,000, Noumea.

Doebrich, J.L., Wahl, R.R., Ludington, S.D., Chirico, P.G., Wandrey, C.J., Bohannon, R.G., Orris, G.J., Bliss, J., 2006. Geologic age and lithology of Afghanistan (glgafg.shp) (U.S. Geological Survey Open File Report: Issue Identification number 2006-1038). U.S. Geological Survey, Denver, CO. U.S.A.

Dürr, H.H., Meybeck, M., Dürr, S.H., 2005. Lithologic composition of the Earth's continental surfaces derived from a new digital map emphasizing riverine material transfer. Global Biogeochemical Cycles, 19(4).

Economic and Social Commission for Asia and the Pacific, 1989. Atlas of mineral resources of the ESCAP region: Sri Lanka, comprising the geological, metamorphic and mineral resources maps of Sri Lanka, scale 1:1,013,760, U. N. Publ., Blue Ridge Summit, Pa. [Available at http://www.orrbodies.com/].

Egger, H., Krenmayer, H.G., Mandl, G.W., Matura, A., Nowotny, A., Pascher, G., Pestal, G., J., P., Rockenschaub, M., Schnabel, W., 1999. Geologische Übersichtskarte der Republik Österreich, scale 1:1,500,000. Geol. Bundesanstalt, Vienna.

Ehlers, J., Gibbard, P.L., Hughes, P.D., 2011. Quaternary glaciations-extent and chronology: a closer look, 15. Elsevier.

Ermann, K.A., O'Keife, K., 1999. State Surficial Geology Map of Alaska, Greenhorne & O'Mara, Inc., St. Petersburg.

Escher, J.C., Pulvertaft, T.C.R., 1995. Geological map of Greenland. Geol. Survey of Greenl., Copenhagen.

Fekete, B.M., Vörösmarty, C.J., Grabs, W., 2002. High-resolution fields of global runoff combining observed river discharge and simulated water balances. Global Biogeochemical Cycles, 16(3): 15-01-15-10.

Ferrier, K.L., Riebe, C.S., Jesse Hahm, W., 2016. Testing for supply-limited and kinetic-limited chemical erosion in field measurements of regolith production and chemical depletion. Geochemistry, Geophysics, Geosystems, 17(6): 2270-2285.

Food and Agriculture Organization of the United Nations, Di Gregorio, A., Institut geographique du Burundi, Hakizimana, C., 2003a. Burundi Geomorphology: Landform and Lithology. Harvard Map Collection, Harvard College Library, Cambridge, Massachusetts.

Food and Agriculture Organization of the United Nations, Di Gregorio, A., Rwanda. Ministere des terres, d.l.r.e.d.l.p.d.l.e., Burabyo, E.R., 2003b. Rwanda Geomorphology: Landform and Lithology. Harvard Map Collection, Harvard College Library, Cambridge, Massachusetts.

Freire, P., Andrade, C., Coutinho, R., Cruz, J.V., 2013. Fluvial geochemistry in Sao Miguel Island (Azores, Portugal): source and fluxes of inorganic solutes in an active volcanic environment. Science of the Total Environment, 454-455: 154-69.

French, C.D., Schenk, C.J., 2004. Surface Geology of the Caribbean Region (geo6bg). U.S. Geological Survey, Central Energy Resources Team, Denver, Colorado.

Fullerton, D.S., Bluemle, J.P., Clayton, L., Steece, F.V., Tipton, M.J., Bretz, R., Goebel, J.E., 2011. Quaternary Geologic Map of the Dakotas 4° x 6° Quadrangle, United States, Miscellaneous Investigations Series, Map I-1420 (NL-14). U.S. Geological Survey, Denver, Colorado.

Fullerton, D.S., Christiansen, E.A., Schreiner, B.T., Colton, R.B., Clayton, L., 2007. Quaternary Geologic Map of the Regina 4° X 6° Quadrangle, United States and Canada, U.S. Geological Survey Miscellaenous Investigations Series, Map I-1420 (NM-13). U.S. Geological Survey, Denver, Colorado.

Fullerton, D.S., Cowan, W.R., Sevon, W.D., Goldthwait, R.P., Farrand, W.R., Muller, E.H., Behling, R.E., Stravers, J.A., 1991. Quaternary Geologic Map of the Lake Erie 4° x 6° Quadrangle, United States and Canada, Miscellaneous Investigations series, Map I-1420 (NK-17). US Geological Survey, Denver, Colorado.

Fullerton, D.S., Ringrose, S.M., Clayton, L., Schreiner, B.T., Goebel, J.E., 2000. Quaternary geologic map of the Winnipeg 4°× 6° quadrangle, United States and Canada, Miscellaneous Investigations Series, Map I-1420 (NM-14). U.S. Geological Survey, Denver, Colorado.

Fullerton, D.S., Sevon, W.D., Muller, E.H., Judson, S., Black, R.F., Wagner, P.W., Hartshorn, J.H., Chapman, W.F., Cowan, W.D., 2005. Quaternary Geologic Map of the Hudson River 4° x 6° Quadrangle, United States and Canada, Miscellaneous Investigations series, Map I-1420 (NK-18). US Geological Survey, Denver, Colorado.

Fulton, R., 1995. Surficial materials of Canada. In Geological Survey of Canada (Editor), Map 1880A, scale 1:5 000 000. In: Geological Survey of Canada (Editor), Map 1880A, scale 1:5 000 000. Natural Resources Canada, Ottawa, Canada.

Gaillardet, J., Calmels, D., Romero-Mujalli, G., Zakharova, E., Hartmann, J., 2018. Global climate control on carbonate weathering intensity. Chemical Geology.

Gaillardet, J., Dupré, B., Louvat, P., Allègre, C.J., 1999. Global silicate weathering and CO2 consumption rates deduced from the chemistry of large rivers. Chemical Geology, 159(1–4): 3-30.

Gaillardet, J., Rad, S., Rivé, K., Louvat, P., Gorge, C., Allègre, C.J., Lajeunesse, E., 2011. Orography-driven chemical denudation in the Lesser Antilles: Evidence for a new feed-back mechanism stabilizing atmospheric CO2. American journal of science, 311(10): 851-894.

Garrity, C.P., Hackley, P.C., Urbani, F., Geological Survey (U.S.), 2006. Digital geologic map and GIS database of Venezuela. 2327-638X, Reston, Va.?

GeoBolivia, 2000. Mapa geologico de Bolivia, 2000. Servicio Nacional de Geología y Técnico de Minas - SERGEOTECMIN.

Geologian tutkimuskeskus, 2013. Maaperä 1:1,000,000. Quaternary geological/superficial deposits map.

Geological Survey Institute of Indonesia, 1993. INA GRDC 1:1M combined bedrock and superficial geology and age, Bandung, Indonesia.

Geological Survey of India, 2005. Geological map of the Himalaya, Calcutta, India.

Geological Survey of Japan AIST (ed.), 2009. Seamless digital geological map of Japan 1:200,000. Dec 15, 2009 version. Research Information Database DB084, https://gbank.gsj.jp/seamless/download/downloadIndex_e.html, accessed May 2016. Geological Survey of Japan, National Institute of Advanced Industrial Science and Technology, Japan.

Geological Survey of Sweden, 2014. JORDARTER 1:1 miljon. Geological Survey of Sweden.

Geological Survey of Tanzania, Geo-Economic Data (1:2M) - Geology, http://www.gmis-tanzania.com/, accessed May 2016

Geologische Bundesanstalt (GBA), 2013. Kartographisches Modell 1:500000 Austria - Geologie, Wien, Austria.

Gibbs, M.T., Kump, L.R., 1994. Global chemical erosion during the last glacial maximum and the present: sensitivity to changes in lithology and hydrology. Paleoceanography and Paleoclimatology, 9(4): 529-543.

Gioncada, A., Gonzalez-Ferran, O., Lezzerini, M., Mazzuoli, R., Bisson, M., Rapu, S.A., 2010. The volcanic rocks of Easter Island (Chile) and their use for the Moai sculptures. European Journal of Mineralogy, 22(6): 855-867.

Gleeson, T., Moosdorf, N., Hartmann, J., van Beek, L.P.H., 2014. A glimpse beneath earth's surface: GLobal HYdrogeology MaPS (GLHYMPS) of permeability and porosity. Geophysical Research Letters, 41(11): 3891-3898.

Gleeson, T., Smith, L., Moosdorf, N., Hartmann, J., Dürr, H.H., Manning, A.H., van Beek, L.P.H., Jellinek, A.M., 2011. Mapping permeability over the surface of the Earth. Geophysical Research Letters, 38(2): n/a-n/a.

Goddéris, Y., Brantley, S.L., François, L.M., Schott, J., Pollard, D., Déqué, M., Dury, M., 2013. Rates of consumption of atmospheric CO 2 through the weathering of loess during the next 100 yr of climate change. Biogeosciences, 10(1): 135-148.

Goddéris, Y., Donnadieu, Y., Nédélec, A., Dupré, B., Dessert, C., Grard, A., Ramstein, G., François, L.M., 2003. The Sturtian 'snowball' glaciation: fire and ice. Earth and Planetary Science Letters, 211(1–2): 1-12.

Goff, J.A., Jenkins, C.J., Williams, S.J., 2008. Seabed mapping and characterization of sediment variability using the usSEABED data base. Continental Shelf Research, 28(4-5): 614-633.

Goll, D.S., Moosdorf, N., Hartmann, J., Brovkin, V., 2014. Climate-driven changes in chemical weathering and associated phosphorus release since 1850: Implications for the land carbon balance. Geophysical Research Letters, 41(10): 3553-3558.

Gomez Tapias, J., Nivia Guevara, A., Montes Ramirez, N.E., Diederix, H., Almanza Melendez, M.F., Alcarcel Gutierrez, F.A., Madrid Montoya, C.A., 2015. Explanatory notes: Geological Map of Colombia. In: Gomez, J., Almanza, M.F. (Eds.), Compilando la geologia de Colombia: Una vision a 2015. Servicio Geologico Colombiano, Publicaciones Geológicas Especiales 33, Bogotá, pp. 35-60.

González, M.E., 2000. Mapa geológico de Paraguay, Viceministerio de Minas y Energia Paraguay, San Lorenzo, Paraguay.

Gray, H.H., Bleuer, N.K., Lineback, J.A., Swadley, W.C., Richmond, G.M., Miller, R.A., Goldthwait, R.P., Ward, R.A., 2011. Quaternary Geologic Map of the Louisville 4° X 6° Quadrangle, United States, Miscellaneous Investigations series, Map I-1420 (NJ-16). U.S. Geological Survey, Denver, Colorado.

Haase, D., Fink, J., Haase, G., Ruske, R., Pecsi, M., Richter, H., Altermann, M., Jäger, K.-D., 2007. Loess in Europe—its spatial distribution based on a European Loess Map, scale 1: 2,500,000. Quaternary Science Reviews, 26(9): 1301-1312.

Haghipour, A., Saidi, A., 2010. International geological map of the Middle East, second edition, scale 1:5,000,000,. Comm. for the Geol. World Map, Paris.

Hallberg, G.R., Lineback, J.A., Mickelson, D.M., Knox, J.C., Goebel, J.E., Hobbs, H.C., Whitfield, J.W., Ward, R.A., Boellstorff, J.D., Swinehart, J.B., Dreeszen, V.H., 2008. Quaternary Geologic Map of the Des Moines 4° x 6° Quadrangle, United States, Miscellaneous Investigations series, Map I-1420 (NK-15). U.S. Geological Survey, Denver, Colorado.

Hartmann, J., 2009. Bicarbonate-fluxes and CO 2-consumption by chemical weathering on the Japanese Archipelago—application of a multi-lithological model framework. Chemical Geology, 265(3): 237-271.

Hartmann, J., Jansen, N., Dürr, H.H., Kempe, S., Köhler, P., 2009. Global CO2-consumption by chemical weathering: What is the contribution of highly active weathering regions? Global and Planetary Change, 69(4): 185-194.

Hartmann, J., Lauerwald, R., Moosdorf, N., 2014a. A brief overview of the GLObal RIver CHemistry Database, GLORICH. Procedia Earth and Planetary Science, 10: 23-27.

Hartmann, J., Li, G., West, A.J., 2017. Running out of gas: Zircon 18O-Hf-U/Pb evidence for Snowball Earth preconditioned by low degassing. Geochemical Perspectives Letters, 4: 41-46.

Hartmann, J., Moosdorf, N., 2011. Chemical weathering rates of silicate-dominated lithological classes and associated liberation rates of phosphorus on the Japanese Archipelago—implications for global scale analysis. Chemical Geology, 287(3): 125-157.

Hartmann, J., Moosdorf, N., 2012. The new global lithological map database GLiM: A representation of rock properties at the Earth surface. Geochemistry, Geophysics, Geosystems, 13(12): Q12004.

Hartmann, J., Moosdorf, N., Lauerwald, R., Hinderer, M., West, A.J., 2014b. Global chemical weathering and associated P-release—The role of lithology, temperature and soil properties. Chemical geology, 363: 145-163.

Hartmann, J., West, A.J., Renforth, P., Köhler, P., De La Rocha, C.L., Wolf-Gladrow, D.A., Dürr, H.H., Scheffran, J., 2013. Enhanced chemical weathering as a geoengineering strategy to reduce atmospheric carbon dioxide, supply nutrients, and mitigate ocean acidification. Reviews of Geophysics, 51(2): 113-149.

Hijmans, R.J., Cameron, S.E., Parra, J.L., Jones, P.G., Jarvis, A., 2005. Very high resolution interpolated climate surfaces for global land areas. International journal of climatology, 25(15): 1965-1978.

Holbrook, D.F., Gilliland, W.A., Luza, K.V., Pope, D.E., Wermund, E.G., Miller, R.A., Bush, W.V., Jensen, K.M., Fishman, W.D., 2012. Quaternary Geologic Map of the Vicksburg 4° X 6° Quadrangle, United States, Miscellaneous Investigations series, Map I-1420 (NI-15). U.S. Geological Survey, Denver, Colorado.

Hosono, T., Hartmann, J., Louvat, P., Amann, T., Washington, K.E., West, A.J., Okamura, K., Böttcher, M.E., Gaillardet, J., 2018. Earthquake-induced structural deformations enhance long-term solute fluxes from active volcanic systems. Scientific Reports, 8(1): 14809.

Huang, J., Zhang, W., Zuo, J., Bi, J., Shi, J., Wang, X., Chang, Z., Huang, Z., Yang, S., Zhang, B., Wang, G., Feng, G., Yuan, J., Zhang, L., Zuo, H., Wang, S., Fu, C., Jifan, C., 2008. An overview of the Semi-arid Climate and Environment Research Observatory over the Loess Plateau. Advances in Atmospheric Sciences, 25(6): 906.

Huscroft, J., Gleeson, T., Hartmann, J., Börker, J., 2018. Compiling and mapping global permeability of the unconsolidated and consolidated Earth: GLobal HYdrogeology MaPS 2.0 (GLHYMPS 2.0). Geophysical Research Letters, 45(4): 1897-1904.

Institute of Mineral Research and Exploration, 1961. Geology map of Turkey, scale 1:500,000, 18 sheets, Ankara.

Instituto de Geologia y Mineria, 1975. Mapa geologico del Peru, scale 1:1,000,000, Minist. de Energia y Minas, San Borja, Peru.

Instituto Geológico y Minero de España, 1988. Mapa del Cuaternario de España a escala 1:1.000.000.

Jacobson, A.D., Grace Andrews, M., Lehn, G.O., Holmden, C., 2015. Silicate versus carbonate weathering in Iceland: New insights from Ca isotopes. Earth and Planetary Science Letters, 416: 132-142.

Jenkins, C., 1997. Building offshore soils databases. Sea Technology, 38: 25-28.

Jenkins, C.J., 2018. dbSEABED: Information Integration System for Marine Substrates. Univ. Colorado, Boulder, USA. http://tinyurl.com/dbseabed/dbseabed.htm, accessed 23 Dec 2018.

Jungclaus, J., Giorgetta, M., Reick, C., Legutke, S., Brovkin, V., Crueger, T., Esch, M., Fieg, K., Fischer, N., Glushak, K., Gayler, V., Haak, H., Hollweg, H.-D., Kinne, S., Kornblueh, L., Matei, D., Mauritsen, T., Mikolajewicz, U., Müller, W., Notz, D., Pohlmann, T., Raddatz, T., Rast, S., Roeckner, E., Salzmann, M., Schmidt, H., Schnur, R., Segschneider, J., Six, K., Stockhause, M., Wegner, J., Widmann, H., Wieners, K.-H., Claussen, M., Marotzke, J., Stevens, B., 2012a. CMIP5 simulations of the Max Planck Institute for Meteorology (MPI-M) based on the MPI-ESM-P model: The lgm experiment, served by ESGF.

Jungclaus, J., Giorgetta, M., Reick, C., Legutke, S., Brovkin, V., Crueger, T., Esch, M., Fieg, K., Fischer, N., Glushak, K., Gayler, V., Haak, H., Hollweg, H.-D., Kinne, S., Kornblueh, L., Matei, D., Mauritsen, T., Mikolajewicz, U., Müller, W., Notz, D., Pohlmann, T., Raddatz, T., Rast, S., Roeckner, E., Salzmann, M., Schmidt, H., Schnur, R., Segschneider, J., Six, K., Stockhause, M., Wegner, J., Widmann, H., Wieners, K.-H., Claussen, M., Marotzke, J., Stevens, B., 2012b. CMIP5 simulations of the Max Planck Institute for Meteorology (MPI-M) based on the MPI-ESM-P model: The midHolocene experiment, served by ESGF

Jungclaus, J., Giorgetta, M., Reick, C., Legutke, S., Brovkin, V., Crueger, T., Esch, M., Fieg, K., Fischer, N., Glushak, K., Gayler, V., Haak, H., Hollweg, H.-D., Kinne, S., Kornblueh, L., Matei, D., Mauritsen, T., Mikolajewicz, U., Müller, W., Notz, D., Pohlmann, T., Raddatz, T., Rast, S., Roeckner, E., Salzmann, M., Schmidt, H., Schnur, R., Segschneider, J., Six, K., Stockhause, M., Wegner, J., Widmann, H., Wieners, K.-H., Claussen, M., Marotzke, J., Stevens, B., 2012c. CMIP5 simulations of the Max Planck Institute for Meteorology (MPI-M) based on the MPI-ESM-P model: The piControl experiment, served by ESGF.

Kalenic, M., Filipovic, I., Dolic, D., Rakic, M.O., Krstic, B., Banjesevic, M., Stejic, P., Glavas-Trbic, B., 2015. Geological Map of the Republic of Serbia. Geological Survey of Serbia, Belgrade.

Karpinsky, A.P., 1983. Geological map of the USSR and adjoining water-covered areas, Minist. of Geol. of the USSR, St. Petersburg, Russia.

Kent, D.V., Muttoni, G., 2013. Modulation of Late Cretaceous and Cenozoic climate by variable drawdown of atmospheric pCO2 from weathering of basaltic provinces on continents drifting through the equatorial humid belt. Clim. Past, 9(2): 525-546.

Kohfeld, K.E., Harrison, S.P., 2001. DIRTMAP: the geological record of dust. Earth-Science Reviews, 54(1-3): 81-114.

Kohfeld, K.E., Muhs, D.R., 2001. Mid-continental USA Gridded Maps of Loess Thickness. In: Paleoclimatology, I.P.W.D.C.f. (Editor), Data Contribution Series #2001-049. NOAA/NGDC Paleoclimatology Program, Boulder CO, USA.

Krasnov, I., Duphorn, K., Voges, A., 1971. Internationale Quartär-Karte von Europa, 1: 2 500 000. Blatt, Moskva. Bundesanstalt für Bodenforschung. UNESCO.

Kump, L., Alley, R.B., 1994. Global chemical weathering on glacial time scales. Material Fluxes on the Surface of the Earth: 46-60.

Lacquement, F., Prognon, F., Courboulelx, S., Quesnel, F., Prognon, C., Karnay, G., Thomas, E., 2009. Carte Géologique du Régolithe de la France Métropolitaine - Formations allochtones. BRGM.

Lambeck, K., Rouby, H., Purcell, A., Sun, Y., Sambridge, M., 2014. Sea level and global ice volumes from the Last Glacial Maximum to the Holocene. Proceedings of the National Academy of Sciences, 111(43): 15296-15303.

Landcare Research NZ Ltd, 2010. NZ Land Resource Inventory - Soil. Landcare Research NZ Ltd.

Le Maréchal, A., 1975. Carte geologique de l'ouest du Cameroun et de l'Adamaoua. ORSTOM.

Le Maréchal, A., 1976. Géologie et géochimie des sources thermominérales du Cameroun, 59. Orstom.

Lefort, J.-P., Danukalova, G., Monnier, J.-L., 2013. Why the Submerged Sealed beacheS, laSt remnantS of the loW StandS of the upper pleiStocene regreSSion, are better expreSSed in the WeStern than in the eaStern engliSh channel? Geo-Eco-Marina(19): 5.

Li, G., Elderfield, H., 2013. Evolution of carbon cycle over the past 100 million years. Geochimica et Cosmochimica Acta, 103: 11-25.

Li, G., Hartmann, J., Derry, L.A., West, A.J., You, C.-F., Long, X., Zhan, T., Li, L., Li, G., Qiu, W., Li, T., Liu, L., Chen, Y., Ji, J., Zhao, L., Chen, J., 2016. Temperature dependence of basalt weathering. Earth and Planetary Science Letters, 443: 59-69.

Li, T., Wang, C., Li, P., 2013. Loess Deposit and Loess Landslides on the Chinese Loess Plateau. In: Wang, F., Miyajima, M., Li, T., Shan, W., Fathani, T.F. (Eds.), Progress of Geo-Disaster Mitigation Technology in Asia. Springer Berlin Heidelberg, Berlin, Heidelberg, pp. 235-261.

Lineback, J.A., Bleuer, N.K., Mickelson, D.M., Farrand, W.R., Goldthwait, R.P., 2001. Quaternary Geologic Map of the Chicago 4° x 6° Quadrangle, United States, Miscellaneous Investigations series, Map I-1420 (NK-16). US Geological Survey, Denver, Colorado.

Liu, S.F., Raymond, O.L., Stewart, A.J., Sweet, I.P., Duggan, M.B., Charlick, C., Phillips, D., Retter, A.J., 2006. Surface geology of Australia 1:1,000,000 scale, Northern Territory [digital dataset]. Geosci. Aust., Canberra, A.C.T., Australia.

Louvat, P., Allègre, C.J., 1997. Present denudation rates on the island of Reunion determined by river geochemistry: basalt weathering and mass budget between chemical and mechanical erosions. Geochimica et Cosmochimica Acta, 61(17): 3645-3669.

Ludwig, W., Amiotte-Suchet, P., Probst, J.-L., 1999. Enhanced chemical weathering of rocks during the last glacial maximum: a sink for atmospheric CO2? Chemical Geology, 159(1): 147-161.

Mahowald, N., Kohfeld, K., Hansson, M., Balkanski, Y., Harrison, S.P., Prentice, I.C., Schulz, M., Rodhe, H., 1999. Dust sources and deposition during the last glacial maximum and current climate: A comparison of model results with paleodata from ice cores and marine sediments. Journal of Geophysical Research: Atmospheres, 104(D13): 15895-15916.

Maldonado, F., Mengal, J.M., Khan, S.H., Thomas, J.-C., 2011. Digital geologic map and Landsat image map of pars of Loralai, Sibi, Quetta, and Khuzar Divisions, Balochistan Province, west-central Pakistan. U.S. Geological Survey, Geological Survey of Pakistan.

Meehan, E.D.R., 2013. The Merging of Quaternary Map Datasets - End of Project Report on Project Outputs (Draft Version 1.1). Geological Survey of Ireland, Quaternary Mapping Programme, pp. 107.

Meng, X., Liu, L., Balsam, W., Li, S., He, T., Chen, J., Ji, J., 2015. Dolomite abundance in Chinese loess deposits: A new proxy of monsoon precipitation intensity. Geophysical Research Letters, 42(23): 10,391-10,398.

Meybeck, M., 1987. Global chemical weathering of surficial rocks estimated from river dissolved loads. American journal of science, 287(5): 401-428.

Miller, R.A., Maher, S.W., Copeland, J.C.W., Rheams, K.F., LeNeathery, T., Gilliland, W.A., Friddell, M.S., Van Nostrand, A.K., Wheeler, W.H., Holbrook, D.F., Bush, W.V., 2008. Quaternary Geologic Map of the Lookout Mountain 4° X 6° Quadrangle, United States. Miscellaneous Investigations series, Map I-1420 (NI-16). U.S. Geological Survey, Denver, Colorado.

Ministria E Energjise dhe Industrise Sherbimi Gjeologjik Shqiptar, 2014. Harta Gjeologjike Shkalla 1:100 000.

Möller, D., 1990. The Na/Cl ratio in rainwater and the seasalt chloride cycle. Tellus B, 42(3): 254-262.

Mollock, D.I.J., 1974. Geological map of the New Hebrides condominium, scale 1:1,000,000. Geol. Surv. of the New Hebrides, Port Vila.

Moore, R.B., 1990. Volcanic geology and eruption frequency, São Miguel, Azores. Bulletin of Volcanology, 52(8): 602-614.

Moosdorf, N., Hartmann, J., Lauerwald, R., Hagedorn, B., Kempe, S., 2011. Atmospheric CO 2 consumption by chemical weathering in North America. Geochimica et Cosmochimica Acta, 75(24): 7829-7854.

Muhs, D.R., Bettis, E., 2003. Quaternary loess-paleosol sequences as examples of climate-driven sedimentary extremes. Special Papers-Geological Society of America: 53-74.

Muhs, D.R., Bettis, E.A., 2000. Geochemical variations in Peoria Loess of western Iowa indicate paleowinds of midcontinental North America during last glaciation. Quaternary Research, 53(1): 49-61.

Muhs, D.R., Budahn, J.R., 2006. Geochemical evidence for the origin of late Quaternary loess in central Alaska. Canadian Journal of Earth Sciences, 43(3): 323-337.

Muhs, D.R., Cattle, S.R., Crouvi, O., Rousseau, D.-D., Sun, J., Zárate, M.A., 2014. Loess records, Mineral Dust. Springer, pp. 411-441.

Munhoven, G., 2002. Glacial–interglacial changes of continental weathering: estimates of the related CO2 and HCO3− flux variations and their uncertainties. Global and Planetary Change, 33(1-2): 155-176.

Nehlig, P., Quinquis, J., Bucelle, M., Odon, O., 2006. Carte géologique de la Réunion, Bur. de Rech. Geol. et Min., Orleans, France. BRGM, Bur. de Rech. Geol. et Min., Orleans, France.

New Zealand Geological Survey, 1972. Geological map of New Zealand, scale 1:1,000,000, Dep. of Sci. and Ind. Res., Wellington, New Zealand.

Norges geologiske undersøkelse, 2016. LosmasserN1000. Geological Survey of Norway.

Ortega, E., Freile, P., Longo, R., Baldock, J., 1982. National Geological Map of the Republic of Ecuador, scale 1:1,000,000, Minist. de Recursos Nat. y Energéticos, Quito.

Paone, A., Yun, S.-H., 2016. Pyroclastic Density Current Hazards at the Baekdusan Volcano, Korea: Analyses of Several Scenarios from a Small-Case to the Worst-Case Colossal Eruption, Updates in Volcanology-From Volcano Modelling to Volcano Geology. InTech.

Pawlewicz, M.J., Steinshouer, D.W., Gautier, D.L., 1997. Map showing geology, oil and gas fields, and geologic provinces of Europe including Turkey, U.S. Geol. Surv. Open File Rep., 97-470I, 14 pp.

Pécsi, M., 1990. Loess is not just the accumulation of dust. Quaternary International, 7: 1-21.

Persits, F.M., Wandrey, C.J., Milici, R.C., Manwar, A., 2001. Digital geologic and geophysical data of Bangladesh, *U.S. Geol. Surv. Open File Rep., OFR-97-470-H*.

Pollastro, R.M., Karshbaum, A.S., Viger, R.J., 1997. Maps showing geology, oil and gas fields and geologic provinces of the Arabian Peninsula, scale 1:4,500,000, U.S. Geol. Surv., Reston, Va.

Pollastro, R.M., Persits, F., Steinshouer, D., 1999. Surficial geology of Iran (geo2cg). U.S. Geological Survey, Central Energy Ressources Team.

Pope, D.E., Gilliland, W.A., Wermund, E.G., 2012. Quaternary Geologic Map of the White Lake 4° x 6° Quadrangle, United States, Miscellaneous Investigations series, Map I-1420 (NH-15). U.S. Geological Survey, Denver, Colorado.

Porder, S., Vitousek, P.M., Chadwick, O.A., Chamberlain, C.P., Hilley, G.E., 2007. Uplift, Erosion, and Phosphorus Limitation in Terrestrial Ecosystems. Ecosystems, 10(1): 159-171.

Price, R., McCulloch, M., Smith, I., Stewart, R., 1992. Pb-Nd-Sr isotopic compositions and trace element characteristics of young volcanic rocks from Egmont Volcano and comparisons with basalts and andesites from the Taupo Volcanic Zone, New Zealand. Geochimica et cosmochimica acta, 56(3): 941-953.

Purdy, E.G., 1974. Reef configurations: cause and effect.

Pye, K., 1984. Loess. Progress in Physical Geography, 8(2): 176-217.

Rad, S., Rivé, K., Vittecoq, B., Cerdan, O., Allègre, C.J., 2013. Chemical weathering and erosion rates in the Lesser Antilles: An overview in Guadeloupe, Martinique and Dominica. Journal of South American Earth Sciences, 45: 331-344.

Ran, L., Li, L., Tian, M., Yang, X., Yu, R., Zhao, J., Wang, L., Lu, X., 2017a. Riverine CO2 emissions in the Wuding River catchment on the Loess Plateau: Environmental controls and dam impoundment impact. Journal of Geophysical Research: Biogeosciences, 122(6): 1439-1455.

Ran, L., Lu, X.X., Liu, S., 2017b. Dynamics of riverine CO 2 in the Yangtze River fluvial network and their implications for carbon evasion. Biogeosciences, 14(8): 2183-2198.

Ran, L., Lu, X.X., Richey, J.E., Sun, H., Han, J., Yu, R., Liao, S., Yi, Q., 2015. Long-term spatial and temporal variation of CO₂ partial pressure in the Yellow River, China. Biogeosciences, 12(4): 921-932.

Raymond, O.L., Liu, S., Gallagher, R., Highet, L.M., Zhang, W., 2012. Surface Geology of Australia, 1:1 million scale, dataset 2012 edition. Commonwealth of Australia (Geoscience Australia), Canberra.

Raymond, O.L., Liu, S.F., Kilgour, P., 2007a. Surface geology of Australia 1:1,000,000 scale, Tasmania-3rd edition [digital dataset]. Geosci. Asutralia, Canberra, A.C.T., Australia.

Raymond, O.L., Liu, S.F., Kilgour, P., Retter, A.J., Connolly, D.P., 2007b. Surface geology of Australia 1:1,000,000 scale, Victoria-3rd edition [digital dataset]. Geosci. Aust., Canberra, A.C.T., Australia.

Raymond, O.L., Liu, S.F., Kilgour, P., Retter, A.J., Stewart, A.J., Stewart, G., 2007c. Surface geology of Australia 1:1,000,000 scale, New South Wales-2nd edition [digital dataset]. Geosci. Aust., Canberra, A.C.T., Australia.

Rivé, K., Gaillardet, J., Agrinier, P., Rad, S., 2013. Carbon isotopes in the rivers from the Lesser Antilles: origin of the carbonic acid consumed by weathering reactions in the Lesser Antilles. Earth Surface Processes and Landforms, 38(9): 1020-1035.

Romero-Mujalli, G., Hartmann, J., Börker, J., 2018a. Temperature and CO2 dependency of global carbonate weathering fluxes – Implications for future carbonate weathering research. Chemical Geology.

Romero-Mujalli, G., Hartmann, J., Börker, J., Gaillardet, J., Calmels, D., 2018b. Ecosystem controlled soil-rock pCO2 and carbonate weathering – Constraints by temperature and soil water content. Chemical Geology.

Rousseau, D.D., Chauvel, C., Sima, A., Hatté, C., Lagroix, F., Antoine, P., Balkanski, Y., Fuchs, M., Mellett, C., Kageyama, M., 2014. European glacial dust deposits: Geochemical constraints on atmospheric dust cycle modeling. Geophysical Research Letters, 41(21): 7666-7674.

Ryan, W.B., Major, C.O., Pitman, W.C., Shimkus, K.S., Moscalenko, V., Jones, G.A., Dimitrov, P., Saking, M., Seyir, H.Y., 1997. An abrupt drowning of the Black Sea shelf at 7.5 kyr BP. Geo-Eco-Marina, 2: 115-125.

Schaller, M.F., Wright, J.D., Kent, D.V., Olsen, P.E., 2012. Rapid emplacement of the Central Atlantic Magmatic Province as a net sink for CO2. Earth and Planetary Science Letters, 323–324: 27-39.

Schobbenhaus, C., Bellizia, A., 2001. Geological map of South America, scale 1: 5,000, 000. Comm. for the Geol. Map of the World, Brasilia.

Selvaraj, K., Chen, C.-T.A., 2006. Moderate chemical weathering of subtropical Taiwan: constraints from solid-phase geochemistry of sediments and sedimentary rocks. The Journal of Geology, 114(1): 101-116.

Servicio Geológico Mexicano, 1996. Carta Geológico-Minera Matehuala, F14-1 San Luis Potosí, Nuevo León, Zacatecas, Tamaulipas, Esc. 1:250,000. Consejo de Recursos Minerales, Pachuca, Hgo. México.

Servicio Geológico Mexicano, 1997a. Carta Geológico-Minera Chihuahua, H13-10 Chihuahua, Esc. 1:250,000. Consejo de Recursos Minerales, Pachuca, Hgo. México.

Servicio Geológico Mexicano, 1997b. Carta Geológico-Minera Ciudad Valles, F14-8, San Luis Potosí, Querétaro, Veracruz, Hidalgo, Guanajuato, Esc. 1:250,000. Consejo de Recursos Minerales, Pachuca, Hgo. México.

Servicio Geológico Mexicano, 1997c. Carta Geológico-Minera Guanajuato, F14-7 Guanajuato, San Luis Potosí, Jalisco, Zacatecas, Aguascalientes y Queretaro, Esc. 1:250,000. Consejo de Recursos Minerales, Pachuca, Hgo. México.

Servicio Geológico Mexicano, 1997d. Carta Geológico-Minera Guerrero Negro, G11-3 Baja California Sur, Esc. 1:250,000. Consejo de Recursos Minerales, Pachuca, Hgo. México.

Servicio Geológico Mexicano, 1997e. Carta Geológico-Minera Los Mochis G12-9, Sinaloa Esc. 1:250,000. Consejo de Recursos Minerales, Pachuca, Hgo. México.

Servicio Geológico Mexicano, 1997f. Carta Geológico-Minera Pachuca F14-11, Hidalgo, Querétaro, Estado de México, Veracruz, Puebla, Esc. 1:250,000. Consejo de Recursos Minerales, Pachuca, Hgo. México.

Servicio Geológico Mexicano, 1997g. Carta Geológico-Minera Santa Rosalía, G12-1 Baja California Sur, Esc. 1:250,000. Consejo de Recursos Minerlaes, Pachuca, Hgo. México.

Servicio Geológico Mexicano, 1997h. Carta Geológico-Minera Zacatecas, F13-6 Zacatecas, San Luis Potosí, Jalisco, Aguascalientes, Esc. 1:250,000. Consejo de Recursos Minerales, Pachuca, Hgo. México.

Servicio Geológico Mexicano, 1998a. Carta Geológico-Minera Aguascalientes F13-9, Aguascalientes, Jalisco, Zacatecas y Nayarit, Esc. 1:250,000. Consejo de Recursos Minerales, Pachuca, Hgo. México.

Servicio Geológico Mexicano, 1998b. Carta Geológico-Minera Buenaventura, H13-7 Chihuahua, Esc. 1:250,000. Consejo de Recursos Minerales, Pachuca, Hgo. México.

Servicio Geológico Mexicano, 1998c. Carta Geológico-Minera Chilpancingo E14-8, Guerrero, Oaxaca, Puebla, Esc. 1:250,000. Consejo de Recursos Minerales, Pachuca, Hgo. México.

Servicio Geológico Mexicano, 1998d. Carta Geológico-Minera Cuernavaca E14-5, Morelos, Puebla, Guerrero, Estado de México, Oaxaca, Esc. 1:250,000. Consejo de Recursos Minerales, Pachuca, Hgo. México.

Servicio Geológico Mexicano, 1998e. Carta Geológico-Minera Durango, G13-11 Durango y Sinaloa, Esc. 1:250,000. Consejo de Recursos Minerales, Pachuca, Hgo. México.

Servicio Geológico Mexicano, 1998f. Carta Geológico-Minera Fresnillo, F13-3 Zacatecas, Durango y San Luis Potosí, Esc. 1:250,000. Consejo de Recursos Minerales, Pachuca, Hgo. México.

Servicio Geológico Mexicano, 1998g. Carta Geológico-Minera Isla San Esteban, H12-10 Baja California y Sonora, Esc. 1:250,000. Consejo de Recursos MInerales, Pachuca, Hgo. México.

Servicio Geológico Mexicano, 1998h. Carta Geológico-Minera Monclova, G14-4 Coahuila y Nuevo. Consejo de Recursos Minerales, Pachuca, Hgo. México.

Servicio Geológico Mexicano, 1998i. Carta Geológico-Minera Morelia, E14-1,Michoacán, Edo. de México, Guanajuato, Esc. 1:250,000. Consejo de Recursos Minerales, Pachuca, Hgo. México.

Servicio Geológico Mexicano, 1998j. Carta Geológico-Minera Nacozari H12-6, Sonora, Chihuahua, Esc. 1:250,000. Consejo de Recursos Minerales, Pachuca. Hgo. México.

Servicio Geológico Mexicano, 1998k. Carta Geológico-Minera San Isidro, G12-4 Baja California Sur, Esc. 1:250,000. Consejo de Recursos Minerales, Pachuca, Hgo. México.

Servicio Geológico Mexicano, 1998l. Carta Geológico-Minera San Luis Potosí, F14-4 San LuisPotosí, Zacatecas, Aguascalientes, Jalisco,Tamaulipas, Esc. 1:250,000. Consejo de Recursos Minerales, Pachuca, Hgo. México.

Servicio Geológico Mexicano, 1998m. Carta Geológico-Minera Tepic, F13-8 Nayarit, Jalisco, Esc. 1:250,000. Consejo de Recursos Minerales, Pachuca, Hgo. México.

Servicio Geológico Mexicano, 1998n. Carta Geológico-Minera Tlahualilo de Zaragoza, G13-6 Coahuila, Durango, Chihuahua, Esc. 1:250,000. Consejo de Recursos Minerales, Pachuca, Hgo. México.

Servicio Geológico Mexicano, 1999a. Carta Geológico-Minera Cananea, H12-5 Sonora, Esc.1:250,000. Consejo de Recursos Minerales, Pachuca, Hgo. México.

Servicio Geológico Mexicano, 1999b. Carta Geológico-Minera Ciudad Mante F14-5, San Luis Potosí, Tamaulipas, Veracruz, Esc. 1:250,000. Consejo de Recursos Minerales, Pachuca, Hgo. México.

Servicio Geológico Mexicano, 1999c. Carta Geológico-Minera Colima, E13-3 Colima, Jalisco, Michoacán, Esc. 1:250,000. Consejo de Recursos Minerales, Pachuca, Hgo. México.

Servicio Geológico Mexicano, 1999d. Carta Geológico-Minera Culiacan, G13-10 Sinaloa, Durango, Esc. 1:250,000. Consejo de Recursos Minerales, Pachuca, Hgo. México.

Servicio Geológico Mexicano, 1999e. Carta Geológico-Minera Escuinapa, F13-5 Nayarit, Durango, Zacatecas, Sinaloa y Jalisco, Esc. 1:250,000. Consejo de Recursos Minerales, Pachuca, Hgo. México.

Servicio Geológico Mexicano, 1999f. Carta Geológico-Minera Guachochi, G13-4 Chihuahua, Sinaloa y Durango, Esc. 1:250,000. Consejo de Recursos Minerales, Pachuca, Hgo. México.

Servicio Geológico Mexicano, 1999g. Carta Geológico-Minera Hermosillo, H12-8 Sonora, Esc. 1:250,000. Consejo de Recursos Minerales, Pachuca, Hgo. México.

Servicio Geológico Mexicano, 1999h. Carta Geológico-Minera Juan Aldama, G13-12 Durango, Zacatecas y Coahuila, Esc. 1:250,000. Consejo de Recursos Minerales, Pachuca, Hgo. México.

Servicio Geológico Mexicano, 1999i. Carta Geológico-Minera La Paz, G12-10-11 Baja California Sur, Esc. 1:250,000. Consejo de Recursos Minerales, Pachuca, Hgo. México.

Servicio Geológico Mexicano, 1999j. Carta Geológico-Minera Madera H12-9, Sonora, Chihuahua, Esc. 1:250,000. Consejo de Recursos Minerales, Pachuca, Hgo. México.

Servicio Geológico Mexicano, 1999k. Carta Geológico-Minera Mazatlán, F13-1 Sinaloa, Esc. 1:250.000. Consejo de Recursos Minerales, Pachuca, Hgo. México.

Servicio Geológico Mexicano, 1999l. Carta Geológico-Minera Pericos, G13-7 Sinaloa, Durango y Chihuahua, Esc. 1:250,000. Consejo de Recursos Minerales, Pachuca, Hgo. México.

Servicio Geológico Mexicano, 1999m. Carta Geológico-Minera Puerto Vallarta, F13-11 Jalisco, Nayarit, Esc. 1:250,000. Consejo de Recursos Minerales, Pachuca, Hgo. México.

Servicio Geológico Mexicano, 1999n. Carta Geológico-Minera Queretaro, F14-10 Queretaro, Guanajuato, Michoacán, Jalisco y Estado de México, Esc. 1:250,000. Consejo de Recursos Minerales, Pachuca, Hgo. México.

Servicio Geológico Mexicano, 1999o. Carta Geológico-Minera San Felipe, H11-3 Baja California y Sonora, Esc. 1: 250,000. Consejo de Recursos Minerales, Pachuca, Hgo. México.

Servicio Geológico Mexicano, 1999p. Carta Geológico-Minera Zihuatanejo E14-7-10, Guerrero, Esc. 1:250,000. Consejo de Recursos Minerales, Pachuca, Hgo. México.

Servicio Geológico Mexicano, 2000a. Carta Geológico-Minera Acapulco E14-11, Guerrero, Oaxaca, Esc. 1:250,000. Consejo de Recursos Minerales, Pachuca, Hgo. México.

Servicio Geológico Mexicano, 2000b. Carta Geológico-Minera Ciudad Altamirano, E14-4 Guerrero, Michoacán y Estado de México, Esc. 1:250,000. Consejo de Recursos Minerales, Pachuca, Hgo. México.

Servicio Geológico Mexicano, 2000c. Carta Geológico-Minera Ciudad Camargo, G13-2 Chihuahua, Esc. 1:250,000. Consejo de Recursos Minerales, Pachuca, Hgo. México.

Servicio Geológico Mexicano, 2000d. Carta Geológico-Minera Ciudad Delicias, H13-11 Chihuahua, Esc. 1:250,000. Consejo de Recursos Minerales, Pachuca, Hgo. México.

Servicio Geológico Mexicano, 2000e. Carta Geológico-Minera Concepción del Oro G14-10, Zacatecas, Nuevo León, Coahuila y San Luis Potosí, Esc. 1:250,000. Consejo de Recursos Minerales, Pachuca, Hgo. México.

Servicio Geológico Mexicano, 2000f. Carta Geológico-Minera El Salto, F13-2 Durango, Sinaloa, Zacatecas y Nayarit, Esc. 1:250,000. Consejo de Recursos MInerales, Pachuca, Hgo. México.

Servicio Geológico Mexicano, 2000g. Carta Geológico-Minera Guadalajara, F13-12 Jalisco, Michoacán y Guanajuato, Esc. 1:250,000. Consejo de Recursos Minerales, Pachuca, Hgo. México.

Servicio Geológico Mexicano, 2000h. Carta Geológico-Minera Hidalgo del Parral, G13-5 Chihuahua y Durango, Esc. 1:250,000. Consejo de Recursos Minerales, Pachuca, Hgo. México.

Servicio Geológico Mexicano, 2000i. Carta Geológico-Minera Huatabampo, G12-6 Sonora, Sinaloa, Chihuahua, Esc. 1:250,000. Consejo de Recursos Minerales, Pachuca, Hgo. México.

Servicio Geológico Mexicano, 2000j. Carta Geológico-Minera Juchitán E15-10 D15-1, Oaxaca, Chiapas, Esc. 1:250,000. Consejo de Recursos Minerales, Pachuca, Hgo. México.
Servicio Geológico Mexicano, 2000k. Carta Geológico-Minera Manzanillo, E13-2-5 Colima y Jalisco, Esc. 1:250,000. Consejo de Recursos Minerales, Pachuca, Hgo. México.
Servicio Geológico Mexicano, 2000l. Carta Geológico-Minera Minatitlán E15-7 Veracruz, Oaxaca, Tabasco, Esc. 1:250,000. Consejo de Recursos Minerales, Pachuca, Hgo. México.
Servicio Geológico Mexicano, 2000m. Carta Geológico-Minera Monterrey, G14-7 Nuevo León y Coahuila, Esc. 1:250,000. Consejo de Recursos Minerales, Pachuca, Hgo. México.
Servicio Geológico Mexicano, 2000n. Carta Geológico-Minera Nogales, H12-2 Sonora, Esc. 1:250,000. Consejo de Recursos Minerales, Pachuca, Hgo. México.
Servicio Geológico Mexicano, 2000o. Carta Geológico-Minera Nueva Rosita, G14-1 Coahuila y Nuevo León, Esc. 1:250,000. Consejo de Recursos Minerales, Pachuca, Hgo. México.
Servicio Geológico Mexicano, 2000p. Carta Geológico-Minera Oaxaca E14-9, Oaxaca, Puebla, Esc. 1:250,000. Consejo de Recursos Minerales, Pachuca, Hgo. México.
Servicio Geológico Mexicano, 2000q. Carta Geológico-Minera Ocampo, G13-3 Coahuila y Chihuahua, Esc. 1:250,000. Consejo de Recursos Minerales, Pachuca, Hgo. México.
Servicio Geológico Mexicano, 2000r. Carta Geológico-Minera San Juanito, G13-1 Chihuahua, Esc. 1:250,000. Consejo de Recursos Minerales, Pachuca, Hgo. México.
Servicio Geológico Mexicano, 2000s. Carta Geológico-Minera Santiago Papasquiaro, G13-8 Durango, Esc. 1:250,000. Consejo de Recursos Minerales, Pachuca, Hgo. México.
Servicio Geológico Mexicano, 2000t. Carta Geológico-Minera Sierra Libre, H12-11 Sonora, Esc. 1:250,000. Consejo de Recursos Minerales, Pachuca, Hgo. México.
Servicio Geológico Mexicano, 2000u. Carta Geológico-Minera Tecoripa, H12-12 Sonora, Chihuahua, Esc. 1:250,000. Consejo de Recursos Minerales, Pachuca, Hgo. México.
Servicio Geológico Mexicano, 2000v. Carta Geológico-Minera Torreón, G13-9 Coahuila, Durango, Zacatecas, Esc. 1:250,000. Consejo de Recursos Minerales, Pachuca, Hgo. México.
Servicio Geológico Mexicano, 2000w. Carta Geológico-Minera Villa Constitución G12-7-8 Baja California Sur, Esc. 1:250,000. Consejo de Recursos Minerales, Pachuca, Hgo. México.
Servicio Geológico Mexicano, 2000x. Carta Geológico-Minera Zaachila E14-12, Oaxaca, Esc. 1:250,000. Consejo de Recursos Minerales, Pachuca, Hgo. México.
Servicio Geológico Mexicano, 2001. Carta Geológico-Minera Orizaba E14-6, Veracruz, Puebla, Oaxaca, Esc. 1:250,000. Consejo de Recursos Minerales, Pachuca, Hgo. México.
Servicio Geológico Mexicano, 2002a. Carta Geológico-Minera Caborca H12-4, Sonora, Esc. 1:250,000. Consejo de Recursos Minerales, Pachuca, Hgo. México.
Servicio Geológico Mexicano, 2002b. Carta Geológico-Minera Ciudad de México E14-2, Edo. de México,Tlaxcala, Puebla, Hidalgo, Morelos, Esc. 1:250,000. Consejo de Recursos Minerales, Pachuca, Hgo. México.
Servicio Geológico Mexicano, 2002c. Carta Geológico-Minera Ciudad Obregón, G12-3 Sonora, Chihuahua, Sinaloa, Esc. 1:250,000. Consejo de Recursos Minerales, Pachuca, Hgo. México.
Servicio Geológico Mexicano, 2002d. Carta Geológico-Minera Guaymas, G12-2 Sonora y Baja California Sur, Esc.1:250,000. Consejo de Recursos Minerales, Pachuca, Hgo. México.
Servicio Geológico Mexicano, 2002e. Carta Geológico-Minera Isla Ángel de la Guarda, H12-7 Baja California y Sonora, Esc. 1:250,000. Consejo de Recursos Minerales, Pachuca, Hgo. México.
Servicio Geológico Mexicano, 2002f. Carta Geológico-Minera Isla Cedros, H11-12 Baja California, Esc. 1: 250,000. Consejo de Recursos Minerales, Pachuca, Hgo. México.
Servicio Geológico Mexicano, 2002g. Carta Geológico-Minera Lázaro Cárdenas, E13-6-9, Michoacán, Colima, Guerrero, Jalisco, Esc. 1: 250,000. Consejo de Recursos Minerales, Pachuca, Hgo. México.
Servicio Geológico Mexicano, 2002h. Carta Geológico-Minera Loreto, G12-5 Baja California Sur, Esc. 1:250,000. Consejo de Recursos Minerales, Pachuca, Hgo. México.
Servicio Geológico Mexicano, 2002i. Carta Geológico-Minera Los Vidrios, I12-10 Sonora, Esc. 1:250,000. Consejo de Recursos Minerales, Pachuca, Hgo. México.

Servicio Geológico Mexicano, 2002j. Carta Geológico-Minera Nueva Casas Grandes, H13-4 Chihuahua, Esc. 1:250,000. Consejo de Recursos Minerales, Pachuca, Hgo. México.
Servicio Geológico Mexicano, 2002k. Carta Geológico-Minera Puerto Escondido D14-3, Oaxaca, Esc. 1:250,000. Consejo de Recursos Minerales, Pachuca, Hgo. México.
Servicio Geológico Mexicano, 2002l. Carta Geológico-Minera Puerto Peñasco, H12-1 Sonora, Esc. 1:250,000. Consejo de Recursos Minerales, Pachuca, Hgo. México.
Servicio Geológico Mexicano, 2002m. Carta Geológico-Minera Punta San Antonio, H11-9 Baja California, Esc. 1: 250,000. Consejo de Recursos Minerales, Pachuca, Hgo. México.
Servicio Geológico Mexicano, 2002n. Carta Geológico-Minera San José del Cabo, F12-2-3-5-6 Baja California Sur, Esc. 1:250,000. Consejo de Recursos Minerales, Pachuca, Hgo. México.
Servicio Geológico Mexicano, 2002o. Carta Geológico-Minera Veracruz E14-3, Veracruz, Puebla, Tlaxcala, Esc. 1:250,000. Consejo de Recursos Minerales, Pachuca, Hgo. México.
Servicio Geológico Mexicano, 2003a. Carta Geológico-Minera Agua Prieta, H12-3 Sonora, Chihuahua Esc. 1:250,000. Consejo de Recursos Minerales, Pachuca, Hgo. México.
Servicio Geológico Mexicano, 2003b. Carta Geológico-Minera Ciudad Acuña, H14-7 Coahuila, Esc. 1:250,000. Consejo de Recursos Minerales, Pachuca, Hgo. México.
Servicio Geológico Mexicano, 2003c. Carta Geológico-Minera Ciudad Juárez H13-1, El Porvenir H13-2, Chihuahua, Esc. 1:250,000. Consejo de Recursos Minerales, Pachuca, Hgo. México.
Servicio Geológico Mexicano, 2003d. Carta Geológico-Minera Ensenada, H11-2 Baja California, Esc. 1: 250,000. Consejo de Recursos Minerales, Pachuca, Hgo. México.
Servicio Geológico Mexicano, 2003e. Carta Geológico-Minera Manuel Benavides H13-9, Chihuahua y Coahuila, Esc. 1:250,000. Consejo de Recursos Minerales, Pachuca, Hgo. México.
Servicio Geológico Mexicano, 2003f. Carta Geológico-Minera Mexicali, I11-12 Baja California y Sonora, Esc. 1: 250,000. Consejo de Recursos Minerales, Pachuca, Hgo. México.
Servicio Geológico Mexicano, 2003g. Carta Geológico-Minera Ojinaga, H13-8 Chihuahua, Esc. 1:250,000. Consejo de Recursos Minerales, Pachuca, Hgo. México.
Servicio Geológico Mexicano, 2003h. Carta Geológico-Minera Piedras Negras H14-10, Coahuila, Esc. 1:250,000. Consejo de Recursos Minerales, Pachuca, Hgo. México.
Servicio Geológico Mexicano, 2003i. Carta Geológico-Minera San Antonio del Bravo H13-5, Chihuahua, Esc. 1:250,000. Consejo de Recursos Minerales, Pachuca, Hgo. México.
Servicio Geológico Mexicano, 2003j. Carta Geológico-Minera San Miguel, H13-12 Coahuila, Chihuahua, Esc. 1:250,000. Consejo de Recursos Minerales, Pachuca, Hgo. México.
Servicio Geológico Mexicano, 2003k. Carta Geológico-Minera Tijuana, I11-11 Baja California, Esc. 1: 250,000. Consejo de Recursos Minerales, Pachuca, Hgo. México.
Servicio Geológico Mexicano, 2004a. Carta Geológico-Minera Ciudad Victoria, F14-2, Tamaulipas,Nuevo León, S.L.P Esc. 1:250,000. Consejo de Recursos Minerales, Pachuca, Hgo. México.
Servicio Geológico Mexicano, 2004b. Carta Geológico-Minera Coatzacoalcos, E15-1-4 Veracruz, Oaxaca, Tabasco, Esc. 1:250,000. Consejo de Recursos Minerales, Pachuca, Hgo. México.
Servicio Geológico Mexicano, 2004c. Carta Geológico-Minera Frontera E15-5, Tabasco, Campeche, Esc. 1:250,000. Consejo de Recursos Minerales, Pachuca, Hgo. México.
Servicio Geológico Mexicano, 2004d. Carta Geológico-Minera Linares, G14-11 Tamaulipas y Nuevo León, Esc. 1:250,000. Consejo de Recursos Minerales, Pachuca, Hgo. México.
Servicio Geológico Mexicano, 2004e. Carta Geológico-Minera Matamoros, G14-6-9-12 Tamaulipas, Esc. 1:250,000. Consejo de Recursos Minerales, Pachuca, Hgo. México.
Servicio Geológico Mexicano, 2004f. Carta Geológico-Minera Nuevo Laredo, G14-2 Tamaulipas, Nuevo León y Coahuila, Esc. 1:250,000. Consejo de Recursos Minerales, Pachuca, Hgo. México.
Servicio Geológico Mexicano, 2004g. Carta Geológico-Minera Poza Rica F14-12, Veracruz, Puebla, Hidalgo, Esc. 1:250,000. Consejo de Recursos Minerales, Pachuca, Hgo. México.
Servicio Geológico Mexicano, 2004h. Carta Geológico-Minera Reynosa, G14-5 Tamaulipas y Nuevo León, Esc. 1:250,000. Consejo de Recursos Minerales, Pachuca, Hgo. México.

Servicio Geológico Mexicano, 2004i. Carta Geológico-Minera Río Bravo G14-8, Tamaulipas, Nuevo León, Esc. 1:250,000. Consejo de Recursos Minerales, Pachuca, Hgo. México.
Servicio Geológico Mexicano, 2004j. Carta Geológico-Minera Tamiahua, F14-9, Veracruz, Esc. 1:250,000. Consejo de Recursos Minerales, Pachuca, Hgo. México.
Servicio Geológico Mexicano, 2004k. Carta Geológico-Minera Tampico, F14-3-6 Tamaulipas, Veracruz. Esc. 1:250,000. Consejo de Recursos Minerales, Pachuca, Hgo. México.
Servicio Geológico Mexicano, 2005a. Carta Geológica-Minera Calkini F15-9-12, Camp., Esc. 1:250,000. Consejo de Recursos Minerales, Pachuca, Hgo. México.
Servicio Geológico Mexicano, 2005b. Carta Geológica-Minera Campeche E15-3, Camp., Esc. 1:250,000. Consejo de Recursos Minerales, Pachuca, Hgo. México.
Servicio Geológico Mexicano, 2005c. Carta Geológica-Minera Chetumal E16-4-7, Q. Roo., Esc. 1:250,000. Consejo de Recursos Minerales, Pachuca, Hgo. México.
Servicio Geológico Mexicano, 2005d. Carta Geológica-Minera Ciudad del Carmen E15-6, Camp., Esc. 1:250,000. Consejo de Recursos Minerales, Pachuca, Hgo. México.
Servicio Geológico Mexicano, 2005e. Carta Geológica-Minera Huixtla D15-2, Chis., Esc. 1:250,000. Consejo de Recursos Minerales, Pachuca, Hgo. México.
Servicio Geológico Mexicano, 2005f. Carta Geológica-Minera Tapachula D15-5, Chis., Esc. 1:250,000. Consejo de Recursos Minerales, Pachuca, Hgo. México.
Servicio Geológico Mexicano, 2005g. Carta Geológica-Minera Tuxtla Gutiérrez E15-11, Chis., Esc. 1:250,000. Consejo de Recursos Minerales, Pachuca, Hgo. México.
Servicio Geológico Mexicano, 2005h. Carta Geológica-Minera Villahermosa E15-8, Tab., Esc. 1:250,000. Consejo de Recursos Minerales, Pachuca, Hgo. México.
Servicio Geológico Mexicano, 2006a. Carta Geológica-Minera Bahía Ascensión E16-2-5, Q. Roo., Esc. 1:250,000. Consejo de Recursos Minerales, Pachuca, Hgo. México.
Servicio Geológico Mexicano, 2006b. Carta Geológica-Minera Cancún F16-8, Q. Roo., Esc. 1:250,000. Consejo de Recursos Minerales, Pachuca, Hgo. México.
Servicio Geológico Mexicano, 2006c. Carta Geológica-Minera Cozumel F16-11, Q. Roo., Esc. 1:250,000. Consejo de Recursos Minerales, Pachuca, Hgo. México.
Servicio Geológico Mexicano, 2006d. Carta Geológica-Minera Felipe Carrillo Puerto F16-1, Q. Roo., Esc. 1:250,000. Consejo de Recursos Minerales, Pachuca, Hgo. México.
Servicio Geológico Mexicano, 2006e. Carta Geológica-Minera Las Margaritas E15-12_D15-3, Chis., Esc. 1:250,000. Consejo de Recursos Minerales, Pachuca, Hgo. México.
Servicio Geológico Mexicano, 2006f. Carta Geológica-Minera Mérida F16-10, Yuc., Esc. 1:250,000. Consejo de Recursos Minerales, Pachuca, Hgo. México.
Servicio Geológico Mexicano, 2006g. Carta Geológica-Minera Tenosique E15-9, Chis., Esc. 1:250,000. Consejo de Recursos Minerales, Pachuca, Hgo. México.
Servicio Geológico Mexicano, 2006h. Carta Geológica-Minera Tizimín F16-7, Yuc., Esc. 1:250,000. Consejo de Recursos Minerales, Pachuca, Hgo. México.
Servicio Geologico Minero Argentino, 1997. Mapa geológico de la República Argentina, scale 1:2,500,000, Buenos Aires.
Servicio Nacional de Geología y Minería, 2004. Mapa geológico de Chile: Versión digital, Santiago.
Serviço Geológico do Brasil - CPRM 2014. Unidades geológico-ambientais 1:1.000.000
Smets, B., Wauthier, C., d'Oreye, N., 2010. A new map of the lava flow field of Nyamulagira (DR Congo) from satellite imagery. Journal of African Earth Sciences, 58(5): 778-786.
Soller, D.R., Reheis, M.C., Garrity, C.P., Van Sistine, D.R., 2009. Map database for surficial materials in the conterminous United States. US Geological Survey Data Series, 425.
Stallard, R.F., 1995. Tectonic, environmental, and human aspects of weathering and erosion: a global review using a steady-state perspective. Annual Review of Earth and Planetary Sciences, 23(1): 11-39.
Stearns, H.T., Macdonald, G.A., 1946. Geology and ground-water resources of the island of Hawaii, Honolulu Advertising.

Steinshouer, D.W., Qiang, J., McCabe, P.J., Ryder, R.T., 1999. Maps Showing geology, oil and gas fields, and geologic provinces of the Asia Pacific region; Plate 2: Southeast Asia, Cent. Energy Resour. Team, U.S. Geol. Surv., Denver, Colo.

Stewart, A.J., Sweet, I.P., Needham, R.S., Raymond, O.L., Whitaker, A.J., Liu, S.F., Phillips, D., Retter, A.J., Connolly, D.P., Stewart, G., 2008. Surface geology of Australia 1:1,000,000 scale, Western Australia [digital dataset]. Geosci. Aust., Canberra, A.C.T., Australia.

Swinehart, J.B., Dreeszen, V.H., Richmond, G.M., Tipton, M.J., Bretz, R., Steece, F.V., Hallberg, G.R., Goebel, J.E., 2006. Quaternary geologic map of the Platte River 4°× 6° quadrangle, United States, US Geological Survey Miscellaneous Investigations Series Map I-1420 (NK-14). U.S. Geological Survey, Denver, Colorado.

Taylor, A., Blum, J.D., 1995. Relation between soil age and silicate weathering rates determined from the chemical evolution of a glacial chronosequence. Geology, 23(11): 979-982.

Tefera, M., Chernet, T., Haro, W., 1996. Geological Map of Ethiopia. Ministry of Mines, Geological Survey of Ethiopia, GSE, Addis Ababa, Ethiopia.

Teitler, Y., Le Hir, G., Fluteau, F., Philippot, P., Donnadieu, Y., 2014. Investigating the Paleoproterozoic glaciations with 3-D climate modeling. Earth and Planetary Science Letters, 395: 71-80.

Tokic, S., 1986. Geological Map of Quaternary Basic Types Lithofacies of Bosnia and Herzegovina.

Turner, C.C., 1978. Shortland Islands, Solomon Islands, 1:100,00 geological map. Solomon Islands Geol. Surv., Honiara.

U.S. Geological Survey/The Nature Conservancy, 2009. Africa Surficial Lithology. U.S. Geological Survey / The Nature Conservancy, Reston, VA.

United States. Army. Corps of Engineers, 1974. Illinois Waterway Duplicate Locks: Environmental Impact Statement.

van Engelen, V., Verdoodt, A., Dijkshoorn, J., Van Ranst, E., 2006. Soil and Terrain Database of Central Africa (DR of Congo, Burundi and Rwanda). Report 2006/07, (available through: http://www.isric.org). ISRIC - World Soil Information, Wageningen.

Violante, R.A., Paterlini, C.M., Marcolini, S.I., Costa, I.P., Cavallotto, J.L., Laprida, C., Dragani, W., García Chapori, N., Watanabe, S., Totah, V., Rovere, E.I., Osterrieth, M.L., 2014. Chapter 6 The Argentine continental shelf: morphology, sediments, processes and evolution since the Last Glacial Maximum. Geological Society, London, Memoirs, 41(1): 55-68.

Walker, J.C.G., Hays, P.B., Kasting, J.F., 1981. A negative feedback mechanism for the long-term stabilization of Earth's surface temperature. Journal of Geophysical Research: Oceans, 86(C10): 9776-9782.

Wandrey, C.J., Law, B.E., 1998. Geologic map of South Asia (geo8ag), Cent. Energy Resour. Team, U.S. Geol. Surv., Denver, Colo.

Whitaker, A.J., Champion, D.C., Sweet, I.P., Kilgour, P., Connolly, D.P., 2007. Surface geology of Australia 1:1,000,000 scale, Queensland-2nd edition [digital dataset]. Geosci. Aust., Canberra, A.C.T., Australia.

Whitaker, A.J., Glanville, H.D., English, P.M., Stewart, A.J., Retter, A.J., Connolly, D.P., Stewart, G.A., Fisher, C.L., 2008. Surface geology of Australia 1:1,000,000 scale, South Australia-1st edition [digital dataset]. Geosci. Aust., Canberra, A.C.T., Australia.

Whitfield, J.W., Ward, R.A., Denne, J.E., Holbrook, D.F., Bush, W.V., Lineback, J.A., Luza, K.V., Jensen, K.M., Fishman, W.D., 2011. Quaternary geologic map of the Ozark Plateau 4° x 6° Quadrangle, United States, US Geological Survey, Miscellaneous Investigations Series, Map I-1420 (NJ-15).

Wolff-Boenisch, D., Gislason, S.R., Oelkers, E.H., 2006. The effect of crystallinity on dissolution rates and CO2 consumption capacity of silicates. Geochimica et Cosmochimica Acta, 70(4): 858-870.

Wright, J., 2001. Making loess-sized quartz silt: data from laboratory simulations and implications for sediment transport pathways and the formation of ‘desert’loess deposits associated with the Sahara. Quaternary International, 76: 7-19.

Xiao, J., Zhang, F., Jin, Z., 2016. Spatial characteristics and controlling factors of chemical weathering of loess in the dry season in the middle Loess Plateau, China. Hydrological Processes, 30(25): 4855-4869.

Zárate, M., 2003. Loess of southern South America. Quaternary Science Reviews, 22(18-19): 1987-2006.

Zastrozhnov, A.S., Minim, E.A., Shkatova, V.K., Tarnogradsky, V.D., Krutkina, O.N., Ryzhkova, V.M., Astakhov, V.I., Gusev, E.A., 2014. Map of the Quaternary Formations of the Russian Federation. Ministry of Natural Resources and Ecology of the Russian Federation, Federal Agency on Mineral Resources, Federal State Unitary Enterprise "A.P. Karpinsky Russian Geological Research Institute" (VSEGEI), Federal State Unitary Enterprise "I.S. Gramberg Russian Research Institute for Geology and Mineral Resources of the Ocean" (VNIIOkeangeologia).

Zhang, F., Jin, Z., Li, F., Yu, J., You, C.-F., Zhou, L., 2013. The dominance of loess weathering on water and sediment chemistry within the Daihai Lake catchment, northeastern Chinese Loess Plateau. Applied geochemistry, 35: 51-63.

Appendix

Appendix A: Development of the Global Unconsolidated Sediments Map database (GUM) – Definitions, Sources, Methods

A.1 Description of the Database

The information about sediment types, provided by the original map databases, had to be translated to a uniform new classification for the GUM. The quality of information varies enormously regarding the different sources for input data.

The database from the USA (see Tab. A.2) for example provided very detailed sediment descriptions with up to 130 words, describing the sediment type, the grainsize, the age and the thickness.

Other databases, e.g., for Bolivia, provided rather sparse information, complicated to translate. For example, one unit was labelled "Depositos aluviales, fluvio-lacustres, fluvioglaciales, coluviales, lacustres, morrenas y dunas", which was translated to "Alluvial, fluvial-lacustrine, glaciofluvial, colluvial, lacustrine, moraines and dune deposits" and since no unique sediment description was obtainable, classified as "Us", sediments undifferentiated. Another unit in Bolivia was called "Gravas, arenas y arcillas" which gave only information on the grainsize distribution, but not about the sediment type (gravel, sand and clay). Hence, it was defined as "Us" as well, but with the grainsize information in information level YY.

These examples of very heterogeneous input data show the motivation for developing a new classification system that will be explained in the following.

A.2 The sediment classification

The sediment classification was developed based on the availability of sediment descriptions in the input data sets, which is now represented by a ten-symbol code: "*XXYYZZAADD*," where "*XX*" represents the sediment type. The second to fifth level information provides further information considering sediment characteristics and is optional. The code "nn" in the database attribute table represents the lack of information. Tab. A.1 lists all sediment classes and subclasses.

A.2.1 First level: sediment types (XX)

All units in the GUM feature information on the first level class *XX*, which describes the sediment type. The first large letter indicates the dominant group type in case of alluvial sediments (*A*), aeolian sediments (*E*), glacial sediments (*G*), coastal sediments (*Y*), organic sediments (*O*), evaporitic sediments (*P*), colluvial sediments (*C*) and water bodies (*W*). The second letter of those groups indicates a subgroup of the type, which is described below. Exceptions are marine deposits (*Mu*), Lacustrine deposits (*Lu*), pyroclastic material (*Iy*), undifferentiated sediments (*Us*),

anthropogenic deposits (*Zu*) and Ice and glaciers (*Du*), where no further subtype differentiation was done.

A.2.1.1 Alluvial sediments (A-)

These are sediments that are deposited in an alluvial system. Sometimes the word "fluvial" was used to describe these sediments. They can be subdivided into alluvial fan sediments (*Af*), alluvial terrace sediments (*At*) or into alluvial floodplain sediments (*Ap*). If not only of alluvial origin, alluvial-aeolian sediments (*Ae*) or alluvial-lacustrine sediments (*Al*) can be described. The general term is "*Au*" for undifferentiated alluvial sediments.

A.2.1.2 Colluvial sediments (C-)

Colluvial sediments are here defined as mass-transported sediments by gravity. Original terms describing these sediments were for example "slope deposits", "talus", "deserptium" or "solifluction". In case of an alluvial influence they were classified as colluvial-alluvial sediments (*Ca*). "*Cu*" is defining colluvial sediments without further information.

A.2.1.3 Aeolian sediments (E-)

The Aeolian sediments group can be subdivided into Dune sands (*Ed*) and Loess deposits (*El*, *Er*, *Ea*).

Loess is typically defined as silt-dominated sediment that has been entrained, transported and deposited by the wind (Muhs et al., 2014). Primary aeolian loess should be separated from reworked loess and weathered loess. Loessoid deposits describe a mixture of aeolian dust and other material. Loess-like deposits are silt deposits but not of aeolian origin (e.g. alluvial loess, colluvial loess) (Pye, 1984). This results in a final loess classification as:

1. Loess deposits (windblown silt) - *El*
2. Loess derivates (reworked loess, loessoid deposits) - *Er*
3. Loess-like deposits – *Ea*

The general term describing aeolian sediments without further information regarding their origin is "*Eu*".

A.2.1.4 Glacial sediments (G-)

Glacially derived sediments can be either of a glacio-fluvial origin (*Gf*), a glacio-lacustrine origin (*Gl*), a glacio-marine origin (*Gm*) or directly transported by the glacier in form of till sediments (*Gt*). Besides, there are proglacial deposits (*Gp*) and glacial deposits undifferentiated (*Gu*).

A.2.1.5 Coastal sediments (Y-)

Coastal deposits consist of beach deposits (*Yb*), deltaic deposits (*Yd*), lagoonal deposits (*Yl*), marsh deposits (*Ym*) or swamps (*Ys*). In many regions where sediments were defined as alluvial/marine sediments they were reclassified into general coastal deposits (*Yu*).

A.2.1.6 Marine sediments (Mu)

These sediments are deposited in a marine environment. Most of these areas were not considered in the GUM because they are covered by water.

A.2.1.7 Organic deposits (O-)
Organic deposits can comprise peat and bog deposits (*Op*), modern reefs (*Or*) or undifferentiated organic deposits (*Ou*).

A.2.1.8 Lacustrine sediments (Lu)
These are sediments that are of lacustrine origin.

A.2.1.9 Evaporitic deposits (P-)
Evaporitic deposits can be subdivided into gypsum deposits (*Pg*), salt deposits (*Ps*) or playa deposits (*Pp*). The general term is "*Pu*".

A.2.1.10 Pyroclastic sediments (Iy)
For the pyroclastic material it was challenging to distinguish between consolidated and unconsolidated sediments. Therefore, pyroclastic material was only considered where it was clearly described as for example "ash", "lapilli" or "tephra". Note, there is an additional datalayer available reporting pyroclastic sediments including those areas, where it was not possible to determine if the sediment is consolidated or unconsolidated, without recherche going beyond the project time available.

A.2.1.11 Undifferentiated sediments (Us)
These sediments are either not further described or they consist of a mixture of different sediment types.

A.2.1.12 Anthropogenic deposits (Zu)
Anthropogenic deposits are described very rarely and can consist for example of dams, urban areas, mine waste deposits etc.

A.2.1.13 Water bodies (W-)
Water bodies, not sediments, comprise the following subunits: lakes (*Wl*) and rivers (*Wr*). Undifferentiated water bodies are classified as "*Wu"*.

A.2.1.14 Ice and Glaciers (Du)
The term "*Du*" defines regions that are covered by ice.

*A.2.2 Grainsize information (***YY***)*
If grainsize information was available in the original database, this was reclassified as following:

1. sand or coarser (*su*)
2. sand and silt (*sl*) – often described as coarse-grained deposits
3. sand and clay (*sc*)
4. silt (*lu*)
5. silt and clay (*lc*) – often described as fine-grained deposits
6. clay or finer (*cu*)

7. mixed (*mx*) – if a mixture of grainsizes was reported

*A.2.3 Mineralogical information (*ZZ*)*

In some maps, there was information available regarding the mineralogical composition of a sediment. If it was reported that sediments were derived from igneous rocks that are acidic, meaning they contain higher levels of SiO_2, they were classified as "acidic" (*ac*). In case of a basic igneous origin with less SiO_2, containing relevant amounts of mafic minerals, the sediments were called "mafic" (*ma*).

Sediments that were derived from carbonate rocks or that have a primarily carbonatic composition, like reefs, are classified as "carbonatic sediments" (*ca*). Meanwhile, sediments containing a lot of silicate minerals, and which are derived by sandstones, siltstones or shales for example are called "siliciclastic" (*ss*).

Where a mixed mineralogy of the above named was mentioned the sediment was given the attribute "mixed" (*mx*).

*A.2.4 Age information (*AA*)*

Regarding the age classification of the sediments different types of classes could be identified. The most common are "Quaternary" (*qu*), meaning both Holocene and/or Pleistocene. Sediments of Holocene age in general (*hu*) can be further subdivided into "middle Holocene" (*hm*) or "late Holocene" (*hl*). Pleistocene age in general is indicated with "*pu*", whereas there exist also sediments of early Pleistocene age (*pe*), of the middle Pleistocene (*pm*) or the late Pleistocene (*pl*). Sediments of Pliocene-Pleistocene age are indicated with "*pp*". The Tertiary age is classified as "*tu*" and sediments of either Quaternary or Tertiary age or both have the index "*qt*".

But there are also older sediments identified, herein reclassified as "older than Tertiary" (*ot*). These sediments cover only small regions, only in maps of the former Soviet Union, Belgium and the Netherlands.

*A.2.5 Thickness information (*DD*)*

Thickness data of the individual sediments were obtained and implemented in the global database. The values are given either in meters or feet, visible in the attribute table. The term "*dis*" represents a reported discontinuous or patchy coverage.

Table A.1: List of all the sediment classes of the GUM.

Code	Description
XX – Sediment type	
Au	Alluvial, undifferentiated
Ae	Alluvial-aeolian
Af	Alluvial fans
Al	Alluvial-lacustrine
Ap	Alluvial plains
At	Alluvial terraces
Cu	Colluvial, undifferentiated
Ca	Colluvial-alluvial
Du	Ice and glaciers
Eu	Aeolian, undifferentiated
Ea	Loess-like silt
Ed	Dunes
El	Loess
Er	Loess derivates
Gu	Glacial, undifferentiated
Gf	Glacio-fluvial
Gl	Glacio-lacustrine
Gm	Glacio-marine
Gp	Proglacial
Gt	Till
Iy	Pyroclastics
Lu	Lacustrine
Mu	Marine
Ou	Organic, undifferentiated
Op	Peat
Or	Reef
Pu	Evaporites, undifferentiated
Pg	Gypsum
Pp	Playa
Ps	Salt
Us	Sediments, undifferentiated
Wu	Water bodies, undifferentiated
Wl	Lakes
Wr	Rivers
Yu	Coastal, undifferentiated
Yb	Beach
Yd	Deltaic
Yl	Lagoonal
Ym	Marshes
Ys	Swamps
Zu	Anthropogenic
YY – Grainsize information	
su	Sand or coarser
sl	Sand/silt
lu	Silt
lc	Silt/clay
cu	Clay or finer
sc	Sand/clay
mx	Mixed
ZZ – Mineralogical information	
ac	Acidic
ma	Basic

ss	Siliciclastic
ca	Carbonatic
mx	Mixed
AA – Age information	
hl	Late Holocene
hm	Middle Holocene
hu	Holocene
ot	older than Tertiary
pe	Early Pleistocene
pl	Late Pleistocene
pm	Middle Pleistocene
pp	Pliocene-Pleistocene
pu	Pleistocene
qt	Quaternary-Tertiary
qu	Quaternary
tu	Tertiary
DD – Thickness information	
absolute values	in [m] or [ft]
dis	discontinuous or patchy

A.3 Sources of the GUM

All sources of the GUM are listed in Tab. A.2. If possible, state-wide geological maps were used, but also maps of larger or smaller regions were implemented.

Table A.2: Sources of the GUM.

Region (country)	**Source**	**Original Format**	**Scale**
Alaska	Ermann and O'Keife (1999)	Shapefile	1:1,584,000
Alaska	Muhs and Budahn (2006)	PDF	Not known
Canada	Fulton (1995)	Shapefile	1:5,000,000
Greenland	GLiM; Escher and Pulvertaft (1995)	Shapefile	1:2,500,000
USA	Soller et al. (2009)	Shapefile	1:5,000,000
USA – Regina	Fullerton et al. (2007)	Shapefile	1:1,000,000
USA – Chicago	Lineback et al. (2001)	Shapefile	1:1,000,000
USA – Des Moines	Hallberg et al. (2008)	Shapefile	1:1,000,000
USA – Dakotas	Fullerton et al. (2011)	Shapefile	1:1,000,000
USA – Hudson River	Fullerton et al. (2005)	Shapefile	1:1,000,000
USA – Lake Erie	Fullerton et al. (1991)	Shapefile	1:1,000,000
USA – Lookout Mountain	Miller et al. (2008)	Shapefile	1:1,000,000
USA – Louisville	Gray et al. (2011)	Shapefile	1:1,000,000

USA – Ozark Plateau	Whitfield et al. (2011)	Shapefile	1:1,000,000
USA – Platte River	Swinehart et al. (2006)	Shapefile	1:1,000,000
USA – Quebec	Borns et al. (2005)	Shapefile	1:1,000,000
USA – White Lake	Pope et al. (2012)	Shapefile	1:1,000,000
USA – Wichita	Denne et al. (2011)	Shapefile	1:1,000,000
USA – Winnipeg	Fullerton et al. (2000)	Shapefile	1:1,000,000
USA – Vicksburg	Holbrook et al. (2012)	Shapefile	1:1,000,000
USA – Peoria Loess	Kohfeld and Muhs (2001)	ASCII	1:1,000,000
USA – Snake River Plain and Palouse Loess	Bettis et al. (2003)	PDF	Not known
Mexico – Acapulco	Servicio Geológico Mexicano (2000a)	Shapefile	1:250,000
Mexico – Agua Prieta	Servicio Geológico Mexicano (2003a)	Shapefile	1:250,000
Mexico – Aguascalientes	Servicio Geológico Mexicano (1998a)	Shapefile	1:250,000
Mexico – Bahía Ascensión	Servicio Geológico Mexicano (2006a)	Shapefile	1:250,000
Mexico – Buenaventura	Servicio Geológico Mexicano (1998b)	Shapefile	1:250,000
Mexico – Caborca	Servicio Geológico Mexicano (2002a)	Shapefile	1:250,000
Mexico – Calkini	Servicio Geológico Mexicano (2005a)	Shapefile	1:250,000
Mexico – Campeche	Servicio Geológico Mexicano (2005b)	Shapefile	1:250,000
Mexico – Cananea	Servicio Geológico Mexicano (1999a)	Shapefile	1:250,000
Mexico – Cancún	Servicio Geológico Mexicano (2006b)	Shapefile	1:250,000
Mexico – Chetumal	Servicio Geológico Mexicano (2005c)	Shapefile	1:250,000
Mexico – Chihuahua	Servicio Geológico Mexicano (1997a)	Shapefile	1:250,000
Mexico – Chilpancingo	Servicio Geológico Mexicano (1998c)	Shapefile	1:250,000
Mexico – Ciudad Acuña	Servicio Geológico Mexicano (2003b)	Shapefile	1:250,000
Mexico – Ciudad Altamirano	Servicio Geológico Mexicano (2000b)	Shapefile	1:250,000
Mexico – Ciudad Camargo	Servicio Geológico Mexicano (2000c)	Shapefile	1:250,000
Mexico – Ciudad del Carmen	Servicio Geológico Mexicano (2005d)	Shapefile	1:250,000
Mexico – Ciudad Delicias	Servicio Geológico Mexicano (2000d)	Shapefile	1:250,000
Mexico – Ciudad de México	Servicio Geológico Mexicano (2002b)	Shapefile	1:250,000
Mexico – Ciudad Juárez	Servicio Geológico Mexicano (2003c)	Shapefile	1:250,000
Mexico – Ciudad Mante	Servicio Geológico Mexicano (1999b)	Shapefile	1:250,000
Mexico – Ciudad Obregón	Servicio Geológico Mexicano (2002c)	Shapefile	1:250,000

Mexico – Ciudad Valles	Servicio Geológico Mexicano (1997b)	Shapefile	1:250,000
Mexico – Ciudad Victoria	Servicio Geológico Mexicano (2004a)	Shapefile	1:250,000
Mexico – Colima	Servicio Geológico Mexicano (1999c)	Shapefile	1:250,000
Mexico – Concepción del Oro	Servicio Geológico Mexicano (2000e)	Shapefile	1:250,000
Mexico – Cozumel	Servicio Geológico Mexicano (2006c)	Shapefile	1:250,000
Mexico – Coatzacoalcos	Servicio Geológico Mexicano (2004b)	Shapefile	1:250,000
Mexico – Cuernavaca	Servicio Geológico Mexicano (1998d)	Shapefile	1:250,000
Mexico – Culiacan	Servicio Geológico Mexicano (1999d)	Shapefile	1:250,000
Mexico – Durango	Servicio Geológico Mexicano (1998e)	Shapefile	1:250,000
Mexico – El porvenir	Servicio Geológico Mexicano, http://mapasims.sgm.gob.mx/CartasDisponibles/, accessed March 2016	Shapefile	1:250,000
Mexico – El Salto	Servicio Geológico Mexicano (2000f)	Shapefile	1:250,000
Mexico – Ensenada	Servicio Geológico Mexicano (2003d)	Shapefile	1:250,000
Mexico – Escuinapa	Servicio Geológico Mexicano (1999e)	Shapefile	1:250,000
Mexico – Felipe Carrillo Puerto	Servicio Geológico Mexicano (2006d)	Shapefile	1:250,000
Mexico – Fresnillo	Servicio Geológico Mexicano (1998f)	Shapefile	1:250,000
Mexico – Frontera	Servicio Geológico Mexicano (2004c)	Shapefile	1:250,000
Mexico – Guachochi	Servicio Geológico Mexicano (1999f)	Shapefile	1:250,000
Mexico – Guadalajara	Servicio Geológico Mexicano (2000g)	Shapefile	1:250,000
Mexico – Guanajuato	Servicio Geológico Mexicano (1997c)	Shapefile	1:250,000
Mexico – Guaymas	Servicio Geológico Mexicano (2002d)	Shapefile	1:250,000
Mexico – Guerrero Negro	Servicio Geológico Mexicano (1997d)	Shapefile	1:250,000
Mexico – Hermosillo	Servicio Geológico Mexicano (1999g)	Shapefile	1:250,000
Mexico – Hidalgo Del Parral	Servicio Geológico Mexicano (2000h)	Shapefile	1:250,000
Mexico – Huatabampo	Servicio Geológico Mexicano (2000i)	Shapefile	1:250,000
Mexico – Huixtla	Servicio Geológico Mexicano (2005e)	Shapefile	1:250,000
Mexico – Isla Ángel de la Guarda	Servicio Geológico Mexicano (2002e)	Shapefile	1:250,000
Mexico – Isla Cedros	Servicio Geológico Mexicano (2002f)	Shapefile	1:250,000
Mexico – Isla Cerralvo	Servicio Geológico Mexicano, http://mapasims.sgm.gob.mx/CartasDisponibles/, accessed March 2016	Shapefile	1:250,000
Mexico – Isla San Esteban	Servicio Geológico Mexicano (1998g)	Shapefile	1:250,000

Mexico – Islas Marías	Servicio Geológico Mexicano, http://mapasims.sgm.gob.mx/CartasDisponibles/, accessed March 2016	Shapefile	1:250,000
Mexico – Juan Aldama	Servicio Geológico Mexicano (1999h)	Shapefile	1:250,000
Mexico – Juchitán	Servicio Geológico Mexicano (2000j)	Shapefile	1:250,000
Mexico – La Paz	Servicio Geológico Mexicano (1999i)	Shapefile	1:250,000
Mexico – Las Margaritas	Servicio Geológico Mexicano (2006e)	Shapefile	1:250,000
Mexico – Lázaro Cárdenas	Servicio Geológico Mexicano (2002g)	Shapefile	1:250,000
Mexico – Lazarosouth	Servicio Geológico Mexicano, http://mapasims.sgm.gob.mx/CartasDisponibles/, accessed March 2016	Shapefile	1:250,000
Mexico – Linares	Servicio Geológico Mexicano (2004d)	Shapefile	1:250,000
Mexico – Loreto	Servicio Geológico Mexicano (2002h)	Shapefile	1:250,000
Mexico – Los Mochis	Servicio Geológico Mexicano (1997e)	Shapefile	1:250,000
Mexico – Los Vidrios	Servicio Geológico Mexicano (2002i)	Shapefile	1:250,000
Mexico – Madera	Servicio Geológico Mexicano (1999j)	Shapefile	1:250,000
Mexico – Manuel Benavides	Servicio Geológico Mexicano (2003e)	Shapefile	1:250,000
Mexico – Matamoros	Servicio Geológico Mexicano (2004e)	Shapefile	1:250,000
Mexico – Matehuala	Servicio Geológico Mexicano (1996)	Shapefile	1:250,000
Mexico – Manzanillo	Servicio Geológico Mexicano (2000k)	Shapefile	1:250,000
Mexico – Mazatlán	Servicio Geológico Mexicano (1999k)	Shapefile	1:250,000
Mexico – Mérida	Servicio Geológico Mexicano (2006f)	Shapefile	1:250,000
Mexico – Mexicali	Servicio Geológico Mexicano (2003f)	Shapefile	1:250,000
Mexico – Minatitlán	Servicio Geológico Mexicano (2000l)	Shapefile	1:250,000
Mexico – Monclova	Servicio Geológico Mexicano (1998h)	Shapefile	1:250,000
Mexico – Monterrey	Servicio Geológico Mexicano (2000m)	Shapefile	1:250,000
Mexico – Morelia	Servicio Geológico Mexicano (1998i)	Shapefile	1:250,000
Mexico – Nacozari	Servicio Geológico Mexicano (1998j)	Shapefile	1:250,000
Mexico – Nueva Casas Grandes	Servicio Geológico Mexicano (2002j)	Shapefile	1:250,000
Mexico – Nogales	Servicio Geológico Mexicano (2000n)	Shapefile	1:250,000
Mexico – Nueva Rosita	Servicio Geológico Mexicano (2000o)	Shapefile	1:250,000
Mexico – Nuevo Laredo	Servicio Geológico Mexicano (2004f)	Shapefile	1:250,000
Mexico – Oaxaca	Servicio Geológico Mexicano (2000p)	Shapefile	1:250,000

Mexico – Ocampo	Servicio Geológico Mexicano (2000q)	Shapefile	1:250,000
Mexico – Ojinaga	Servicio Geológico Mexicano (2003g)	Shapefile	1:250,000
Mexico – Orizaba	Servicio Geológico Mexicano (2001)	Shapefile	1:250,000
Mexico – Pachuca	Servicio Geológico Mexicano (1997f)	Shapefile	1:250,000
Mexico – Pericos	Servicio Geológico Mexicano (1999l)	Shapefile	1:250,000
Mexico – Piedras Negras	Servicio Geológico Mexicano (2003h)	Shapefile	1:250,000
Mexico – Poza Rica	Servicio Geológico Mexicano (2004g)	Shapefile	1:250,000
Mexico – Puerto Escondido	Servicio Geológico Mexicano (2002k)	Shapefile	1:250,000
Mexico – Puerto Peñasco	Servicio Geológico Mexicano (2002l)	Shapefile	1:250,000
Mexico – Puerto Vallarta	Servicio Geológico Mexicano (1999m)	Shapefile	1:250,000
Mexico – Punta San Antonio	Servicio Geológico Mexicano (2002m)	Shapefile	1:250,000
Mexico – Queretaro	Servicio Geológico Mexicano (1999n)	Shapefile	1:250,000
Mexico – Reynosa	Servicio Geológico Mexicano (2004h)	Shapefile	1:250,000
Mexico – Río Bravo	Servicio Geológico Mexicano (2004i)	Shapefile	1:250,000
Mexico – San Antonio del Bravo	Servicio Geológico Mexicano (2003i)	Shapefile	1:250,000
Mexico – San Felipe	Servicio Geológico Mexicano (1999o)	Shapefile	1:250,000
Mexico – San Isidro	Servicio Geológico Mexicano (1998k)	Shapefile	1:250,000
Mexico – San José del Cabo	Servicio Geológico Mexicano (2002n)	Shapefile	1:250,000
Mexico – San Juanito	Servicio Geológico Mexicano (2000r)	Shapefile	1:250,000
Mexico – San LuisPotosí	Servicio Geológico Mexicano (1998l)	Shapefile	1:250,000
Mexico – San Miguel	Servicio Geológico Mexicano (2003j)	Shapefile	1:250,000
Mexico – Santa Rosalía	Servicio Geológico Mexicano (1997g)	Shapefile	1:250,000
Mexico – Santiago Papasquiaro	Servicio Geológico Mexicano (2000s)	Shapefile	1:250,000
Mexico – Sierralibre	Servicio Geológico Mexicano (2000t)	Shapefile	1:250,000
Mexico – Tamiahua	Servicio Geológico Mexicano (2004j)	Shapefile	1:250,000
Mexico – Tampico	Servicio Geológico Mexicano (2004k)	Shapefile	1:250,000
Mexico – Tapachula	Servicio Geológico Mexicano (2005f)	Shapefile	1:250,000
Mexico – Tecoripa	Servicio Geológico Mexicano (2000u)	Shapefile	1:250,000
Mexico – Tenosique	Servicio Geológico Mexicano (2006g)	Shapefile	1:250,000
Mexico – Tepic	Servicio Geológico Mexicano (1998m)	Shapefile	1:250,000
Mexico – Tijuana	Servicio Geológico Mexicano (2003k)	Shapefile	1:250,000

Mexico – Tizimín	Servicio Geológico Mexicano (2006h)	Shapefile	1:250,000
Mexico – Tlahualilo de Zaragoza	Servicio Geológico Mexicano (1998n)	Shapefile	1:250,000
Mexico – Torreón	Servicio Geológico Mexicano (2000v)	Shapefile	1:250,000
Mexico – Tuxtla Gutiérrez	Servicio Geológico Mexicano (2005g)	Shapefile	1:250,000
Mexico – Veracruz	Servicio Geológico Mexicano (2002o)	Shapefile	1:250,000
Mexico – Villa Constitución	Servicio Geológico Mexicano (2000w)	Shapefile	1:250,000
Mexico – Villahermosa	Servicio Geológico Mexicano (2005h)	Shapefile	1:250,000
Mexico – Zaachila	Servicio Geológico Mexicano (2000x)	Shapefile	1:250,000
Mexico – Zacatecas	Servicio Geológico Mexicano (1997h)	Shapefile	1:250,000
Mexico – Zihuatanejo	Servicio Geológico Mexicano (1999p)	Shapefile	1:250,000
Guatemala y el Caribe	French and Schenk (2004)	Shapefile	1:2,500,000
Colombia	Gomez Tapias et al. (2015)	Shapefile	1:1,000,000
Venezuela	Garrity et al. (2006)	Shapefile	1:750,000
Guyana, Suriname, Trinidad and Tobago	GLiM; Schobbenhaus and Bellizia (2001)	Shapefile	1:5,000,000
Ecuador	GLiM; Ortega et al. (1982)	Shapefile	1:1,000,000
Peru	GLiM; Instituto de Geologia y Mineria (1975)	Shapefile	1:1,000,000
Uruguay	GLiM; Dirección Nacional de Minería y Geología (1985)	Shapefile	1:500,000
Paraguay	GLiM; González (2000)	Shapefile	1:2,500,000
Chile	GLiM; Servicio Nacional de Geología y Minería (2004)	Shapefile	1:1,000,000
Brazil – Aracajú, Araguaia, Asunción, Belém, Belo Horizonte, Boa Vista, Brasilia, Campo Grande, Contamana, Corumbá, Cuiabá, Curitiba, Fortaleza, Goiânia, Goiás, Guaporé, Ica, Iguapé, Jaguaribe, Javari, Juruá, Juruena, Lago Amirim, Macapaindio, Manaus, Natal, Paranapanema, Pico Da Neblina, Porto Alegre, Porto Velho, Purus, Recife, Rio Branco, Rio de Janeiro, Rio Doce, Rio São Francisco, Salvador, Santarém, São Luis, Tapajós, Teresina, Tocantins, Tumucumaque, Uruguaiana, Vitória	Serviço Geológico do Brasil - CPRM (2014)	Shapefile	1:1,000,000
Bolivia	GeoBolivia (2000)	Shapefile	1:1,000,000

Argentina	GLiM; Servicio Geologico Minero Argentino (1997)	Shapefile	1:2,500,000
Burundi	Food and Agriculture Organization of the United Nations et al. (2003a)	Shapefile	1:350,000
Congo	van Engelen et al. (2006)	Shapefile	1:2,000,000
Kenya	Dijkshoorn (2007)	Shapefile	1:1,000,000
Malawi	Dijkshoorn et al. (2016)	Shapefile	1:1,000,000
Rwanda	Food and Agriculture Organization of the United Nations et al. (2003b)	Shapefile	1:350,000
Senegal, Gambia	Dijkshoorn and Huting (2014)	Shapefile	1:1,000,000
Southern Africa	Dijkshoorn and van Engelen (2003)	Shapefile	1:2,000,000
Tanzania	Geological Survey of Tanzania, Geo-Economic Data (1:2M) – Geology http://www.gmis-tanzania.com/, accessed May 2016	Shapefile	1:2,000,000
Ethiopia	Tefera et al. (1996)	PDF	1:2,000,000
Tunisia	Dijkshoorn and Huting (2009)	Shapefile	1:1,000,000
Afrique du nord	Alimen et al. (1973)	Paper map	1:2,500,000
Sahara Occidental	Alimen et al. (1978b)	Paper map	1:2,500,000
Sahara Central	Alimen et al. (1978a)	Paper map	1:2,500,000
Africa	U.S. Geological Survey/The Nature Conservancy (2009)	Raster file	1:5,000,000
Peat in Congo	Dargie et al. (2017)	Raster file	50m
Loess in Africa	Crouvi et al. (2010)	PDF	Not known
Australia	Raymond et al. (2012)	Shapefile	1:1,000,000
New Zealand	GLiM; New Zealand Geological Survey (1972)	Shapefile	1:1,000,000
New Zealand – Loess	Landcare Research NZ Ltd (2010)	Shapefile	1:50,000
Antarctica	GLiM	Shapefile	1:10,000,000
Bangladesh	GLiM; Persits et al. (2001)	Shapefile	1:1,000,000
Cambodia	GLiM; Coordinating Committee for Geoscience Programmes in East and Southeast Asia (2004)	Shapefile	1:2,000,000
Philippines	GLiM; Coordinating Committee for Geoscience Programmes in East and Southeast Asia (2004)	Shapefile	1:2,000,000

Indonesia	GLiM; Geological Survey Institute of Indonesia (1993)	Shapefile	1:1,000,000
Papua New Guiney	GLiM; Coordinating Committee for Geoscience Programmes in East and Southeast Asia (2004)	Shapefile	1:2,000,000
Solomon Islands	GLiM; Steinshouer et al. (1999) and Turner (1978)	Shapefile	1:5,000,000 1:100,000
Fiji	GLiM; Colley (1976)	Shapefile	1:250,000
Australia	GLiM; Whitaker et al. (2007)	Shapefile	1:1,000,000
	GLiM; Raymond et al. (2007c)		
	GLiM; Raymond et al. (2007b)		
	GLiM; Raymond et al. (2007a)		
	GLiM; Whitaker et al. (2008)		
	GLiM; Stewart et al. (2008)		
	GLiM; Liu et al. (2006)		
Vanuatu	GLiM; Mollock (1974)	Shapefile	1:1,000,000
New Caledonia	GLiM; Direction de l'Industrie des Mines et de l'Energie (DIMENC) (1981)	Shapefile	1:200,000
Brunei	GLiM; Coordinating Committee for Geoscience Programmes in East and Southeast Asia (2004)	Shapefile	1:2,000,000
Laos	GLiM; Coordinating Committee for Geoscience Programmes in East and Southeast Asia (2004)	Shapefile	1:2,000,000
Malaysia	GLiM; Coordinating Committee for Geoscience Programmes in East and Southeast Asia (2004)	Shapefile	1:2,000,000
Myanmar	GLiM; Coordinating Committee for Geoscience Programmes in East and Southeast Asia (2004)	Shapefile	1:2,000,000
Thailand	GLiM; Coordinating Committee for Geoscience Programmes in East and Southeast Asia (2004)	Shapefile	1:2,000,000
Vietnam	GLiM; Coordinating Committee for Geoscience Programmes in East and Southeast Asia (2004)	Shapefile	1:2,000,000
Afghanistan	Doebrich et al. (2006)	Shapefile	1:500,000

Arabian Peninsula	GLiM; Pollastro et al. (1997)	Shapefile	1:4,500,000
Arabian Peninsula – Loess	Crouvi et al. (2010)	PDF	Not known
China	China Geological Survey (2002)	Shapefile	1:2,500,000
Himalaya	GLiM; Geological Survey of India (2005)	Shapefile	1:1,000,000
India	GLiM; Dasgupta and Chakravorty (1998)	Shapefile	1:2,000,000
Iran	Pollastro et al. (1999)	Shapefile	1:2,500,000
Japan	Geological Survey of Japan AIST (ed.) (2009), https://gbank.gsj.jp/seamless/download/downloadIndex_e.html, accessed May 2016	Shapefile	1:200,000
Mongolia	GLiM; Steinshouer et al. (1999)	Shapefile	1:5,000,000
Nepal, Bhutan	GLiM; Wandrey and Law (1998)	Shapefile	1:10,000,000
Pakistan	Maldonado et al. (2011)	Shapefile	1:250,000
Pakistan	GLiM; Haghipour and Saidi (2010)	Shapefile	1:5,000,000
Sri Lanka	GLiM; Economic and Social Commission for Asia and the Pacific (1989)	Shapefile	1:1,000,000
Turkey	GLiM; Institute of Mineral Research and Exploration (1961)	Shapefile	1:500,000
Russia	Zastrozhnov et al. (2014)	PNG	1:2,500,000
Soviet Union (former)	GLiM; Karpinsky (1983)	Shapefile	1:2,500,000
Kazakhstan – M41/42, M40/41, N40/41, N43/44, L39/40, L38/39, L43/44, L44/45, M44/45, M38/39	карта четвертичных образований, http://webmapget.vsegei.ru/index.html, accessed June 2017	WMS	1:1,000,000
Kazakhstan/Usbekistan – L40/41, K41/42	карта четвертичных образований, http://webmapget.vsegei.ru/index.html, accessed June 2017	WMS	1:1,000,000
Kazakhstan/Usbekistan/Turkmenistan – K39/40	карта четвертичных образований, http://webmapget.vsegei.ru/index.html, accessed June 2017	WMS	1:1,000,000
Usbekistan/Turkmenistan – K40/41	карта четвертичных образований, http://webmapget.vsegei.ru/index.html, accessed June 2017	WMS	1:1,000,000
Kazakhstan/ Kyrgyzstan – K43/44	карта четвертичных образований, http://webmapget.vsegei.ru/index.html, accessed June 2017	WMS	1:1,000,000
Kazakhstan/ Kyrgyzstan /Usbekistan/Tajikistan – K42/43	карта четвертичных образований, http://webmapget.vsegei.ru/index.html, accessed June 2017	WMS	1:1,000,000

Usbekistan/Turkmenistan/Tajikistan – J41/42	карта четвертичных образований, http://webmapget.vsegei.ru/index.html, accessed June 2017	WMS	1:1,000,000
Tajikistan – J42/43	карта четвертичных образований, http://webmapget.vsegei.ru/index.html, accessed June 2017	WMS	1:1,000,000
Finland	Geologian tutkimuskeskus (2013)	Shapefile	1:1,000,000
Great Britain	British Geological Survey (2008)	Shapefile	1:625,000
Ireland	Meehan (2013)	Shapefile	1:25,000
Norway	Norges geologiske undersøkelse (2016)	Shapefile	1:250,000
Sweden	Geological Survey of Sweden (2014)	Shapefile	1:1,000,000
Austria	Geologische Bundesanstalt (GBA) (2013) and GLiM; Egger et al. (1999)	Shapefile	1:500,000 1:1,500,000
Belgium	GLiM; One Geology Europe Consortium (Surface geological maps of Europe, 2010, available at http://www.onegeology-europe.org/, accessed 17 January 2011) (hereinafter referred to as One Geology Europe Consortium 2010)	Shapefile	1:1,000,000
Czech Republic	GLiM; One Geology Europe Consortium 2010	Shapefile	1:1,000,000
Denmark	GLiM; One Geology Europe Consortium 2010	Shapefile	1:1,000,000
France	Lacquement et al. (2009)	PDF	1:1,000,000
Germany	Bundesanstalt für Geowissenschaften und Rohstoffe (2007)	Shapefile	1:200,000
Hungary	GLiM; One Geology Europe Consortium 2010	Shapefile	1:1,000,000
Italy	GLiM; One Geology Europe Consortium 2010	Shapefile	1:1,000,000
Luxembourg	GLiM; One Geology Europe Consortium 2010	Shapefile	1:1,000,000
Netherlands	GLiM; One Geology Europe Consortium 2010	Shapefile	1:1,000,000
Poland	GLiM; One Geology Europe Consortium 2010	Shapefile	1:1,000,000
Portugal	GLiM; One Geology Europe Consortium 2010	Shapefile	1:1,000,000

Slovak Republic	GLiM; One Geology Europe Consortium 2010	Shapefile	1:1,000,000
Slovenia	GLiM; One Geology Europe Consortium 2010	Shapefile	1:1,000,000
Spain	Instituto Geológico y Minero de España (1988)	Shapefile	1:1,000,000
Switzerland	GLiM; Bundesamt für Landestopografie (2005)	Shapefile	1:500,000
European Loess Map	Haase et al. (2007)	Raster	1:2,500,000
Albania	Ministria E Energjise dhe Industrise Sherbimi Gjeologjik Shqiptar (2014), https://geoportal.asig.gov.al, accessed February 2017	WMS-Server	1:100,000
Bosnia and Herzegovina	Tokic (1986)	Tiff	1:1,500,000
Bulgaria	Cheshitev et al. (1989)	JPG	1:500,000
Serbia	Kalenic et al. (2015)	PDF	1:300,000
Balkan	GliM; Pawlewicz et al. (1997)	Shapefile	1:5,000,000
Estonia	GLiM; One Geology Europe Consortium 2010	Shapefile	1:1,000,000
Lithuania/Belarus – N34/35	карта четвертичных образований, http://webmapget.vsegei.ru/index.html, accessed June 2017	WMS	1:1,000,000
Moldova/Ukraine – L35/36	карта четвертичных образований, http://webmapget.vsegei.ru/index.html, accessed June 2017	WMS	1:1,000,000
Ukraine/Moldova/Belarus – M35/36	карта четвертичных образований, http://webmapget.vsegei.ru/index.html, accessed June 2017	WMS	1:1,000,000
Belarus/Ukraine – N35/36	карта четвертичных образований, http://webmapget.vsegei.ru/index.html, accessed June 2017	WMS	1:1,000,000
Ukraine – L36/37	карта четвертичных образований, http://webmapget.vsegei.ru/index.html, accessed June 2017	WMS	1:1,000,000
Latvia	Krasnov et al. (1971)	Tiff	1:2,500,000

A.4 Geographical Combination Methods

In order to transform the diverse formats of the original maps into maps of a specified format they needed to be homogenized. Most of the maps could be directly downloaded in a digital format via websites of geological surveys. Often, those data were already in a shapefile format and could be directly read in into ArcMap.

Since the workflow of map processing is dependent of the original format (provided in Tab. A.2), the different data transformations are described and can be seen in Fig. 1.

1. Paper maps were scanned as pixel images at a resolution of 280 DPI (e.g. Northern Africa). Literature studies were also part of the data compilation method. Some pictures with loess distributions were taken from scientific papers and georeferenced for further processing in ArcMap.

2. Using ArcMap the pixel image maps were transformed into shapefiles by digitizing the individual polygons.

3. Some maps were only available on WMS servers. These maps needed to be digitized due to a lack of feature information.

4. For the dataset of the Russian territory shapefiles were obtained with SAGA GIS (Conrad et al., 2015). Based on RGB codes of the individual units and running a majority filter (4x) it was possible to vectorize the grid classes to derive a shapefile. Erroneous white spaces due to structural geological features and map annotations that were also classified, were removed by the ArcMap tool "Euclidean Allocation".

5. For the Peoria loess (Kohfeld and Muhs, 2001), an Excel file with coordinates and point information was transformed into a raster file and then to a shapefile with ArcMap.

6. Collected shapefiles were imported into an ESRI file geodatabase and transformed to the Eckert IV projection.

In some cases the geometry of some maps had to be repaired because of "self-intersections" within the map. This was done by the "Repair geometry" tool in ArcMap (e.g., surficial lithology of Africa).

If maps still covered information on bedrock, these parts were deleted, as well as residual deposits. Some maps contained polygons that were covered by ocean (e.g., Canada, Sweden or Venezuela) or showed state territory of neighboring countries. These polygons were deleted manually from the maps if appropriate.

Due to the fact that not all maps provided data on water bodies or glaciated areas, all water bodies, ice, and glacier areas were taken from the GLiM (Hartmann and Moosdorf, 2012) and merged with the GUM.

The attribute tables of the original maps were then joined with the reclassified sediment descriptions (see section A.2) and merged to state-wide and regional/continental shapefiles.

In cases of overlapping polygons, the parts of minor priority were deleted, favoring *i*) loess areas, *ii*) polygons with more detailed sediment description and *iii*) higher resolution data. The erase order within a country (several input datasets per country) and a detailed description of regional data source handling is given below.

Alaska

For Alaska two input files were used; the State Surficial Geological Map and additional digitized data by Muhs and Budahn (2006). Where no loess data (*El* or *Er*) in the State Surficial Geological Map was available, the data by Muhs and Budahn (2006) was used.

USA

If no loess data (*El*) in the surface geological map were available, the loess (*El*) was taken out from the regional maps and merged with the surface geological map. The same was done for the loess derivates (*Er*) and the loess-like silt deposits (*Ea*). Where data was overlapping, the first order priority was "*El*", second "*Er*" and third "*Ea*". The Palouse loess distribution (*El*) was only considered where no El-information of the surface geological map and the regional maps were available. Since the loess data from the Snake River and Palouse were digitized manually it was considered as (*Er*). These loess patterns were only included where no other loess data (*El*, *Ea*, *Er*) was available.

North America (Alaska, Canada, USA) and Greenland

For the finalization of the North American map several other processing steps needed to be done. Since there was an *Er* occurrence in the Alaskan map within the Canadian territory, this polygon was erased from the Alaskan map and merged into the Canadian map. In some regions at the Canadian-American border the Canadian sediment information was more detailed. Only if the USA map had no loess occurrence the Canadian sediments information was included into the American map. Finally Greenland was merged to the North American map.

Mexico

The Mexican map had to be translated into English and was compiled from 120 individual shapefiles.

Central America (Mexico and Guatemala y el Caribe)

The Mexican map was preferred over the Guatemala y el Caribe map.

Colombia, Uruguay, Paraguay, Chile, Brasil, Bolivia, Argentina

These maps had to be translated to English.

South America (Colombia, Venezuela, Guyana/Suriname/Trinidad and Tobago, Bolivia, Ecuador, Peru, Chile, Argentina, Uruguay, Brazil, Paraguay)

The maps were merged with following priority: Brazil, Uruguay/Chile/Colombia, Ecuador/Argentina, Bolivia/Paraguay, Peru/Guyana/Suriname/Trinidad and Tobago/Venezuela.

Africa (Burundi, Congo, Kenya, Malawi, Rwanda, Senegal/Gambia, Southern Africa, Tanzania, Ethiopia, Tunisia, Northern Africa (1,2,3), Loess in Africa, African Surficial Lithology, Peat in Congo)

For the African continent, several maps had to be digitized (Ethiopia, Northern Africa 1,2,3; Loess in Africa). In case of overlapping areas after merging, the data of the more detailed map were kept. The digitized loess areas (Namibia, West Africa, Tunisia/Libya and Nigeria) were merged with the African map, as well as the peat data set for the Congo basin. The African Surficial Lithology map is kept as background data where no other data were available. The order of priority while merging Africa: Peat/Loess, Tunisia/Senegal_Gambia/Ethiopia, Kenya/Northern Africa 1, Rwanda/Northern Africa 2, Burundi/Northern Africa 3, Congo, Malawi, Tanzania, Southern Africa, African Surficial Lithology Map.

New Zealand

In case of New Zealand two different input files were used; the geological map derived from the GLiM and data of the New Zealand soil bureau. Loess was only classified where "Lo" is on top. Remaining symbology was classified as loess derivates, a mixture of loess and other material (see table A.3).

Table A.3: Example of the classification of loess classes of the NZ soil bureau.

ROCK	TOPROCK	BASEROCK	*XX*
(Al+Lo)/St1	St1	St1	*Er*
Al/Lo	Al	Lo	*Er*
Al+(Lo)	Al	Al	*Er*
Al+Lo	Al	Al	*Er*
Al+Lo/Gr	Al	Al	*Er*
Lo/Al+Vo	Lo	Al	*El*
Lo+Tb	Lo	Lo	*Er*

Where no loess information in the GLiM map for New Zealand was given, the loess polygons of the New Zealand soil bureau were implemented.

Aus/NZ/Antarctica (Australia, New Zealand, Antarctica)

These files were merged without bordering conflicts.

Southeast Asia (Bangladesh, Cambodia, Australasia, Laos, Myanmar, Thailand, Vietnam)

In case of overlapping areas following merge order was used: Australasia/Bangladesh/Myanmar, Laos, Vietnam, Cambodia, Thailand, Malaysia.

Arabian Peninsula

For the Arabian Peninsula two datasets were available; the map derived from the GLiM and additional literature data about loess deposits in Yemen, Israel and UAE. These loess patterns were merged into the GLiM map of the Arabian Peninsula.

China

The Quaternary Geological Map of China was only available in Chinese language and no symbol explanation could be found. Therefore, the units were re-interpreted from the individual polygon descriptions. Where no clear sediment type could be identified, the unit was defined as "Us" (sediments, undifferentiated). In addition to the original Quaternary Geological Map of China, three other maps were available: Loess deposits (classified to *El*), loess-like deposits (classified to *Ea*) and deserts of China (classified to *Ed*). These four maps were combined following the priority: 1) Loess deposits, 2) Loess-like deposits, 3) deserts, 4) Quaternary Geological Map of China.

Japan

The Japanese geological map was compiled from 175 different individual maps.

Pakistan

For Pakistan two datasets were available, the map derived by the GliM covering the whole state and a more detailed map showing only a part of Pakistan. Where no information on loess was available, the smaller higher resolution map was merged into the GUM.

Asia (Afghanistan, Arabian Peninsula, China, Himalaya, India, Iran, Japan, Mongolia, Nepal/Bhutan, Pakistan, Sri Lanka, Turkey)

In case of overlapping areas the map with the better classification or better geographic continuity was used, following the priority: China, Mongolia/Japan/Nepal/Bhutan/Afghanistan, Himalaya/Pakistan, India/Sri Lanka/Turkey, Iran, Arabian Peninsula.

Russia

Since the Russian map was too large to be digitized manually in a reasonable timeframe, png-formatted images were downloaded and processed with SAGA GIS (Conrad et al. (2015)). Based on the RGB colors and applying a majority filter (4x) a grid file was created, which was then transformed into a shapefile. Each color grid was given a classification after the original map. Remaining gaps due to technical issues were then filled in ArcMap with the Euclidean Allocation tool.

WMS-files for Central Asia (Kazakhstan, Uzbekistan, Tajikistan, Kyrgyzstan, Turkmenistan)

For Central Asia 11 WMS-files were fully digitized, in 6 files only the loess areas were digitized, leaving room for refinements in the future.

North Asia (Russia, Soviet Union, WMS-files)

The available files had the following priority during the merging process: Russia, M44/45/L43/44/M40/41, M41/42/N40/41/M38/39/L39/40, N43/44/K39/40, K40/41, L40/41, L38/39/J41/42, J42/43, K42/43, K41/42 / K43/44, Soviet Union.

Finland and Norway

The Finnish and Norwegian map had to be translated into English.

Northern Europe (Finland, Great Britain, Ireland, Norway, Sweden)

In case of overlapping areas the map with the better classification or better geographic continuity was used, following the priority: Ireland/Finland, Great Britain/Sweden, Norway.

Austria

The Austrian map consists of three different input datasets; the Geological Map of The Geological Survey of Austria (Geologische Bundesanstalt (GBA), 2013), the GLiM map (Hartmann and Moosdorf, 2012) and the Haase loess map covering Austria (Haase et al., 2007). These maps were merged in the same priority order named above.

France

The French surficial geology map had to be translated into English and digitized manually.

Germany

The German map was compiled from 55 individual maps, which had to be reclassified before merging.

Italy, Slovakia, Slovenia

The loess distribution of the Haase map for Italy (Haase et al., 2007), Slovakia and Slovenia was included into the primary map sources derived from the GLiM.

Spain

The Spanish Quaternary Geological Map had to be translated into English.

Central Europe (Austria, Belgium, Czech Republic, Denmark, France, Germany, Hungary, Italy, Luxembourg, Netherlands, Poland, Portugal, Slovakia, Slovenia, Spain, Switzerland)

In case of overlapping areas the map with the better classification and/or loess information or better geographic continuity was used following the order: Netherlands, Germany, Denmark/Hungary, Poland/Czech Republic, Slovakia, Slovenia, Belgium, Luxembourg, Spain, Portugal/Switzerland, France/Italy, Austria.

Albania

Ten different Albanian geological maps were only available from a WMS server. They were digitized manually and translated into English before merging. Additionally, loess patterns were included from Haase et al. (2007).

Bosnia and Herzegovina

The geological map of quaternary basic types lithofacies of Bosnia and Herzegovina had to be digitized manually and the loess distribution of Haase et al. (2007) was implemented.

Bulgaria

The Bulgarian geological map had to be digitized manually.

Serbia

The Serbian geological map had to be digitized manually. Two *Ea* sections were changed manually to *El* (Slobodan Markovic, pers. comm., 2016) and two polygons of the map of Haase et al. (2007) were inserted (Slobodan Markovic, pers. comm., 2016).

Balkan (Albania, Bosnia and Herzegovina, Bulgaria, Serbia, Romania, Greece, Macedonia, Kosova, Montenegro, Croatia)

In case of overlapping areas the map with the better classification and/or loess information or better geographic continuity was used, following the order: Loess (Haase et al., 2007) for Croatia/Romania/Macedonia/Kosovo/Montenegro, Serbia, Bosnia and Herzegovina/Albania/Bulgaria, Romania/Greece/Macedonia/Montenegro/Kosovo/Croatia.

Latvia.

For Latvia a tiff-format pixel image was digitized.

WMS-files for Lithuania, Belarus, Ukraine and Moldova.

Five WMS-files were digitized.

Eurasia (Belarus, Latvia, Lithuania, Estonia, Moldova, Ukraine)

Order of merging: Estonia/M3536, L3637, Moldova, N3536, Lithuania, Latvia, Soviet Union, Haase_loess.

Merging the world

Following order: North America/South America, Mexico, Caribe, Northern Europe/Central Europe, Balkan, Eurasia, Australia/New Zealand/Antarctica, SE Asia, Asia, Northern Asia, Africa.

Pyroclastic layer

An additional layer of pyroclastics was created considering the unit *Iy* from GUM and a second pyroclastics unit: *Ic* (consolidated or not reported if consolidated or unconsolidated).

"*Ic*" was derived by the GUM input data (Mexico, Caribe y Guatemala, Colombia, Ecuador, Peru, Uruguay, Chile, Tanzania, Ethiopia, New Zealand, Australasia, Afghanistan, Japan, Russia, Czech Republic, Germany, Hungary, Portugal, Spain, Switzerland) and the GLiM (py) (Hartmann and Moosdorf, 2012).

Priority while merging: "*Iy*" from GUM, "*Ic*" from Mexico/Caribe/Colombia/Ecuador/Peru/Uruguay/Chile/Tanzania/Ethiopia/New Zealand/Australasia/Afghanistan/Japan/Russia/Hungary/Portugal/Spain/Switzerland/Germany, Czech Republic, "py" from GLiM.

A.5 Contributors to GUM

Without many helping hands the GUM project could not have been realized. Thank you all for the project support.

Some of the digitizing of the maps was done by students: Rick Warwas (Northern Africa + Ethiopia), Marvin Keitzel (Lithuania), Tom Kiehn (help with Russian map, parts of Tajikistan, Uzbekistan and Turkmenistan). Further technical support was given by Dr. Olaf Conrad (SAGA GIS) (Conrad et al., 2015). Elina Plesca and Oleksandr Bobryshev are thanked for translating text.

Persons who helped with map acquisition are Petar Stejic (Serbia), Joanne Tremblay (Geogratis Canada), Roger Sayre (USGS, Africa), M. Teresa Orozco Cuenca (IGME, Spain), Ulf Wall and Jan-Ake Nilsson (SGU, Sweden), Suada Buric (Bosnia and Herzegovina), Hélène Tissoux (BRGM, France), Jon Engström, Jukka-Pekka Palmu, Hanna Virkki (GTK, Finland), Gaojun Li (China) and Greta Dargie (Peat in Congo Basin).

A number of loess experts helped with consulting and provided data for the map, specifically Slobodan Markovic, Ian Smalley, Kenneth O'Hara-Dhand, Daniel Muhs and Dagmar Haase.

For general consulting we would like to thank Kristine Asch (Bundesanstalt für Geowissenschaften und Rohstoffe), Tom Gleeson (University of Victoria) and Jordan Huscroft (University of Victoria, McGill University).

A.6 Acknowledgements

This work has been has been funded by German Science Foundation (DFG) through the Cluster of Excellence CLISAP2 (DFG Exec177, Universität Hamburg), and PALMOD project BMBF-project PALMOD (Ref 01LP1506C) through the German Ministry of Education and Science (BMBF) as Research for Sustainability initiative (FONA). We thank the editor and the reviewer for commenting on the manuscript and PANGAEA for hosting the GUM database at https://doi.org/10.1594/PANGAEA.884822.

Appendix B: Chemical weathering of loess during the Last Glacial Maximum, the Mid-Holocene and today

B.1 Loess on the shelves

English Channel

Lefort et al. (2013) describe loess deposits on ancient beach deposits, which developed during low stands of the sea in the English Channel. These loess deposits of Upper Pleistocene age have been eroded during transgressional phases.

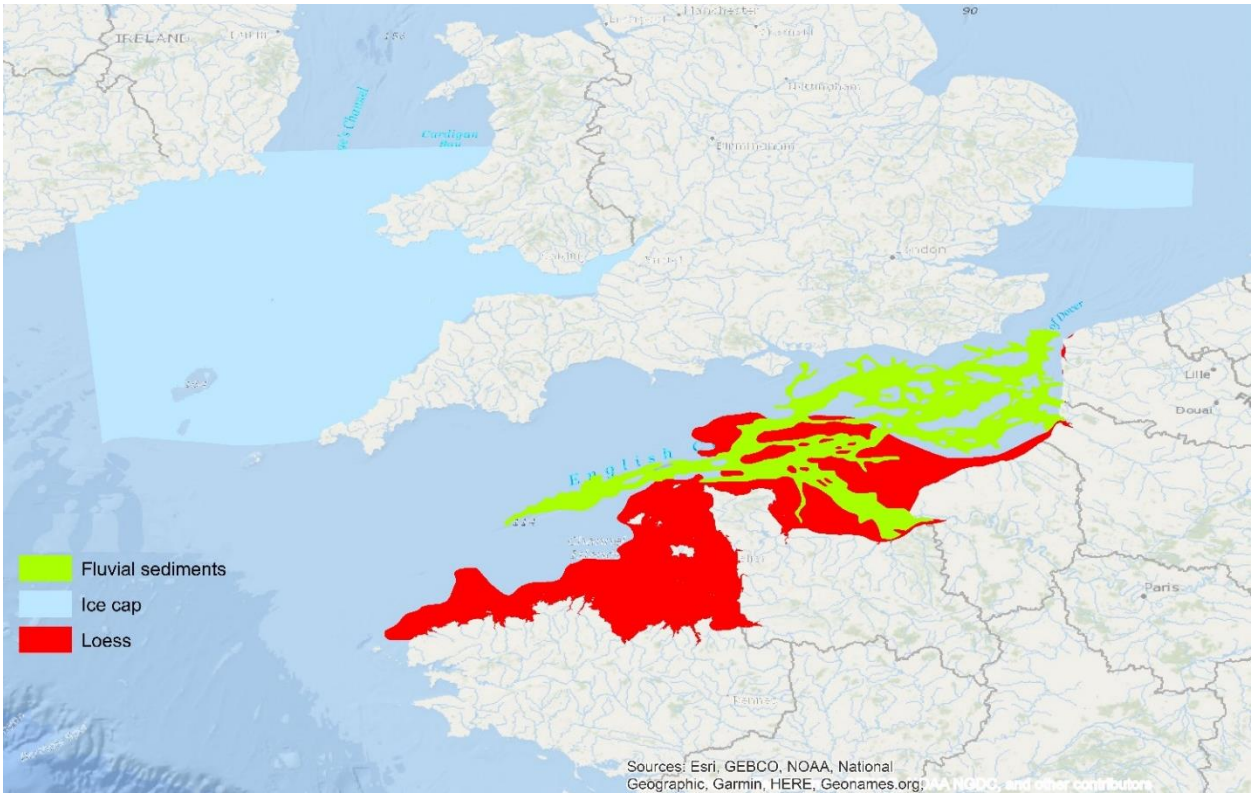

Figure B.1: Loess deposits in the English Channel redrawn after Lefort et al. (2013).

Arctic Shelf

Biryukov et al. (1988) show a set of paleogeographic maps of the Eurasian Arctic Shelf during the last glacial maximum. While the western part is characterized by large areas of glaciation, the eastern part shows an ice-free lowland with tundra character and various different sediments.

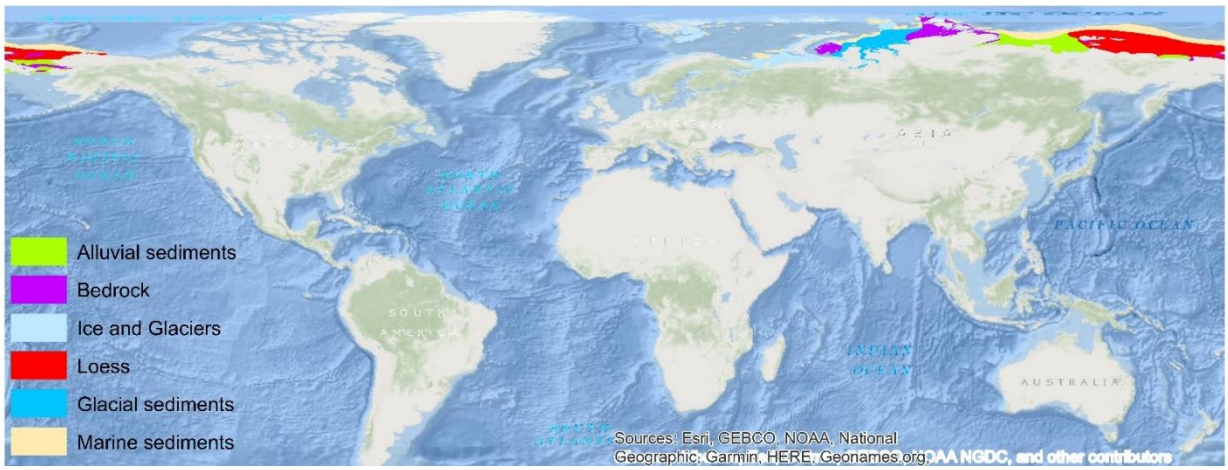

Figure B.2: Paleogeographic distribution of the sediments of the Arctic Shelf redrawn after Biryukov et al. (1988).

Black Sea Shelf

Ryan et al. (1997) provide a map of sediments of the Neoeuxine stage (late Quaternary) on the Black Sea Shelf. Shown lithologies in the map are wind-blown loess, alluvial deposits and an ancient littoral zone.

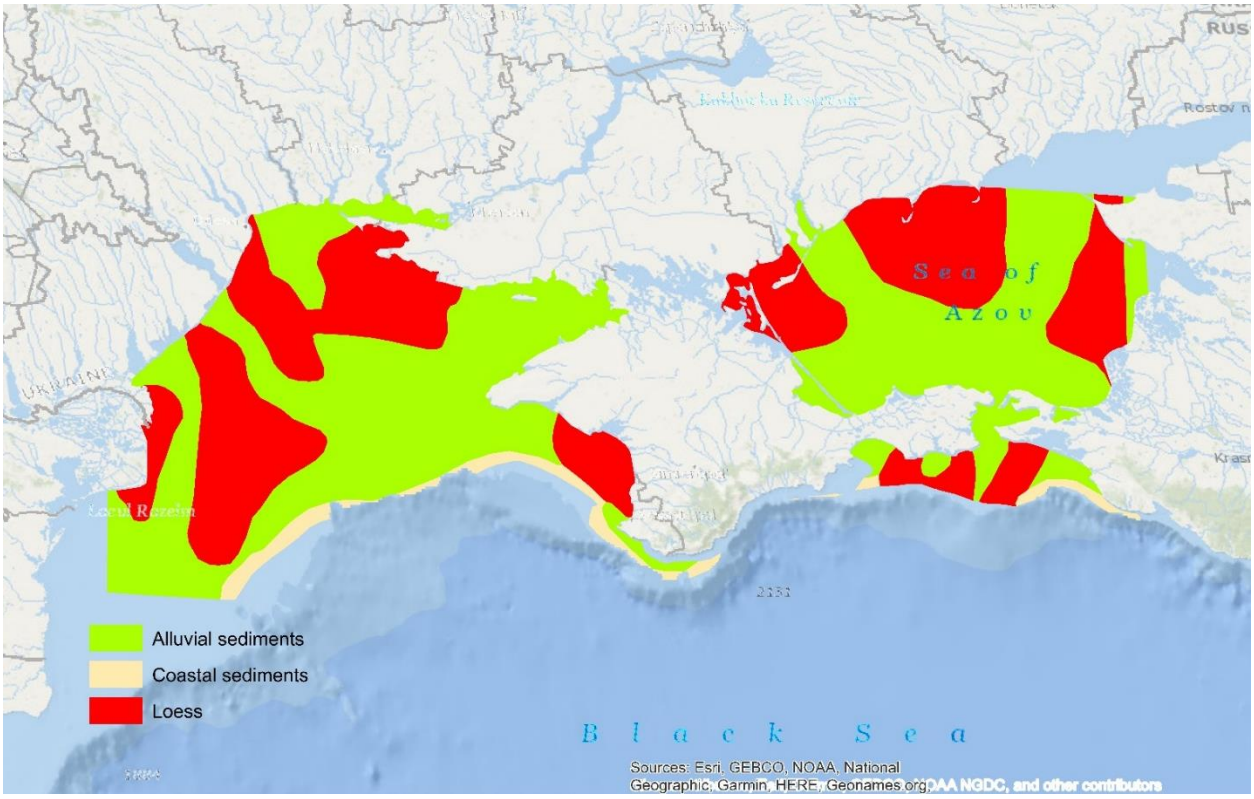

Figure B.3: Redrawn map of Ryan et al. (1997) showing parts of the Black Sea Shelf with its sedimentary deposits.

Argentinian Shelf

For the Argentinian Continental Shelf the lithology for pre-LGM sequences can be described as "Continental (aeolian-lacustrine) semi-consolidated, reddy, browny and yellowish, silty to loessic sediments. Exceptionally littoral sands" (Violante et al., 2014), and were redrawn as loess deposits.

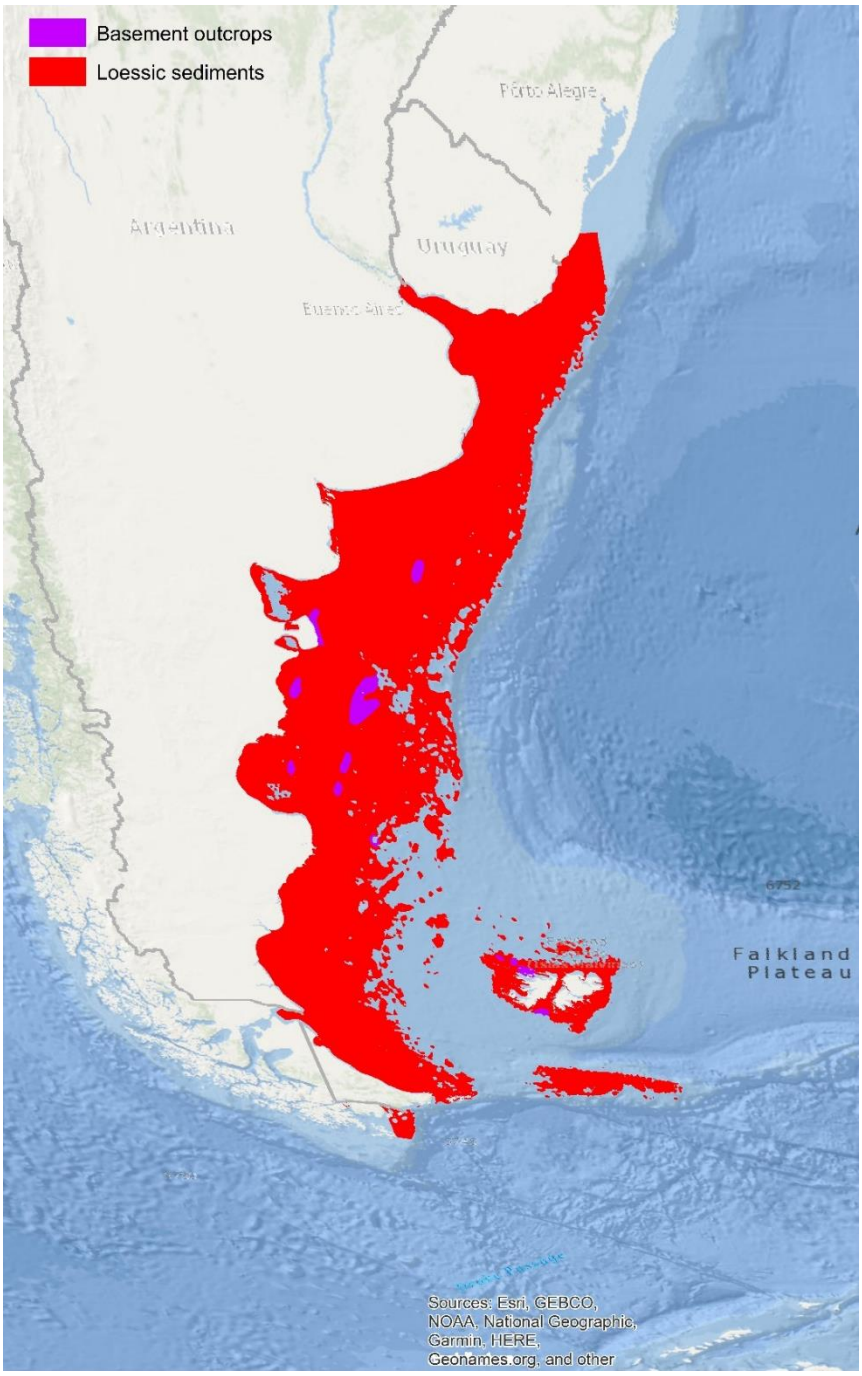

Figure B.4: The Argentinian continental shelf with loess deposits drawn after Violante et al. (2014).

Additional regions

Li et al. (2013) and references therein report on loess deposits in the Atlantic off West Africa, in the north Arabian Sea, the Japan Sea and around the Philippines.

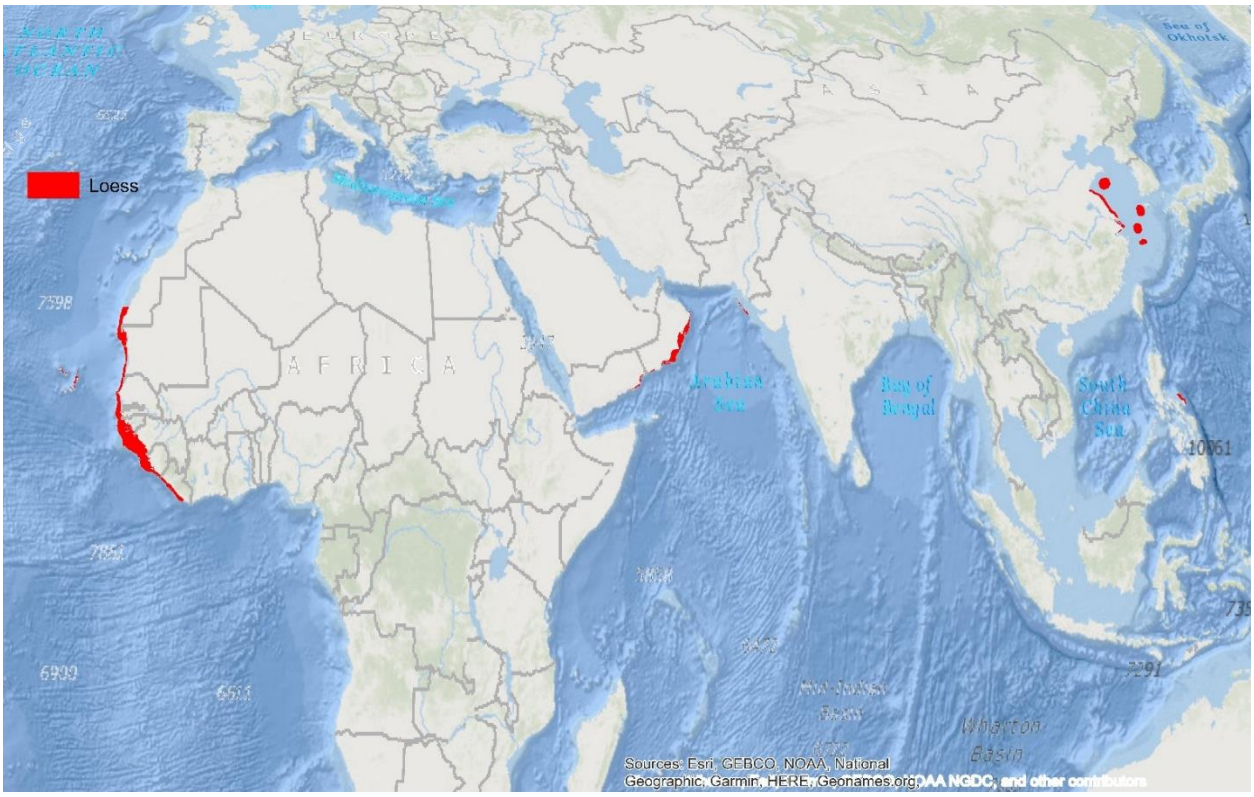

Figure B.5: Loess deposits redrawn after Li et al. (2013).

B.2 Additional figures analyzing loess weathering and the different carbonate weathering models

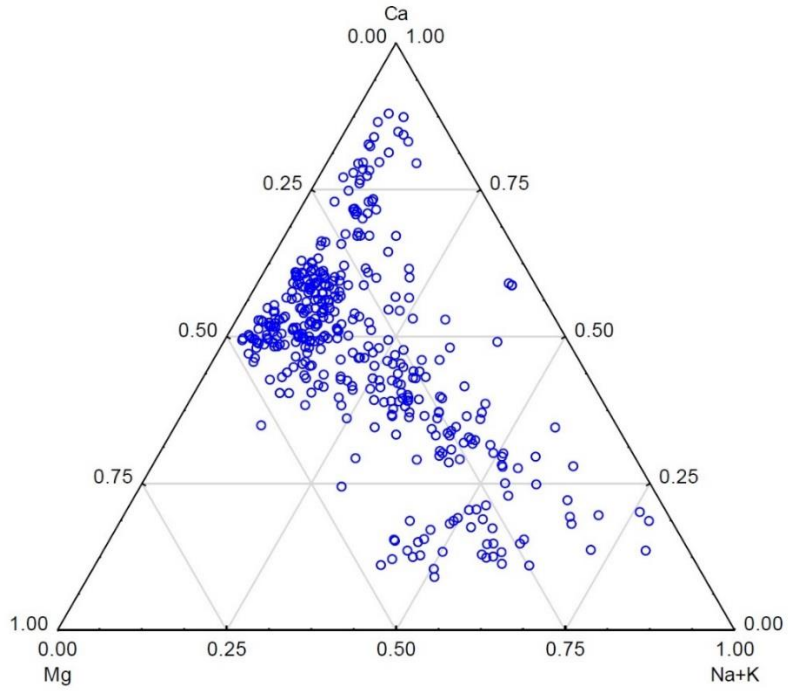

Figure B.6: Ternary plot showing major cations (concentrations in equivalent) for the water samples draining loess deposits (fraction >0.2).

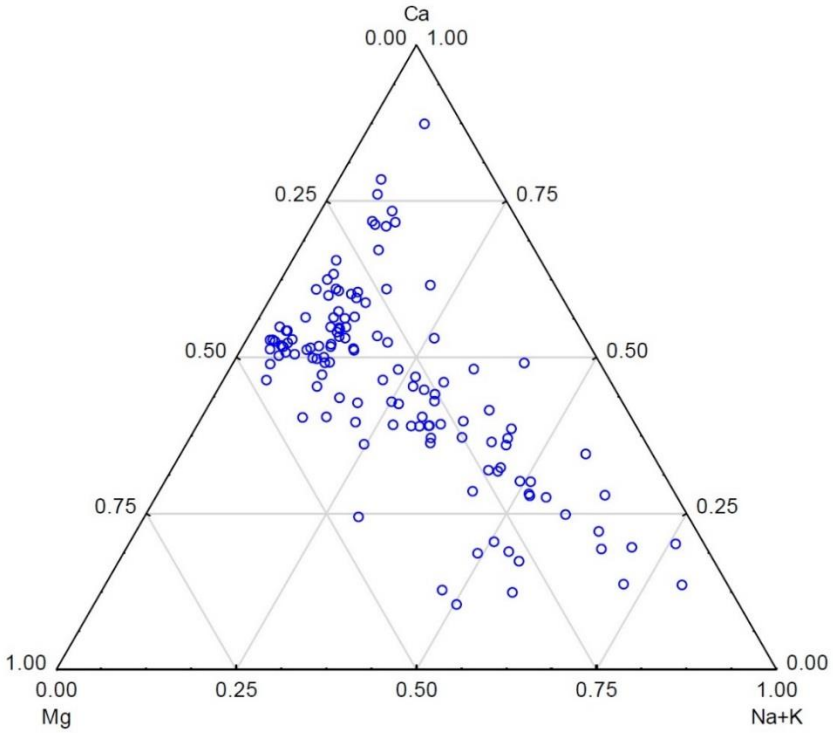

Figure B.7: Ternary plot showing major cations (concentrations in equivalent) for the water samples draining loess deposits (fraction >0.2), excluding carbonate sedimentary rocks below (sc >0.2).

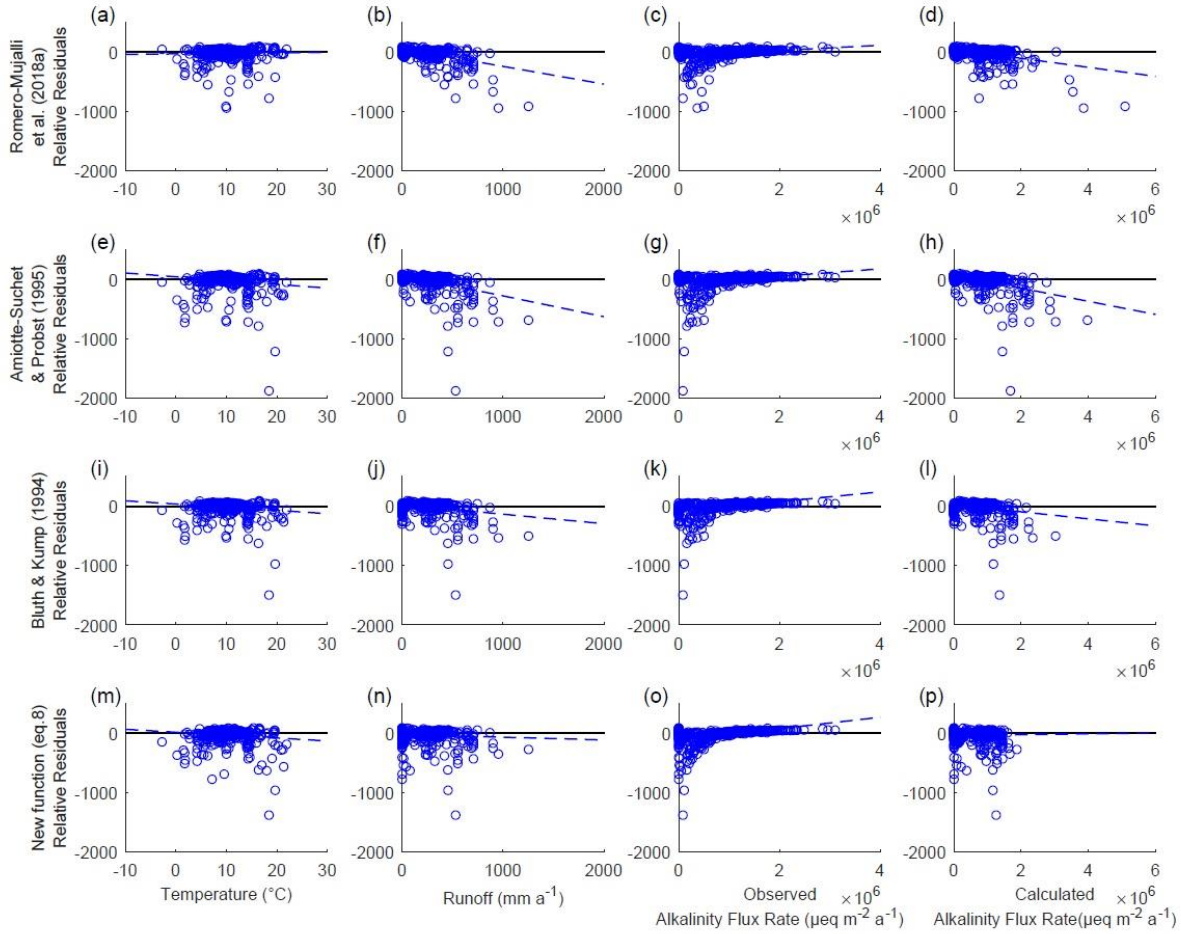

Figure B.8: Relative residual analyses ((observed flux-predicted flux)/observed flux, in %) compared to different variables of the four models for Romero-Mujalli et al. (2018a) (a-d), Amiotte-Suchet and Probst (1995) (e-h), Bluth and Kump (1994) (i-l), and the new function (eq. 8), (m-p). Trendlines are shown in dashed blue.

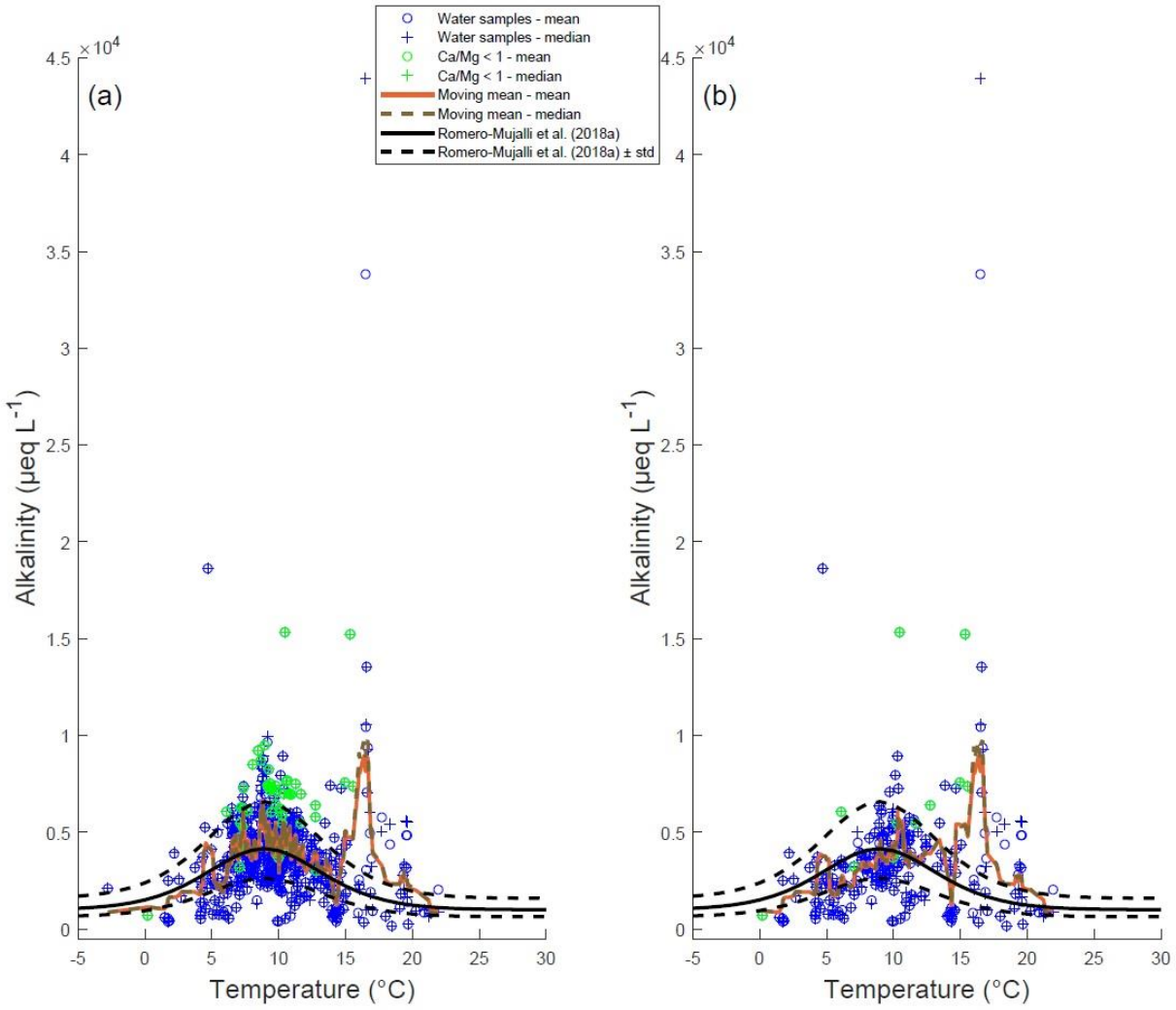

Figure B.9: Alkalinity concentration of river catchments with a loess fraction >0.2, dependent on temperature, showing the differences between mean and median values (a). Carbonate sedimentary rocks as underlying lithology were excluded (sc >0.2) to test their influence on the alkalinity concentrations (b). The solid black line in both plots represents the function for carbonate weathering identified by Romero-Mujalli et al. (2018a) with the range of uncertainty as dashed lines for typical calcite weathering. The green markers indicate water samples with $Ca^{2+}/Mg^{2+}<1$ and shows that outliers are partly because of elevated Mg^{2+} concentrations. Additionally the moving mean values of alkalinity concentration are shown.

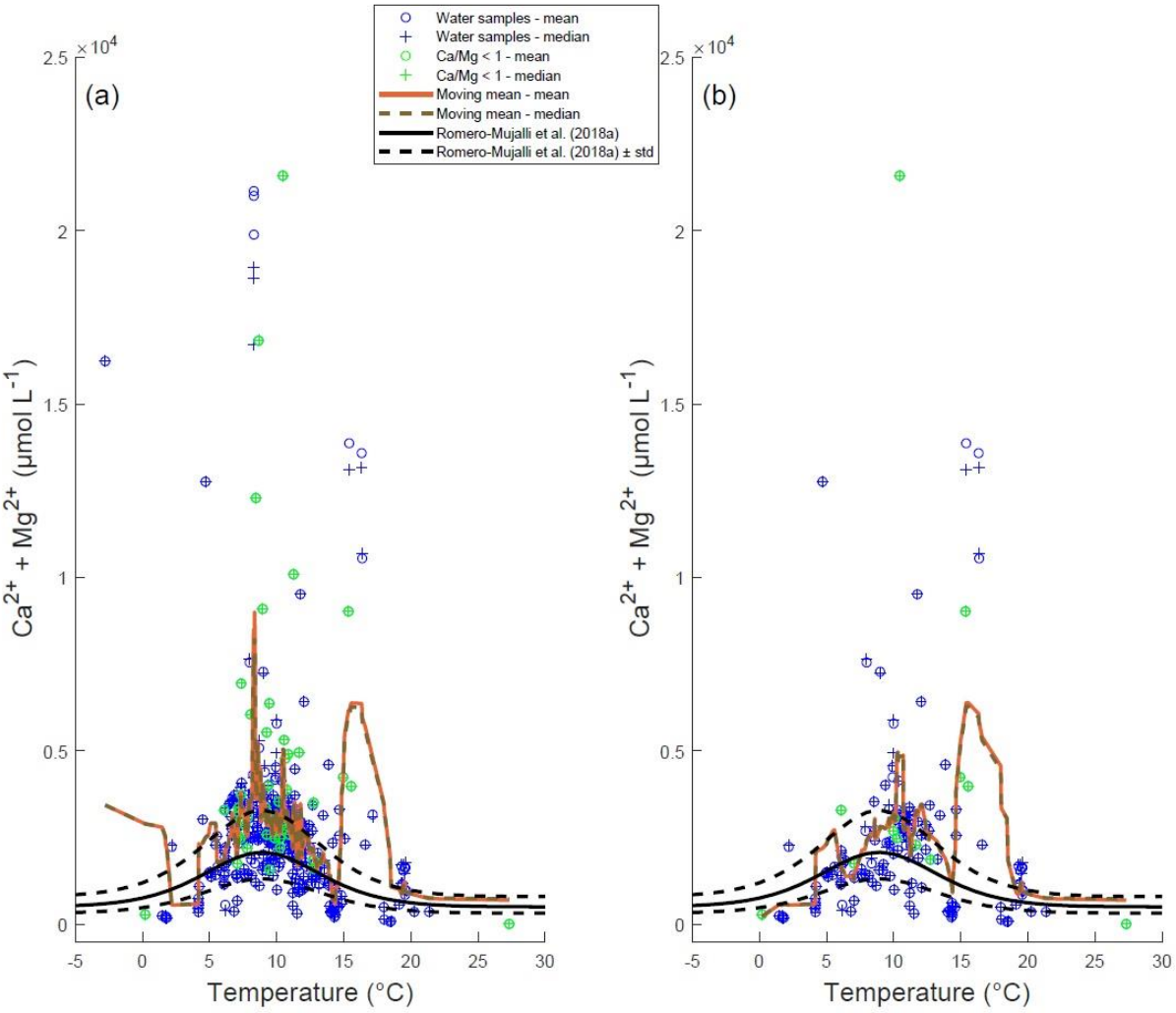

Figure B.10: Ca^{2+}+Mg^{2+} concentration of river catchments with a loess fraction >0.2, dependent on temperature, showing the differences between mean and median values (a). Carbonate sedimentary rocks as underlying lithology were excluded (sc >0.2) to test their influence on the water chemical species (b). The solid black line represents in both plots the function for carbonate weathering identified by Romero-Mujalli et al. (2018a) with the range of uncertainty as dashed lines for typical calcite weathering. The green markers indicate water samples with Ca^{2+}/Mg^{2+}<1. Additionally the moving mean values of the Ca^{2+}+Mg^{2+} concentrations are shown.

B.3 Equations used for the global calculations for all lithologies besides carbonate rocks and loess

The parameters are taken from Hartmann (2009a) and Hartmann et al. (2014b). For the calculation of the CO_2 consumption rates silicate and carbonate weathering are considered (Tab. B.1).

Table B.1: Parameters for the equations for calculating CO_2 consumption rates.

Lithology	Parameter b = b	Proportion on silicate weathering = sp	Activation energy silicates = sa	Proportion on carbonate weathering = cp	Activation energy carbonates = ca	CO_2 consumption of carbonates = 0.5 x bicarbonate = cc
su	0.003364	1	60	0	14	0.5
vb	0.007015	1	50	0	14	0.5
pb	0.007015	1	50	0	14	0.5
py	0.0061	1	46	0	14	0.5
va	0.002455	1	60	0	14	0.5
vi	0.007015	1	50	0	14	0.5
ss	0.005341	0.64	60	0.36	14	0.5
pi	0.007015	0.58	60	0.42	14	0.5
sm	0.012481	0.24	60	0.76	14	0.5
mt	0.007626	0.25	60	0.75	14	0.5
pa	0.005095	0.58	60	0.42	14	0.5

$$CO_2 = q * s * b * \left(sp * e^{\left(\frac{1000*sa}{R}\right)*\left(\left(\frac{1}{284.2}\right)-\left(\frac{1}{T}\right)\right)} + cp * cc * e^{\left(\frac{1000*ca}{R}\right)*\left(\left(\frac{1}{284.2}\right)-\left(\frac{1}{T}\right)\right)} \right) \quad \text{(eq. B.1)}$$

with CO_2 = CO_2 consumption in $g\ C * m^{-2} a^{-1}$

s = soil shield

q = runoff in $kg * a^{-1} * m^{-2}$

R = gas constant in $J * mol^{-1} * K^{-1}$

T = Temperature in Kelvin.

B.4 Data from a laboratory experiment of loess weathering

A loess weathering column experiment was conducted under laboratory conditions to demonstrate the effect of soil-pCO_2 on loess weathering. The loess sample for this experiment was taken from Schwalbenberg, located in Germany (50.561098N, 7.243509E). Two identical loess columns (height: 25cm, diameter: 5.6cm) were watered daily, simulating rain conditions of 11,115 mm/a to achieve maximum weathering rates. One loess column was kept under ambient atmospheric CO_2 conditions (~460 ppm of the laboratory), while the other was kept at CO_2-saturated conditions. In the latter case, the columns head space air was fully CO_2-saturated as well as the water which was used to simulate the rain. This is considered to be the upper boundary for providing reactants of the dissolution due to water CO_2 interaction. 70-80g of the outlet water were manually titrated to obtain alkalinity.

The loess column experiment reveals different results for the CO_2-saturated column and the column under atmospheric pCO_2 conditions. In general, the alkalinity concentrations of the CO_2-saturated column show that the elevated pCO_2 can increase the alkalinity concentrations by a factor of 3 compared to the column under atmospheric conditions, which highlights the importance of soil pCO_2 for weathering. But it also represents the upper and lower boundaries for loess weathering regarding its sensitivity with respect to the CO_2-concentration abundance in soils, which varies with climate (Romero-Mujalli et al., 2018b). The mean alkalinity concentration of the column with atmospheric pCO_2 conditions after 12 days was ~5000 µeq/L, whereas the column with saturated pCO_2 conditions showed a mean alkalinity of ~15,000 µeq/L (Fig. 18a). Since the simulated runoff of the loess experiment is extreme (~11,115 mm/a) the data of the experiment can be used to point to intensive weathering conditions, as data from most loess areas today are from arid to moderately humid areas only.

As they plot in a direct line without points representing dilution, they possibly represent a condition without surface runoff dilution, which, on the other hand, seem to happen at the catchment scale. Some water is not penetrating the soil/loess and is directly flowing at the surface into the river, thus diluting alkalinity concentration in some cases and not representing the optimal upper boundary line.

Appendix C: Aging of basalt volcanic systems and decreasing CO_2 consumption

Appendix C.1 to C.7 describe available information on the used volcanic, basalt dominated areas and the calculation procedures. For the active volcanic fields (AVF) a detailed description of the calculation for the fraction of the Holocene area on the total area is given. Additionally, a description of the newly introduced alkalinity flux scaling law for young active basaltic areas and for the calculation of the global fluxes is provided.

C.1 Summary of data compilation as applied in the main text

Table C.1: Summary of the data of Inactive Volcanic Fields (IVFs) and Active Volcanic Fields (AVFs) used for the analysis in the main text (Li et al., 2016), as well as calculated Holocene fraction and Reactivity R.

No.	Name	Volcanic activity	T (°C)	σ_T	Runoff (mm/yr)	σ_{Runoff}	Alkalinity (μmol/L)	$\sigma_{Alkalinity}$	Alkalinity flux rate (10^6 mol/km^2/yr)	$\sigma_{Alkalinity\ flux\ rate}$	Latitude (°)	Longitude (°)	Holocene fraction (%)	Calculated Reactivity R
1	Massif Central	Inactive	8.70	0.65	406	20	916	46	0.372	0.026	45.7700	2.9600	0	0.96
2	South Africa	Inactive	12.70	1.80	244	55	1728	1078	0.420	0.130	-25.2758	29.6324	0	0.85
3	Karelia	Inactive	-2.00	1.00	285	20	460	41	0.131	0.007	65.0000	31.0000	0	0.64
4	Coastal Deccan	Inactive	25.10	0.50	1690	150	657	17	1.110	0.103	16.9300	73.5100	0	1.07
5	Interior Deccan	Inactive	25.40	0.50	401	48	2839	170	1.138	0.152	21.0000	74.0000	0	1.08
6	Siberian Traps	Inactive	-8.50	0.65	254	25	501	89	0.127	0.019	65.0000	100.0000	0	0.92
7	Mt. Emei	Inactive	6.20	1.00	1350	75	238	23	0.321	0.036	27.4462	103.3255	0	0.96
8	Leiqiong	Inactive	24.00	1.00	797	100	1923	165	1.532	0.233	20.4600	110.1800	0	1.58
9	Nanjing	Inactive	15.20	1.00	330	48	1595	63	0.526	0.079	32.7400	118.3900	0	0.92
10	Xiaoxinganling	Inactive	-1.00	1.00	243	50	1065	132	0.259	0.062	49.0942	128.1704	0	1.19
11	Tumen River	Inactive	-4.00	2.00	273	50	763	50	0.208	0.041	42.5000	128.5000	0	1.15
12	Mudan River	Inactive	3.20	2.00	209	46	977	87	0.204	0.048	43.7500	128.7200	0	0.73
13	Southeast Australia	Inactive	13.00	0.10	74	14	5956	657	0.441	0.097	-38.1883	142.8587	0	0.88
14	Tasmania	Inactive	10.10	0.25	221	30	1704	437	0.377	0.109	-42.1900	146.7600	0	0.89
15	North Island, NZ	Inactive	13.00	2.00	920	161	478	131	0.439	0.143	-38.0000	176.0000	0	0.88
16	Kauai, Hawaii	Inactive	21.58	0.65	1747	539	588	251	1.026	0.303	22.0000	-159.5000	0	1.22
17	Columbia Plateau	Inactive	7.40	2.00	204	191	927	215	0.189	0.060	44.0000	-118.5000	0	0.53
18	Northeast America	Inactive	0.70	2.30	507	129	465	316	0.235	0.075	47.0483	-75.3229	0	0.98
19	Madeira Island	Inactive	13.50	1.50	1065	100	580	43	0.618	0.074	32.8000	-17.0000	0	1.19
20	Easter Island	Active	20.60	1.00	580	100	1306	132	0.757	0.151	-27.1200	-109.3700	3.36	0.96
21	Mt. Cameroon	Active	14.00	2.00	2120	500	2368	110	5.020	1.207	4.0000	9.0000	96.57	9.42

22	Mt. Etna	Active	14.90	0.20	640	80	9286	539	5.943	0.819	37.7514	14.9974	79.56	10.57
23	Virunga	Active	20.80	1.30	1709	380	2646	1757	4.522	2.110	-1.5000	29.5000	47.95	5.64
24	La Réunion	Active	17.00	2.00	1712	652	1243	290	2.127	0.031	-21.1200	55.5400	27.73	3.33
25	Wudalianchi Lake	Active	-1.00	1.00	243	50	1919	190	0.466	0.106	48.7010	126.1411	14.82	2.15
26	Japan	Active	10.99	1.12	1236	64	584	73	0.722	0.107	35.9234	135.3560	8.7	1.62
27	Kamchatka	Active	-3.50	2.00	520	50	854	100	0.444	0.067	55.0000	159.0000	2.28	2.38
28	Taranaki	Active	10.00	3.00	1296	223	667	34	0.864	0.155	-39.3000	174.0000	8	2.06
29	Big Island, Hawaii	Active	15.44	2.00	935	269	951	424	0.889	0.303	19.5000	-155.5000	14.08	1.53
30	High Cascades	Active	6.81	0.47	382	172	776	175	0.296	0.108	45.1924	-121.6844	0.2	0.86
31	Iceland	Active	0.70	0.65	1734	136	498	74	0.864	0.109	65.0000	-18.0000	13.19	3.60
32	São Miguel Island	Active	16.00	1.00	879	50	2331	200	2.047	0.211	37.7700	-25.5000	9.35	3.41
33	Tianchi Lake	Active	-7.30	2.00	291*	100	2445	300	0.711	0.260	42.0000	128.0500	65.34	4.79

*The runoff for Tianchi Lake was recalculated after Fekete et al. (2002).

C.2 New data for active volcanic fields as described in Tab. C.1, in addition to Li et al. (2016)

In the following, all active volcanic provinces used for this study are described. Note, that for all inactive fields a detailed description of the input data can be found in Li et al. (2016), as well as the origin of the temperature, runoff and alkalinity/DIC concentration data for active and inactive volcanic fields. If watersheds are considered for the calculations of the Holocene area, they are based on the locations of the sampling points (see Li et al. (2016)).

For the calculation of the Holocene fraction area for each volcanic field, based on mapped basic volcanic rocks only (e.g., "vb" in the GLiM), we used several time spans. A polygon with an age description of Holocene (0-11.7 ka) was classified as a "Holocene"-area. If a polygon had an age description, which laid in the time interval of 0 to 2.58 Ma, but it was not clearly defined as of Holocene or Pleistocene age, we defined it as "Quaternary" and applied a theoretical Holocene fraction by the ratio of Holocene time span and Quaternary time span. All other polygons with age descriptions older than Holocene and not defined as "Quaternary" were defined as "non-Holocene".

Numbers behind a region indicate the number in the summary table C.1.

Easter Island (No.20)

Easter Island is a volcanic island in the eastern Pacific. Its volcanic nature is related to the Easter Island Hotspot. The geologic map used for this study was digitized after a map of Gioncada et al. (2010) and references therein. The island is composed mostly of hawaiites, mugearites and olivine basalts and it comprises volcanic ages from 3 Ma to recent. The different age classifications and lithologies are listed in the table below. Due to the precise age information the rocks are directly classified into Holocene rocks and non-Holocene rocks. The total basaltic area of the island is 162.27 km^2, the Holocene area 5.45 km^2 and the non-Holocene area 156.82 km^2, resulting in a Holocene area fraction of 3.36%.

Table C.2: Classification of the map data of Easter Island. The first three columns provide the original map data, whereas the column "System/Series" shows our interpretation of the map data.

Name	Description	Age	System/Series
TE1	Terevaka, hawaiites and olivine basalts	0.3-1.9 Ma	non-Holocene
TE2	Terevaka, hawaiites and olivine basalts	0.3-1.9 Ma	non-Holocene
TE3	Terevaka, hawaiites and olivine basalts	0.3-1.9 Ma	non-Holocene
HH2	Anakena, Hiva-Hiva, hawaiites and olivine basalts	0-2,000 a ago	Holocene
RA1	Rano Aroi, hawaiites, olivine basalts and mugearites	0.2 Ma	non-Holocene
RA5	Rano Aroi, hawaiites, olivine basalts and mugearites	0.2 Ma	non-Holocene
RA4	Rano Aroi, hawaiites, olivine basalts and mugearites	0.2 Ma	non-Holocene
RA2	Rano Aroi, hawaiites, olivine basalts and mugearites	0.2 Ma	non-Holocene
RA8	Rano Aroi, hawaiites, olivine basalts and mugearites	0.2 Ma	non-Holocene
RA7	Rano Aroi, hawaiites, olivine basalts and mugearites	0.2 Ma	non-Holocene
RA6	Rano Aroi, hawaiites, olivine basalts and mugearites	0.2 Ma	non-Holocene
RA3	Rano Aroi, hawaiites, olivine basalts and mugearites	0.2 Ma	non-Holocene
HH1	Anakena, Hiva-Hiva, hawaiites and olivine basalts	0-2,000 a ago	Holocene
PO2	Polke, alkali basalts, hawaiites to mugearites	0.61-3 Ma	non-Holocene
PO1	Polke, alkali basalts, hawaiites to mugearites	0.61-3 Ma	non-Holocene
PO5	Polke, alkali basalts, hawaiites to mugearites	0.61-3 Ma	non-Holocene
PO4	Polke, alkali basalts, hawaiites to mugearites	0.61-3 Ma	non-Holocene
TR	Maunga Orito, rhyolite; Maunga Parehe, trachyte	not known	not considered
PO3	Polke, alkali basalts, hawaiites to mugearites	0.61-3 Ma	non-Holocene
RK1	Rano Kau, alkali basalts, hawaiites to benmoreites	0.2-2.5 Ma	non-Holocene
RK2	Rano Kau, alkali basalts, hawaiites to benmoreites	0.2-2.5 Ma	non-Holocene
TA4	Tangaroa, hawaiites, olivine basalts and mugearites	0.2 Ma	non-Holocene
TA1	Tangaroa, hawaiites, olivine basalts and mugearites	0.2 Ma	non-Holocene
TA2	Tangaroa, hawaiites, olivine basalts and mugearites	0.2 Ma	non-Holocene
TA6	Tangaroa, hawaiites, olivine basalts and mugearites	0.2 Ma	non-Holocene
TA3	Tangaroa, hawaiites, olivine basalts and mugearites	0.2 Ma	non-Holocene
TA5	Tangaroa, hawaiites, olivine basalts and mugearites	0.2 Ma	non-Holocene
TA7	Tangaroa, hawaiites, olivine basalts and mugearites	0.2 Ma	non-Holocene

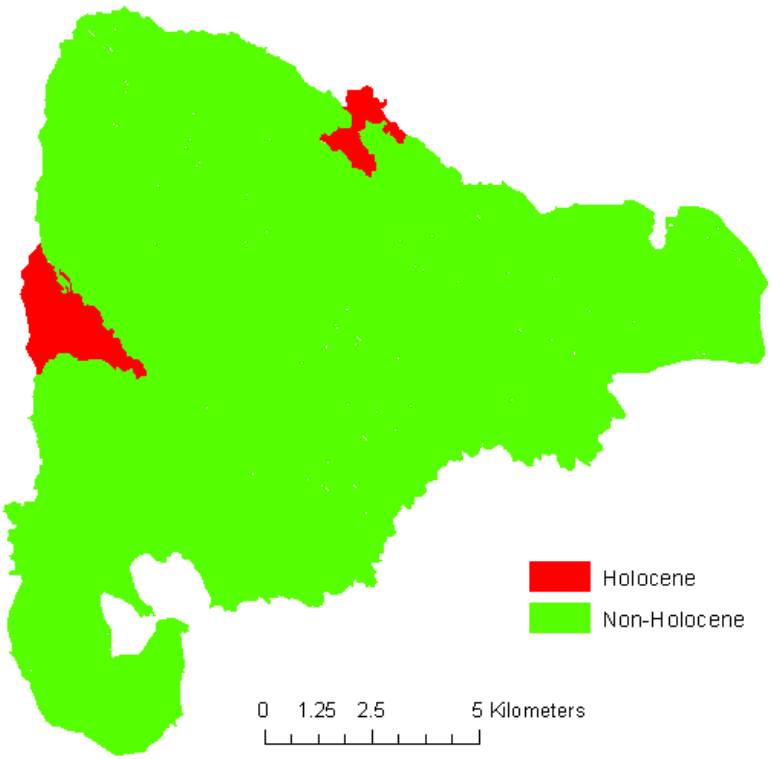

Figure C.1: Map of Easter Island showing the Holocene and non-Holocene areas.

Table C.3: Calculated areas for Easter Island. The Holocene fraction is derived by the ratio of Holocene area/Total area.

Area Holocene (km^2)	**Area Non-Holocene (km^2)**	**Area Quaternary (km^2)**	**Total Area (km^2)**	**Holocene (%)**
5.45	156.82	0	162.27	3.36

Mount Cameroon (No.21)

Mount Cameroon is part of a volcanic chain at the coast of West Africa. The geological map was digitized from Le Maréchal (1975). The location of the sampling points were derived from Benedetti et al. (2003). The age classification (see table below) results in a Holocene fraction of 96.57%.

Table C.4: Classification of the surface ages of Mt. Cameroon. Note that the first three columns display the original map data, the column "System/Series" provides the authors interpretation.

Name	Description	Age	System/Series
beta1	Séries inférieures: basaltes parfois andésitiques sous forme de coulées et de dykes	Oligocene-Eocene	non-Holocene
beta3	Séries supérieures: basaltes parfois andésitiques sous forme de coulées et cinérites	quatenaire récente	Holocene

The interpretation of the ages of Mount Cameroon was difficult, since the ages are not well determined (Ateba et al., 2009). Le Maréchal (1976) describes the ages of the basalts, as well as an unpublished map in Ateba et al. (2009) that shows "young basalts" in the center of Mount Cameroon so that we assumed an age of "recent Quaternary" for "beta3".

Table C.5: Area calculation of Mt. Cameroon. The Holocene fraction is derived by the ratio of Holocene area/Total area.

Area Holocene (km^2)	Area non-Holocene (km^2)	Area Quaternary (km^2)	Total Area (km^2)	Holocene (%)
1,112.63	39.48	0	1,152.11	96.57

Figure C.2: Map of Mount Cameroon showing the Holocene and non-Holocene area.

Mount Etna (No.22)

Mount Etna is located at a subduction zone in Italy. Its geological map was digitized from Branca et al. (2011a) and is described in Branca et al. (2011b). The detailed description of the lithologies is shown below and allows for a classification into Holocene, non-Holocene and Quaternary.

The Quaternary rocks are of an age of 3.9 ka to 15 ka, so that they have a time span of 11.1 ka. 7.8 ka is within the Holocene period (3.9 ka to 11.7 ka) considering the Holocene time period going from 0 to 11.7 ka. The fraction of Holocene coverage was than calculated by:

$$Holocene\ fraction = \frac{Area\ Holocene + \left(Area\ Quaternary * \left(\frac{7.8}{11.1}\right)\right)}{Total\ Area} \quad \text{(eq. C.1)}$$

resulting in a Holocene fraction area of 79.56%.

Table C.6: Classification of Etna basaltic rocks showing the original map data (first four columns) and our interpretation of the data ("System/Series").

Symbol	Name	Description	Age	System/Series
26u	Lava flows, cinder cones and bastions, and fall deposits	basaltic to benmoreitic	122 b.C. – 4 ka	Holocene
27-1	Castings, cinder cones and bastions, and fall deposits	basaltic to mugearitica	1669 - 122 b.C.	Holocene
27-2	Castings, cinder cones and bastions, and fall deposits	basaltic to mugearitica	1971 - 1669	Holocene
27-3	Lava flows, cinder cones and bastions, and fall deposits	basaltic to mugearitica	current - 1971	Holocene
CB26u	Cono e bastione di scorie			Holocene
CB27-1	Cono e bastione di scorie			Holocene
CB27-2	Cono e bastione di scorie			Holocene
CB27-3	Cono e bastione di scorie			Holocene
10a	Intercalated flows in a powerful pyroclastic flow deposit	mugearitica	nn	non-Holocene
14	Succession of alternating flows in pyroclastic deposits	hawaiitica to mugearitica	nn	non-Holocene
15	Flows intercalated with clastic deposits	mugearitica to benmoreitic	nn	non-Holocene
17	Casting interbedded with clastic deposits	benmoreite	nn	non-Holocene
18	Flows	mugearitica-benmoreitic	nn	non-Holocene
18a	Bodies subvulcanici materials come from lavas	mugearitica-benmoreitic	nn	non-Holocene
1a	Bodies subvolcanici		nn	non-Holocene
21b	Porfirichi flows	hawaiitica to mugearitica	nn	non-Holocene
22b	Casting succession	hawaiitica	nn	non-Holocene
24	Of breccia autoclastic often altered to hydrothermalism, associated with lava flows	benmoreitic	nn	non-Holocene
26b	Deposit of debris avalanche monogenic, formed by lava mugearitica blocks	nn	nn	Quaternary
3b	Massive lava flows	basaltic	nn	non-Holocene

1	Underwater transitional composition of volcanics in tholeiitica consist of pillow lavas	tholeiitica	496.1 - 542.2 ka	non-Holocene
10b	Flows intercalated with breccias autoclastic and deposits epiclastici	hawaiitica to mugearitica	101.9ka	non-Holocene
11	Brecce autoclastic and deposits epiclastici	benmoreitic	99.1 - 107.2 ka	non-Holocene
12	Deposits associated with pyroclastic flows	mainly mugearitica	99.9 - 101.8 ka	non-Holocene
13	Castings and slag deposits	hawaiitica	93.0 ka	non-Holocene
14a	Subvulcanici bodies formed by lava massive	mugearitica	85.3 ka	non-Holocene
16	Casting intercalated with thin epiclastici deposits	mugearitica to benmoreitic	85.6 ka	non-Holocene
19	Thin flows to the base, followed by a thick succession pyroclastic	mugeraitica	70.2 - 79.6 ka	non-Holocene
2	Lava flows	tholeiitica	332.4 ka	non-Holocene
20	Fall and pyroclastic flow deposits	hawaiitica to benmoreitic	41.3 - 56.6 ka	non-Holocene
21a	Massive flows and autoclastic interbedded with breccia deposits	hawaiitica to mugearitica	29.1-32.5 ka	non-Holocene
22	Castings, scoria cones and fall deposits	hawaiitica to benmoreitic	28.7-42.1 ka	non-Holocene
25b	Reomorfiche flows	benmoreitic	15.0 - 15.4 ka	non-Holocene
2a	Subvolcanico body structure		320.0 ka	non-Holocene
3a	Strongly altered lava flows	basaltic	180.2 ka	non-Holocene
4a	Massive lava flows	basaltic to mugearitica	129.9 - 154.9 ka	non-Holocene
4b	Thin lava flows	basaltic to mugearitica	134.2 ka	non-Holocene
6	Lave cataclasate	basaltic to mugearitica	128.7 ka	non-Holocene
7	Succession Lava	mugearitica	126.4 ka	non-Holocene
8	Succession lava with thin interbedded deposits epiclastici	hawaiitica to mugearitica	111.9 - 121.2 ka	non-Holocene
9	Lava flows interbedded with massive deposits of local epiclastici	hawaiitica to benmoreitic	105.8 ka	non-Holocene
CB2	Cono e bastione di scorie			non-Holocene
CB22	Cono e bastione di scorie			non-Holocene
CB3a	Cono e bastione di scorie			non-Holocene
CB7	Cono e bastione di scorie			non-Holocene
26l	Lava flows, cinder cones and bastions, and fall deposits	basaltic to benmoreitic	4 - 15ka	Quaternary
CB26l	Cono e bastione di scorie			Quaternary

Table C.7: Table showing the calculated areas for Mount Etna. Note that the Holocene fraction is calculated by the above-mentioned equation considering Holocene area, Quaternary area and total area.

Area Holocene (km^2)	**Area non-Holocene (km^2)**	**Area Quaternary (km^2)**	**Total Area (km^2)**	**Holocene (%)**
636.16	123.90	338.39	1,098.45	79.56

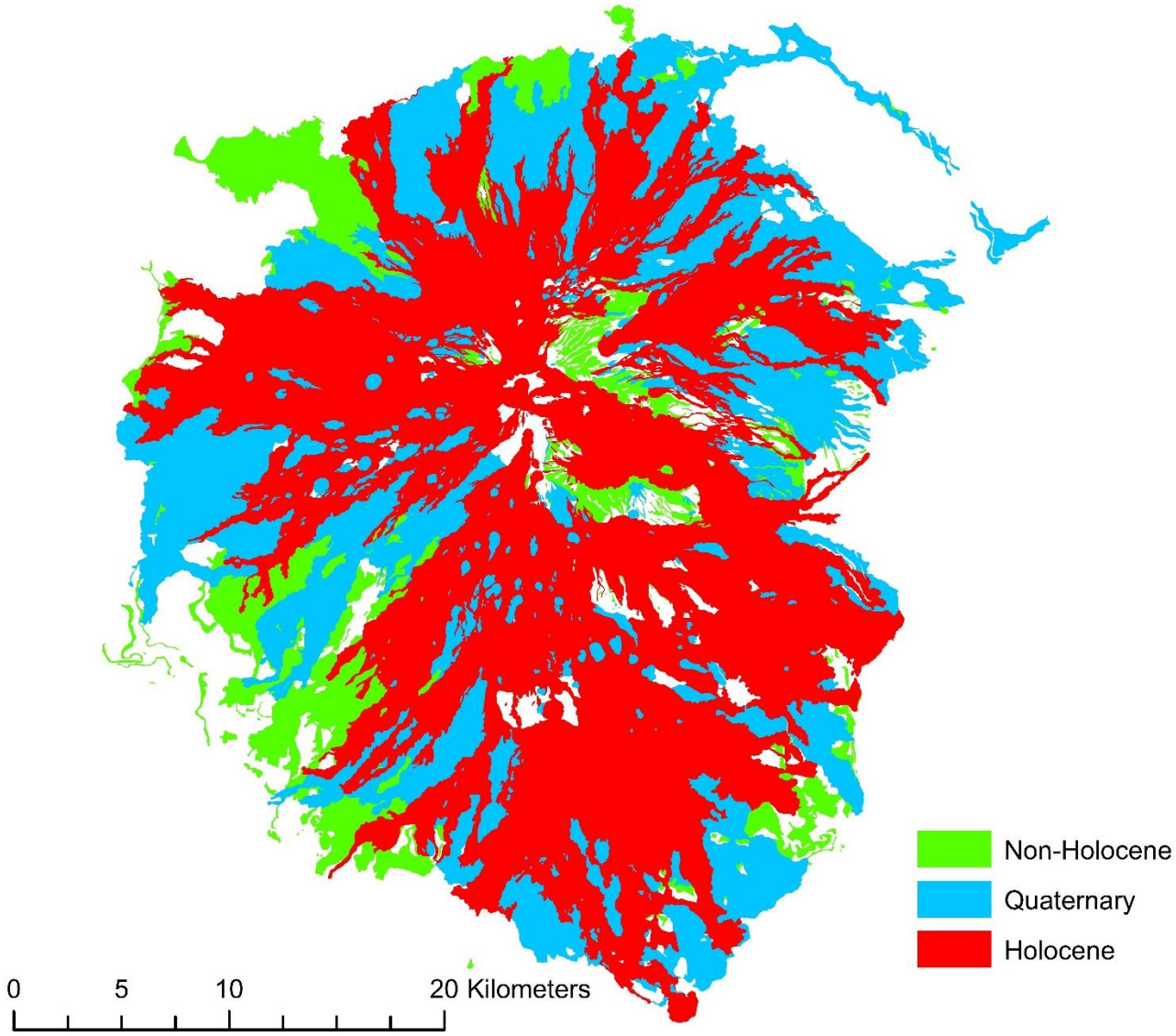

Figure C.3: Map of Etna volcano showing the age distribution of basaltic rocks.

Virunga (No.23)

The Virunga Volcanic province is located in eastern central Africa and is related to the East African Rift system. The geologic map of this area was compiled from four different maps published by Antun et al. (1971), De Mulder et al. (1986), Smets et al. (2010) and Balagizi et al. (2015).

We assume that the volcanic areas of Nyiragongo and Nyamuragira are of Holocene age, since they are classified as Africa's most active volcanoes, and erupted frequently in the past (Balagizi et al., 2015; Smets et al., 2010). The remaining volcanoes are assumed to be of quaternary age (not older than Pleistocene according to Antun et al. (1971)). For the northeastern part of the map the surface age could not be determined clearly, and was therefore defined as "not known", and included in the calculations as "non-Holocene".

Considering that the Quaternary age period ranges from 0 to 2.58 Ma, the Holocene percentage of the Quaternary area is calculated by the ratio of 11,700 a / 2,580,000 a. The total theoretical Holocene areal percentage is 47.95% using:

$$Holocene\ fraction = \frac{Area\ Holocene + \left(Area\ Quaternary * \left(\frac{11{,}700}{2{,}580{,}000}\right)\right)}{Total\ area} \quad \text{(eq. C.2)}$$

Table C.8: Classification of basaltic rocks in the Virunga province showing the individual volcanoes and our interpretation of their age.

Id	Volcano	System/Series
0	Nyiragongo	Holocene
1	Nyamuragira	Holocene
2	Muhabura	Quaternary
3	Gahinga	Quaternary
4	Synabaye	Quaternary
5	Bisoke-Sabinyo	Quaternary
6	Bisoke-Sabinyo	Quaternary
7	Bisoke-Sabinyo	Quaternary
8	Karisimbi	Quaternary
9	Remaining areas	not known

Table C.9: Calculated areas for Virunga province. The Holocene fraction is derived by applying the above-mentioned equation considering the Holocene area, Quaternary area and total area.

Area Holocene (km^2)	Area Non-Holocene (km^2)	Area Quaternary (km^2)	Total Area (km^2)	Holocene (%)
1,518.62	791.26	865.16	3,175.04	47.95

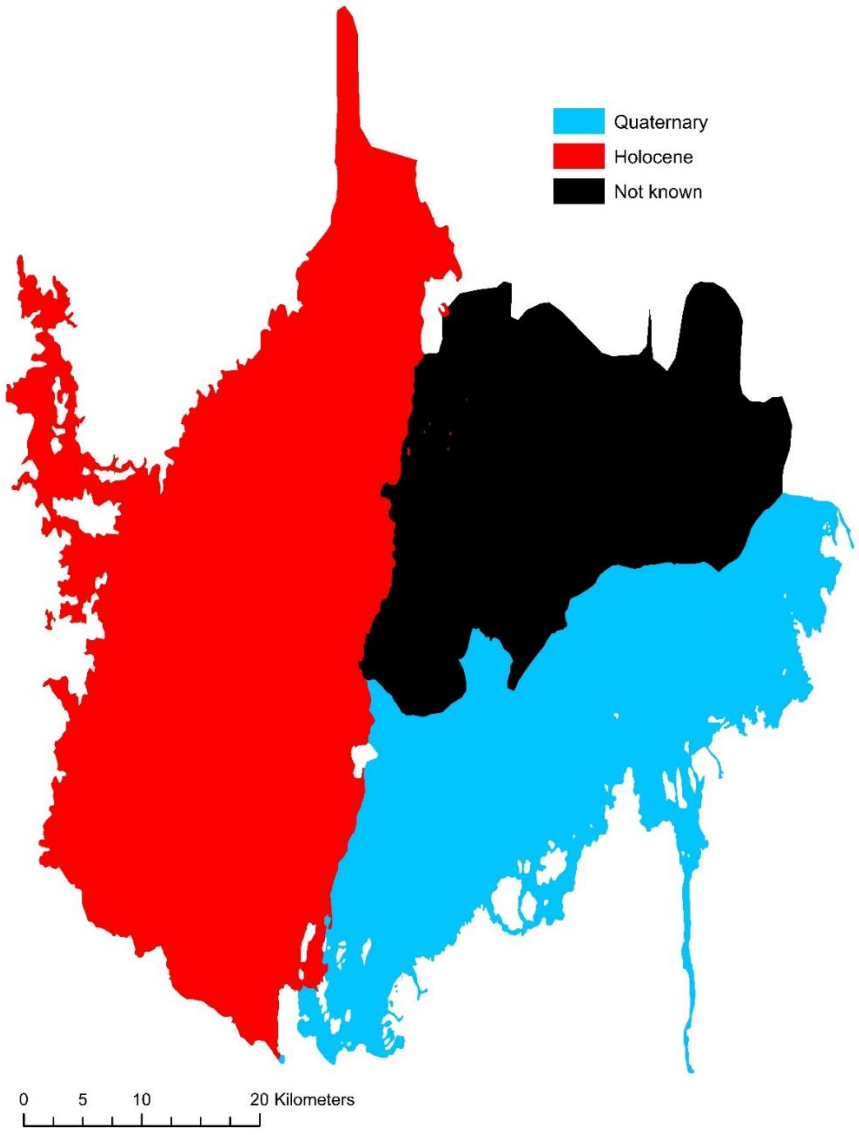

Figure C.4: Map of the Virunga province showing the different areas of basalt classified after age.

La Réunion (No.24)

The volcanic island La Réunion belongs to a Hot Spot in the Indian Ocean and is comprised of Holocene, Quaternary and older volcanic rocks. The geological map was digitized from Nehlig et al. (2006). The watershed area considered for this study is derived from Louvat and Allègre (1997). The rocks are divided into Holocene, non-Holocene and two different types of Quaternary rocks (Qu1, Qu2).

Qu1 is described as being younger than 340 ka, which results in a theoretical Holocene fraction of 11.7 ka / 340 ka.

The age of Qu2 ranges from 5 ka to 65 ka, providing a time span of 60 ka. 6.7 ka lay within the Holocene time span (11.7 ka – 5 ka), so that the Holocene fraction can be calculated by the ratio of 6.7 ka / 60 ka.

Thus, the total Holocene fraction is calculated by:

$$Holocene\ fraction = \frac{\left(Area\ Holocene + \left(Area\ Qu1 * \left(\frac{11.7}{340}\right)\right) + \left(Area\ Qu2 * \left(\frac{6.7}{60}\right)\right)\right)}{Total\ area} \quad \text{(eq. C.3)}$$

providing a value of 28.13%.

Table C.10: Classification of the basaltic rocks of La Réunion with the original data (first three columns) and our interpretation ("System/Series"). Note that "nn" represents that the age of the lithology is not known.

ID	Definition	Type	System/Series
beta4	Coulées basaltiques	Massif du Piton de La Fournaise - Série du bouclier ancien (450,000 à 150,000 ans)	non-Holocene
tfp	Pitons et projections	Massif du Piton de La Fournaise	nn
beta7	Coulées basaltiques	Massif du Piton de La Fournaise - Série de la Plaine des Cafres (65,000 à 5,000 ans)	Quaternary2
beta6	Coulées basaltiques	Massif du Piton de La Fournaise - Série Plaine des Sables (65,000 à 5,000 ans)	Quaternary2
beta8	Coulées basaltiques	Massif du Piton de La Fournaise - Série volcanique subactuelle (<5,000 ans)	Holocene
beta5	Coulées basaltiques	Massif du Piton de La Fournaise - Série des Remparts (150,000 à 65,000 ans)	non-Holocene
beta3	Coulées différencciées	Massif du Piton de La Fournaise - Série alcaline anté-Fournaise (530,000 à 450,000 ans)	not considered
beta8e	Coulées basaltiques dans l'Enclos	Massif du Piton de La Fournaise - Série volcanique subactuelle (<5,000 ans)	Holocene
beta1	Coulées basaltiques à olivine	Massif du Piton des Neiges - Série des océanites (>340,000 ans)	non-Holocene
beta2	Coulées (basalte, hawaites, mugéarites)	Massif du Piton des Neiges - Série différenciée (<340,000 ans)	Quaternary1
Br	Brèches d'avalanches de débris de Saint Gilles	Massif du Piton des Neiges - Série différenciée (<340,000 ans)	Quaternary1
pc	Coulées ignimbritiques	Massif du Piton des Neiges - Série différenciée (<340,000 ans)	Quaternary1

Tau	Coulées trachytiques du plateau de Belouve	Massif du Piton des Neiges - Série différenciée (<340,000 ans)	not considered

Table C.11: Summary of calculated areas of La Réunion. Note that "tfp" is considered as of non-Holocene age. The Holocene fraction is calculated by the above-mentioned equation considering Holocene area, Qu1 area, Qu2 area and the total area.

Area Holocene (km^2)	**Area non-Holocene (km^2)**	**Area Qu1 (km^2)**	**Area Qu2 (km^2)**	**Total Area (km^2)**	**Holocene (%)**
208.11	285.29	157.71	199.37	850.48	27.73

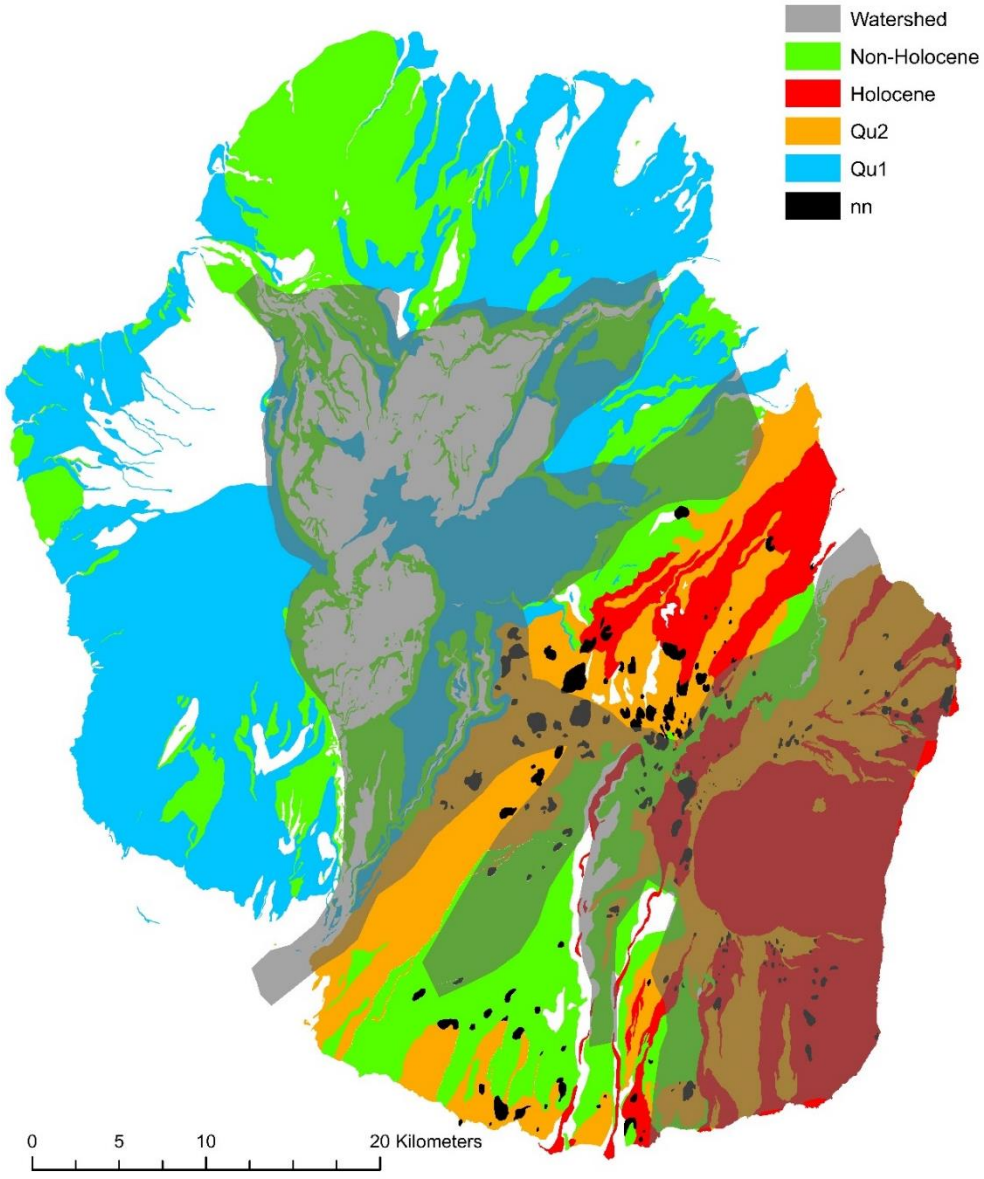

Figure C.5: Map of La Réunion showing the basaltic ages and additionally the watershed of the water samples. Only the watershed area was considered for this study.

Wudalianchi Lake (No.25)

The basaltic rocks of Wudalianchi Lake are located in NE China and are of intraplate volcanic origin. The Geomap of Wudalianchi region was digitized after a map of the Ministry of Land and Resources of PRC, 2003 (unpublished work). The basalts are of Holocene and non-Holocene age. The Holocene fraction is 14.82%.

Table C.12: Classification of basalts of Wudalianchi Lake with the original map data (first three columns) and our interpretation shown in the column "System/Series".

Symbol	Litho	Age	System/Series
betaQ2w	basalt	Middle Pleistocene	non-Holocene
betaQ1j	basalt	Lower Pleistocene	non-Holocene
betaQ2b	basalt	Middle Pleistocene	non-Holocene
betaQ1g	basalt	Tertiary	non-Holocene
betaQ42l	basalt	Holocene	Holocene

Table C.13: Calculated areas of Wudalianchi Lake. The Holocene fraction is calculated by Holocene area/Total area.

Area Holocene (km^2)	Area non-Holocene (km^2)	Area Quaternary (km^2)	Total Area (km^2)	Holocene (%)
69.68	400.35	0	470.03	14.82

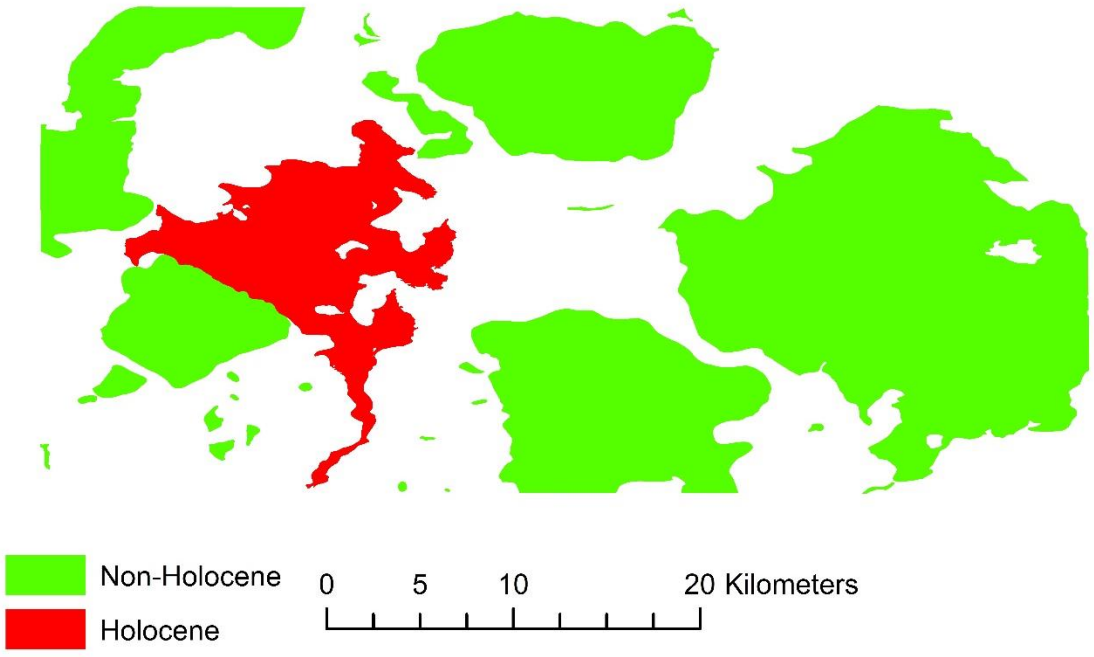

Figure C.6: Map of Wudalianchi Lake showing the distribution of Holocene and non-Holocene basaltic rocks.

Japan (No.26)

The geological data was taken from the Global Lithological Map (GLiM) by Hartmann and Moosdorf (2012). Only watersheds of sample locations from the GLORICH database (Hartmann et al., 2014a) were used. The basaltic rocks (attribute xx = 'vb' in the GLiM) are classified into Holocene, non-Holocene and Quaternary rocks. The calculation procedure of the Holocene fraction of Quaternary rocks is the same as for the Virunga Province (No.23), and a final Holocene percentage of 8.70% is calculated.

Table C.14: Classification of basaltic rocks for Japan after the GLiM (first three columns) and our interpretation "System/Series".

xx	Age_Min	Age_Max	System/Series
vb	Holocene	Holocene	Holocene
vb	Neogene	Neogene	non-Holocene
vb	Paleogene	Paleogene	non-Holocene
vb	Paleozoic	Proterozoic	non-Holocene
vb	Pleistocene	Pleistocene	non-Holocene
vb	Pliocene	Pliocene	non-Holocene
vb	Quaternary	Quaternary	Quaternary

Table C.15: Calculated areas for the basaltic watersheds in Japan. Note that the Holocene fraction is calculated considering Holocene area, Quaternary area and total area.

Area Holocene (km^2)	Area non-Holocene (km^2)	Area Quaternary (km^2)	Total Area (km^2)	Holocene (%)
243.30	2,216.41	354.44	2,814.15	8.70

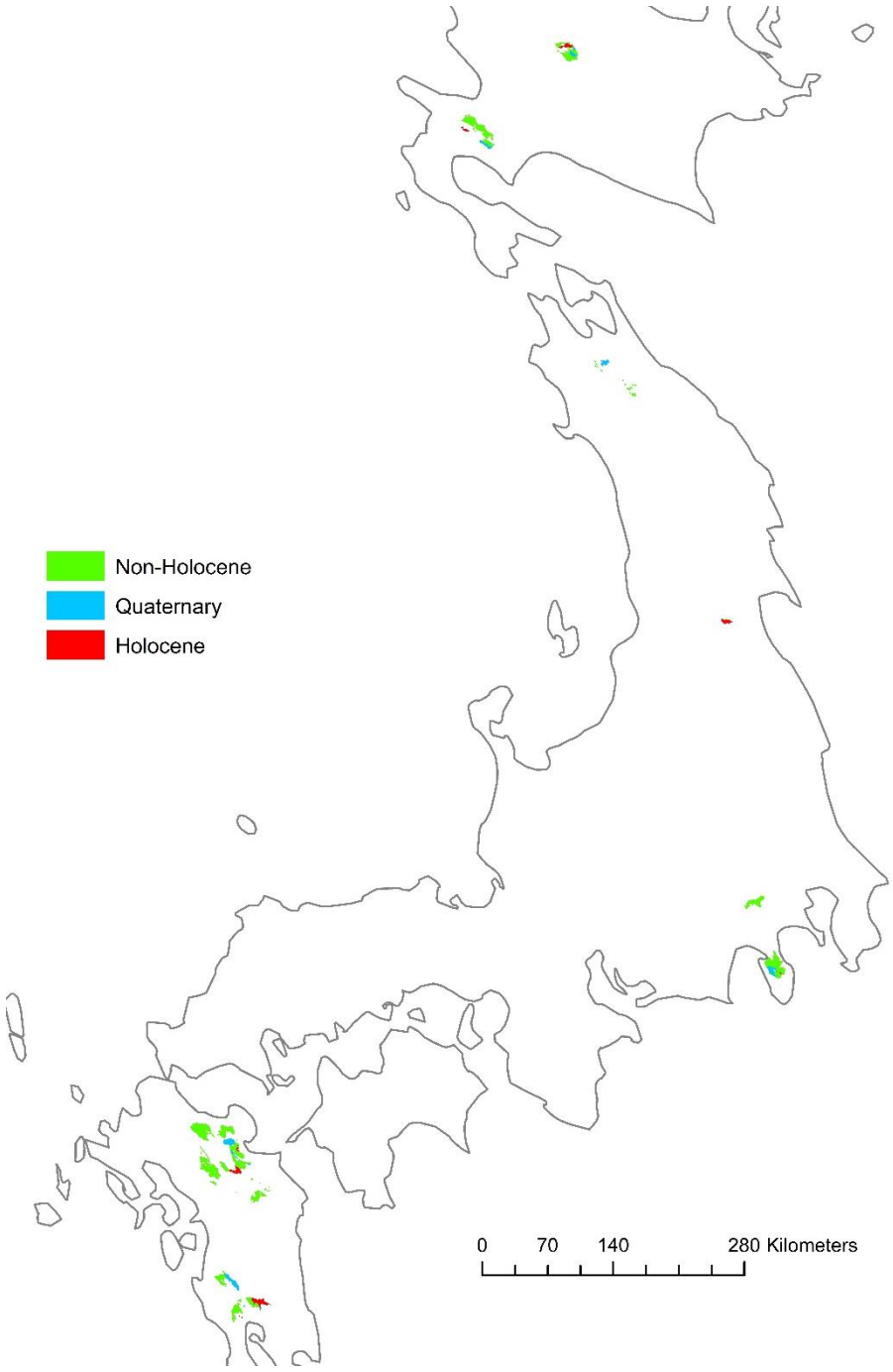

Figure C.7: Map showing the watersheds and age classification of basaltic rocks for Japan.

Kamchatka (No.27)

The information of the basaltic rocks of the Kamchatka Peninsula is taken from the GLiM, attribute xx=’vb’ (Hartmann and Moosdorf, 2012) with the age classes Holocene, non-Holocene and Quaternary. The Holocene fraction was calculated as for the Virunga province (No.23). The watershed was calculated using sampling locations of Dessert et al. (2009). The Holocene fraction of the watershed of the Kamchatka Peninsula is 2.28%.

Table C.161: Classification of basaltic rocks of the Kamchatka Peninsula after the GLiM (first three columns) and our interpretation (“System/Series”).

Rock_Description	Age_Min	Age_Max	System/Series
Basalte, Andesite und deren Tuffe	Lower Quaternary	Lower Quaternary	non-Holocene
Basalte, Andesite und deren Tuffe	Middle Quaternary	Middle Quaternary	non-Holocene
Volcanogenic formations, basic composition	Pliocene	Pliocene	non-Holocene
Basalte, Andesite und deren Tuffe	Quaternary	Quaternary	Quaternary
Volcanogenic formations, basic composition	Upper Cretaceous	Upper Cretaceous	non-Holocene
Basalte, Andesite und deren Tuffe	Upper Quaternary	Middle Quarernary	Quaternary
Basalte, Andesite und deren Tuffe	Upper Quaternary	Upper Quaternary	Holocene

Table C.17: Calculated areas of the Kamchatka Peninsula. Note that the Holocene fraction is calculated considering Holocene area, Quaternary area and total area.

Area Holocene (km^2)	Area Non-Holocene (km^2)	Area Quaternary (km^2)	Total Area (km^2)	Holocene (%)
183.60	5,588.34	2,850.52	8,622.46	2.28

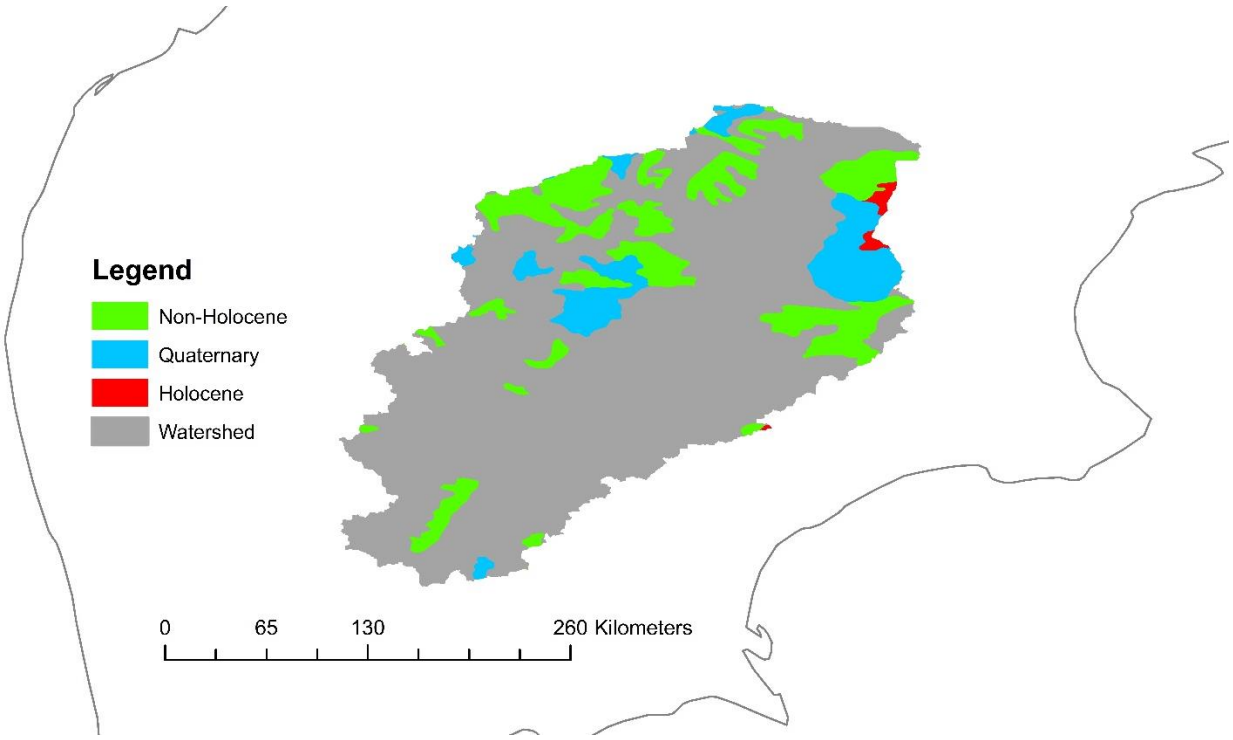

Figure C.8: Map showing the watershed of the Kamchatka Peninsula.

Taranaki (No.28)

The Taranaki volcano is located in the southern part of the Northern Island of New Zealand. Price et al. (1992) define four different regions of the Taranaki Volcanics (Paritutu, Kaitake, Pouakai and Egmont), with Mt. Egmont as the youngest one. After Price et al. (1992) and references therein the cone of Mt. Egmont represents about 8% of the total eruptive mass and is of an age of about 10 ka (Holocene). Note that Mt. Egmont is not only composed of basalts but also of basaltic andesites and andesites (Price et al., 1992). We assume here a predominantly basaltic composition.

Big Island, Hawaii' (No.29)

The geological map of Big Island of Hawaii' was digitized after a map of Stearns and Macdonald (1946). The Holocene fraction of the Kilauea and Mauna Loa was calculated as:

$$Holocene\ fraction\ of\ Quaternary\ areas = Area\ Quaternary * (\frac{11{,}700}{126{,}000}) \quad \text{(eq. C.4)}$$

with the assumption that "Latest Pleistocene" = Upper Pleistocene (0.126Ma).

The total Holocene fraction is 14.08%, calculated by:

$$Holocene\ fraction = \frac{\left(Area\ Holocene + Area\ Quaternary * \left(\frac{11{,}700}{126{,}000}\right)\right)}{Total\ area} \quad \text{(eq. C.5)}$$

Table C.18: Classification of the basaltic rocks of Big Island of Hawaii' after Stearns and Macdonald (1946) and our interpretation ("System/Series").

Id	Volcano	Description	Age	System/Series
0	Kohala Mountain	Hawii' Volcanic Series, Andesite	Pleistocene	not considered
1	Kohala Mountain	Pololu Volcanic Series	Pliocene and older	non-Holocene
2	Mauna Kea Volcano	Recent lavas	Holocene	Holocene
3	Mauna Kea Volcano	Pleistocene lavas	Pleistocene	non-Holocene
4	Mauna Kea Volcano	Hamakua Volcanic Series, capped by Pahala ash	Pleistocene	non-Holocene
5	Hualalai Volcano	Historic lavas	Holocene	Holocene
6	Hualalai Volcano	Prehistoric lavas, partly younger or older than Waawaa volcanics	Quaternary	non-Holocene
7	Hualalai Volcano	Waawaa Volcanics (pumice cone, trachyte lava flow, partly covered with basaltic lavas and Pahala ash)	Pleistocene	not considered
8	Kilauea Volcano	Historic lavas	Holocene	Holocene
9	Kilauea Volcano	Prehistoric lavas	Recent and latest Pleistocene	Quaternary
10	Kilauea Volcano	Hilina Volcanic Series, capped by Pahala ash	Pleistocene	non-Holocene
11	Mauna Loa Volcano	Historic lavas	Holocene	Holocene
12	Mauna Loa Volcano	Prehistoric lavas	Recent and latest Pleistocene	Quaternary
13	Mauna Loa Volcano	Kahuku Volcanic Series, capped by Pahala ash	Pleistocene	non-Holocene
14	Mauna Loa Volcano	Ninole Volcanic Series	Pliocene or older	non-Holocene

Table C.19: Summary of the calculated areas for Big Island of Hawaii'. The Holocene fraction was calculated applying the above-mentioned equation considering the Holocene area, Quaternary area and total area.

Area Holocene (km^2)	Area Non-Holocene (km^2)	Area Quaternary (km^2)	Total Area (km^2)	Holocene (%)
929.17	3,786.30	5,535.87	10,251.34	14.08

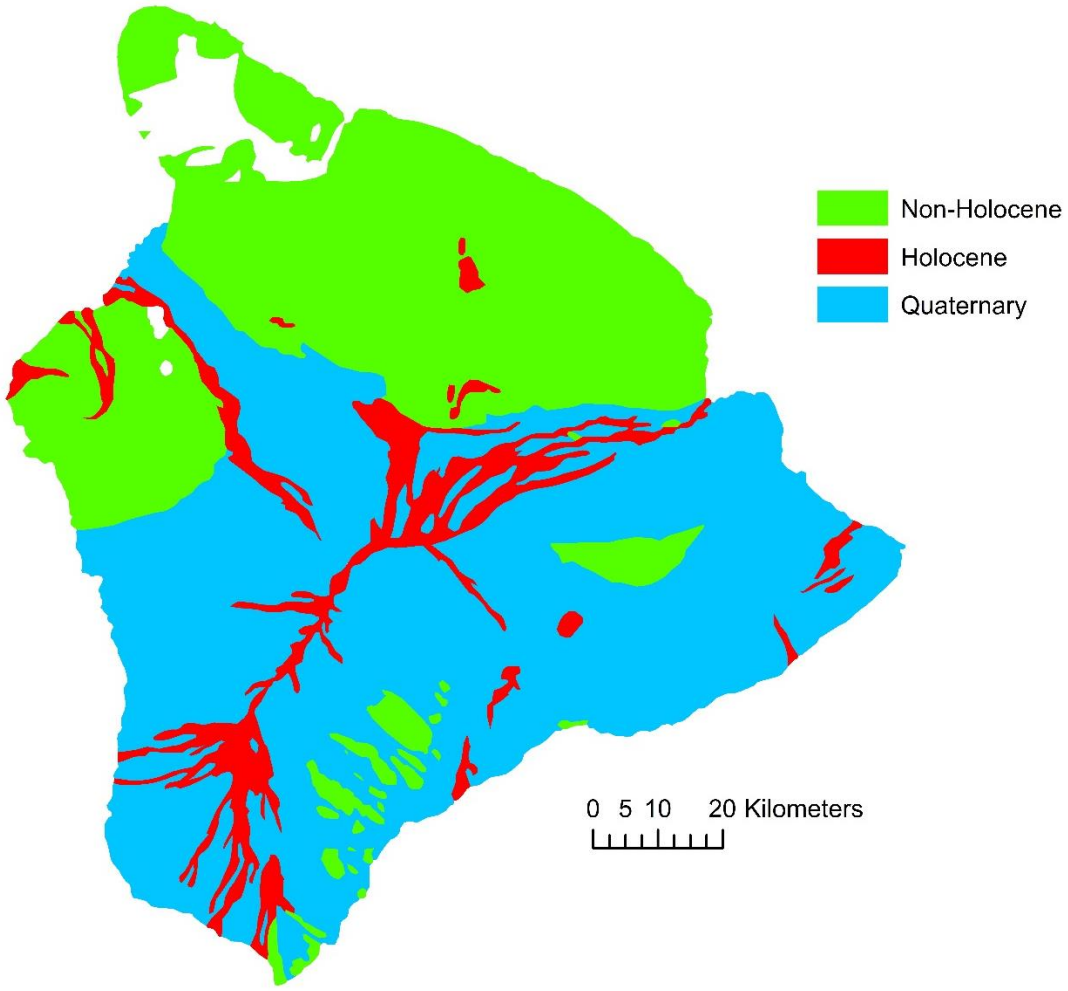

Figure C.9: Map of Big Island of Hawaii' showing the different age distributions of basaltic rocks.

High Cascades (No.30)

The geological information for the High Cascades was taken from the GLiM by Hartmann and Moosdorf (2012). The Holocene fraction was calculated as for the Virunga province (No.23) and is 0.20%. The shapefiles of the watersheds are based on the GLORICH database (Hartmann et al., 2014a).

Table C.20: Classification of the basaltic rocks of the High Cascades Region after the Global Lithological Map, attribute xx='vb' (first three columns) and our interpretation ("System/Series").

Rock_Description	Age_Min	Age_Max	System/Series
Basalt;	Early to Middle Miocene	Early to Middle Miocene	non-Holocene
Tholeiite; siltstone	Eocene	Eocene	non-Holocene
Basalt; andesite	Late Eocene to Oligocene	Late Eocene to Oligocene	non-Holocene
Mafic volcanic rock;	Late Miocene to Pliocene	Late Miocene to Pliocene	non-Holocene
Basalt; volcanic breccia (agglomerate)	Middle Eocene to Late Eocene	Middle Eocene to Late Eocene	non-Holocene
Basalt (tholeiite); andesite	Middle Miocene	Middle Miocene	non-Holocene
Basalt;	Middle Miocene	Middle Miocene	non-Holocene
Andesite; basalt	Middle to Late Miocene	Middle to Late Miocene	non-Holocene
Basalt; andesite	Miocene	Miocene	non-Holocene
Basalt; rhyolite	Miocene-Pliocene	Miocene-Pliocene	non-Holocene
Basalt; volcanic breccia (agglomerate)	Oligocene to Miocene	Oligocene to Miocene	non-Holocene
Basalt; andesite	Pleistocene to Holocene	Pleistocene to Holocene	Quaternary
Basalt; andesite	Pliocene to Pleistocene	Pliocene to Pleistocene	non-Holocene
Andesite; basalt	Quaternary	Quaternary	Quaternary
Andesite; basalt	Tertiary (2-24 Ma)	Tertiary (2-24 Ma)	non-Holocene
Andesite; basalt	Miocene	Miocene	non-Holocene

Table C.21: Summarized area calculation for the watersheds of the High Cascades. The Holocene fraction was calculated as for the Virunga province (No. 23).

Area Holocene (km^2)	Area Non-Holocene (km^2)	Area Quaternary (km^2)	Total Area (km^2)	Holocene (%)
0	3,033.92	2,479.39	5,513.31	0.20

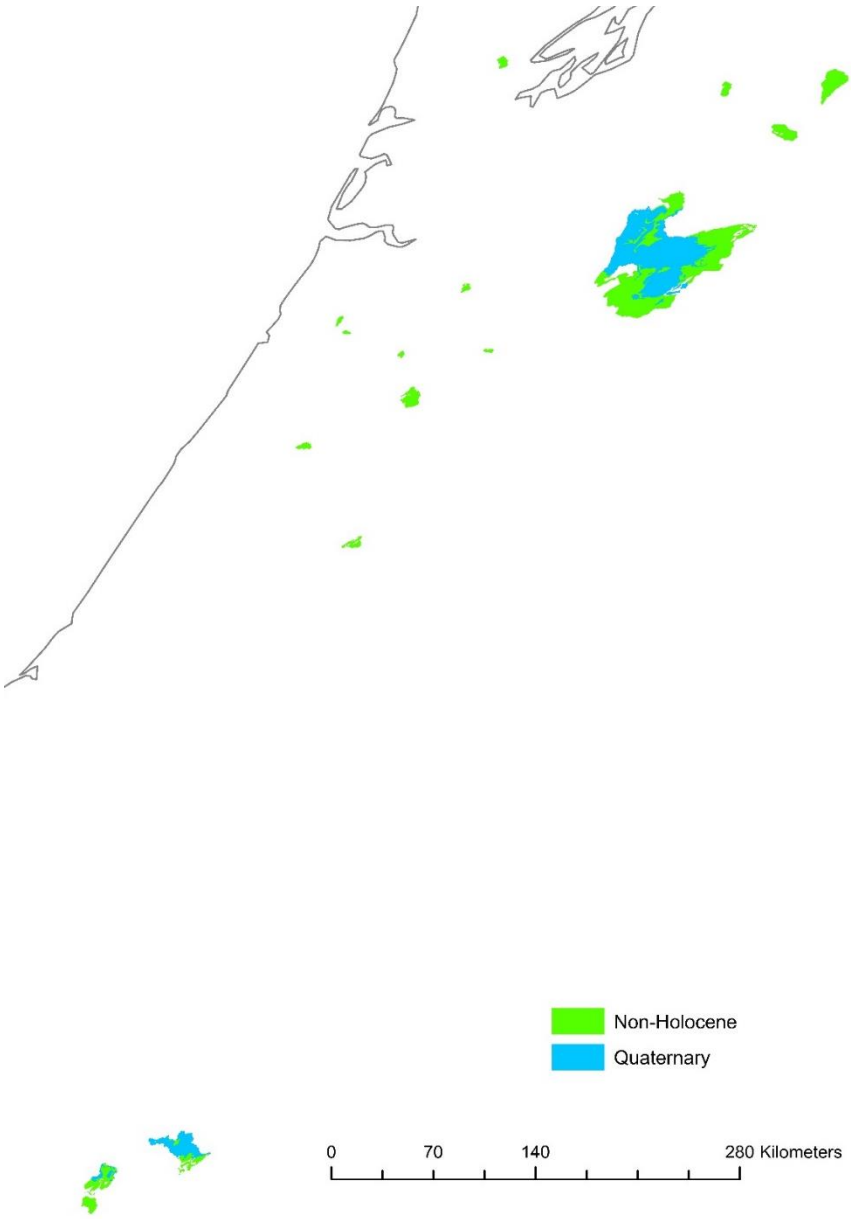

Figure C.10: Map of the watersheds of the High Cascades.

Iceland (No.31)

The information of the basaltic rocks of Iceland are taken from the GLiM (Hartmann and Moosdorf, 2012) and are classified into Holocene, non-Holocene and Quaternary (for the calculation see Virunga Province, No. 23) and results in a Holocene coverage of 13.19%.

Table C.22: Description of the basaltic rocks of Iceland after the GLiM, attribute xx='vb' (first three columns) and our interpretation ("System/Series").

Rock_Description	Age_Min	Age_Max	System/Series
Basalt and andesite	Holocene (postglacial time)	Holocene (postglacial time)	Holocene
Basic and intermediate hyaloclastites, lavas and associated sediments	Late Pleistocene	Late Pleistocene	non-Holocene
Basic and intermediate lavas and pyroclastic rocks (mainly hyaloclastite)	Late Pliocene, Early Pleistocene, 3.3 -	Late Pliocene, Early Pleistocene, 3.3 -	non-Holocene
Ocean-floor basalt; on land also intermediate volcanic rocks and sedimentary rocks	Miocene	Miocene	non-Holocene
Basic and intermediate volcanic rocks with intercalated sedimentary rocks	Miocene-Early Pliocene, older than 3.3 M	Miocene-Early Pliocene, older than 3.3 M	non-Holocene
Ocean-floor basalt	Pliocene	Pliocene	non-Holocene
Ocean-floor basalt	Quaternary	Quaternary	Quaternary

Table C.23: Summary of the area calculation for Iceland. Note that the Holocene fraction is calculated as for the Virunga province (No. 23).

Area Holocene (km^2)	Area Non-Holocene (km^2)	Area Quaternary (km^2)	Total Area (km^2)	Holocene (%)
13,196.86	86,773.61	104.36	100,074.83	13.19

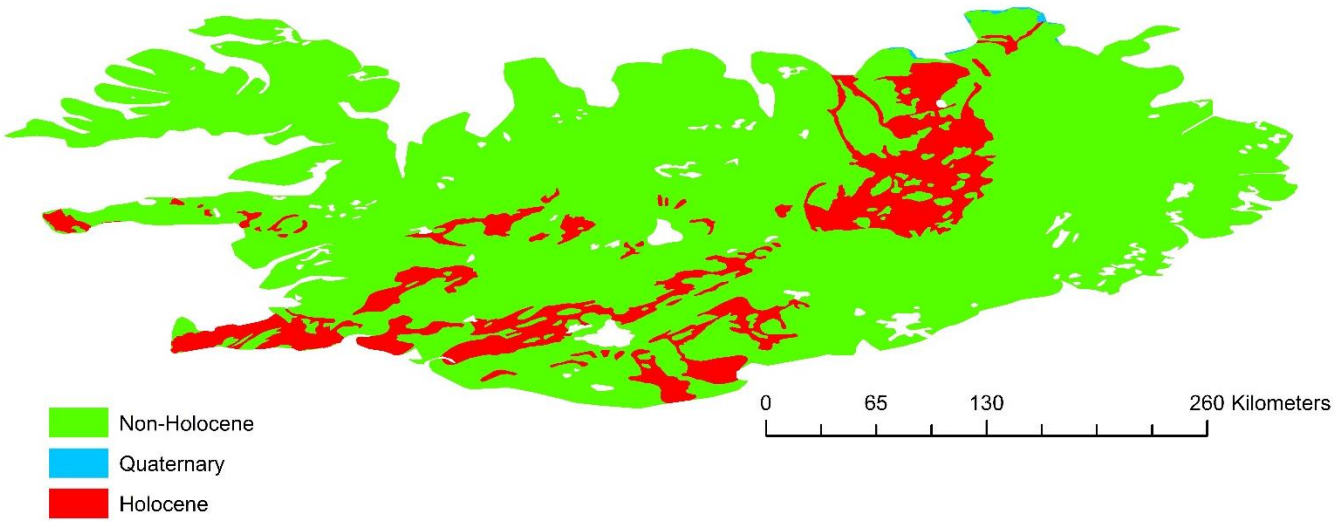

Figure C.11: Map of Iceland showing the distribution of the age of basaltic rocks.

São Miguel Island (No.32)

São Miguel Island is related to a Hot Spot in the northern Atlantic. The geological map was digitized after Moore (1990). There are only two watersheds considered in this study (Freire et al., 2013). It was assumed that the Holocene area is proportional to the Holocene time span relative to the given mapped Quaternary age:

Qu1 (Agua de Pau Volcano, 0 – 200 ka):

$$Holocene\ fraction = Area\ Qu1 * (\frac{11{,}700}{200{,}000}) \quad \text{(eq. C.6)}$$

Qu2 (Furnas Volcano, 0 – 100 ka):

$$Holocene\ fraction = Area\ Qu2 * (\frac{11{,}700}{100{,}000}) \quad \text{(eq. C.7)}$$

The final Holocene fraction is 9.35% and is calculated by:

$$Holocene\ fraction = \frac{Area\ Qu1 * \left(\frac{11{,}700}{200{,}000}\right) + Area\ Qu2 * \left(\frac{11{,}700}{100{,}000}\right)}{Total\ Area} \quad \text{(eq. C.8)}$$

The watershed areas are of trachytic composition, therefore São Miguel was excluded from the calculations (eq. 14) but were kept for comparison because of the generally basaltic environment of the island.

Table C.24: Classification of the rocks of the watersheds of São Miguel from the original data and our interpretation ("System/Series").

Id	Name	Type	Age	System/Series
2	Agua de Pau Volcano	Trachyte stratovolcano	0-200ka	Qu1
4	Furnas Volcano	Trachyte stratovolcano	0-100ka	Qu2

Table C.25: Summary of the calculated areas of the watersheds of São Miguel. The Holocene fraction was calculated by the above-mentioned equation.

Area Holocene (km^2)	Area Non-Holocene (km^2)	Area Qu1 (km^2)	Area Qu2 (km^2)	Total Area (km^2)	Holocene (%)
0	0	18.86	28.18	47.04	9.35

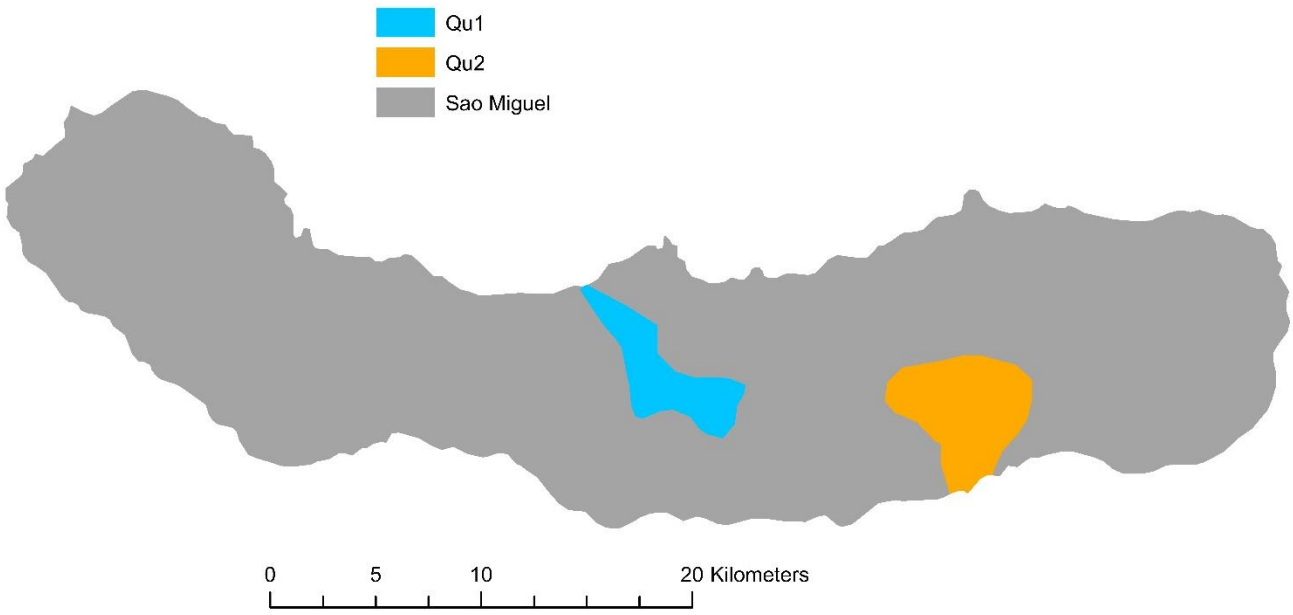

Figure C.12: Map of São Miguel showing the two watersheds considered in this study.

Tianchi Lake (No.33)

The geological map of the Tianchi Lake region was digitized after Paone and Yun (2016). The rocks are directly separated into Holocene and non-Holocene age. The total catchment area is 11.31 km² and the Holocene fraction area is 65.34%. The value for the runoff was calculated after Fekete et al. (2002).

Table C.26: Description of the rocks of Tianchi Lake after Paone and Yun (2016) (first column) and our interpretation ("System/Series").

Description	**System/Series**
Second fan-shaped debris flow - Holocene	Holocene
Rock-fall deposit - Holocene?	Holocene
1668 dark trachytic ignimbrite and surge - Holocene	Holocene
Third fan-shaped debris flow - Holocene	Holocene
1903 phreatomagmatic eruption - Holocene	Holocene
Baitoushan III upper trachyte cone with comendite, 0.02-0.22 Ma	non-Holocene
Baithoushan II middly trachyte cone and ignimbrite, 0.25-0.44 Ma	non-Holocene

Since the lithology is mostly described as trachytic, Tianchi Lake was excluded from the calculations (eq. 14) but kept in this study for comparison.

Table C.27: Summary of the area calculation for Tianchi Lake. The Holocene fraction was calculated by the ratio of Holocene area/Total area.

Area Holocene (km^2)	**Area non-Holocene (km^2)**	**Area Quaternary (km^2)**	**Total Area (km^2)**	**Holocene (%)**
7.39	3.92	0	11.31	65.34

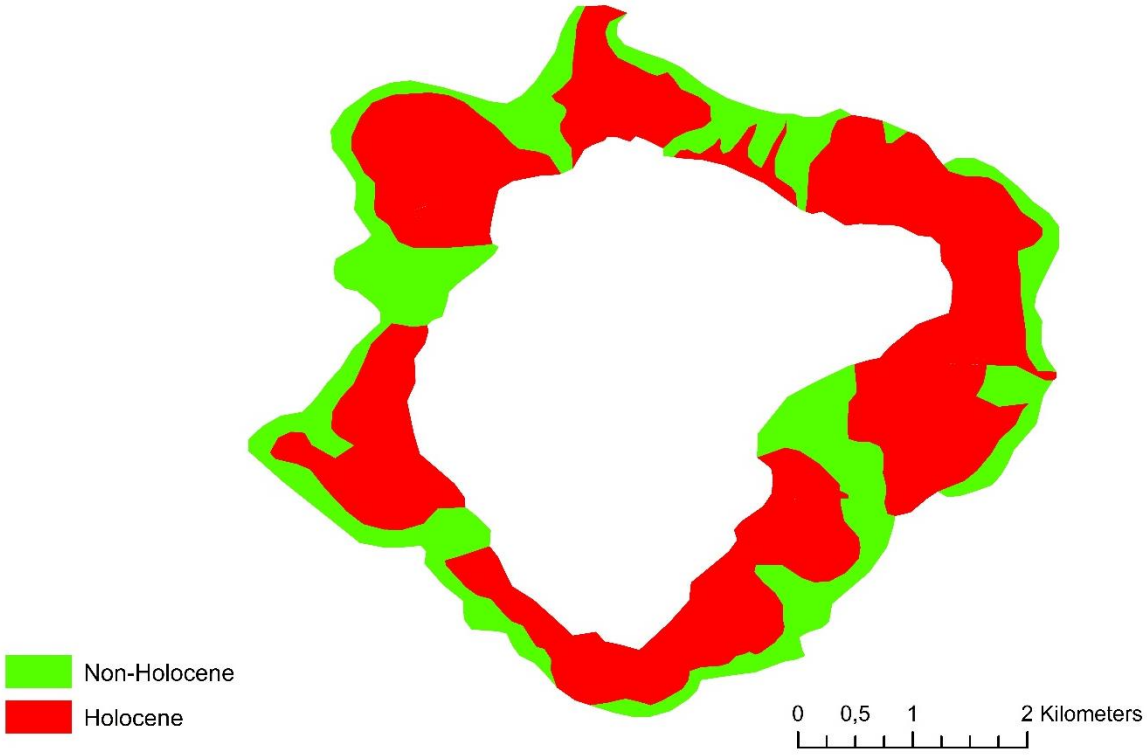

Figure C.13: Map of Tianchi Lake and its surrounding lithology showing the distribution of the age of rocks.

C.3 Saturation state with respect to calcite

Data used in the previous study of Li et al. (2016) was derived by published literature and the GLORICH database (Hartmann et al., 2014a), but also new river sites of China are included (for more details see Supplementary information of Li et al. (2016). Li et al. (2016) used either alkalinity or DIC concentrations to calculate the alkalinity flux rates of the individual basaltic volcanic areas. They calculated the alkalinity flux rates by multiplying the mean concentration of dissolved inorganic carbon (DIC) by the annual runoff.

For six areas full water chemistry data are available (High Cascades, Japan, Northeast America, Southeast Australia, South Africa and Tasmania), while for others either pH or major cations were not available. For these available data (103 catchments) the saturation index for calcite was calculated. In general, water samples are undersaturated with respect to calcite (77%). From the oversaturated samples 50% have values close to 0 with a saturation index SI < 0.5. A SI ~ 0.5 is the typical value for rivers in limestone areas (Romero-Mujalli et al., 2018a). The other 12 values are between SI = 0.5 and 0.9 and according water sample locations are mostly in dry areas of South Africa or Australia.

In general, younger active areas have significant contributions of magmatic SO_4 or Cl, which shifts the saturation states normally further to lower, negative values. We cannot conclude from the river data what happens in the aquifer system but reference the study of Jacobson et al. (2015) in the main text. They quantified the contribution of trace calcite dissolution from basalt using Ca-isotope data.

C.4 Additional relations between Alkalinity, Reactivity and Holocene area fraction

In addition to results provided in the main text further relationships among applied parameters are shown.

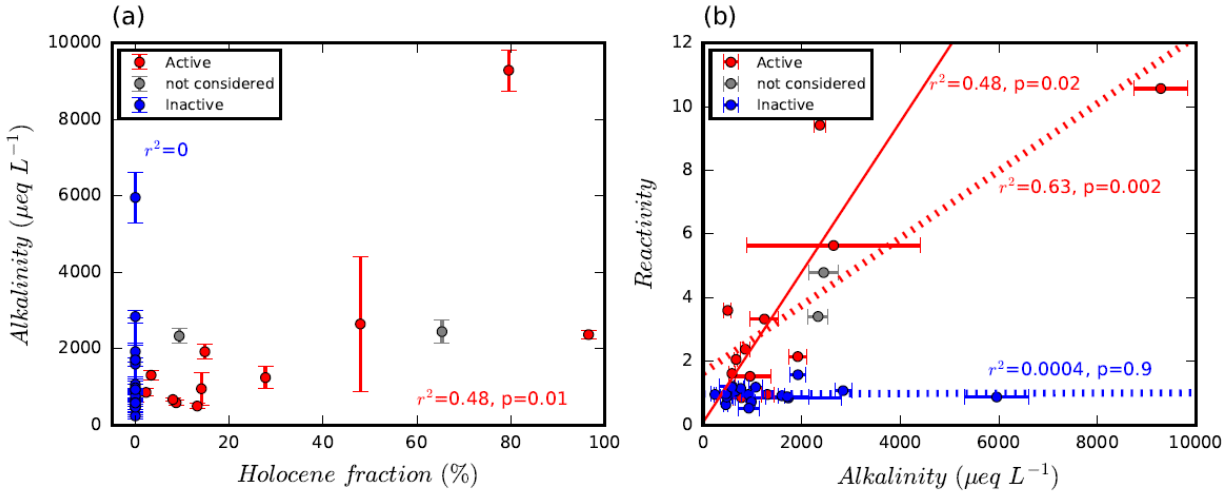

Figure C.14: Scatterplot relationships between alkalinity, Holocene fraction and Reactivity. a) Holocene fraction versus alkalinity concentrations (blue: IVFs, red: AVFs). b) Alkalinity concentration versus Reactivity: For the AVFs the coefficient of determination is r^2=0.63 (p=0.002). However, if removing the one "outlier" with elevated alkalinity concentration (Mt. Etna), it is not concluded that elevated alkalinity concentrations are responsible in general for observed elevated Reactivity of AVFs, considering the

alkalinity concentration distribution for IVF. However, a relevant correlation exists between alkalinity and Reactivity for AVFs. The solid red regression line shows the correlation of AVFs excluding Mt. Etna (r^2=0.48, p=0.02).

C.5 Estimation of the parameters for the new scaling law

The new scaling law for alkalinity fluxes (eq. 14) was derived by a Monte Carlo method. Temperature and alkalinity flux rates were selected randomly 10,000 times within the range of ± one standard deviation for each volcanic field:

$$X = \bar{x} + std * (2 * rand - 1) \quad \text{(eq. C.9)}$$

With X = calculated random value for temperature or alkalinity flux rate,

$\bar{x}$ = mean value of temperature or alkalinity flux rate,

std = standard deviation of temperature or alkalinity flux rate

"Rand" is a function from Matlab software, which creates uniformly distributed random numbers between 0 and 1 (The MathWorks Inc.: MATLAB R2016a).

The calculated standard deviations of weighted mean values σ_m for temperature and alkalinity flux rates (Tab. C.1) are taken from Li et al. (2016). The new scaling law is represented by the equation:

$$Alkalinity\ flux\ rate = (1 + b1 * Holocene\ fraction) * b2 * e^{b3 * Temperature} \quad \text{(eq. C.10)}$$

Applying the Levenberg-Marquardt algorithm to the 10,000 sets of alkalinity flux rates and temperature the following mean b-parameters of the equation were found:

b_1 = 0.10 with standard deviation=0.02 and median = 0.10

b_2 = 0.23 with standard deviation=0.09 and median = 0.23

b_3 = 0.06 with standard deviation=0.02 and median = 0.06

The root mean square error (RMSE) of eq. 14 is 0.3, calculated by the following equation:

$$RMSE = \sqrt{\frac{\sum(residual)^2}{n-2}} \quad \text{(eq. C.11)}$$

Calculating the regression of calculated alkalinity flux rates and estimated alkalinity flux rates by the new scaling law provides an r^2=0.96 and $p<10^{-3}$.

The linear regression of Holocene fractions and Reactivity for AVFs gives an r^2=0.93 and p=0.01.

C.6 Global calculations of CO_2 consumption by basalt weathering

The global CO_2 consumption fluxes (Tab. C.28 and C.29, and Tab. 7) were calculated 10,000 times for each grid cell using the produced set of b-parameters (Levenberg-Marquardt-algorithm see above, Appendix C.5), global temperature and runoff information (Fekete et al., 2002; Hijmans et al., 2005), as well as the new global basalt map (Fig. C.15). Finally, we calculated the mean values of the set of global CO_2 consumption rates, the standard deviations and the percentiles for 25% and 75% of the global fluxes. The standard deviations and percentiles represent the dispersion of random correlations and not the uncertainty given by the residuals.

The global basalt map, mostly based on the GLiM (Fig. C.15) distinguishes Holocene, Cenozoic and non-Cenozoic basaltic areas. The calculations were conducted with a 20 km grid resolution.

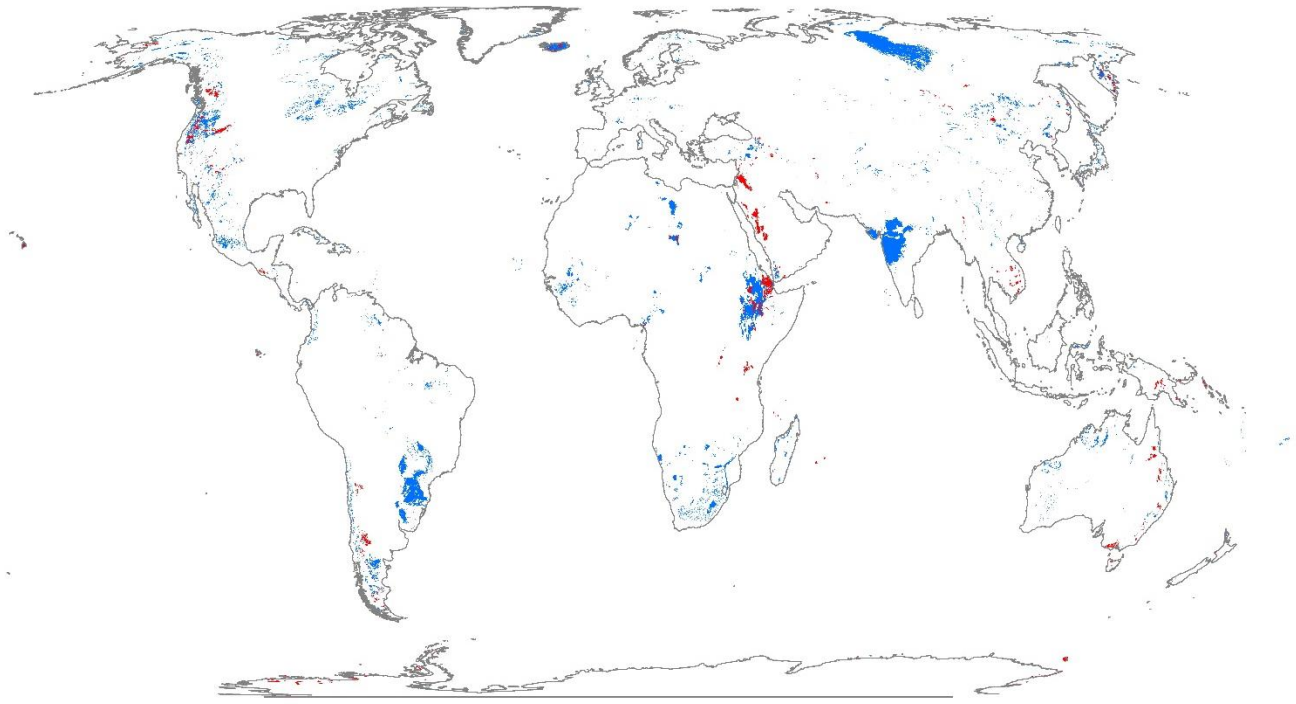

Figure C.15: Global distribution of basalt areas distinguishing Cenozoic (red) and Non-Cenozoic areas (blue). The reported Holocene fractions of the Cenozoic areas are considered in the global calculation. Some areas with missing age information were considered as of non-Holocene age and may result in a smaller global Holocene area fraction applied for global calculations. The map is described in Appendix C.7.

For comparison the global CO_2 consumption was calculated only once by applying the new scaling law with the mean of the set of three b-parameters to every grid cell, and using the global datasets of temperature and runoff (Fekete et al., 2002; Hijmans et al., 2005), as well as the global basalt map. Here, the global flux with runoff restriction is 2×10^{12} mol a^{-1}.

Adding the root mean square error of the 10,000 global calculations of the CO_2 consumption from above to every grid cell results in a flux of 3×10^{12} mol a^{-1} and substracting the root mean square

error to every grid cell results in 1 x 10^{12} mol a^{-1}, which is representing the range of uncertainty. This range of uncertainty might be overestimating the uncertainty for low CO_2 consumption values and underestimating the uncertainty for high CO_2 consumption values, since the residuals are not normally distributed.

Table C.28: Global calculations of CO_2 consumption for areas with a runoff >74mm/a. As reference previous global empirical equations (Amiotte-Suchet and Probst, 1995; Bluth and Kump, 1994; Dessert et al., 2003; Goll et al., 2014, without soil shielding to mimic the relevance of temperature) were applied to derive global CO_2 consumption values. The values of the new scaling law in this table and in Tab. C.29 are given by simulating 10,000 runs (see above). "p25" and "p75" represent the calculated percentiles of 25% and 75%, respectively and "std" the standard deviation.

	Total Area [km^2]	Holocene Area [km^2]	% of global basalt area	CO_2 consumption [10^6 mol/a]								Area [km^2] for q>74mm/a	Holocene area [km^2] for q>74mm/a
				Goll et al., 2014	Dessert et al., 2003	Amiotte-Suchet & Probst, 1995	Bluth & Kump, 1994	New scaling law	p25	p75	std		
Fluxes from purely Holocene areas	48,593	48,593	0.92	15,531	17,453	13,560	10,060	100,037	89,216	109,234	14,487	29,213	29,213
Raster with Holocene influence (Cenozoic)	903,600	48,593	17.03	225,938	239,122	112,221	88,208	283,726	276,351	292,969	13,074	338,800	29,213
Raster without Holocene influence (Non-Cenozoic)	4,401,200	-	82.97	1,340,243	1,430,216	750,618	658,218	1,646,033	1,586,658	1,708,683	91,215	3,059,600	-
TOTAL	5,304,800	48,593	100.00	1,566,181	1,669,338	862,839	746,427	1,929,759	1,868,357	1,992,574	92,519	3,398,400	29,213

Table C.29: Global CO_2 consumption by basalt weathering without runoff restriction as applied in Tab. C.28.

	Total Area [km^2]	Holocene Area [km^2]	% of global basalt area	CO_2 consumption [10^6 mol/a]							
				Goll et al., 2014	Dessert et al., 2003	Amiotte-Suchet & Probst, 1995	Bluth & Kump, 1994	New scaling law	p25	p75	std
Fluxes from purely Holocene areas	48,593	48,593	0.92	15,646	17,577	13,628	10,209	209,602	195,275	223,222	19,264
Raster with Holocene influence (Cenozoic)	903,600	48,593	17.03	227,716	241,036	113,265	90,347	735,004	707,519	763,323	38,618
Raster without Holocene influence (Non-Cenozoic)	4,401,200	-	82.97	1,351,814	1,442,505	756,928	670,733	2,534,801	2,434,265	2,646,095	161,340
TOTAL	5,304,800	48,593	100.00	1,579,530	1,683,541	870,193	761,081	3,269,805	3,150,147	3,404,366	193,745

C.7 Enhanced global basalt map beyond GLiM

A new global basalt map was created combining several datasets. Main input is the Global Lithological Map (GLiM) (Hartmann and Moosdorf, 2012). New, additional data were taken from geological maps that were considered for the development of the Global Unconsolidated Sediments Map database (GUM) (Börker et al., 2018) and the individual active volcanoes described in this study. For the individual calculation of Holocene percentages see following tables.

Table C.30: Table showing the ages of the basaltic fields of the GLiM with the authors interpretation (third column). Note that only areas with Holocene fraction are listed. All other age descriptions of the GLiM were considered as of non-Holocene age.

Age_Min	**Age_Max**	**HoloceneArea**
Cainozoic	Cainozoic	0.02
Cenozoic	Cenozoic	0.02
Oligocene	Cainozoic	0.02
Quaternary	Tertiary	0.02
Quaternary	Cainozoic	0.02
Quaternary and Tertiary	Quaternary and Tertiary	0.02
QUATERNARY OR TERTIARY	QUATERNARY OR TERTIARY	0.02
Tertiary(?) and Quaternary	Tertiary(?) and Quaternary	0.02
Tertiary-Quaternary	Tertiary-Quaternary	0.02
Oligocene and younger	Oligocene and younger	0.03
Holocene	Miocene	0.05
Miocene to Holocene	Miocene to Holocene	0.05
Miocene to Quaternary	Miocene to Quaternary	0.05
Neogene	Quaternary	0.05
Neogene to Holocene	Neogene to Holocene	0.05
Quaternary	Neogene	0.05
PLIOCENO-PLEISTOCENO-HOLOCENO	PLIOCENO-PLEISTOCENO-HOLOCENO	0.22
Quaternary	Pliocene	0.22
Quaternary to Pliocene	Quaternary to Pliocene	0.22
Quaternary (0-4 Ma)	Quaternary (0-4 Ma)	0.29
Middle Pliocene to Holocene	Middle Pliocene to Holocene	0.33
Holocene	Pleistocene	0.45
Pleistocene to Holocene	Pleistocene to Holocene	0.45
Quaternary	Upper Quaternary	0.45
Quaternary	Pleistocene	0.45
Quaternary	Quaternary	0.45
Upper Quaternary	Middle Quarernary	0.45
Late Pleistocene to Holocene	Late Pleistocene to Holocene	9.29
Holocene	Holocene	100
Holocene (postglacial time)	Holocene (postglacial time)	100
Upper Quaternary	Upper Quaternary	100

Table C.31: Table showing the age classifications of additional data of several geological maps that were used for the GUM database with our interpretation (third column). Only the quaternary lithologies were considered. Map sources are: Afghanistan (Doebrich et al., 2006), Australia (Raymond et al., 2012), Austria (Geologische Bundesanstalt (GBA), 2013), Canada (Fulton, 1995), China (China Geological Survey, 2002), Colombia (Gomez Tapias et al., 2015), Ethiopia (Tefera et al., 1996), Japan (Geological Survey of Japan AIST (ed.), 2009), Germany (Bundesanstalt für Geowissenschaften und Rohstoffe, 2007), Tanzania (Geological Survey of Tanzania, Geo-Economic Data (1:2M) - Geology, http://www.gmis-tanzania.com/, accessed May 2016), USA (Soller et al., 2009).

Age_Min	**Age_Max**	**HoloceneArea**
1 M	0.26 M	0
2.5 M	0.26 M	0
0.215 M	0.19 M	0
Sarmatian/Pannonian	Plio/Pleistocene	0
Pliocene	Pleistocene	0
2.5 M	0.01 M	0
Early Pleistocene	Early Pleistocene	0
0.780	0.126	0
Middle Pleistocene	Middle Pleistocene	0
Late Pleistocene	Late Pleistocene	0
Pleistocene	Pleistocene	0
Middle Pleistocene	Late Pleistocene	0
Early Pleistocene	Middle Pleistocene	0
Cenozoic	Cenozoic	0.02
23 Ma	0 Ma	0.05
Pliocene	Holocene	0.22
Quaternary	Quaternary	0.45
Late Pleistocene	Holocene	9.29
Holocene	Holocene	100

Appendix D: Individual contributions to the list of publications

Börker, J., Hartmann, J., Amann, T., and Romero-Mujalli, G.: Terrestrial Sediments of the Earth: Development of a Global Unconsolidated Sediments Map Database (GUM), Geochemistry, Geophysics, Geosystems, 19, 997-1024, 10.1002/2017gc007273, 2018.

Authors's contribution: Idea, methods and data acquisition, results and discussion

Börker, J., Hartmann, J., Amann, T., Romero-Mujalli, G., 2018. Global Unconsolidated Sediments Map Database v1.0 (shapefile and gridded to 0.5° spatial resolution), https://doi.org/10.1594/PANGAEA.884822, Supplement to: Börker, J., Hartmann, J., Amann, T., and Romero-Mujalli, G.: Terrestrial Sediments of the Earth: Development of a Global Unconsolidated Sediments Map Database (GUM), Geochemistry, Geophysics, Geosystems, 19, 997-1024, 10.1002/2017gc007273, 2018.

Author's contribution: Provided map database for upload

Börker, J., Hartmann, J., Romero-Mujalli, G., and Li, G.: Aging of basalt volcanic systems and decreasing CO2 consumption by weathering, Earth Surf. Dynam., 7, 191-197, 10.5194/esurf-7-191-2019, 2019.

Author's contribution: Methods, results and discussion

Huscroft, J., Gleeson, T., Hartmann, J., and **Börker, J.**: Compiling and mapping global permeability of the unconsolidated and consolidated Earth: GLobal HYdrogeology MaPS 2.0 (GLHYMPS 2.0), Geophysical Research Letters, 45, 1897-1904, 10.1002/2017GL075860, 2018.

Author's contribution: Provided the map as basis for the development of the GLHYMPS 2.0. Furthermore, discussion part and methods section.

Romero-Mujalli, G., Hartmann, J., **Börker, J.**, Gaillardet, J., and Calmels, D.: Ecosystem controlled soil-rock pCO2 and carbonate weathering – Constraints by temperature and soil water content, Chemical Geology, https://doi.org/10.1016/j.chemgeo.2018.01.030, 2018.

Author's contribution: discussion

Romero-Mujalli, G., Hartmann, J., and **Börker, J.**: Temperature and CO2 dependency of global carbonate weathering fluxes – Implications for future carbonate weathering research, Chemical Geology, https://doi.org/10.1016/j.chemgeo.2018.08.010, 2018.

Author's contribution: discussion

In preparation:

Börker, J., Hartmann, J., Amann, T., Romero-Mujalli, G., Moosdorf, N. and Jenkins, C.: Chemical weathering of loess during the Last Glacial Maximum, Mid-Holocene and today.

Author's contribution: methods, data acquisition, results and discussion

Acknowledgments

First of all, I want to thank my supervisor Jens Hartmann for his continuous support, as well as Thorben Amann, who always had an open ear. Moreover, I would like to thank Lars Kutzbach for his support during the PhD project. Besides, I would like to thank Victor Brovkin and the PalMod-project for their support.

I also want to thank my work colleagues Tom, Peggy and Wagner. I am delighted by being part of such a nice working group.

SICSS is thanked for financial support and crosscutting discussions, and many new friendships that came out of it.

Tausend Dank an meine Familie, die mich immer unterstützt und motiviert hat, insbesondere an Petra, Jörg und Bina, danke, dass ihr immer an mich geglaubt habt. Ich bin euch sehr sehr dankbar! Vieles von dieser Arbeit hätte ich ohne Euch nicht realisieren können.

Gibran, you were not only my officemate but with the time became a really good friend. Muchas gracias por todo! And Jairo, thank you for always taking good care of me in the stressful phases, thanks for being part of my team.

Eidesstattliche Versicherung

Hiermit versichere ich an Eides statt, dass ich die vorliegende Dissertation mit dem Titel: „Quantifications of global chemical weathering fluxes applying new lithological maps and new parameterizations“ selbstständig verfasst und keine anderen als die angegebenen Hilfsmittel – isnbesondere keine im Quellenverzeichnis nicht benannten Internet-Quellen – benutzt habe. Alle Stellen, die wörtlich oder sinngemäß aus Veröffentlichungen entnommen wurden, sind als solche kenntlich gemacht. Ich versichere weiterhin, dass ich die Dissertation oder Teile davon vorher weder im In- noch im Ausland in einem anderen Prüfungsverfahren eingereicht habe und die eingereichte schriftliche Fassung der auf dem elektronischen Speichermedium entspricht.

Hamburg, den 06.03.2019

Janine Börker